Alma Mater Studiorum - Università di Bologna

DOTTORATO DI RICERCA IN

INGEGNERIA BIOMEDICA, ELETTRICA E DEI SISTEMI

Ciclo 33

Settore Concorsuale: 09/E2 - INGEGNERIA DELL'ENERGIA ELETTRICA

Settore Scientifico Disciplinare: ING-IND/33 - SISTEMI ELETTRICI PER L'ENERGIA

TESTING AND MODELLING NANOSTRUCTURED INSULATION FOR CAPACITOR AND CABLES USED FOR STORAGE AND DELIVERY OF ELECTRICAL ENERGY

Presentata da: Hadi Naderiallaf

Coordinatore Dottorato

Michele Monaci

Supervisore

Gaetano Pasini

Esame finale anno 2021

Alma Mater Studiorum - Università di Bologna

Abstract

Department of Electrical, Electronic and Information Engineering "Guglielmo Marconi"

Doctor of Philosophy

Testing and modelling nanostructured insulation for capacitor and cables used for storage and delivery of electrical energy

by Hadi Naderiallaf

The measurement of partial discharges (PD) is a commonly used tool to evaluate the healthiness of electrical insulation materials in high voltage systems such as HVDC cables. PD measurement is an important non-destructive test from predictive maintenance and asset management of high voltage equipment point of view which its activity can lead to premature failure. Modelling PD characteristics such as PD charge amplitude, PD repetition rate and partial discharge inception voltage (PDIV) is performed to provide an effective fundamental tool for the development of reliable quality control, commissioning tests and diagnostics procedures. In addition, a theoretical and analytical PD model can help in planning tests and evaluating the likelihood and meaningfulness of test data.

In this PhD thesis PD characteristics such as charge amplitude, repetition rate and PDIV are modelled base on PD RC equivalent circuit from AC to DC. The PD models were validated against experimental data obtained from laboratory testing on multilayer specimens at University of Bologna. The PDIV model under DC applying voltage was also validated after performing PD measurements on MV cable as a function of different temperatures (loads) in Technical University of Berlin. Then, the PD models were used to design a real HVDC insulation system to endure electrical and thermal stresses under operation using COMSOL Multiphysics simulations.

Finally, the effect of adding nano Silica with different functionalization to cable grade polymeric materials on electric and dielectric properties such as space charge, electrical conductivity, dielectric strength, and life test were investigated and evaluated experimentally.

Contents

Acknowledgements

The realization of this thesis was greatly assisted by the support and friendship of many people throughout my time at Bologna.

I am very grateful to my main supervisor, Prof. Gian Carlo Montanari, for his consistent support and unique commitment to comment and correct my weekly reports for more than 110 weeks as well as his precious insightful discussions even after leaving University of Bologna. I would like to thank my secondary supervisor, Dr. Paolo Seri, for his discussions and advice. My gratitude also goes to Prof. Andrea Cavallini and Prof. Gaetano Pasini for their scientific and technical support and insight that improved my own understanding.

In all respects and during my research, I have been constantly assisted by the encouragement of my wife and family. I am eternally very thankful for the love and support of my wife, Zahra, along with her sage advice to occasionally stop working and for her enthusiasm and interest in my research. I am profoundly grateful for the love and good humor of my mother and my father.

I am also grateful to Fabrizio Palmieri and Leonardo Cirioni for their technical support during my experiments.

This project has received funding from the European Union's Horizon 2020 research and innovation program under grant agreement No 720858 which is gratefully acknowledged.

Chapter 1

Introduction

DC power cables are taking an increasing share of R&D projects, owing to the growing need of transmission on long distances, the diffusion of renewable power generation, as well as the increasing reliability and decreasing conversion losses. One of the plausible accelerated aging factors is partial discharges, PD, which can incept in insulation defects (cavities or interfaces) leading to insulation breakdown in times shorter than those specified and considered at the design stage.

Partial discharge (PD) measurement is a prevalent technique to evaluate both the quality of insulation system during manufacturing and commissioning as well as a powerful diagnostic tool in service. Indeed, PD can be the cause of insulation premature failure, being able to break organic polymer bonds, but also the result of aging mechanisms driven by operating stresses, for instance thermal (load) cycling, mechanical and electrical stresses such as energization and polarity inversion. Hence, measuring PD is a fundamental diagnostic tool to ensure insulation system reliability.

There are considerable HVDC and EHVDC projects undergoing, and already existing installations involving DC cables. Compared to AC, the major issue related to DC PD measurements is the absence of time-resolved patterns which complicates dramatically the problems of noise rejection and PD source identification. Under AC, the phase-resolved PD (PRPD) pattern can help experts to discriminate PD from other pulses, such as noise or external disturbances as well as diagnose the type of defect generating PD.

Modelling the effect of supply voltage frequency and temperature on PD characteristics, mainly PD charge amplitude, PD repetition rate and PD inception voltage (PDIV), going from AC to DC, can be considered as a fundamental tool for the development of reliable quality control, commissioning tests and diagnostics procedures. The reason for this is that a theoretical fundamental PD model can help in planning tests and evaluating the likelihood and meaningfulness of test data. Also, modelling PD from AC to DC can help understanding their harmfulness, in terms of degradation rate (damage concept) to provide inputs to insulation system design and diagnostics.

1.1 Aims

The original aims of this thesis are as follows:

1. Deriving analytical models for PD characteristics such as PD charge amplitude, PD repetition rate and PD inception voltage (PDIV) based on PD RC equivalent circuit from AC to DC as well as evaluation and validation of the derived models based on experimental data performed on polymeric multilayer specimens as well as MV cable.
2. Implementation of the derived PD models by COMSOL Multiphysics for designing a HVDC insulation system to endure electrical and thermal stresses under operation as well as dielectric lifetime estimation in the presence of AC PD (during transient condition) and DC PD (under steady state condition).
3. Experimentally evaluation of the effect of adding nano Silica with different functionalization to cable grade polymeric materials on electric and dielectric properties such as space charge, electrical conductivity, PDIV, dielectric strength, and life test.

1.2 Contributions

There are three key improvements of the introduced PD models in this thesis over earlier works in the literature such as following:

1. Although there were already some PD charge amplitude models in literature, this is the first time that PD repetition rate model based on PD RC equivalent circuit from AC, very low frequency (VLF) and DC are introduced in this thesis. The importance of PD repetition rate model is highlighted after possibility of its implementation for cylindrical geometry insulation such as HVDC cable insulation and using it to estimate the damage resulting from PD activity and following that dielectric life estimation.
2. Moreover, this is the first time that partial discharge inception voltage (PDIV) model is derived from PD RC equivalent circuit and introduced in this thesis valid from AC to DC.
3. An unexpected additional source of partial discharges in DC cables known as load power variations is introduced and investigated through COMSOL Multiphysics simulations and the effect of temperature and electric field dependence coefficients of electrical

conductivity on the electric field inside cavity near inner and outer conductor is investigated in detail to illuminate the existence shadows regarding their effects clearly.

1.3 Contents

This work is divided into chapters such as:

1. Chapter 1 - A brief introduction, outlining the research conducted for the thesis.
2. Chapter 2 - Modelling of supply voltage frequency effect on partial discharge repetition rate and charge amplitude from AC to DC at room temperature.
3. Chapter 3 - Partial discharge inception voltage and magnitude in polymeric multilayer specimens under AC and DC voltage supply.
4. Chapter 4 - Measuring partial discharges in MV cables under DC voltage: procedures and results in steady state conditions.
5. Chapter 5 - Investigating conditions for an unexpected additional source of partial discharges in DC cables: load power variations.
6. Chapter 6 - Designing a HVDC insulation system to endure electrical and thermal stresses under operation.
7. Chapter 7 - Adding nanofillers in polymeric insulating materials: so far so good? The case of polypropylene for DC cables.
8. Chapter 8 - The conclusions of the work are presented, and future projects that could be developed from this work discussed.

Chapter 2

Modelling supply voltage frequency effect on partial discharges repetition rate and charge amplitude from AC to DC at room temperature

This chapter has the aim to introduce and prove an analytical model ("continuum" model) able to characterize the behavior of partial discharges (PD) repetition rate and charge amplitude, referring to an embedded cavity in polymeric insulation, as a function of the frequency of supply voltage, going from AC power supply frequency (50-60 Hz) to DC. In the range between DC and 50-60 Hz, it is concentrated on data resulting from tests under AC sinewave with very low frequency (VLF) such as 0.1 Hz and 0.01 Hz, which are commonly used for cable testing. It is indicated that the proposed "continuum" model for PD repetition rate and charge amplitude can provide reasonably good fit to the experimental results obtained in the range DC to 60 Hz. It is shown that the PD equivalent circuit should be modified from that commonly used and made by fully-capacitive or resistive components, to take into account the change of polarization mechanisms which may play a non-negligible role to establish the PD repetition rate from low frequency to DC power supply depending on dielectric material. Furthermore, it is indicated that the residual voltage after a PD event inside cavity should be increased with decrease of frequency to provide good fitting of the models to the experimental data. In addition, it is demonstrated through the Weibull distribution that PD charge amplitude under DC and VLF can be lower than under AC 50-60 Hz owing to the delay time of firing electron while the dispersion of PD charge amplitudes decreases (shape/slope parameter increases) with decrease of frequency reaching to the less dispersion (the most shape/slope parameter) under DC. Consequently, measured PD charge amplitude changes with frequency depending on material, defect typology and location.

2.1 Introduction

The characteristics of partial discharges (PD) occurring in defective regions embedded in dielectric materials are considerably affected by statistical time lag, memory effect and supply voltage rate of rise (slew rate) [1-5]. Regarding offline testing of power cables, alternatives to 50/60 Hz are often required to provide voltage supply systems that are compact enough to be deployed in the field. These alternatives include resonant test sets (RTS), very low frequency

(VLF) systems, oscillating wave test sets (OWTS) and DC voltage supply [6-10]. Depending on cable length or capacitance, resonant test sets (RTS) can be used up to EHV to generate sinusoidal voltage at frequencies that can be higher than the supply frequency for instance 100 to 300 Hz [5]. However, weight and size of RTS does not promote their use in MV, while very long cables may have too high capacitance for RTS. Thus, less expensive, and lighter systems such as VLF and OWTS, are getting more and more common after implementing diagnostic testing solutions.

Regarding DC insulation systems, PD measurements during factory quality control and commissioning tests are performed generally under AC. The reason for this is the lack of availability of testing procedures for PD measurement under DC power supply due to difficulty to recognize PD and noise rejection in the absence of a phase-resolved PD pattern.

Therefore, modelling the effect of supply voltage frequency on PD characteristics, mainly charge amplitude, repetition rate, going from AC to DC, is performed in this chapter to provide a theoretical background to help in planning tests and evaluating the likelihood and meaningfulness of test data.

2.2 Symbol and definitions

The symbols and definitions are listed below:

V_i: ignition (firing) voltage across an embedded cavity triggering a discharge event at time t_i

V_r: residual voltage after a discharge event

V_{cs}: voltage across cavity in steady state condition

$q_{i(AC)}$: charge amplitude for the discharge event at time t_i when supply voltage is sinusoidal AC (at various frequencies).

$q_{i(DC)}$: charge amplitude for the discharge event at time t_i under DC voltage.

t_{L_i}: mean time lag of the discharge event at t_i

t_{R_i}: mean recovery time of the discharge event at t_i

Δt_i: mean time interval between discharge events at t_{i-1} and at t_i ($\Delta t_i = t_{L_i} + t_{R_i}$)

$n_{i(AC)}$: mean PD repetition rate for all frequency ranges of applied AC sine voltage of the discharge event at t_i

$n_{i(DC)}$: mean PD repetition rate under DC supply for the i^{th} discharge event

V_{supply}: AC sine supply voltage for all frequencies

V_0: DC supply voltage

ρ: DC resistivity

2.3 PD equivalent circuits

The deterministic analytical approach introduced and demonstrated in this chapter refers to PD occurring in an insulation cavity filled by air at the atmospheric pressure (Figure 2.1).

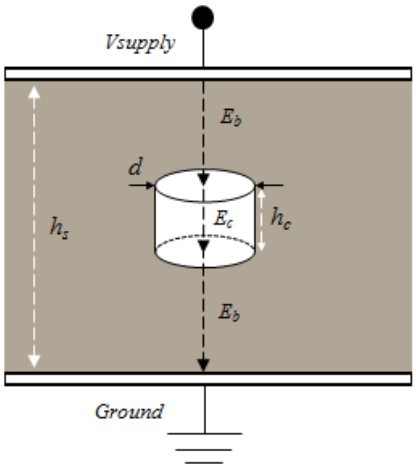

Figure 2.1 Scheme of insulation with thickness h_s, including a cylindrical embedded cavity with diameter d, and height h_c.

The simplest equivalent RC circuit which can be used to model the scheme of Figure 2.1 is indicated in Figure 2.2 [3, 4]. As a first and preliminary approximation, it is assumed that such circuit can be valid at any supply voltage frequency, from AC (50-60 Hz) to DC.

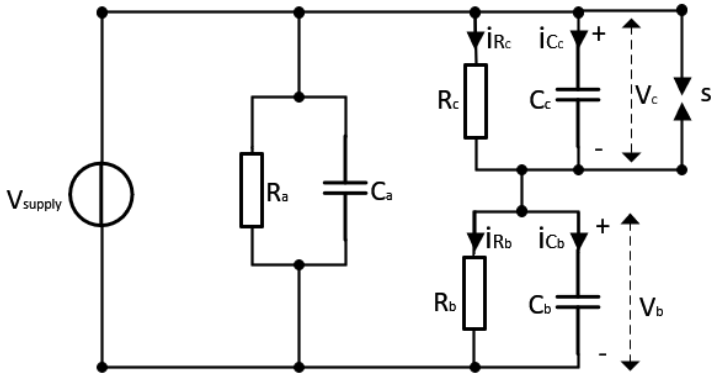

Figure 2.2 Equivalent charging circuit for the calculation of PD repetition rate, from Figure 2.1. C_c and R_c are capacitance and resistance of the cavity where discharges occur, C_b and R_b are capacitance and resistance of the dielectric in series with the cavity, and C_a, R_a are the remaining capacitance and resistance of the test object.

The discharging circuit for PD pulses, which is employed generally to model PD charge amplitude, is the so-called *abc* circuit illustrated in Figure 2.3. It can be speculated that it holds at any frequency from AC power supply frequency to DC due to very high frequency content of PD spectra.

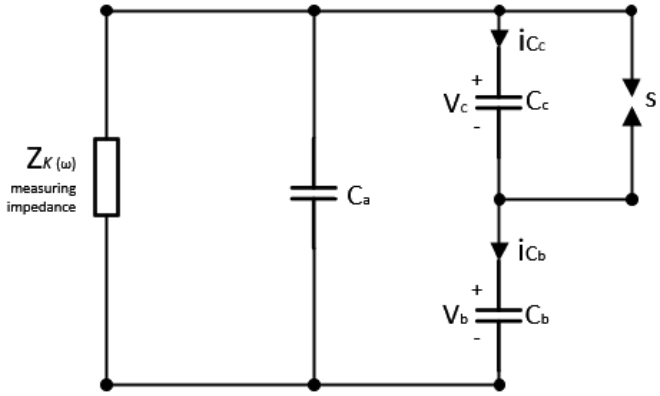

Figure 2.3. Discharging circuit (*abc* model). Z_k is an impedance considering the external PD measurement arrangement.

The voltage across the cavity as a function of time under DC is sketched in Figure 2.4 (after [3]). The scheme does not change referring to AC supply waveform, according to Figure 2.2, apart from the much shorter times involved and the value of V_{cs}. It is noteworthy to recall that under DC steady state, electric field is ruled by conductivity, not permittivity as in AC.

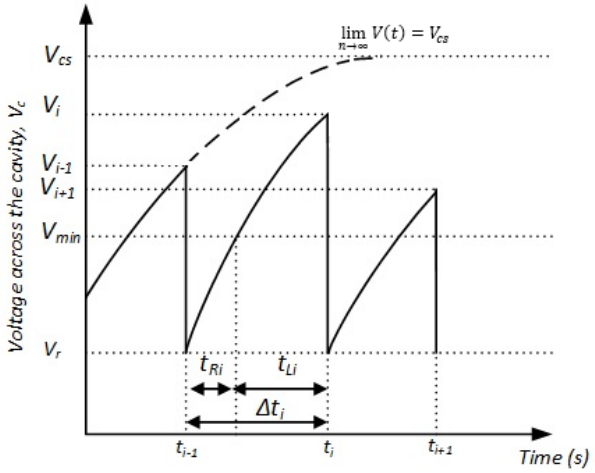

Figure 2.4. Voltage across the embedded cavity under DC voltage supply (*after* [3]).

2.4 General model for PD charge amplitude and repetition rate

Occurrence time t_i and PD firing voltage V_i have statistical distribution because PD is a stochastic phenomenon governed by a Bayesian law (conditional probability) [5]. To simplify the following analytical approach, it will be considered that the PD-associated parameters will be represented by mean values of V_i and Δt_i.

In a deterministic framework, which means that there is the assumption of infinite starting electron availability, each PD event with inception voltage V_{min} happens at time $t_{i-1}+t_{Ri}$, , meaning that there is no delay between the moment the electric field exceeds the minimum inception field and that in which a free electron is available to start an avalanche. Hence, PD pulses would have the same magnitude, which does not hold in reality for both DC and AC owing to the stochastic nature of a PD event, but it might be less approximation under DC compare with AC. In other words, PD charge amplitude dispersion could be larger in AC than in DC. Furthermore, under AC (power supply frequency) models resort often to the simplification of infinite memory effect. It means that the electric field originated by the deposited charge inside the cavity, i.e. the local field, would not decrease between PD events. This might not hold under AC VLF, and certainly not under DC (otherwise we should not detect any further PD after the first one in DC). Consequently, finite memory (due to charge relaxation/recombination) must be considered since the decrease of local field will play a main role to initiate the discharges particularly under DC. In addition, there is a possibility that PD repetition rate can be affected by interface charge trapping/polarization mechanisms under DC and VLF which could be considered, in relation to the availability rate of electron at the cavity/insulation interface, that is, to the firing electron harvesting process [11, 12].

2.4.1 PD repetition rate from the charging circuit

Considering Figure 2.2, the following general equations hold:

$$i_{Cb} + i_{Rb} = i_{Cc} + i_{Rc} \tag{2.1}$$

$$C_b \frac{dV_b}{dt} + \frac{V_b}{R_b} = C_c \frac{dV_c}{dt} + \frac{V_c}{R_c} \tag{2.2}$$

2.4.1.1 AC

From Figure 2.2, $V_{supply}=V_b+V_c=V_0\ sin\ \omega t$, then:

$$(C_b + C_c)\frac{dV_c}{dt} = -\left(\frac{1}{R_b} + \frac{1}{R_c}\right)V_c + C_b V_0 \omega cos\ \omega t + \frac{V_0 sin\ \omega t}{R_b} \tag{2.3}$$

$$\frac{dV_c}{dt} = -\left(\frac{R_b + R_c}{R_b R_c (C_b + C_c)}\right)V_c + \frac{V_0}{(C_b + C_c)}\left(C_b \omega cos\ \omega t + \frac{sin\ \omega t}{R_b}\right) \tag{2.4}$$

Introducing the constants:

$$A = \left(\frac{R_b + R_c}{R_b R_c (C_b + C_c)}\right)$$

$$B = \frac{V_0}{(C_b + C_c)}$$

$$C = C_b \omega$$

$$E = \frac{1}{R_b}$$

and reminding that for $E \neq 0\ and\ \left|tg^{-1}\left(\frac{C}{E}\right)\right| < \frac{\pi}{2}$ it can be written:

$$C\ cos\ \omega t + E\ sin\ \omega t = \sqrt{C^2 + E^2}\ sin\left(\omega t + tg^{-1}\left(\frac{C}{E}\right)\right) \tag{2.5}$$

Considering the introduced triangular conversion by (2.5), Equation (2.4) can be rewritten as:

$$\frac{dV_c}{dt} = -AV_c + B(C\ cos\ \omega t + E\ sin\ \omega t) \tag{2.6}$$

Then, from Equations (2.4) to (2.6):

$$\frac{dV_c}{dt} + AV_c = D\ sin(\omega t + F) \tag{2.7}$$

where

$$D = B\sqrt{C^2 + E^2}$$

$$F = tg^{-1}\left(\frac{C}{E}\right)$$

By multiplying both sides by the integration factor of e^{At}, and using partial derivatives,

$$\frac{d}{dt}(e^{At}V_c) = D\, e^{At}\ sin(\omega t + F) \tag{2.8}$$

Assuming $t_{i-1} = 0$ and integrating Equation (2.8) from t_{i-1} (immediately after the previous PD event) to $t < \Delta t_i$ (before a new PD event), to obtain the upper limit for the time interval between PD, results in:

$$e^{At}V_c(t) - V_r = D \int_0^t e^{At}\ sin(\omega t + F)dt \tag{2.9}$$

After transformations, the expression of the voltage across the cavity becomes:

$$V_c(t) = \frac{D}{A^2 + \omega^2}[A\ sin\ (\omega t + F) - \omega\ cos(\omega t + F) + e^{-At}(\omega\, cos(F) - Asin(F))] + e^{-At}\, V_r \tag{2.10}$$

Recalling Equation (2.5), and considering $A\Delta t_i \to 0$ it results:

$$V_c(\Delta t_i) = V_i = \frac{D}{\sqrt{A^2 + \omega^2}}\sin(\omega \Delta t_i + G) + \frac{HD}{A^2 + \omega^2} + V_r \tag{2.11}$$

with $G = F - tg^{-1}\left(\frac{\omega}{A}\right)$, and $H = \omega\cos(F) - Asin(F)$

and:

$$\frac{(V_i - V_r)\sqrt{A^2 + \omega^2}}{D} - \frac{H}{\sqrt{A^2 + \omega^2}} = sin(\omega \Delta t_i + G) \tag{2.12}$$

If $\left|\frac{(V_i - V_r)\sqrt{A^2+\omega^2}}{D} - \frac{H}{\sqrt{A^2+\omega^2}}\right| \leq 1$ and $|\omega \Delta t_i + G| \leq \frac{\pi}{2}$

As a result, the approximate time interval (which is analytically correct only for the first two PD pulses after zero crossing, but it can be nevertheless considered as a rough mean time-interval estimation) can be introduced such as:

$$\Delta t_i = \frac{arc\, sin\left(\frac{(V_i - V_r)\sqrt{A^2 + \omega^2}}{D} - \frac{H}{\sqrt{A^2 + \omega^2}}\right) - G}{\omega} \tag{2.13}$$

The estimation of mean PD repetition rate under AC sinusoidal voltage, n_i, is, thus:

$$n_{i(AC)} = \frac{\omega}{arc\,sin\left(\frac{(V_i - V_r)\sqrt{A^2 + \omega^2}}{D} - \frac{H}{\sqrt{A^2 + \omega^2}}\right) - G} \tag{2.14}$$

At power frequency (50 or 60 Hz), it can be simplified as:

$$n_{i(60Hz)} = \frac{\omega}{arc\,sin\left(\frac{(V_i - V_r)\sqrt{A^2+\omega^2}}{D}\right)} \tag{2.15}$$

while under very low frequency (VLF) ranges, and considering that $sin\omega t \approx \omega t$, $\omega cos\omega t \approx 0$ and $C \approx 0$, it can be concluded that:

$$\Delta t_i = \frac{A}{BE}\frac{(V_i - V_r)}{\omega} = \frac{R_b + R_c}{V_0 R_c}\frac{(V_i - V_r)}{\omega} \tag{2.16}$$

Hence an approximate expression of PD repetition rate under VLF is:

$$n_{i\ (VLF)} = \frac{V_{cs}\omega}{(V_i - V_r)} \tag{2.17}$$

where

$$V_{cs} = \frac{V_0 R_c}{R_b + R_c} \tag{2.18}$$

The estimations of mean PD repetition rate (according to then above definition and limitations) plotted in Figure 2.5 as a function of mean difference between the firing voltage (V_i), and the residual voltage (V_r), according to Equations (2.15) and (2.17), when the supply voltage frequency is 60 Hz and 0.01 Hz. Equation (2.14) is also represented, to show the validity of the simplifications for 60 Hz and very low frequency. Note that V_r is kept constant for all frequencies, and V_i is varied (to simulate what occurs by varying PDIV).

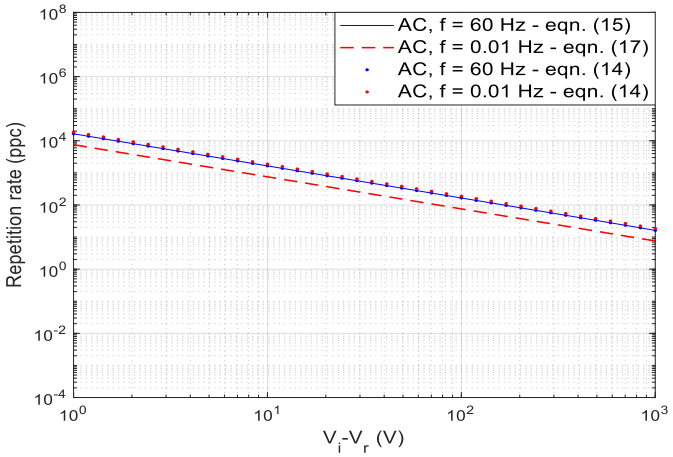

(a)

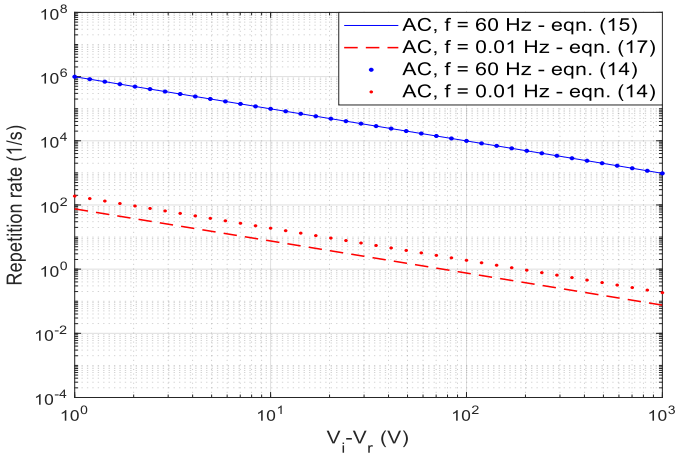

(b)

Figure 2.5. The comparison of mean PD repetition rate in pulse per cycle (a) and pulse per second (1/s) (b), as a function of difference between mean PD firing voltage and residual voltage at 0.01 Hz and 60 Hz, from Equations (2.15) and (2.17), approximating V_{cs} by partial discharge inception voltage (PDIV) measurements. The correct model, Equation (2.14) is also represented (dotted lines). The parameter values of R_c, R_b, C_c and C_b introduced in section 2.5 were used to get these plots.

As shown in Figure 2.5, at room temperature, PD repetition rate from Equation (2.14) at constant V_i - V_r (e. g. 100 V) and different supply voltage frequencies, from 0.01 Hz to 60 Hz, it is almost constant in pulse per cycle, but it increases significantly in pulse per second which is about 5000 times.

2.4.1.2 DC

To calculate the PD repetition rate when the supply voltage is DC, Equation (2.2) should be written such as following:

$$(C_b + C_c)\frac{dV_c}{dt} = -\left(\frac{R_b+R_c}{R_bR_c}\right)V_c + \frac{V_0}{R_b} \tag{2.19}$$

and

$$\frac{dV_c}{dt} = -\left(\frac{R_b+R_c}{R_bR_c(C_b + C_c)}\right)V_c + \frac{V_0}{R_b(C_b + C_c)} \tag{2.20}$$

Defining:

$A = \frac{R_b+R_c}{R_bR_c(C_b+C_c)}$, $B' = \frac{V_0}{R_b(C_b+C_c)}$, then the first order differential equation is:

$$\frac{dV_c}{dt} = -AV_c + B' \tag{2.21}$$

and changing variable:

$$AV_c - B' = u \tag{2.22}$$

Equation (2.22) becomes:

$$A\frac{dV_c}{dt} = \frac{du}{dt} \tag{2.23}$$

and from Equations (2.21) and (2.22):

$$\frac{-1}{A}\frac{du}{u} = dt \tag{2.24}$$

By integrating both sides:

$$\frac{-1}{A}\int_{AV_r-B'}^{AV_i-B'}\frac{du}{u} = \int_0^{\Delta t_i} dt \tag{2.25}$$

$$\frac{-1}{A}(ln(AV_i - B') - ln(AV_r - B')) = \Delta t_i \tag{2.26}$$

$$\Delta t_i = \frac{-1}{A}ln\left(\frac{AV_i - B'}{AV_r - B'}\right) \tag{2.27}$$

Hence, the PD repetition rate, $n_{\mathrm{i(DC)}}$, i.e., the reciprocal of Δt_{i}, is:

$$n_{i(DC)} = \frac{A}{ln\left(\frac{V_{cs} - V_r}{V_{cs} - V_i}\right)} \tag{2.28}$$

It can be understood from Equation (2.28) that, similar to AC, the DC PD repetition rate depends on PD firing voltage (V_i) and on the residual voltage (V_r), see Figure 2.6 (where, as in Figure 2.5, V_r is constant at all frequencies and under DC, which might be a too rough assumption, as shown later).

According to Figures 2.5 and 2.6, it is obvious that at the same value of V_i-V_r, e.g. 100 V, and at room temperature, the PD repetition rate under AC 60 Hz (9.9×10^3 1/s) and at 0.01 Hz (1.9 1/s) are orders of magnitude larger than that under DC (0.02 1/s). This might have considerable effect on aging rate under PD from AC to DC supply.

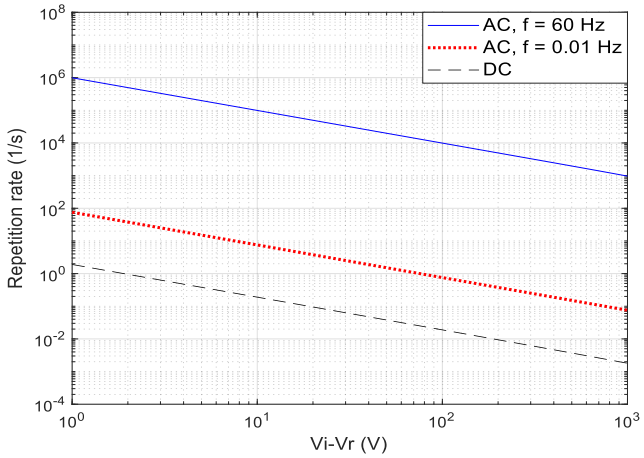

Figure 2.6. The comparison of mean PD repetition rate in pulse per second, as a function of the difference between mean PD firing voltage and residual voltage, under DC, 0.01 Hz and 60 Hz (Equations (2.15), (2.17), (2.28)). The parameter values of R_c, R_b, C_c and C_b introduced in section 2.5 were used to get these plots.

2.4.2 PD charge amplitude from the discharge circuit

2.4.2.1 AC

Considering the discharging circuit (Figure 2.3), it can be argued that discharge times are so fast to consider them independent of supply voltage waveform, at least to quite high supply frequencies.

Resulting from the classic *abc* circuit theory and the current model in Figure 2.3, it derives that the charge amplitude (q_i) of the discharge event at time t_i (which would actually have a stochastic distribution, for what mentioned above), is:

$$q_{i\,(AC)} = C_b\,(V_i - V_r)_{AC} \tag{2.29}$$

Therefore, at the same value of mean V_i-V_r and at room temperature (thus, constant temperature), PD charge amplitude at 0.01 Hz and 60 Hz should be the same under the considered assumption of infinite starting electron availability (deterministic approach). Thus, PD charge amplitude should be almost independent of the supply voltage frequency, at least at low amplitude probability such as 1% or 5% referring to cumulative Weibull distribution (Equation 2.32). It should be mentioned that these PD charge amplitudes with lower probability are related to the discharges where the availability of the firing electron is high. Considering the above models for PD repetition rate and charge amplitude, increase of V_i-V_r results in increase of PD amplitude, while PD repetition rate decreases.

2.4.2.2 DC

Due to very high frequency content of PD spectra, like AC, under DC, Equation (2.29) still valid. As a result, PD charge amplitude under DC is a function of PD firing voltage (V_i) and residual voltage (V_r) as under AC, and they would be equal at the same value of V_i-V_r. Consequently, considering infinite firing electrons availability, one should not detect significant difference of PD amplitude for the same cavity in AC and DC, at the relevant PD inception electric field (that is, PDIV). Because of different electric field distribution in AC and steady-state DC (i.e. permittivity and conductivity driven field, respectively), and considering that conductivity in HV electrical insulating materials is generally considerably lower than in air, then the electric field inside cavity would be much lower than that in dielectric at low temperatures such room temperature as considered in this chapter. Thus, to have the same electric field in the cavity the firing voltage in DC would be mostly higher than that in AC. V_r has also been speculated to depend on the firing voltage V_i [22]. This would also influence on the recorded PD charge amplitudes under different applied frequencies [23], as discussed later.

Another possible difference between PD amplitude in AC and DC is the considerable contribution resulted from the availability of firing electron, which is, practically, not infinite and can result in much higher PD in AC (or even more under power electronics voltage impulses [20]).

Eventually, one could argue that V_r in DC can be affected by the presence of steady space charge accumulated to the cavity-dielectric interface [21], which do not exist under AC (perhaps only at very low frequencies). Therefore, comparison at the same V_i -V_r value may not fit to the model because of possible space charge accumulation under DC.

2.5 Fitting to experimental data

Regarding PD testing at different frequencies down to DC, it should be highlighted that the firing voltage is determined by the field inside the cavity, which can have considerably different values in DC and AC under the same peak voltage and insulation geometry. The reason for this is the dependence of AC field distribution on permittivity, while that of steady-state DC field depends on conductivity and following that on temperature. Thus, to be able to compare PD behavior under AC, VLF and DC, the value of PDIV is required to derive roughly V_i and V_{cs}. Therefore, PDIV must be found at each test frequency through experiments. Eventually, evaluation and comparisons must be performed, at the same overvoltage fraction compared to PDIV for each frequency. It is assumed that V_i can be estimated from the measured value of PDIV at each frequency.

The multilayer flat specimens made by three layers of polymeric films (polypropylene, PP) where the central layer was punctured to create a hole. Considering Figure 2.1, h_s=1.23 mm, h_c=0.41 mm and A_c=9.6 mm^2 are thickness of the specimen, height of the embedded cylindrical cavity and area of the cavity, respectively. Numerical values for the equivalent parameters R_b, C_b, R_c and C_c of Figure 2.2, at room temperature (20°C), are listed below:

$$R_c = \rho_c \frac{h_c}{A_c} = (3.3 \times 10^{14})\left(\frac{0.41\times10^{-3}}{3.06\pi\times10^{-6}}\right) = 1.42 \times 10^{7}\ G\Omega$$

$$R_b = \rho_b \frac{h_s-h_c}{A_c} = (6.1 \times 10^{14})\left(\frac{0.82\times10^{-3}}{3.06\pi\times10^{-6}}\right) = 5.2 \times 10^{7}\ G\Omega$$

$$C_c = \varepsilon_0 \frac{A_c}{h_c} = (8.85 \times 10^{-12})\left(\frac{3.06\pi\times10^{-6}}{0.41\times10^{-3}}\right) = 2.07 \times 10^{-4}\ nF$$

$$C_b = \varepsilon_0\varepsilon_r \frac{A_c}{h_s-h_c} = (8.85 \times 10^{-12})(2.3)\left(\frac{3.06\pi\times10^{-6}}{0.82\times10^{-3}}\right) = 2.39 \times 10^{-4}\ nF$$

The considered value of ρ_b in the following simulations was taken from electrical conductivity measurement at 50 [kV/mm] and 20°C, while that of ρ_c obtained from literature. PD measurements

were performed under AC voltage at 60, 0.1, 0.01 Hz, and under DC steady-state supply, to obtain experimental data for PD charge amplitude and PD repetition rate, as well as estimation of PDIV.

Regarding the experimental setup, a 590 pF PD-free coupling capacitance and a high-frequency current transformer (HFCT), were used as sensors. The PD detectors were an oscilloscope, endowed with dedicated software to cover PD measurements at any frequency, and an ultra-wide-band commercial instrument. The measurement temperature was 20°C. The mean measured values of PD charge amplitude and PD repetition rate are used in the models. The PD charge amplitude was measured in pC after calibration according to IEC 60270.

The experimental results related to PD repetition rate and PD charge amplitude under PDIV, at different frequencies are indicated in Figures 2.7 and 2.8, respectively, besides the values estimated by the models of Equations (2.15), (2.17), (2.28) and (2.29). The values of V_{i} have been estimated from PDIV measurements and Equations (2.15), (2.17), (2.28), while V_{r} was calculated from data fitting to Equation (2.29) at 0.01 Hz (see Table 2.1).

Table 2.1. Model parameter values used to fit the experimental results of Figures 2.7 and 2.8.

Frequency	Symbol	Values [kV]
60 [Hz]	V_i	2.62
	V_r	0.75
0.1 [Hz]	V_i	1.2
	V_r	0.75
0.01 [Hz]	V_i	1.18
	V_r	0.75
DC	V_i	1.14
	V_r	0.75

Considering Figure 2.7, the model indicates a qualitatively good fitting of the PD repetition rate detected from DC to 60 Hz, but not as good quantitatively at low frequencies. As shown in Figure 2.7, PD repetition rate increases as frequency increases.

It can be speculated that the equivalent charging circuit of Figure 2.2 may require some modification to predict satisfactorily the experimental data, and/or that most possibly V_{i}-V_{r} may change with frequency, as indicated in the following Section.

Figure 2.8 provides a very good fit to the experimental data. The model and experimental results related to PD charge amplitude is supported by literature, where it is generally written that PD

amplitude under DC is lower than under AC. However, this is a subtle point that is scrutinized in the next Section.

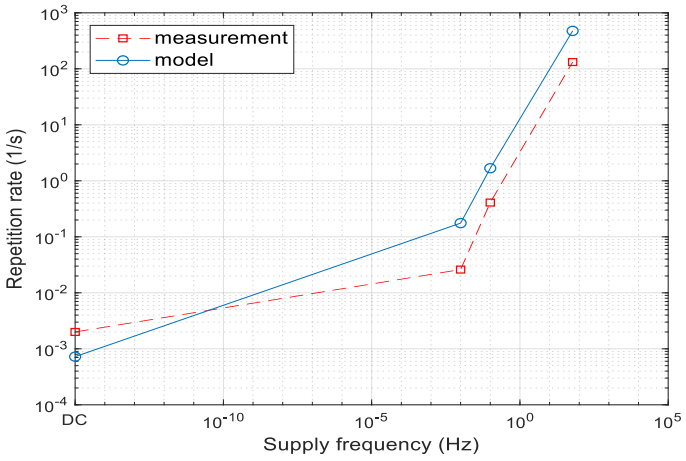

Figure 2.7. Experimental results of mean PD repetition rate as function of frequency under PDIV at 20°C, and fitting to the model of Equations (2.15), (2.17) and (2.28) by employing the constants of Table 2.1. The test object is multi-layer defective specimens.

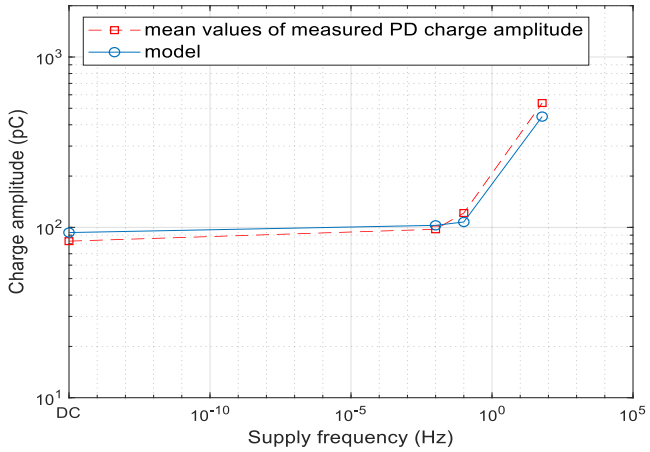

Figure 2.8. Experimental results of mean PD amplitude, as function of frequency under PDIV at 20°C, and fitting to the model of Equations (2.29) and (2.30) by employing the constants introduced in Table 2.2. The test object is multi-layer defective specimens.

2.6 Discussion

2.6.1 PD Repetition rate

Considering Figure 2.7, the comparison between the experimental results and the predicted values by the PD repetition rate model shows that despite a reasonably good qualitative fitting, the model could be further amended to provide better quantitative fitting besides its reasonable qualitative fitting. In practice, this modification could be realized by adding a series resistive-capacitive branch, R_sC_s, in parallel to those modelling the cavity in Figure 2.2 (see: Figure 2.10) to consider the effect of the polarization mechanism on the charging process. This polarization can occur mostly at very low frequencies going towards DC which its ignorance may influence on the predicted PD repetition rate values resulted from the charging circuit. It should be mentioned that Figure 2.10 considers only one type of polarization mechanism which was the prevailing polarization mechanism as observed for the used PP material to make the multilayer test specimen. The polarization mechanism time constant could be estimated or precisely measured by the dielectric analyzer or better by HV-Bridge for each used insulating material depending on the polarization characteristics of the tested material.

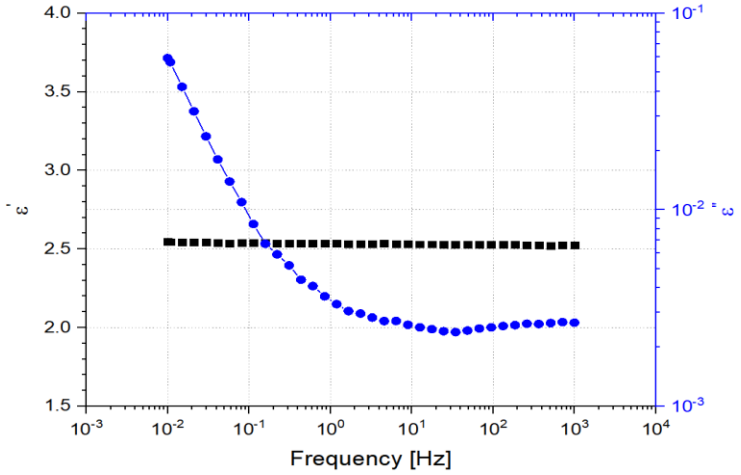

Figure 2.9. Relative permittivity, ε', and loss index, ε'', as a function of frequency for the tested polypropylene material. Measurements performed by a dielectric analyzer (Alpha-A, Novocontrol Technologies) by employing AC voltage of 3 V_{rms}, at room temperature (20°C), sample diameter = 20 mm, sputtered sample thickness = 0.41 mm, and free space capacitance (C_0 = 6.78 pF).

As shown in Figure 2.9, the used PP material has a complex permittivity behavior, which indicates a considerable polarization mechanism variation, as function of frequency, especially at

around 50 Hz, whereas under VLF, such as 0.01 Hz and 0.1 Hz, there is quasi-conduction mechanism. One indicator for the quasi-conduction mechanism is the slope of the imaginary part of the permittivity which is nearly (not exactly) equal to -1 under very low range of supply frequency. According to Figure 2.9, the real part of permittivity is 2.5 and (not 2.3) which already was used to calculate C_b in section 2.5. The reason for this is that the used material for this measurement was a sputtered specimen as stated in the caption of Figure 2.9. The real part of permittivity for an unsputtered specimen was 2.3 as used to calculate C_b and other simulations. Thus, sputtering the specimen leads to obtain higher values for both real and imaginary part of the permittivity when it is measured by the dielectric analyzer.

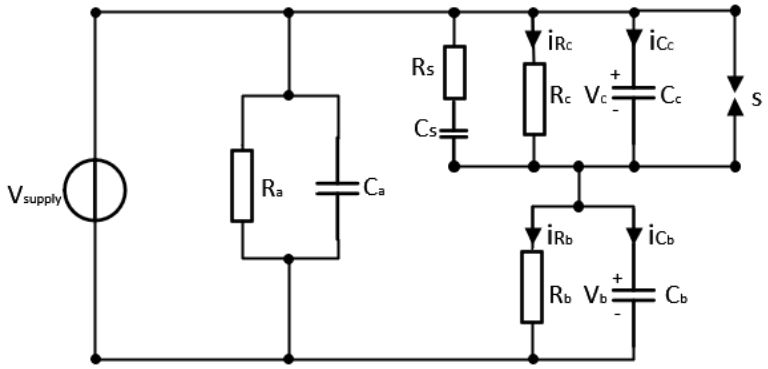

Figure 2.10. The amended equivalent circuit for PD repetition rate from Figure 2.2. The series R_s-C_s branch considers a low-frequency polarization mechanism.

Consequently, and according to Figure 2.10, the values of the cavity resistance (R_c) and capacitance (C_c) in the introduced models for PD repetition rate ((2.15) and (2.17)) are amended into R_{ct} and C_{ct}, respectively:

$$R_{Ct}^{-1} = R_C^{-1} + \left(R_s + \frac{1}{\omega^2 {C_s}^2 R_s}\right)^{-1} \tag{2.30}$$

$$C_{ct} = C_c + \frac{C_s}{1 + (\omega R_s C_s)^2} \tag{2.31}$$

R_s can be obtained using Equation (2.17) fitted to the measured PD repetition rate experimentally at 0.01 Hz, C_s is estimated from Equation (2.15) fitted to the measured PD repetition rate at 60Hz. Figure 2.11a is the revision of Figure 2.7 where the series branch is considered in the charging circuit (Figure 2.10), with $\tau = R_s C_s = 0.21$ s, while the estimated values of resistance and capacitance of the parallel branch are $R_s = 297\ G\Omega$ and $C_s = 6.9 \times 10^{-4}\ nF$. As shown in Figure

2.11a, adding the series R_s-C_s branch to the charging circuit provides considerably better fitting. However, there is still some difference under DC. The reason for that can be addressed to the dependence of V_r on frequency where it can be increased with decrease of frequency down to DC. According to [22], it is not irrational to consider, that the larger the overvoltage or PD firing voltage (V_i) which is estimated at higher frequency values such as 50-60 Hz, then lower V_r would be expected. For instance, if the constants reported in Table 2.2 are considered (thus increasing the residual voltage with decrease of frequency especially under DC), while PDIV under DC was 11.4 kV and under 50 Hz AC was 4.9 kV, then the fitting to experimental results becomes very good quantitatively at any frequency (see: Figure 2.11b). It is required to highlight that the parameter values of V_i in Table 2.2 are the same as is Table 2.1 which were estimated through PDIV measurement using the model introduced in chapter 3 as well as [23]. Considering Figure 2.10 and after adding the series R_s-C_s branch to the charging circuit, the values of V_r were obtained using the data fitting of the PD repetition rate models to the experimental data under 60 Hz, VLF (0.01 Hz and 0.1 Hz) and DC using Equations (2.15), (2.17) and (2.28), respectively.

Table 2.2. The used values of firing voltage and residual voltage to fit the experimental results after the modification of charging circuit.

Frequency	Symbol	Values [kV]
60 [Hz]	V_i	2.62
	V_r	0.05
0.1 [Hz]	V_i	1.2
	V_r	0.65
0.01 [Hz]	V_i	1.18
	V_r	0.74
DC	V_i	1.14
	V_r	0.82

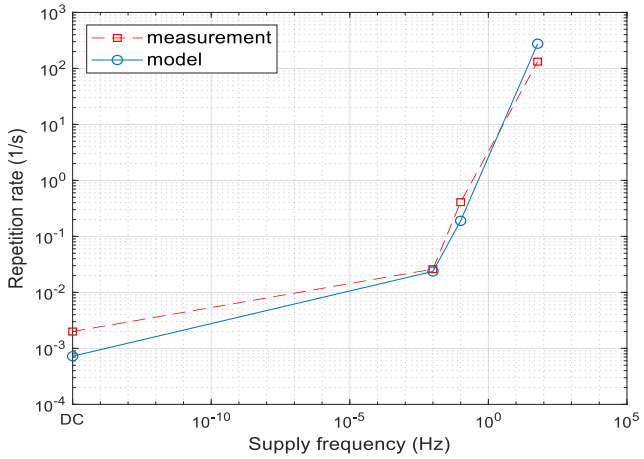

(a)

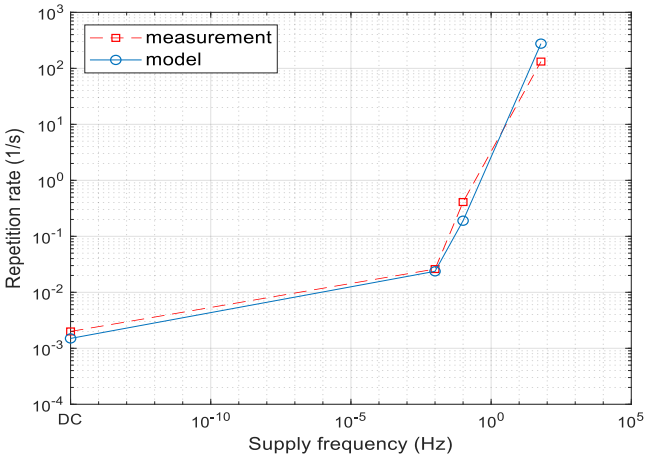

(b)

Figure 2.11. (a) Fitting the estimated values for PD repetition rate to the experimental data (see Figure 2.8) after modification of charging circuit as shown in Figure 2.10. (b) Fitting the DC PD repetition rate model (Equation (2.28)) to the experimental data after the modification of residual voltage which increases as frequency decreases down to DC (Table 2.2).

2.6.2 PD charge amplitude

As shown in Figure 2.8, there is a good fitting between experimental data and model (Equation (2-29)). According to the literature findings (e.g. [3]), it is often reported that PD charge amplitude under DC is lower than in AC. This fact is also illustrated in Figure 2.8. But such difference can be considered as a confusion if one thinks to the physics behind PD phenomena. Here, it should be highlighted that PD inception field in a cavity is independent of voltage waveform shape [17].

In other words, if it is assumed that the availability of starting electrons is large enough to neglect the delay from the time the PDIV is reached to the time the PD is fired, and it is assumed also that the space charge that accumulates at the cavity interface can be neglected. Then, the PD inception field E_{inc} inside the cavity would not vary from AC to DC [23]. This concept will be scrutinized in detail in Chapters 3 and 4.

To compare PD charge amplitude in AC *vs.* DC, it is required to consider the different effect of the firing electron delay on the PD charge amplitude probability distribution. To deal with this issue, it can be referred to the two-parameters Weibull function which is described as follows [24]:

$$F(q) = 1 - e^{-\left(\frac{q}{\alpha}\right)^{\beta}} \tag{2.32}$$

where q is PD charge amplitude, α and β are scale and shape/slope parameters, respectively. α is related to probability of 63.2% while β indicates the data dispersion. According to the cumulative distribution function of Equation (2.32), the Weibull distribution plots of the measured PD charge amplitudes under DC, 0.1 Hz and 60 Hz have been depicted in Figure 2.12. It can be seen from Figure 2.12 that while at low percentiles (low probabilities e.g 1% and 5%) the Weibull plots are very close; they are getting separated at high probability. This separation or distinction is also highlighted for the PD charge amplitudes at 50% probability which is near the mean value which already was considered to show the measured PD charge amplitudes in Figure 2.8. Considering the β values reported in Figure 2.12, higher value of β confirms also that PD data under DC are less dispersed than those under AC. The reason for this is that under DC power supply, there is lower effect of the firing electron delay. However, it is noteworthy that the shape parameter of the Weibull distribution (β) ranges from 2.8 to 4.8 from AC 60 Hz to DC, which is a reasonable value for internal discharges. This point can be used regarding PD-source identification purposes especially under DC PD tests [25].

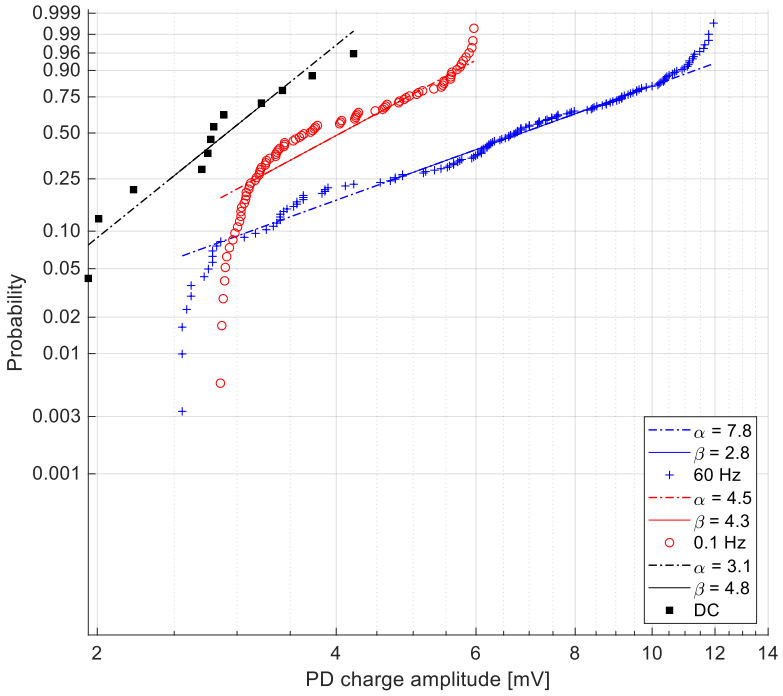

Figure 2.12. Plots for the DC, 0.1 Hz and 60 Hz PD charge amplitudes fitted to the two-parameters Weibull distribution.

2.7 Conclusions

Performing AC PD measurements at different frequency levels of power supply as well as DC power supply, without having a comprehensive model which can describe the PD phenomenology variation from AC to DC, might lead to questionable measurement results corresponding to diagnostics, quality control, commissioning tests. The models for PD charge amplitude and PD repetition rate derived and validated for defects as delamination or embedded cavities in this chapter, demonstrate that PD charge amplitude and PD repetition rate differ from AC power supply frequency to low frequency and DC which depends on the insulating material characteristics and the testing conditions. It was shown that the difference in PD charge amplitude between AC and DC power supply mostly depends on the testing procedures and the data processing. It was demonstrated by referring to the two-parameters Weibull distribution that there is significant effect of availability of the firing electron on PD charge amplitude in such a way that higher values of the PD charge amplitude would be expected when there is higher dv/dt of the supply voltage waveform or higher frequency. Considering PD repetition rate, fitting the derived models to the

experimental data shows that the commonly used charging circuit which has been used in literature may require to be slightly amended. This modification depends on the dielectric material where a parallel branch that includes series resistance and capacitance can be added to the charging circuit. By this approach, the plausible polarization mechanism can be considered. The polarization mechanism can be significant for some insulating materials such as the used Polypropylene in the research reported in this chapter. It can be conjectured that such added branch could account also for injected or accumulated space charge at the semicon as well as the dielectric-cavity interface (in DC or VLF).

It is interesting to highlight that the best fit for both PD repetition rate and PD charge amplitude can be achieved by changing the residual voltage respect to frequency. This fact was already predicted by a few literature papers. However, this variation of the residual voltage significantly complicates the PD charge amplitude and PD repetition rate estimation based e.g., on measurements performed at power supply frequency. Thus, it is required to conduct more research on residual voltage variation as a function of frequency power supply as well as temperature.

It can be reasonably speculated that depending on load conditions and losses, thus on insulation temperature, PD features can change considerably under DC, while this dependency could be much less effective and considerable under AC at power supply frequency. Afterwards, it can be conjectured that since the electric field distribution under DC is determined by conductivity, and the dependence on temperature of conductivity is much more considerable than that of permittivity, PD characteristics will vary as function of temperature under DC, and, maybe slightly, under VLF, whereas this dependency would be more than that under AC.

Regarding partial discharge inception voltage (PDIV), it will be discussed and scrutinized in detail in Chapters 3 and 4. At low temperatures such as room temperature as considered in this chapter, because of lower electrical conductivity of dielectric than that of cavity gas, the electric field in the cavity in DC could be much lower than in AC, and then DC-PDIV could be much larger than AC-PDIV e.g., at room temperature, becoming comparable when load (temperature) increases. As it was mentioned earlier, this concept will also be discussed and modelled in the chapter 3 and 4 [23].

References

[1] F. H. Kreuger, *Partial Discharge Detection in High-Voltage Equipment*, Butterworth-Heinemann, 1990.

[2] F.H. Kreuger, *Industrial High DC Voltage: 1. Fields 2. Breakdowns 3. Tests*, Delft University Press, 1995.

[3] Peter H. F. Morshuis, and Johan J. Smit, "Partial discharges at DC voltage: their mechanism, detection and analysis," IEEE Trans. Dielectr. Electr. Insul., vol. 12, no. 2, pp. 328-340, 2005.

[4] U. Fromm, and Frederik H. Kreuger, "Statistical behaviour of internal partial discharges at DC voltage," Japanese journal of applied physics, vol. 33, no. 12, p. 6708, 1994.

[5] A. Cavallini and G. C. Montanari, "Effect of supply voltage frequency on testing of insulation system," IEEE Trans. Dielectr. Electr. Insul., vol. 13, no. 1, pp. 111-121, 2006.

[6] Maintenance for HV Cables and Accessories, Cigré Working Group B1.04, Brochure 279, 2005-08-1.

[7] IEEE Guide for Partial Discharge Testing of Shielded Power Cable Systems in a Field Environment, IEEE Standard 400.3-2006, 2007-02-5.

[8] Test Methods for Partial Discharges Measurements on Lengths of Extruded Power Cable, IEC 60885-3, second Edition, 2015-04-09.

[9] High-Voltage On-Site Testing with Partial Discharge Measurement, Cigré Working Group D1.33, Brochure 502, 2012-06-01.

[10] Power cables with extruded insulation and their accessories for rated voltages above 30 kV (U_m = 36 kV) up to 150 kV (U_m = 170 kV) – Test methods and requirements, IEC 60840, fourth Edition, 2011-11-01.

[11] S. Serra, G.C. Montanari, and G. Mazzanti, "Theory of inception mechanism and growth of defect-induced damage in polyethylene cable insulation," J. of Apply. Phys., vol. 98, no. 3, pp. 1-15, 2005.

[12] G.C. Montanari, "A contribution to unravel the mysteries of electrical aging under DC electrical stress: where we are and where we need to go," *IEEE Int. Conf. on Dielect., (ICD)*, 2018, pp. 1-15.

[13] H. Edin, "Partial discharges studied with variable frequency of the applied voltage," PhD dissertation, Dept. of Electr. Eng., KTH, Stockholm, 2001.

[14] IEEE Guide for Field Testing of Shielded Power Cable Systems Using Very Low Frequency (VLF) (less than 1 Hz), IEEE Standard 400.2-2013, 2013-06-09.

[15] IEEE Guide for Field Testing of Shielded Power Cable Systems Rated 5 kV and Above with Damped Alternating Current (DAC) Voltage, IEEE Standard 400.4-2015, 2016-01-29.

[16] High-Voltage Test Techniques - Partial Discharge Measurements, IEC 60270, 3.1 Edition, 2015-11-27.

[17] L. Niemeyer, "A generalized approach to partial discharge modeling," IEEE Trans. Dielectr. Electr. Insul., vol. 2, no. 4, pp. 510-528, 1995.

[18] T. W. Dakin, "Electrical Insulation deterioration treated as a chemical rate phenomenon," AIEE Trans. vol. 67, pp. 113-122, 1948.

[19] G. C. Montanari, "A new thermal life model derived by the aging compensation effect," IEEE Trans. Dielectr. Electr. Insul., vol. 25, no. 2, pp. 309-318, 1990.

[20] G.C. Montanari, "Time behavior of Partial Discharges and life of Type II turn insulation specimens under repetitive impulse and sinusoidal waveforms," IEEE Electr. Insul. Mag., vol. 25, no. 8, pp.1-8, Oct. 2017.

[21] D. Fabiani *et al*, "Polymeric HVDC cable design and space charge accumulation. Part 1: insulation/semicon interface," IEEE Trans. Dielectr. Electr. Insul., vol. 23, no. 6, pp. 11-19, 2007.

[22] M. Hikita *et al*, "Measurements of Partial Discharges by Computer and Analysis of Partial Discharge Distribution by the Monte Carlo Method," IEEE Trans. Dielectr. Electr. Insul., vol. 25, no 3, pp. 453-468, June 1990.

[23] G.C. Montanari, R. Hebner, P. Seri, and H. Naderiallaf, "Partial discharge inception voltage and magnitude in polymeric cables under AC and DC voltage supply," Jicable, 2019, pp. 1-4.

[24] M. Cacciari, A. Contin, G. C. Montanari, "Use of a mixed-Weibull distribution for the identification of partial discharge phenomena," IEEE Trans. Dielectr. Electr. Insul., vol. 2, no. 6, pp. 1166-1179, Dec. 1995.

[25] A. Cavallini, M. Conti, A. Contin and G. C. Montanari, "Advanced PD inference in on-field measurements. Part 2: Identification of defects in solid insulation," IEEE Trans. Dielectr. Electr. Insul., vol. 10, no. 3, pp. 528-538, June 2003.

Chapter 3

Partial discharge inception voltage and magnitude in polymeric multilayer specimens under AC and DC voltage supply

The ratio between partial discharge inception voltage, PDIV, under AC and DC voltage supply is introduced in this chapter by an analytical model. Despite the simplifying assumptions, the experimental results confirm that the PDIV in DC can be much higher than in AC, for the same defect, especially at room temperature. However, depending on material conductivity and the rate of variation of conductivity with temperature, the PDIV in DC can become lower than that in AC, at least for the typical XLPE materials used in manufacturing HV AC and DC cables. Hence, PD can incept and extinct during operation as a function of cable loading, posing reliability problems for a cable insulation system that have to be taken care both at the design and at the commissioning stage. Also, the effect of the different PDIV under DC and AC can induce wrong speculations once PD measurements are performed at the same peak voltage in AC and DC.

3.1 Introduction

Partial discharge (PD) measurements are a common technique to evaluate both the quality of insulation system during manufacturing and commissioning and a powerful diagnostic tool in service. Indeed, PD can be the cause of insulation premature failure, being able to break organic polymer bonds, but also the consequence of aging mechanisms driven by operating stresses, such as thermal cycling and mechanical stress. Therefore, measuring PD is a fundamental procedure to ensure insulation system reliability [1-6].

Partial discharge inception voltage (PDIV) is a typical test which can show that an insulation system is free of PD at the nominal operating voltage at the time of manufacturing, commissioning or during life.

Referring to cable insulation, PDIV under AC field is commonly measured from MV to HV and UHV cables, while PDIV measurements under DC field are not performed even in DC cables, for the lack of specified testing procedures, data interpretation methods and even of testing devices. In particular, the difficulty in distinguishing between PD and noise under DC, where the PD measurements cannot be represented by a phase-resolved pattern as under AC, is coupled to the

strong variability of the PDIV value which under DC depends dramatically on temperature (while it is much less variable in AC) [7-10].

The purpose of this chapter is to provide a simple tool to predict DC PDIV in polymeric insulation systems compared to AC PDIV, to support feasibility of PD investigation in cable systems under DC field. In the following, a theoretical approach showing how and why PD and PDIV measured under DC are strongly variable with temperature, and deriving the relationship between DC and AC PDIV, is reported, and validated based on experimental results relevant to multi-layer flat test objects.

3.2 PDIV under DC and AC

Considering, as the defect generating PD, a cavity in insulation (embedded, a delamination near the conductor or the outer semicon), classic discharge models in a cavity can be used to determine PDIV behavior. In this chapter the model usually referred to PD equivalent RC circuit, shown in Figure 3.1, will be used [1,11-13]. This circuit is considered here as valid for both DC and AC investigation, which is a significant approximation that does not consider the change of polarization mechanisms from AC to DC (i.e. only dipolar polarization is considered).

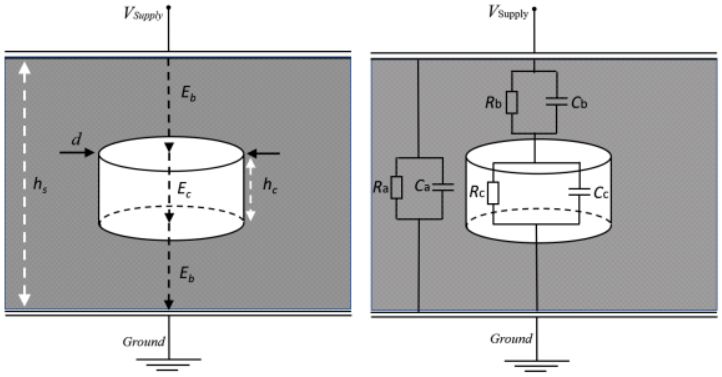

Figure 3.1. Left: scheme of insulation with thickness h_s, having a cylindrical embedded cavity of diameter d, height h_c. Right: equivalent resistive/capacitive circuit (*abc* circuit modified to account also for DC discharge): C_c and R_c are equivalent capacitance and resistance of the cavity where discharges occur, C_b and R_b are equivalent capacitance and resistance of the dielectric in series with the cavity, and C_a, R_a are remaining equivalent capacitance and resistance of the test object. E_c and E_b are field in the cavity and in the insulation in series to the cavity, respectively.

For the sake of simplification, the random delay time of the initial electron is neglected. Thus, it excludes the need to adopt the stochastic approach considered in [11, 12] without affecting the outcomes concluded in this chapter. Therefore, the PDIV can be roughly estimated from the average of PD firing voltage values. Accordingly, the lower limit for PDIV will be assumed to

occur immediately when the PD inception field in a cavity, E_{inc}, and voltage, V_{min}, are reached (see: Figure 2.4). The upper limit under AC would be that corresponding to the maximum voltage in the cavity before discharge (generally occurs after polarity inversion [11]), while under DC it is the steady state voltage in the cavity, V_{cs} (see: Figure 2.4).

The effective parameter for the estimation of PDIV is the field amplification factor (f) which determines the field inside the cavity (E_c) as a function of applied field inside the dielectric (E_b), for either AC or DC supply voltage. The field amplification factor is defined as:

$$f = \frac{E_c}{E_b} \tag{3.1}$$

As known, while the field distribution under AC is permittivity driven, and ε_r, relative permittivity, varies only slightly with temperature (for the typical electrical insulating materials used for MV and HV devices and in the operation temperature range), under DC, the conductivity, γ, determines the electric field distribution, and γ displays significant variations with temperature (it is an exponential function of 1/T, according to the reaction rate theory). As regards the equivalent circuit of Figure 3.1, f has the approximate values (valid for flat cavities [14] and assuming no space charge effects and no frequency dependent interfacial effects) listed below:

- under AC:

$$f_{AC} = \frac{E_c}{E_b} = \frac{\varepsilon_{rb}}{\varepsilon_{rc}} \tag{3.2}$$

- under DC:

$$f_{DC} = \frac{E_c}{E_b} = \frac{\gamma_b}{\gamma_c} \tag{3.3}$$

Referring to a typical cable insulation polymer, e.g., XLPE, in the AC case, $E_c > E_b$, being $\varepsilon_{rc} \approx 1$ and $\varepsilon_{rb} \approx 2.3$. Dealing with DC, on the contrary, it may well happen that the opposite holds, that is, $E_c < E_b$. As an example, considering, at room temperature, $\gamma_b = 1.9 \times 10^{-15}(\mathrm{S/m})$ and $\gamma_c = 3 \times 10^{-15}(\mathrm{S/m})$, (typical value for air only neglecting any surface wall conductivity), it results $E_c = 0.6E_b$.

Therefore, the relationship between PDIV under DC and AC has to consider the relevant relationship between electric field distributions. Due to this fact that, under the simplifying

assumptions previously mentioned, the PD inception field inside the cavity would not vary from AC to DC [11], thus $E_{inc(AC)} = E_{inc(DC)}$, it results:

$$(h_c)E_{inc(DC)} = PDIV_{DC} \cdot \frac{R_c}{R_b + R_c} \tag{3.4}$$

$$(h_c)E_{inc(AC)} = PDIV_{AC} \cdot \frac{|Z_c(\omega)|}{|Z_b(\omega)| + |Z_c(\omega)|} \tag{3.5}$$

Thus:

$$\frac{PDIV_{\mathrm{DC}}}{PDIV_{\mathrm{AC}}} = \frac{|Z_c(\omega)|}{|Z_b(\omega)| + |Z_c(\omega)|} \cdot \frac{R_b + R_c}{R_c} \tag{3.6}$$

At power frequency (50 or 60 Hz), the effect of insulation and cavity gas resistance can be neglected with respect to capacitance, thus:

$$\frac{PDIV_{\mathrm{DC}}}{PDIV_{\mathrm{AC}}} = \frac{C_b}{C_b + C_c} \cdot \frac{G_b + G_c}{G_b} \tag{3.7}$$

From Figure 3.1, it results then:

$$G_c = \gamma_c \frac{A_c}{h_c} \tag{3.8}$$

$$G_b = \gamma_b \frac{A_c}{h_s - h_c} \tag{3.9}$$

$$C_c = \varepsilon_0 \varepsilon_{rc} \frac{A_c}{h_c} \tag{3.10}$$

$$C_b = \varepsilon_0 \varepsilon_{rb} \frac{A_c}{h_s - h_c} \tag{3.11}$$

Then, replacing 3.8 to 3.11 in 3.7 results in:

$$\frac{PDIV_{\mathrm{DC}}}{PDIV_{\mathrm{AC}}} = \frac{\varepsilon_0 \varepsilon_{rb} \frac{A_c}{h_s - h_c}}{\varepsilon_0 \varepsilon_{rb} \frac{A_c}{h_s - h_c} + \varepsilon_0 \varepsilon_{rc} \frac{A_c}{h_c}} \cdot \frac{\gamma_b \frac{A_c}{h_s - h_c} + \gamma_c \frac{A_c}{h_c}}{\gamma_b \frac{A_c}{h_s - h_c}} \tag{3.12}$$

$$\frac{PDIV_{\mathrm{DC}}}{PDIV_{\mathrm{AC}}} = \frac{\varepsilon_{rb} h_c}{\varepsilon_{rb} h_c + \varepsilon_{rc} h_s - h_c} \cdot \frac{\gamma_b h_c + \gamma_c h_s - h_c}{\gamma_b h_c} \tag{3.13}$$

Finally, it can be introduced such as:

$$\frac{PDIV_{DC}}{PDIV_{AC}} = \frac{\varepsilon_{rb}}{\gamma_b}.\frac{\gamma_b h_c + \gamma_c(h_s - h_c)}{\varepsilon_{rb}h_c + \varepsilon_{rc}(h_s - h_c)} \tag{3.14}$$

Equation (3.14) predicts the ratio between AC and DC PDIV in an insulation having a cavity with a given height. Since $E_{inc(DC)} = E_{inc(AC)}$, in the ratio of PDIV under DC to PDIV under AC, E_{inc} is omitted. Therefore, this ratio is not a function of inception field inside the cavity.

In the following the deriving PDIV model as a function of frequency is shown step by step. From Equation (3.5), it can be written such as:

$$PDIV = E_{inc}h_c.\frac{|Y_b(\omega)| + |Y_c(\omega)|}{|Y_b(\omega)|} = E_{inc}h_c\left(1 + \frac{|Y_c(\omega)|}{|Y_b(\omega)|}\right) \tag{3.15}$$

It is known that:

$$Y_c(\omega) = G_c + jC_c\omega \tag{3.16}$$

$$Y_b(\omega) = G_b + jC_b\omega \tag{3.17}$$

Replacing Equations (3.8) to (3.11) in (3.16) and (3.17) results in:

$$\frac{|Y_c(\omega)|}{|Y_b(\omega)|} = \sqrt{\frac{{G_c}^2 + (C_c\omega)^2}{{G_b}^2 + (C_b\omega)^2}} = \sqrt{\frac{{\gamma_c}^2(\frac{A_c}{h_c})^2 + (\varepsilon_0\varepsilon_{rc}\omega)^2(\frac{A_c}{h_c})^2}{{\gamma_b}^2(\frac{A_c}{h_s - h_c})^2 + (\varepsilon_0\varepsilon_{rb}\omega)^2(\frac{A_c}{h_s - h_c})^2}} \tag{3.18}$$

Then, (3.18) can be written such as:

$$\frac{|Y_c(\omega)|}{|Y_b(\omega)|} = \sqrt{\frac{{\gamma_c}^2 + (\varepsilon_0\varepsilon_{rc}\omega)^2}{{\gamma_b}^2 + (\varepsilon_0\varepsilon_{rb}\omega)^2}}.\frac{h_s - h_c}{h_c} \tag{3.19}$$

Eventually, PDIV can be introduced as a function of frequency after replacing (3.19) in (3.15):

$$PDIV = E_{inc}\left(h_c + \sqrt{\frac{{\gamma_c}^2 + (\varepsilon_0\varepsilon_{rc}\omega)^2}{{\gamma_b}^2 + (\varepsilon_0\varepsilon_{rb}\omega)^2}}.(h_s - h_c)\right) \tag{3.20}$$

Considering Equations (3.4) and (3.5) or only Equation (3.20), the exponential dependence of γ_b on temperature as shown in (3.21) (while neglecting the exponential dependence of ε) and referring to a specific section of the cable insulation where the temperature varies with cable ampacity, an example of the relationship between $PDIV_{AC}$ and $PDIV_{DC}$ as a function of temperature is plotted in Figure 3.2 (for an XLPE material used for HV cables). It concludes that while $PDIV_{DC}$ is

significantly higher than $PDIV_{AC}$ at room temperature, it becomes lower when the temperature in the insulation section where the cavity is located is >65 °C.

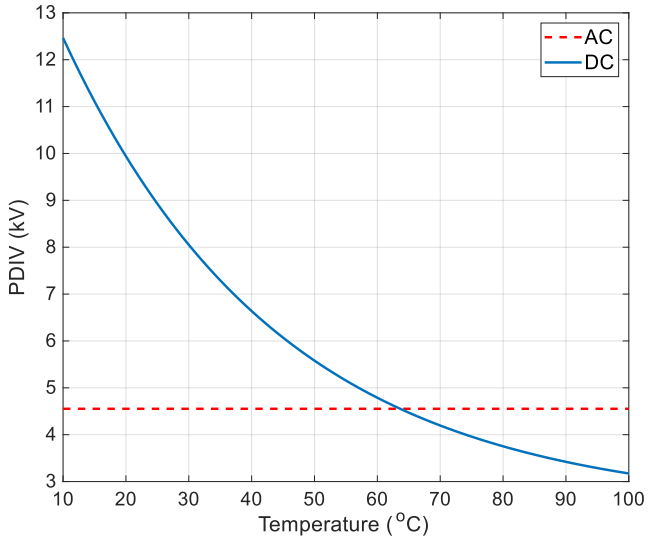

Figure 3.2. Behavior of calculated DC and AC PDIV as a function of temperature for a HV XLPE flat specimen, Equations (3.4) and (3.5) or only (3.20), under DC and AC power frequency. Same cavity size in DC and AC.

In this example, the ratio of $PDIV_{DC}$ to $PDIV_{AC}$ is > 2.2 at 20 °C, while $PDIV_{DC}$ becomes about 70% of $PDIV_{AC}$ at 90 °C. It is clear also that this ratio can vary significantly with the value of conductivity at 0°C, γ_0, and its dependence on temperature (coefficient α), in a way that the lower γ_0 and α, the higher the ratio. Table 3.1 reports values calculated by this approach at various temperatures, for a reference XLPE having the value of permittivity and conductivity reported above. Temperature, thus cable ampacity, plays a fundamental role in establishing PDIV, so that the DC PDIV may vary significantly under operating conditions. It is noteworthy that the approach proposed here refers to a specific cavity at any insulation radius and does not take into account change of field profile (thus the field variation at that radius) which can occur in DC due to the temperature gradient (affected by α).

Table 3.1. Ratio of DC to AC PDIV for a cavity in a XLPE material for HV cables (Figure 3.1, dimensions h_s=1.22 mm, h_c=0.41 mm and A_c=8.8 mm^2) at three operating temperatures. XLPE relative permittivity ε_{rb}=2.3, conductivity at 0°C γ_{0b}=1.09 × 10^{-15}(S/m).

Type of material	Conductivity at 20 kV/mm(S/m)	$PDIV_{DC}/PDIV_{AC}$
XLPE	1.9×10^{-15} (20 °C)	2.2
XLPE	6.2×10^{-15} (60 °C)	1.1
XLPE	1.5×10^{-14} (90 °C)	0.7

While the effect of temperature on permittivity is negligible (in the range of operation temperatures for insulating polymers), its influence on insulating material conductivity is very large, and it goes exponentially with absolute temperature:

$$\gamma_b = \gamma_0 \exp(\alpha T) \tag{3.21}$$

Regarding the relation with temperature, it should be mentioned that it has been approximated by considering T in place of $1/T$, as it would be required referring to the Arrhenius equation [16, 17]. Considering Equation (3.21), i.e. the exponential dependence of γ_b (while neglecting that of ε) assuming a temperature coefficient $\alpha = 0.04\ °C^{-1}$, and referring to a specific section of the cable insulation where the temperature varies with cable ampacity, an example of the ratio between $PDIV_{AC}$ and $PDIV_{DC}$ as a function of temperature is plotted in Figure 3.3 (for a specimen having thickness $h_s = 1.23\,mm$ and cavity height $h_c = 0.41\,mm$), made by polymeric materials designed for HVDC cables (polypropylene, PP, based), having conductivity at 0°C in the range $1.05 \times 10^{-15}\ S/m$ to $3.43 \times 10^{-15}\ S/m$. As can be seen, $PDIV_{DC}$ can be higher than $PDIV_{AC}$ at room temperature when conductivity is relatively low, but it can be lower than $PDIV_{AC}$ when conductivity is higher (for this example $PDIV_{DC}/PDIV_{AC}$ ranges between 1.7 and 0.8). In general, the ratio becomes <1 when the temperature in the insulation section where the cavity is located increases, e.g., at 90 °C $PDIV_{DC}/PDIV_{AC}$ is about 0.5. This ratio can vary significantly with the value of the temperature dependence of conductivity (coefficient α), see Figure 3.4. From Figures 3.3 and 3.4 it is clear that the lower γ_0 and α, the higher the ratio.

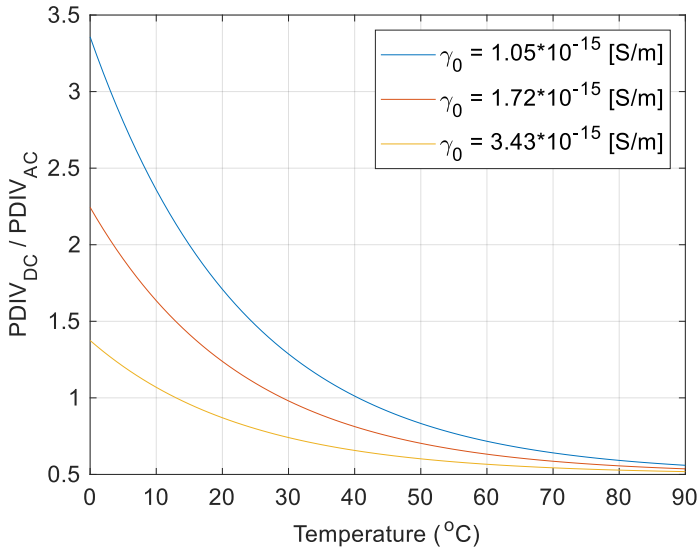

Figure 3.3. Ratio of $PDIV_{DC}$ to $PDIV_{AC}$ as function of temperature and γ_0 with constant temperature coefficient ($\alpha = 0.04\ °C^{-1}$), for a specific defect size.

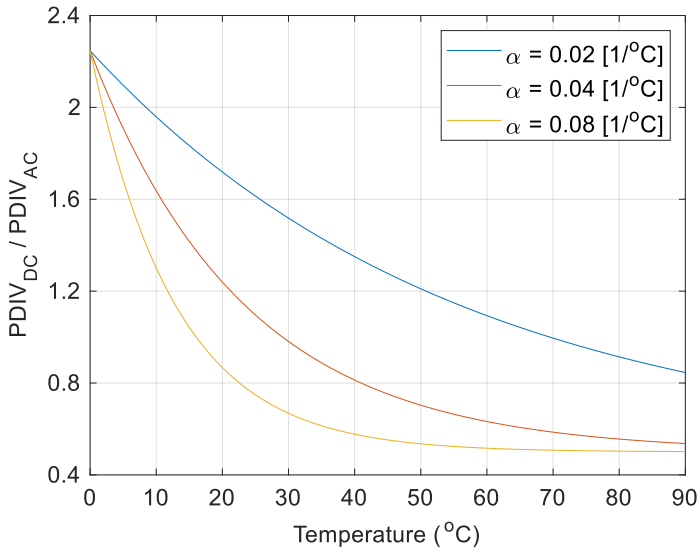

Figure 3.4. Ratio of $PDIV_{DC}$ to $PDIV_{AC}$ as function of temperature and temperature coefficient (α) with constant γ_0 =$1.72 \times 10^{-15}\ S/m$.

Considering Equations (3.20) and (3.21), PDIV as a function of power supply frequency and temperature dependence of electrical conductivity (α) while γ_0 is constant equal to 1.72E-15 [S/m] is plotted and shown in Figure 3.5 (for a specimen having thickness $h_s = 1.23\,mm$ and cavity height $h_c = 0.41\,mm$).

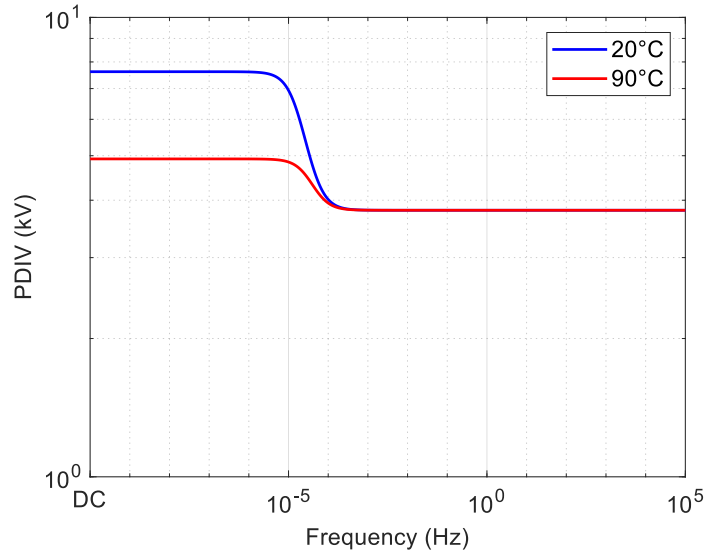

(a) α = 0.01 [°C^{-1}]

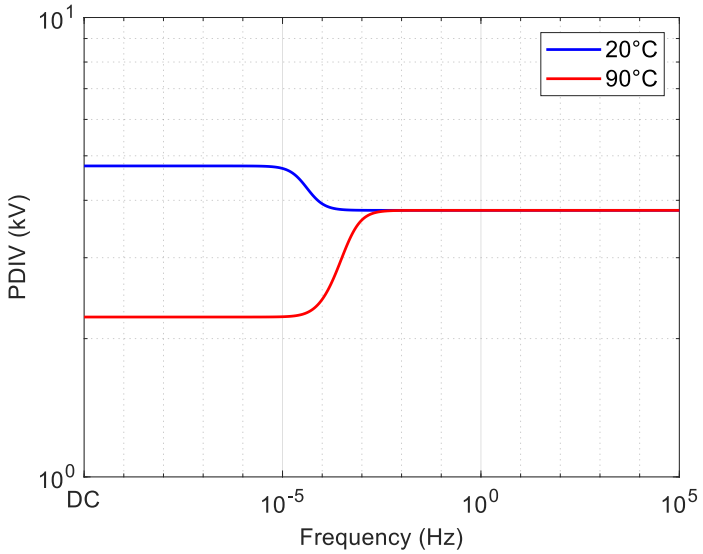

(b) α = 0.04 [°C^{-1}]

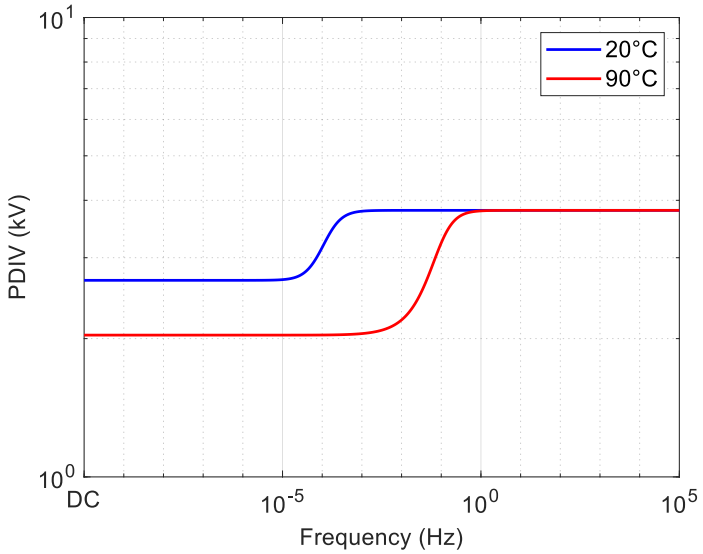

(c) α = 0.1 [°C^{-1}]

Figure 3.5. PDIV as a function of power supply frequency and α from Equations (3.20) and (3.21): (a) α = 0.01, (b) α = 0.04 and (c) α = 0.1 [°C^{-1}].

As shown in Figure 3.5, the PDIV variation as a function of power supply frequency when it decreases from AC (permittivity-driven regime) to DC (conductivity-driven regime) depends on electrical conductivity especially α. For instance, when α has its lowest value such as 0.01 [°C^{-1}], PDIV under DC is higher than that under AC (e.g., 50 Hz) both at 20°C and 90°C (see: Figure3.5a).

However, when α has its highest value such as 0.1 [°C^{-1}], PDIV under DC would be lower than that under 50 Hz both at 20°C and 90°C (see: Figure3.5c). Finally, when α has a middle value such as 0.04 [°C^{-1}], while PDIV under DC is higher than that under 50 Hz at 20°C, it can be lower than PDIV under 50 Hz at 90°C (see: Figure3.5b).

3.3 Experimental results and discussion

The used test object for the PD testing consists in a three-layer flat specimen where the internal layer was punctured to create a hole (see: Figure 3.6). The insulating material used was XLPE. The mean defect dimensions were radius 1.7 mm and height 0.4 mm (cylindrical cavity).

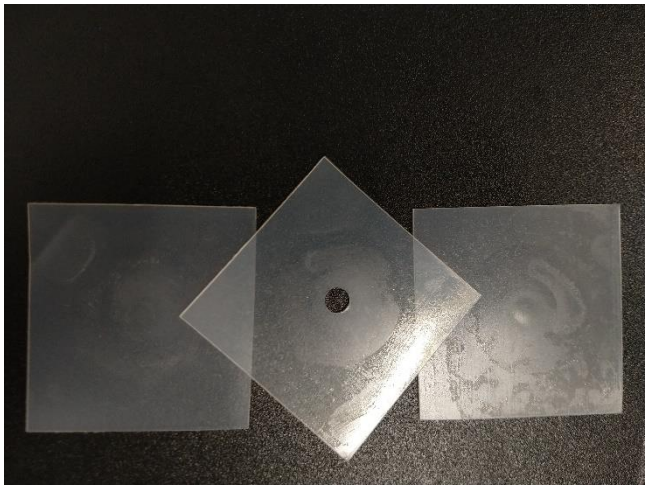

(a)

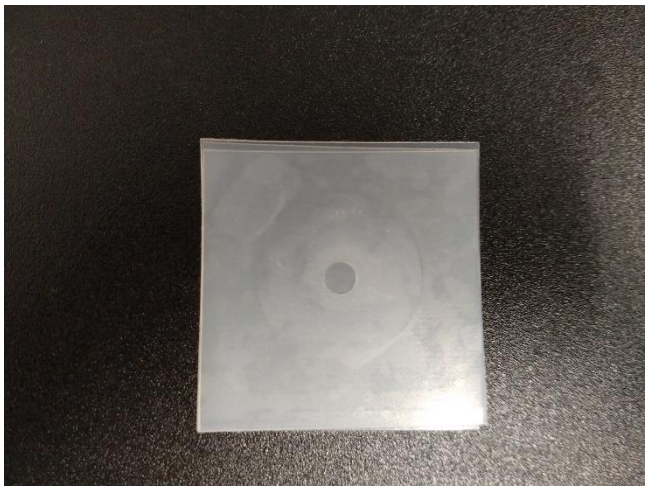

(b)

Figure 3.6. (a) Three flat layers of the XLPE multilayer specimen and (b) the XLPE multilayer specimen used for the PD measurements.

PDIV tests were done increasing voltage stepwise, with step dwell time of 10 s for AC and 30 min for DC. PD were detected under DC while rising voltage, but only those detected in steady state at a specific step were introduced as $PDIV_{DC}$. A 1MΩ resistance was connected in series with the HV supply, and a PD-free capacitance (590 pF) was connected in parallel with the test specimen to perform more effective PD measurements. This configuration reduces the amount of ripple and noise induced on the testing specimen from the chosen power supply. This is particularly important in DC acquisitions. The parallel capacitance also acts as a coupling capacitance and amplifies the amplitude of detected PD pulses. In addition, it provides a low impedance charge source for the test object.

Figure 3.7 shows the PDIV values measured at the three temperatures of 20, 60 and 90 °C on the multi-layer specimens, both in DC and in AC, as well as the fitting to the theoretical model (3.20). A mean XLPE conductivity value of 1.9×10^{-15} S/m at 20°C and 20 kV/mm was measured and used in the model, with the temperature coefficient, α = 0.04 $^{o}C^{-1}$. As can be seen, while the AC PDIV changes only a little with temperature, DC PDIV displays a large dependence on temperature. Regarding the fitting to the model, at 20 °C it is very good for both DC and AC, while some (small) differences can be observed with increasing temperature. Summarizing, a simple circuit model predicts the PD data temperature dependence, i.e., the higher the temperature, the lower is $PDIV_{DC}$, and that, for the chosen cavity and insulation dimensions, $PDIV_{DC}$ can span the range from about 2.2 times $PDIV_{AC}$ to 0.7 $PDIV_{AC}$ (see: Table 3.1).

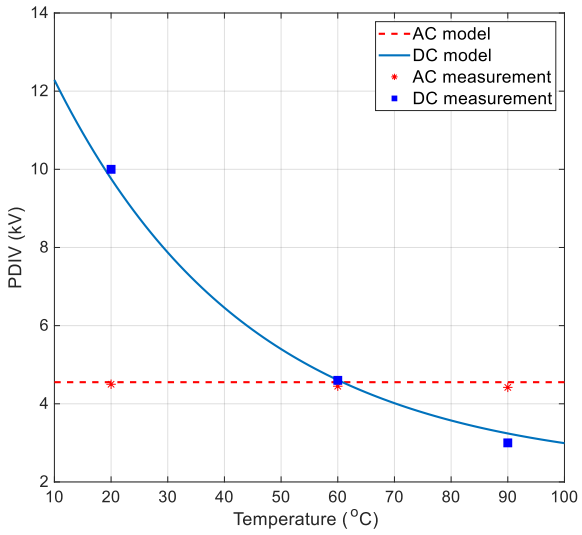

Figure 3.7. Fitting to the theoretical model for the PDIV values measured at the three temperatures on the multi-layer specimens.

The introduced PDIV model might open an interesting perspective from the application point of view, even if, of course, considering this point that cavity size dimensions are generally unknown. Thinking to improve the robustness of PDIV model, it is noteworthy to evaluate the sensitivity of PDIV to cavity size (while the insulation thickness is left unchanged). For instance, Figure 3.8 shows variation of $PDIV_{DC}$ with cavity thickness and area. As indicated in Figure 3.8, the smaller the cavity thickness, the larger the variation of $PDIV_{DC}$ with temperature. In such a way that at room temperature (20°C), the smallest cavity height leads to the highest value of $PDIV_{DC}$, while at higher temperatures (e.g., 90°C) the opposite holds. For example, for the XLPE considered for the modeling in this chapter, there is a cross point at about 65 °C at which this phenomenon occurs.

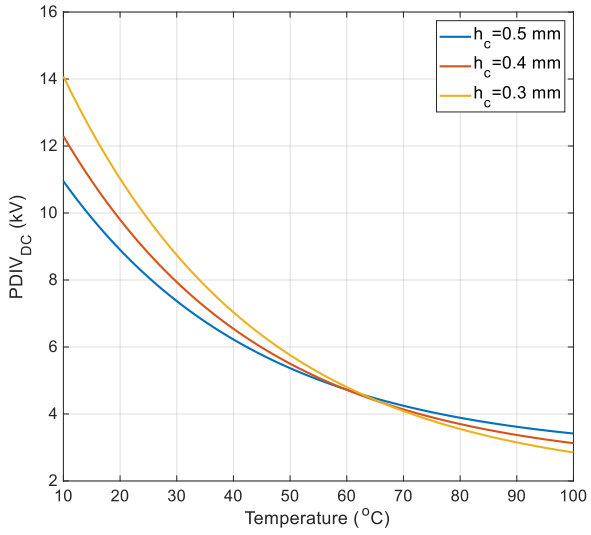

Figure 3.8. Variation of DC PDIV with cavity thickness as a function of temperature.

The above considerations can be scrutinized better in a wider perspective considering the functional dependence implied by Equation (3.14) such as following. Equation (3.14) can be rewritten in a more convenient form like:

$$\frac{PDIV_{DC}}{PDIV_{AC}} = \frac{\frac{h_c}{h_s - h_c} + \frac{\gamma_c}{\gamma_b}}{\frac{h_c}{h_s - h_c} + \frac{\varepsilon_{rc}}{\varepsilon_{rb}}} = \frac{\frac{h}{1-h} + \gamma}{\frac{h}{1-h} + \varepsilon} = \frac{h(1-\gamma) + \gamma}{h(1-\varepsilon) + \varepsilon} \tag{3.22}$$

where the following a-dimensional parameters are introduced:

$$\varepsilon = \frac{\varepsilon_{rc}}{\varepsilon_{rb}} = \frac{1}{f_{AC}} \leq 1 \tag{3.23}$$

$$\gamma = \frac{\gamma_c}{\gamma_b} = \frac{1}{f_{DC}} \tag{3.24}$$

$$h = \frac{h_c}{h_s} < 1 \tag{3.25}$$

The specified restrictions of those parameters are because of physical considerations (e.g., cavity height cannot exceed the thickness of the entire specimen).

Equation (3.22) is a function of the two variables h and γ, described by the surface illustrated in Figure 3.9.

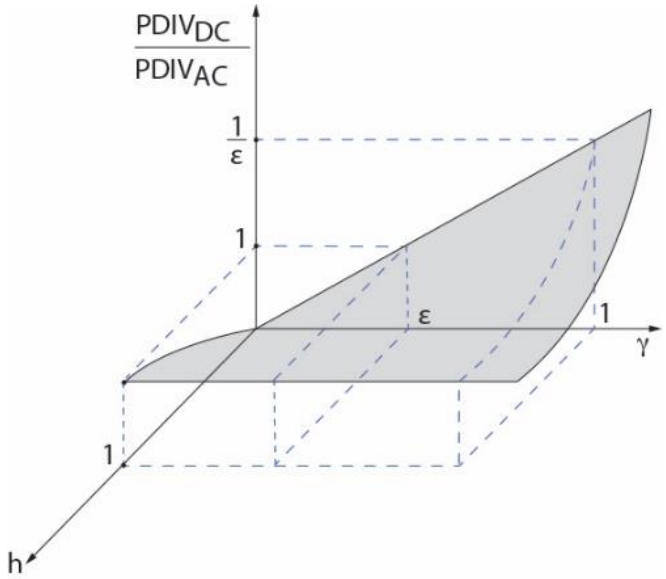

Figure 3.9. Representation of Equation (3.14) as a function of a-dimensional parameters h and γ.

Calculating the partial derivatives of the PDIV ratio with respect to h_c, or equivalently h, and considering that γ is an inverse function of temperature (it decreases if temperature increases), the following conclusions are obtained (as already shown by Figure 3.8):

- At low temperatures such that $\frac{\varepsilon_{rb}}{\varepsilon_{rc}} > \frac{\gamma_b}{\gamma_c}$ the PDIV ratio decreases with increasing h_c.
- At high temperatures such that $\frac{\varepsilon_{rb}}{\varepsilon_{rc}} < \frac{\gamma_b}{\gamma_c}$ the PDIV ratio increases with increasing h_c.
- when the temperature is such that $\frac{\varepsilon_{rb}}{\varepsilon_{rc}} = \frac{\gamma_b}{\gamma_c}$ the PDIV ratio is independent of h_c and equal to 1.

These analytical predictions are confirmed by the plots in Figure 3.8.

Regarding the cavity cross sectional area, as can be speculated from Equation (3.12), it is obvious that the change of cavity diameter is expected to have no influence on the $PDIV_{DC}$, because cavity

diameter is simplified out in the ratios. This proposes that the thickness of cavity is important over the range in values used herein, but the influence of the cavity size over a wider range of variables would possibly need more sophisticated analysis. What has been introduced here is not a comprehensive theory but an endeavor to develop a method to approximate the behavior of relevant components under DC power (e.g., power cables) in the presence of inevitable manufacturing defects and compare it to more extensively documented performance under AC excitation. The results have necessarily a narrow applicability owing to the simplifying assumptions employed and the limited test data but may pave the way to more extensive theory.

3.4 Partial discharge magnitude

Partial discharges (PD) in DC and AC take place under the probability of the presence of an electric field in an insulation defect (cavity, interface) exceeding the inception field, conditioned by the availability of a firing electron:

$$Pr(\,(E_c > E_i)|F) = \frac{Pr(\,(E_c > E_i) \cdot F)}{Pr(\,F)} \tag{3.26}$$

being F the event of firing electron availability and Pr its probability, E_c the field in the defect (cavity), E_i is the PD inception field (peak value), having approximate expression (for air in a spherical defect of diameter d), [11]:

$$E_\mathrm{i} = 25.2p\left(1 + \frac{8.6}{\sqrt{pd}}\right) \quad \left[\frac{V}{m}\right] \tag{3.27}$$

where p represents the gas pressure inside the cavity. This can be adapted to a cylindrical cavity replacing d with h_c (based on our simulations and experiments). The probability of having a firing electron available can be derived approximately from [12]:

$$h_1 = N_{SC}(t)\nu_0 \exp\left(-\frac{\Psi - \sqrt{e\frac{|E_i(t)|}{4\pi\varepsilon_0}}}{KT}\right) \tag{3.28}$$

being h_1 the hazard rate of electron detrapping from insulation/defect interface and $N_{SC}(t)$ the interface charge that can be detrapped at time t. The terms e, ν_0, K, ε_0, T and Ψ are the electron charge, the base phonon frequency, the Boltzmann constant, the vacuum permittivity, temperature and the detrapping work function, respectively.

Thus, PD occurrence is a stochastic process, and its nature reflects on the PD charge amplitude distribution, that can be often described through a two or three parameter Weibull distribution introduced by Equation (2.32) [15].

The Weibull distributions of PD charge amplitude for DC and AC tests at 20°C, performed at 1.1 PDIV under DC and AC are reported in Figure 3.10. As can be seen, the slope is different (being the shape parameter, β_q, 4.8 and 2.8 for DC and AC tests, respectively), particularly higher for DC. This agrees with the assumption that at steady voltage the PD charge amplitude dispersion is lower in DC than in AC, which fits to the speculation that most of PD charge amplitude dispersion is due to the relation between stochastic delay time of the firing electron and the simultaneous supply-voltage amplitude variation. The PD charge amplitude at probability 63.2% (α_q), and even more at high probability, are significantly different, but the PD charge amplitudes at low probability values (e.g., 5%) are very close (1.2 to 3.2 mV in the example of Figure 3.10). This was expected, based on the initial assumption of the validity of Equation (3.27) both in AC and in DC.

Regarding the firing electron availability, the high probability values of the PD charge amplitude distribution are those more largely affected by the firing electron delay. This is an explanation for higher measured values for PD charge amplitudes under AC than DC. This holds much more in AC than under DC, since the higher the delay, the higher the voltage (more in AC than in DC, of course) and thus the field in the cavity at the discharge finally resulting in higher measured PD charge amplitudes under the same fraction of PDIV (the same overvoltage fraction) for AC.

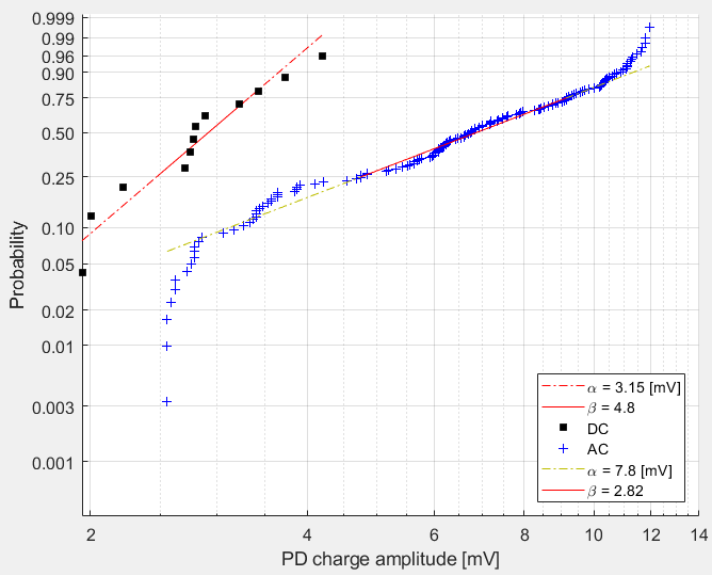

Figure 3.10. Weibull distributions of PD amplitude for DC and AC tests at 20°C, performed at 1.1 PDIV under DC and AC, for the tested specimens (multilayer with cylindrical defect).

3.5 Conclusions

Consequently, a tool based on PD equivalent RC circuit was introduced in this chapter to evaluate the expected PDIV under DC and its relationship with that measured under AC. It should be highlighted that while the latter measurement is relatively easy and largely practiced, the former is still not common and very often incorrect results can be obtained (e.g., because of transient PD during voltage rise or noise misinterpreted as real PD). As a result, the presented PDIV model can also help to evaluate the meaningfulness of experimental DC PD measurements. More research would have value to be conducted from both the modeling point of view and the testing techniques. The latter needs to be specified to make PD DC measurements viable for routine use in DC insulation as explained briefly in the next chapter. However, there are some interesting considerations which can influence on the design and choice of the materials candidate to be used in DC insulation which can be drawn based on the theory reported in this chapter. It was finally highlighted that the right way of approaching the discussion of PD charge magnitude in AC and DC is to consider the same overvoltage fraction and refer to the Weibull distribution. Indeed, effect of firing electron delay time, which is the major cause of the difference between measured PD charge amplitude under AC and DC which would be more significant for the PD charge amplitudes with high probability.

References

[1] F. H. Kreuger, Partial Discharge Detection in High-Voltage Equipment, Butterworth-Heinemann, 1990.

[2] IEEE 400.3, Guide for PD Testing of Shielded Power Cable Systems in a Field Environment, 2006.

[3] IEC 60885-3, Test Methods for Partial Discharges Measurements on Lengths of Extruded Power Cable, second Edition, 2015.

[4] Cigré TB 502, High-Voltage On-Site Testing with Partial Discharge Measurement, 2012.

[5] Cigré Working Group B1.04, Brochure 279, Maintenance for HV Cables and Accessories, 2005.

[6] G.C. Montanari, "Envisaging links between fundamental research in electrical insulation and electrical asset management", IEEE El. Ins. Magazine, Vol. 24, n. 6, pp. 1-21, 2008.

[7] Peter H. F. Morshuis, and Johan J. Smit, "Partial discharges at DC voltage: their mechanism, detection and analysis", IEEE Trans. Dielectr. Electr. Insul., Vol. 12, No. 2, pp. 328-340, 2005.

[8] U. Fromm, and Frederik H. Kreuger, "Statistical behaviour of internal partial discharges at DC voltage", Japanese journal of applied physics, Vol. 33, No. 12, p. 6708, 1994.

[9] G. C. Montanari, P. Seri, L. Cirioni, "Measuring partial discharges in DC insulation systems. A challenge, but also a must", IEEE ICPADM, pp. 128-131, Xi'an, Cina, maggio 2018.

[10] X. Feng, Q. Xiong, A. Gattozzi, G. C. Montanari, P. Seri, R. Hebner, "Cable Commissioning and Diagnostic Tests: The Effect of Voltage Supply Frequency on Partial Discharge Behavior," IEEE ICPADM, Xian, China, May 2018.

[11] L. Niemeyer, "A generalized approach to partial discharge modeling", IEEE Trans. Dielectr. Electr. Insul., Vol. 2, No. 4, pp. 510-528, 1995.

[12] A. Cavallini and G. C. Montanari, "Effect of supply voltage frequency on testing of insulation system", IEEE Trans. Dielectr. Electr. Insul., Vol. 13, No. 1, pp. 111-121, 2006.

[13] A. Cavallini, V. Krotov, G. C. Montanari, P.H.F. Morshuis, L. E. Mariut, "The role of supply frequency in the evaluation of partial discharge inception voltage in XLPE-embedded cavities", IEEE CEIDP, pp. 487-490, Montreal, Canada, October 2012.

[14] A. Pedersen, G. C. Crichton, and I. W. McAllister, "The theory and measurement of partial discharge transients", IEEE Trans. Dielectr. Electr. Insul., Vol. 26, No. 3, pp. 487-497, 1991.

[15] M. Cacciari, A. Contin, G. C. Montanari, "Use of a mixed-Weibull distribution for the identification of partial discharge phenomena", IEEE Trans. on DEI, Vol. 2, n. 6, pp. 1166-1179, 1995.

[16] L.A. Dissado and J.C. Fothergill, *in Electrical Degradation and Breakdown Polymers*. P. Peregrinus press, 1992.

[17] R. Bodega, G.C. Montanari, and P. H. F. Morshuis, "Conduction current measurements on XLPE and EPR insulation," In The 17th Annual Meeting of the IEEE Lasers and Electro-Optics Society (LEOS), 2004, pp. 101-105.

Chapter 4

Measuring partial discharges in MV cables under DC voltage: procedures and results in steady state conditions

Starting from measurements performed on MV cable, estimation of partial discharge inception voltage, PDIV, and inference of the different behavior of PD for a MV cable models are presented and discussed. The estimations are validated through laboratory testing on a MV cable with an artificial defect. As a confirmation for the obtained results in chapter 3, it is shown again that PDIV under DC can become considerably higher or lower than that under AC, depending on temperature and material properties, which affect PD repetition rate as well. However, resorting to the model presented in chapter 3, measuring PD for MV cable under AC will help to identify and validate the results of the PD DC measurements.

4.1 Introduction

Measuring partial discharges (PD) in insulation systems supplied by DC voltage is still a fundamental issue from both the measurement and the data interpretation point of view. However, DC PD measurements are necessary for the sake of reliability of the rapidly increasing amount of MVDC and HVDC installations worldwide.

To recall, comparing with AC, the DC electric field distribution is driven by conductivity, not permittivity [1, 2]. As a result, the electrical stress in AC and in DC can be vastly different, since the latter one highly depends on temperature. In a cable, the electric field in a defect (cavity) will depend on the temperature profile resulted from cable ampacity as well as on the cavity location. Consequently, PD can occur in a certain defect under AC, but not under DC (at the same peak voltage), or *vice-versa* [3, 4]. This indicates that DC cables must be PD-tested under DC, besides under AC supply. The latter is also necessary because, during energization and/or voltage polarity inversion (discussed in chapter 6), electric field is capacitively graded until DC steady state is reached with a time constant which might be not negligible, depending on the permittivity *vs* conductivity ratio known as dielectric time constant [5].

The major issue related to DC PD measurements, compared to AC, is that the absence of time-resolved patterns complicates dramatically the problems of noise rejection and PD source identification. Under AC, the phase-resolved PD (PRPD) pattern can help experts to discriminate

PD from other pulses, such as noise or external disturbances, and also diagnose the type of defect which generates PD (e.g., whether an internal cavity or a surface defect or just corona discharges). Under DC, one can observe only a time series of impulses, without any distinctive patterns [6, 8].

This chapter has the aim of evaluating mathematical model introduced in chapter 3 and test procedures that allow PD to be recognized and measured under steady-state DC supply voltage, varying insulation temperature and voltage for MV cable. Partial discharge inception voltage, PDIV (in DC and AC) is modelled in chapter 3, while measurement procedures, referring to MV cable models with an artificial defect, are presented in chapter 4. In this chapter, the different behavior of PD under DC and AC as a function of temperature for MV cable is discussed.

4.2 Partial discharge inception voltage in AC and DC

Considering a cylindrical cavity embedded in cable insulation, PD equivalent RC circuit being valid for AC and DC is illustrated in Figure 4.1 which can be used to determine partial discharge inception voltage (PDIV) for a cavity in cable insulation (e.g. embedded cavity, delamination near the conductor or the outer semicon), [3,4,9]. This circuit would be valid, as a first approximation, for both DC and AC [3].

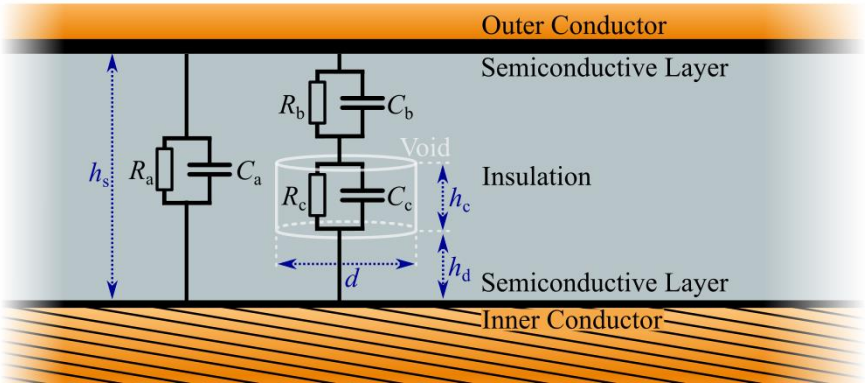

Figure 4.1. Scheme of cable insulation with thickness h_s, having a cylindrical embedded void of diameter d, height h_c,, distance to inner semicon layer h_d and equivalent resistive/capacitive circuit (*abc* circuit): C_c and R_c are equivalent capacitance and resistance of the cavity where discharges occur, C_b and R_b are equivalent capacitance and resistance of the cable insulation in series with the cavity. C_a, R_a are remaining equivalent capacitance and resistance of the cable insulation (dimensions are reported in Table 1).

The relationship between PDIV under DC and AC is governed by the relationship between the corresponding electric field distributions. Considering a uniform-field geometry as shown in Figure

4.1 and neglecting the stochastic aspect of the hazard function discussed in [4], PDIV can be roughly estimated as the minimum of PD firing voltage values. Let us assume that the availability of starting electrons is large enough to neglect the delay from the time the PDIV is reached to the time the PD is fired. Assume also that the space charge that accumulates at the cavity interface can be neglected. Then, the PD inception field E_{inc} inside the cavity would not vary from AC to DC [9], thus PDIV under DC and AC can be estimated using Equations (3.4) and (3.5), respectively. The ratio of PDIV under DC to PDIV under AC with known cavity height can be also approximated using Equation (3.14).

Contrarily to permittivity, cable insulation conductivity displays broad (exponential) variation with temperature, T, and, to minor extent, with electric field E, that can be described by:

$$\gamma_b(T, E) = \gamma_0 \exp(\alpha(T - T_0)) \exp(\beta(E - E_0)) \quad (4.1)$$

where γ_0 is the conductivity at a reference temperature T_0 (in °C) and a reference electric field E_0 (in kV/mm), while α (in °C^{-1}) and β (in mm/kV) are the temperature and field dependence coefficients, respectively. The relationship of electrical conductivity with temperature has been approximated by considering T in place of $1/T$, as it would be required referring to the Arrhenius equation [14, 15]. It should be mentioned that the electric field distribution due to the coaxial cable design and the temperature gradient can be considered in (4.1).

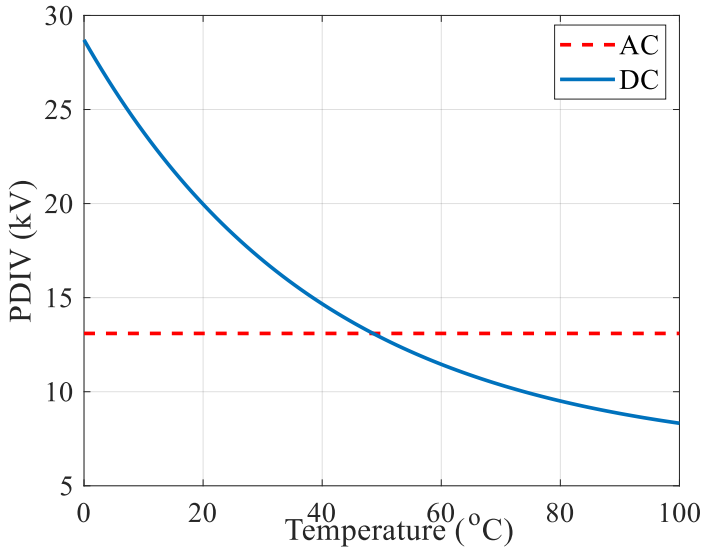

Figure 4.2. Estimation of PDIV in AC and DC as a function of bulk temperature, from Equations (3.4) and (3.5). Model parameters: α = 0.025 °C^{-1}, γ_0 = 2.05E-15 [S/m], T_0 = 0 °C, E_0 = 0 kV/mm, defect dimensions as in Table 4.1, and neglecting β.

Consider (3.4) and (3.5), the exponential dependence of γ_b on temperature and electric field (4.1), and the dependence of temperature profile on cable loading. Assume the inception field is equal in under DC and AC, estimated through the streamer inception criterion [9]. Then, the relationship between $PDIV_{AC}$ and $PDIV_{DC}$ as a function of temperature follows the curve plotted in Figure 4.2. We highlight that $PDIV_{DC}$ is significantly higher than $PDIV_{AC}$ at room temperature, while it becomes lower when the insulation temperature is > 50°C.

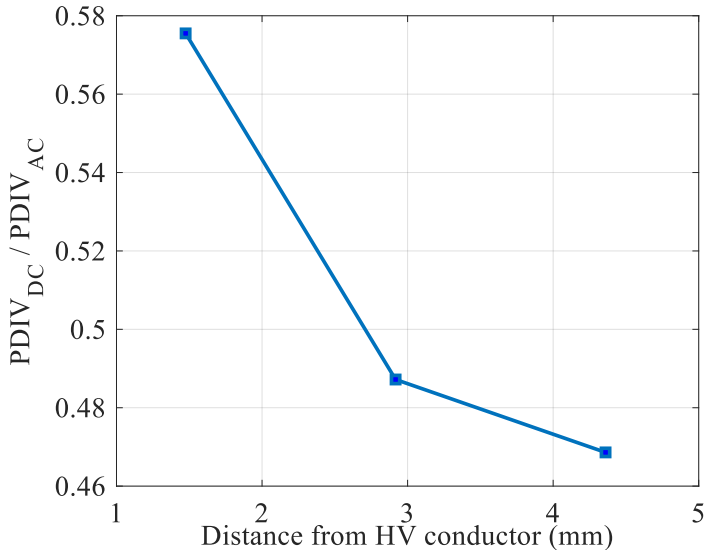

Figure 4.3. $PDIV_{DC}/PDIV_{AC}$ derived from (3.14) and (4.1) for a cylindrical defect (height=1.5 mm) located near the conductor, in the middle, and near to the outer semicon of a MV cable having insulation thickness 5 mm. Temperature difference 12°C, ambient temperature = 20°C.

Equation (3.14) is used to plot Figure 4.3, where the ratio between DC and AC PDIV as a function of cavity position is illustrated. When the temperature across the insulation goes from 90°C at the inner conductor to 78°C at the outer conductor, $PDIV_{DC}$ would be lower than $PDIV_{AC}$ for all cavity positions along insulation radius. When there is a high temperature gradient, the difference between $PDIV_{AC}$ and $PDIV_{DC}$ are expected to be lower for the cavities close to the inner conductor. While, if there is no temperature gradient, the field distribution is more or less the same.

4.3 Experimental procedures and results

In order to perform PDIV measurements, an artificial internal defect was made inside the insulation of a MV cable. To create the defect, the jacket and outer metal shield on top of the outer semiconductive layer were removed. The outer semiconductive layer and insulation layer were cut parallel to the cable inner conductor. A hole was drilled in the insulation layer and then sealed, resulting in an embedded void (Figure 4.4).

(a) Before sealing

(b) After sealing

Figure 4.4 The test cable with drilled void. The defect surface was cleaned using alcohol and compressed air to avoid any contamination. After sealing a copper foil was added around the defect area for measurement reason.

The parameters of the MV cable used for testing are collected in Table 4.1.

Table 4.1. MV cable parameters

Cable parameters	*Test cable*
Conductor material	Al
Insulation material	XLPE
Conductor class	2
Rated voltage	20 kV
Insulation inner radius	8.12 mm
Insulation outer radius	13.12 mm
Relative dielectric constant	2.3
Defect depth	1.5 mm
Defect diameter	6 mm
Defect distance to cylindrical axis	9.82 mm
Gas type in defect	air
Initial pressure in defect	101.32 kPa

The measurement circuit for DC PD measurements is sketched in Figure 4.5. For AC PD measurement, HVAC supply was applied directly to 21.5 kΩ.

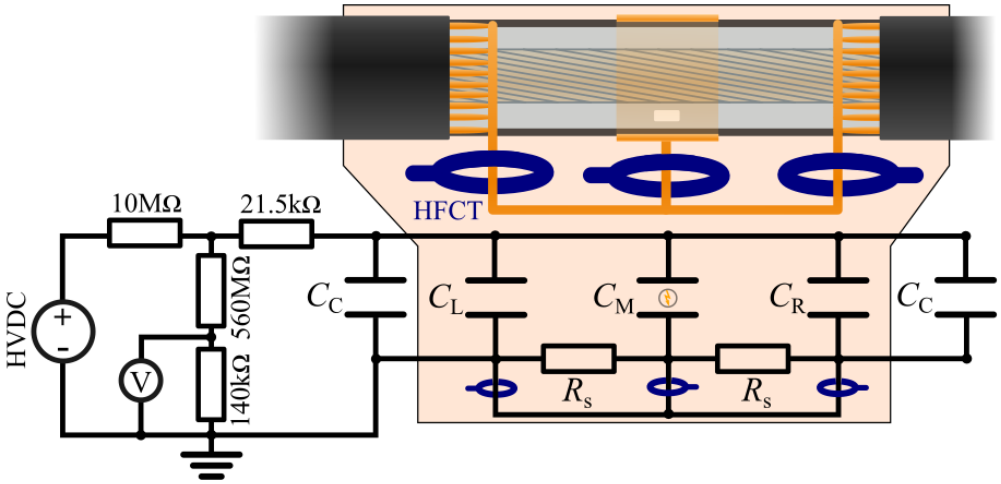

(a)

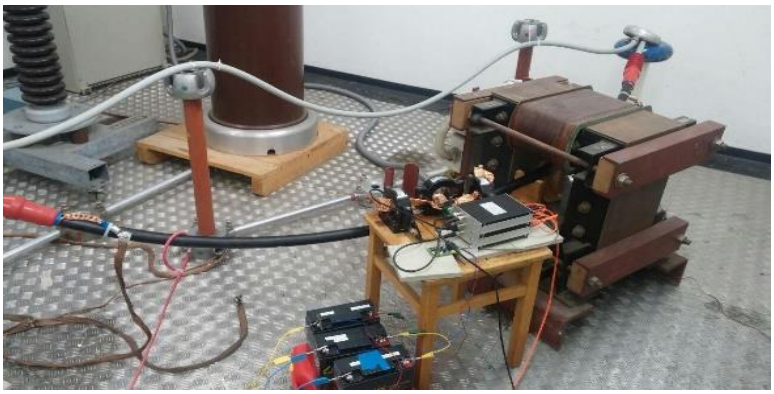

(b)

Figure 4.5. (a) Measurement circuit for DC PD (bottom) and separation of the three capacitances at the cable (top). C_L: cable capacitance on the left side of the defect, C_M: cable capacitance of the defect area (beneath copper foil), C_R: cable capacitance on the right side of the defect, C_C: additional coupling capacitors (1nF) at both cable ends for enhancing the sensitivity, R_s: resistance of the outer semicon layer, Blue: HFCTs as PD coupling devices. (b) Realization of measurement circuit for DC and AC PD.

A selective PD measurement method, based on [7], was employed, to be able to discriminate signals coming from the artificial defect or external PD/disturbances. To realize this measurement method, the cable shield surrounding the defect is separated from the remaining cable shield. A copper foil is wrapped around the defect area acting as capacitance electrode. The shields then are reconnected by a copper wire. This procedure allows the application of an PD High Frequency Current Transformer (HFCT) in the earthing lead of the capacitance of the cable area with defect (C_M). Divided into the three capacitances, see Figure 4.5a, PD coming from the artificial defect can be properly identified comparing PD charge magnitude of the middle HFCT with a second HFCT in the earthing lead of the left cable capacitance C_L, described in detail in [7]. Moreover,

the likelihood of pulse classification can be increased by pulse polarity check with a third HFCT at the earthing lead of the right cable capacitance C_R.

Calibration was done injecting 20 pC at the clamps of C_M (inner conductor connected at the termination). Pulses having magnitudes from 20 to 1000 pC were injected to both ends of the cable and it was verified that such disturbance pulses can be recognized and suppressed. The threshold trigger for the measurement was fixed at 1 pC. The bandwidth of the used digital bandpass filter for quasi-integration was 1.5 MHz at a center frequency of 1.5MHz. Eventually, in order to perform the measurement under steady state conditions, the applied voltage was kept constant at each increasing voltage test step (step dwell time) for a time larger than the estimated dielectric time constant of the cable insulation at each conductor temperature e.g., 20, 60 and 90 °C measured by platinum resistance thermometer (PT1000 sensor) with fiber optic transmitter, whereas the PDs during this transient time are not accounted as DC PD inception. This constant can be calculated as the ratio of permittivity to insulation conductivity, at the test temperature and field [3].

The results of testing under DC voltage under PDIV are depicted in Figure 4.6. As expected, since increasing the temperature the electric field in the insulation close to the outer conductor increases, the PDIV becomes lower. It can be observed also that the PD charge increases along with its statistical dispersion, whereas the repetition rates decreases. This is due to the longer time it takes in going from the residual voltage / field to the inception, since while inception is more or less fixed, residual is lower for higher PD amplitude. These evidences can be explained observing that temperature decreases the time constant of the insulation and favors charge recombination. The combined effect of these two factors leads to larger overvoltages when PD are incepted.

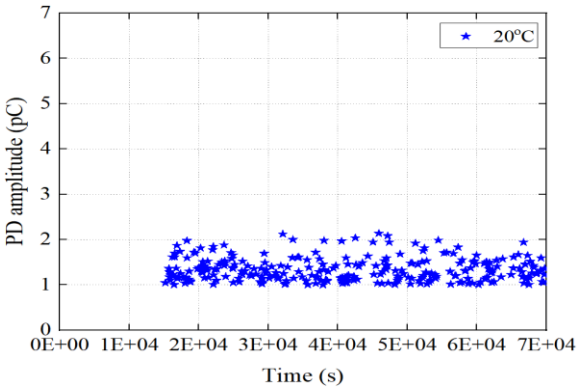

(a)

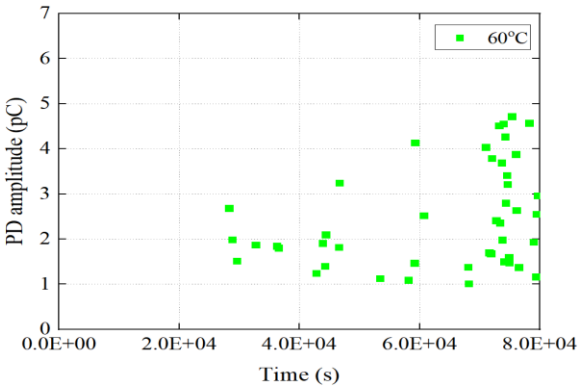

(b)

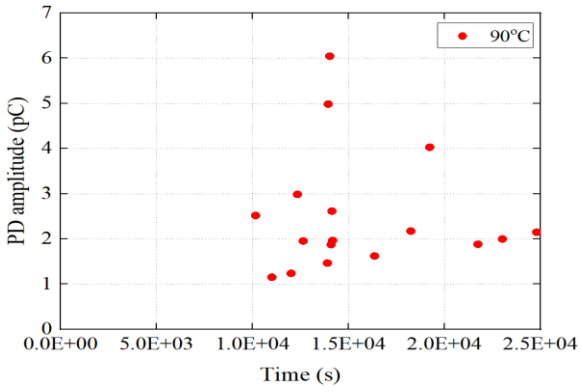

(c)

Figure 4.6. TRPD patterns under DC PDIV at three temperatures (a) 20°C - PDIV = 20 kV, (b) 60°C - PDIV = 12 kV and (c) 90°C - PDIV = 7 kV.

PD occurrence is a stochastic process, and its nature reflects on the PD amplitude distribution, that can be often described through a two or three parameter Weibull distribution introduced by Equation (2.32) [10].

The shape/slope parameter (β_q) of the Weibull distribution of PD charge amplitude is used to identify internal, surface or corona PD [8]. Figures 4.7a and 4.7b report Weibull plots of PD charge amplitudes, for DC and AC measurements, at 20°C, 60°C and 90°C, performed under $PDIV_{DC}$ and $PDIV_{AC}$.

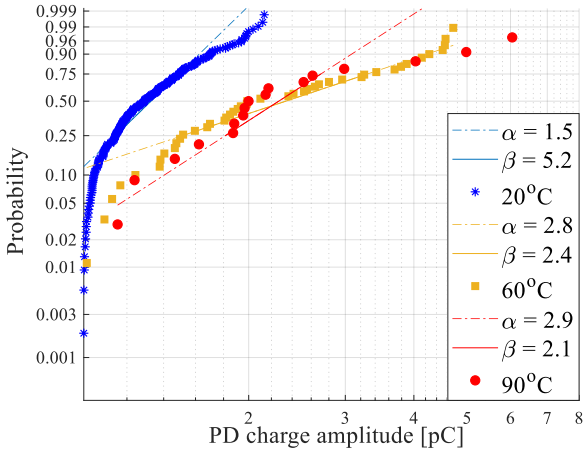

(a)

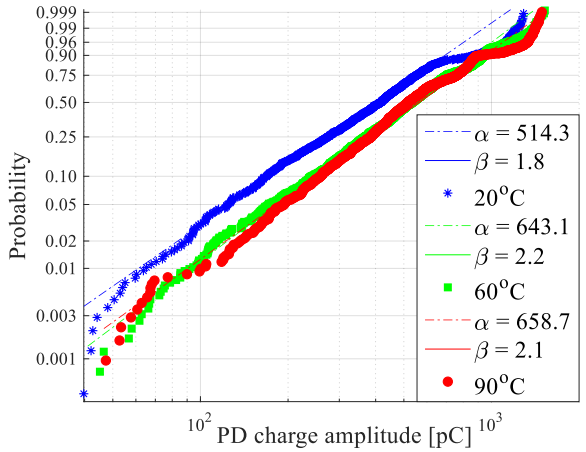

(b)

Figure 4.7. Plots for (a) DC and (b) AC (50 Hz) PD charge amplitudes under PDIV fitted to the two-parameter Weibull distribution.

It comes out that fitting to a two-parameter Weibull function is reasonably acceptable, and that the shape/slope parameter under DC is higher than that under AC, especially at lower temperatures (e.g., at 20°C, the shape parameter, β_q, is 5.2 and 1.8 for DC and AC tests, respectively). On the contrary, at higher temperatures, such as 90°C, β_q is almost the same ($\approx$ 2.1). This can be helpful for PD source identification.

The large difference between the PD magnitudes recorded using AC and DC voltages can be traced back, possibly, to the characteristics of the bandpass filter and to the differences between PD pulses in AC and in DC. Excluding corona discharges, the subject was investigated and reported only rarely [11,12]. However, it seems that PD pulses in DC can have a lower frequency content compared with pulses under AC. Therefore, using a bandpass filter with lower cutoff

frequency equal to 750 kHz might lead to an underestimation of the PD charge in DC. On the other hand, as it was mentioned already in chapter 3, considering the firing electron availability, PD charge amplitudes with high probability are those more largely affected by the firing electron delay. This could be an explanation for higher measured PD charge amplitudes under AC than DC. This holds much more in AC than under DC, because the higher the delay, the higher the voltage (more in AC than in DC, of course) and thus the field in the cavity at the discharge finally leading to higher measured PD charge amplitudes under PDIV for AC.

Regarding AC tests (shown in Figure 4.8), it has been seen that PD incept at each half cycle before zero crossing at lower temperature (e.g. 20°C), shifting to near the zero crossing as temperature increases (as a result of the reduced memory effect). As expected, PD charge amplitude dispersion remains almost constant with temperature (Figure 4.7b) whereas the measured PDIV values under AC were 13.4 kV_{rms}, 13.1 kV_{rms} and 12.3 kV_{rms} at 20°C, 60°C and 90°C, respectively. This slight decrease of PDIV under AC can be explained by Schottky effect where electron availability can increase at higher temperatures. Furthermore, PD under AC are typically characterized by high repetition rates, when compared to DC conditions [13]. This is the reason for the different number of PD pulses in plots of Figure 4.7.

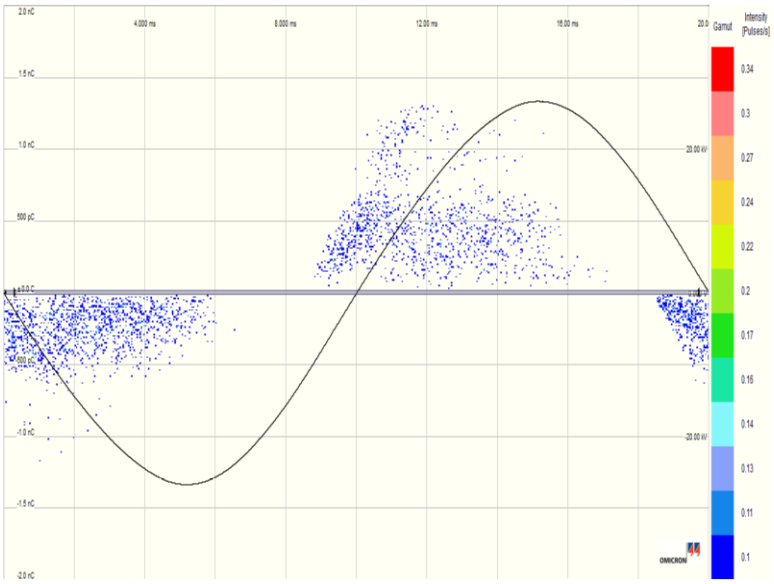

(a)

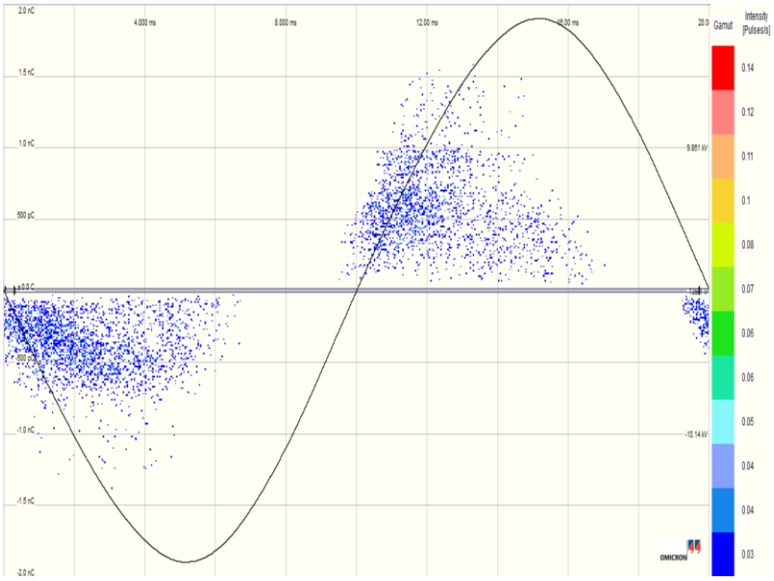

(b)

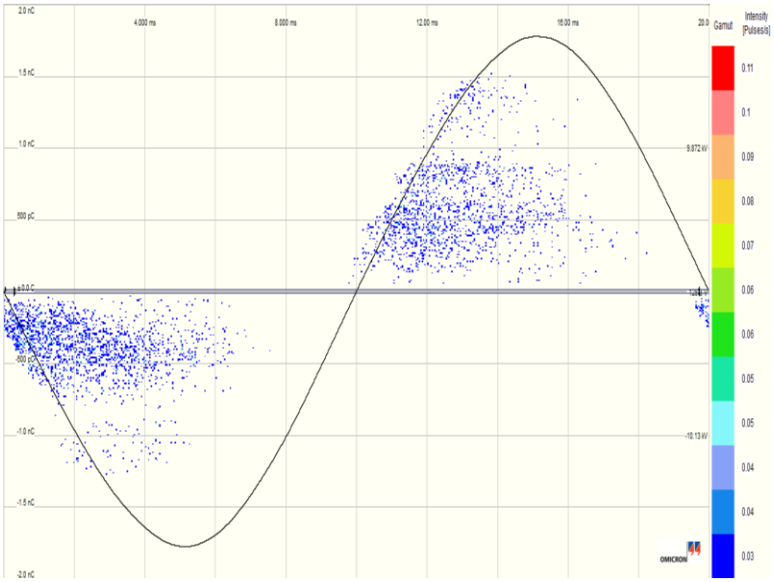

(c)

Figure 4.8. PRPD patterns under AC PDIV at three temperatures (a) 20°C - PDIV = 13.4 kV_{rms}, (b) 60°C - PDIV = 13.1 kV_{rms} and (c) 90°C - PDIV = 12.3 kV_{rms}.

4.4 Discussion and conclusions

The comparison of the calculated $PDIV_{DC}$ to $PDIV_{AC}$ ratio with experimental data at different temperatures, based on the model (3.14) and (4.1), is shown in Figure 4.9. As can be seen, the ratio between PDIV under DC and AC decreases as temperature increases, as predicted in by (3.14), showing a quite good fitting. Of course, as mentioned previously, the values of the ratio and their

dependence on temperature are related to the type of insulating material and its conductivity dependence with temperature (and electric field).

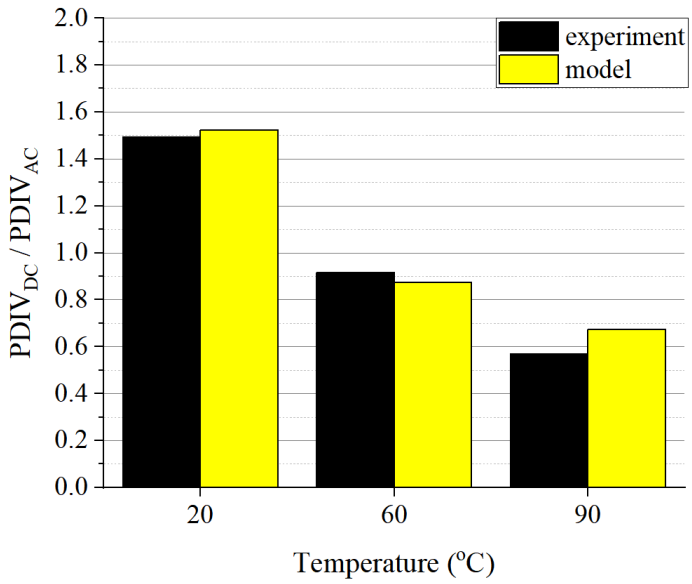

Figure 4.9. Comparison of the PDIV ratio with experimental data at different temperatures, according to model (3.14).

Consequently, the model presented in chapter 3 for multilayer specimen is evaluated by performing precise PD measurement through the sensitive and selective approach for MV cable in chapter 4. As shown in Figure 4.9, the prediction of PDIV under DC and its relationship with that measured under AC can help in the design of insulation systems under steady-state DC field. While the AC PD measurement is relatively easy and largely practiced, PDIV measurement under DC is still not common and misleading results can be obtained very often (due to e.g. transient PD during voltage increase or decrease, [5], or noise misinterpreted as PD). Eventually, the approach proposed here can help and validate DC PD measurements, having carried out analogue AC PD tests, as well as conductivity measurements on the insulating material.

References

[1] F.H. Buller, “Calculation of electrical stress in DC cable insulation,” IEEE Trans. Pow. App. Syst., vol. 86, no. 10, pp. 1169-1178, October 1967.

[2] C. K. Eoll, “Theory of stress distribution in insulation of high voltage d.c. cables. Part I,” IEEE Trans. Electr. Insul., vol. EI-10, no. 1, pp. 27–35, 1975.

[3] P. Seri, L. Cirioni, H. Naderiallaf, G.C. Montanari, R. Hebner, A. Gattozzi, X. Feng, “Partial discharge inception voltage in DC insulation systems: a comparison with AC voltage supply,” IEEE EIC, pp. 1-4, Calgary, Canada, June 2019.

[4] G.C. Montanari, R. Hebner, P. Seri, H. Naderiallaf, “Partial discharge inception voltage and magnitude in polymeric cables under AC and DC voltage supply,” Jicable, pp. 1-4, Varsailles, France, June 2019.

[5] P. Seri, R. Ghosh, H. Naderiallaf, L. Cirioni, G. C. Montanari, “Partial discharge measurements of DC insulation systems: the influence of the energization transient,” IEEE CEIDP, pp.1-4, Richland, Washington, USA, October 2019.

[6] Rotating electrical machines - Part 27-1: Off-line partial discharge measurements on the winding insulation, IEC 60034-27-1, first Edition, 2017-12-13.

[7] F. Esterl and R. Plath, “Sensitive and selective partial discharge measurement method for DC and AC cable joints,” Jicable, pp. 1-6, Varsailles, France, June 2019.

[8] G. C. Montanari, P. Seri, R. Ghosh, L. Cirioni, “Noise rejection and partial discharge source identification in insulation system under DC voltage supply,” IEEE Trans. on Diel. and El. Insulation, vol. 27, no. 2, pp. 1-6, April 2020.

[9] L. Niemeyer, “A generalized approach to partial discharge modeling,” IEEE Trans. on Diel. and El. Insulation, vol. 2, no. 4, pp. 510-528, 1995.

[10] M. Cacciari, A. Contin, G. C. Montanari, “Use of a mixed-Weibull distribution for the identification of partial discharge phenomena,” IEEE Trans. on DEI, vol. 2, no. 6, pp. 1166-1179, 1995.

[11] Udo Fromm, “Partial discharge and breakdown testing at high DC voltage,” PhD thesis, TU Delft, ISBN 90-407-1155-0, 1997.

[12] U. Lühring, D. Wienold and F. Jenau, “Comparative investigation on pulse shape parameters of partial discharges in air under AC and DC voltage stress,” IEEE UPEC, Coimbra, pp. 1-4, September 2016.

[13] P. Seri, H. Naderiallaf, G.C. Montanari, “Modelling of supply voltage frequency effect on partial discharge repetition rate and charge amplitude from AC to DC: room temperature,” IEEE Trans. on Diel. and El. Insulation, vol. 27, no. 3, pp. 764-772, June 2020.

[14] L.A. Dissado and J.C. Fothergill, in Electrical Degradation and Breakdown Polymers. P. Peregrinus press, 1992.

[15] R. Bodega, G.C. Montanari, and P. H. F. Morshuis, “Conduction current measurements on XLPE and EPR insulation,” In The 17th Annual Meeting of the IEEE Lasers and Electro-Optics Society (LEOS), 2004, pp. 101-105.

Chapter 5

Investigating conditions for an unexpected additional source of partial discharges in DC cables: load power variations.

This chapter has the purpose to investigate the variation of electric field inside a HVDC cable insulation, and consequent potentiality of partial discharge inception in a defect upon load current variation. Simulations carried out by COMSOL Multiphysics show that load variations can incept partial discharges during cable operation at a constant voltage, depending on insulating material characteristics, defect size and location, and, in particular, the temperature and field dependence of electrical conductivity. Different values for temperature and field dependency of electrical conductivity, as well as of thermal conductivity and heat capacity are considered and their effect on the field distribution inside cavities near inner and outer semiconducting layer analyzed. For this purpose, a new analytical model to predict the behavior of PD amplitude and repetition rate from cable energization to steady state, including load variation, is introduced. The likelihood of PD inception during load transients, and not only voltage transients as previously demonstrated, poses further attention and constraints to HVDC cable design.

5.1 Introduction

Conducting research on DC power cables is taking an increasing share of R&D projects, owing to the growing need of transmission on long distances, the diffusion of renewable generation, as well as the increasing reliability and decreasing conversion losses. Partial discharges, PD, can incept in cavities or interfaces due to manufacturing, commissioning, or thermo-mechanical aging processes, being thus a consequence of other phenomena. However, because of the high energy involved in a discharge compared to typical organic insulation for HV or MV cables, partial discharges can break chains and bonds of a dielectric and become themselves an extrinsic aging factor, able to grow existing defects till premature breakdown of insulation. PD are, thus, effect of aging (thus a diagnostic property) and cause of accelerated aging. Actually, compared to AC voltage supply, steady-state DC PD have much smaller repetition rate, [1-3], but operation of a DC cable includes voltage transients (e.g., energization and voltage-polarity inversion) during which PD can occur with high repetition rate, as under AC [4]. In steady state conditions, the DC electric field distribution in insulation and insulation defects is driven by conductivity depending on temperature and load. However, during voltage transients, also

permittivity plays a fundamental role. It is demonstrated in [4, 5] that PD phenomenology is like AC which means that it has large repetition rate at the beginning of each voltage transient. It goes slowly towards DC conditions (low repetition rate). This transient condition may take some hours depending on temperature (load). Similar effect is provided by a ripple superimposed to DC voltage, as long as its extent is able to bring the voltage to exceed the AC partial discharge inception voltage [6, 28].

Furthermore, PD can occur in certain defects under transients, but not under DC steady-state (at the same peak voltage), or vice versa [6, 7], because the electric field in defects and the probability of PD inception depend on the temperature gradient inside the insulation (thus load), and cavity location along the insulation radius.

Finally, under DC steady state, an increase of temperature always leads to a decrease of partial discharge inception voltage (PDIV) [8], which furthermore highlights the importance of considering load variation in PD investigation. From cable design point of view and for the sake of reliability, the electric field inside cavities resulted from load variations must be lower than PD inception field.

This chapter concentrates on an aspect of PD generation in DC cables that has not been investigated yet, which is the likelihood of PD inception as a function of load and temperature variations. There are two different types of events that are investigated, depending on the relationship between thermal and dielectric time constants, which can influence in different ways on PD phenomenology.

First, the experimental evidence that electric field transients can lead to inception of PD, being driven by the ratio between permittivity and conductivity of insulation, is briefly addressed, from [4], in Section 5.2. Afterwards, the effect of cable loading variation on the electric field distribution in the presence of an embedded cavity at different locations were investigated. For this purpose, simulations performed by COMSOL Multiphysics on a 320 kV HVDC cable, containing an embedded cylindrical cavity, were carried out, as described in Section 5.3. The effect of temperature and field dependence of electrical conductivity on PD inception is highlighted in Section 5.4. Section 5.5 reports and discusses the results of simulations for a reference cable geometry and insulation. Eventually, the peculiar condition in which the dielectric time constant can prevail on thermal time constant leading to field distribution ruled by permittivity in addition to conductivity when load varies, is introduced and examined in the last part of Section 5.5.

5.2 Evidence of partial discharge activity during supply voltage variations

As previously mentioned, at the beginning of each voltage transient, such as cable energization or voltage polarity inversion, PD phenomenology for DC cables is like that under AC voltage supply, with large repetition rates. PD behavior goes slowly (in times that, depending on temperature, can go up to hours) towards DC condition (i.e., low repetition rate). It is speculated in [4] that such behavior may have significant contribution to aging and premature failure in case of cables subjected to significant voltage transient repetition rate during standard operation.

An example of the effect of voltage supply rise time on PD repetition rate and magnitude is shown in Figure 5.1. The effect of different voltage ramps and PD events have been discussed in detail in [4]. The measurements were carried out on 3-layer specimens, with a cylindrical cavity in the central layer having height 0.1 mm and diameter 3 mm.

The maximum test DC voltage was kept lower than the partial discharge inception voltage in DC steady state ($PDIV_{\mathrm{DC}}$), to focus only on the effects of PD occurring during transient phases. As can be seen, PD are incepted just above the partial discharge inception voltage in AC ($PDIV_{\mathrm{AC}}$) value, confirming that the field in the insulation (and cavity) is driven by permittivity, as in AC.

It can be observed that even if the time required for the electric field to reach a quasi-steady state condition (called dielectric time constant) is $\tau_{\mathrm{d}} \approx 10^4\ s$, PD repetition rate drops to low values already after a few tens of seconds. Consequently, most of the PD activity and relevant damage is straight at the beginning of cable energization. This is what it occurs generally when the steady state voltage is lower than ($PDIV_{\mathrm{DC}}$) that can be calculated e.g., based on the model introduced in [6-9]).

Being the cable subjected or not to PD for most of the operations time (as a consequence, e.g., of the decrease of $PDIV_{\mathrm{DC}}$ with temperature), the large repetition rate and magnitude of PD during energization (or voltage polarity) transient compared to steady-state DC could play a significant role in aging acceleration if voltage transients are frequent [3]. As a note, it can be underlined that conventional (IEC 60270) PD measurements made on DC cables may be not effective in assessing defects that are supposed to activate PD in DC steady-state, because of the length of the tests (due to the confusion between voltage and field transient) and the issues of noise and PD separation under DC (lack of synchronization and phase-resolved PD pattern).

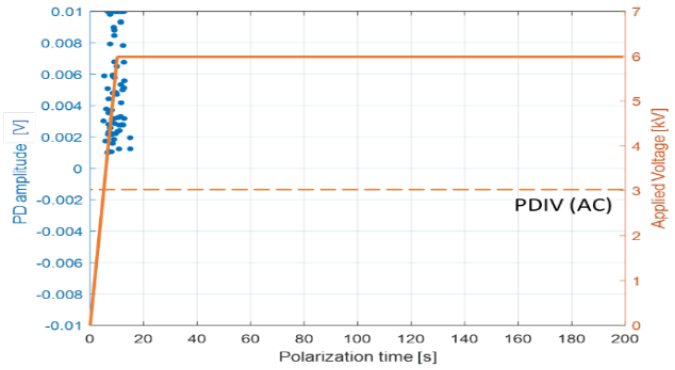

Figure 5.1. Applied DC voltage and PD events measured in three-layer specimens with a cylindrical cavity filled of air punched in the middle layer. Rise time 10s, peak voltage 6kV. Room temperature. *After [4].*

5.3 Modelling and simulation

Coupled thermal and electric field simulations were carried out through the 2D axisymmetric model in COMSOL Multiphysics, referring to the two-dimensional cable geometry of Figure 5.2 and insulating material parameters of Table 5.1 (this is also the consequence of considering the cavity height for PD modelling, rather than cross section and surface).

To perform the simulations, a homogeneous cylindrical insulation layer is considered. The thermal and electrical properties of the implemented insulation material are parametrized in Table 5.2, while the thermal properties are taken from [10, 11].

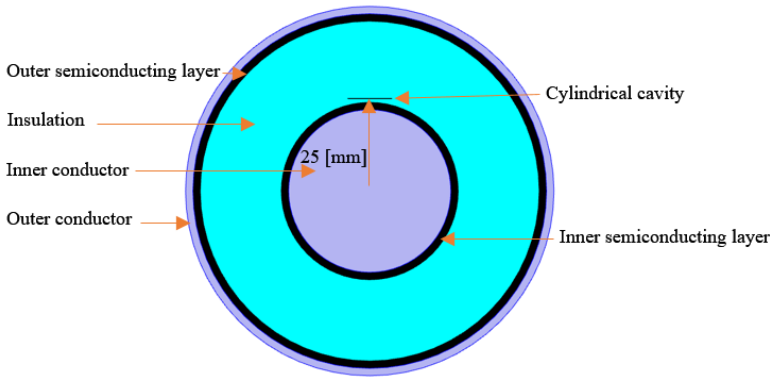

(a)

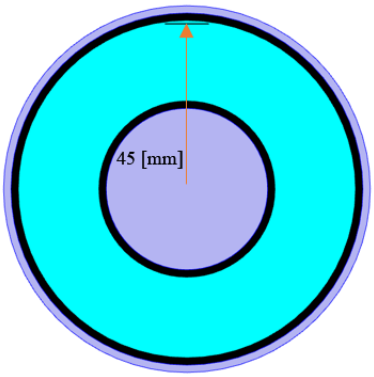

(b)

Figure 5.2. Cable geometry with cavity (a) near inner conductor and (b) near outer semiconducting layer.

Table 5.1. Geometry

Parameter		Radius [mm]
Inner conductor	r_i	22
Inner semiconducting layer	r_{insemi}	24
Insulation layer	r_{insul}	46
outer semiconducting layer	$r_{outsemi}$	48
Outer conductor	r_{outcon}	50
Cavity height	h_c	0.1
Cavity cross section radius	r_c	6

5.3.1 Electrical conductivity modelling

A well-known empirical model was used for the implementation of the dependence of electrical conductivity on temperature and electric field, [8, 12, 13]:

$$\gamma_b\big(T(r,t),E(r,t)\big) = \gamma_0 . e^{\alpha(T(r,t)-T_0)+\beta(E(r,t)-E_0)} \quad (5.1)$$

where γ_0 is the reference electrical conductivity at temperature T_0 (in °C) and a reference electric field E_0 (in kV/mm). The temperature dependence of conductivity is delivered by the temperature coefficient α (in °C^{-1}), whereas β (in mm/kV) represents the field-dependence coefficient. Regarding the relation with temperature, it should be mentioned that it has been approximated by considering T in place of $1/T$, as it would be required referring to the Arrhenius equation [12, 14]. In the typical operating temperature range of polymeric cables, and for the typical values of α, this is an acceptable simplification (actually widely used).

Table 5.2. Insulating material properties

Parameter		Value
Heat capacity	C_P	1900 J/(kg.K)
Thermal conductivity	λ	0.38 W/(m.K)
Permittivity	ε_r	2.3
Reference electrical conductivity	γ_0	2E-17 [S/m]
Temperature dependency coefficient	α	0.1 [°C^{-1}]
Field dependency coefficient	β	0.03 [mm/kV]

5.3.2 Thermal modelling

An energized cable with nominal voltage (U_0) and nominal current (I_0) produces Joule heating at the inner conductor when the load is switched on (neglecting dielectric losses). On the other hand, cooling is expected through the outer surface of cable when load is switched off. According to Fourier law, the temperature distribution during thermal transient (heating and cooling) can be considered by the heat conduction equation [15, 16]:

$$\rho_m C_P \frac{\partial T}{\partial t} = \nabla.(\lambda \nabla T) + Q_{heat} \tag{5.2}$$

where ρ_m is mass density (equal to 900 Kg/m^3 in the simulation), C_P is specific heat or heat capacity at constant pressure in *J/kgK*, *T* is temperature in *K*, λ is thermal conductivity in *W/mK*, and Q_{heat} is the heat source intensity in *W*, which is the sum of the total of heat generated by leakage current through the insulation j and the conductor joule losses:

$$Q_{heat} = \frac{|j|^2}{\gamma_b} + \frac{{I_{load}}^2}{\gamma_{al} . S^2} \tag{5.3}$$

being I_{load} is the load current, γ_{al} the aluminum conductivity. Since $j = \gamma_b . |E_b|$, with E_b the electric field in dielectric, it results:

$$Q_{heat} = \gamma_b . |E_b|^2 + \frac{{I_{load}}^2}{\gamma_{al} . S^2} \tag{5.4}$$

with *S* the cross-sectional area of the aluminum conductor.

A convective heat flux, Q_{conv}, in *W* is applied to the outer conductor as, [10, 11]:

$$Q_{conv} = h . A . (T - T_{ext}) \tag{5.5}$$

where h is the convection heat transfer coefficient in $W/m^2 \cdot K$, A is the surface area of the outer conductor in m^2, T is the surface temperature in K calculated by the simulation and T_{ext} is the external temperature in K.

Boundary conditions for thermal and electrical simulations, are parametrized in Table 3 [10], assuming that the HVDC cable is surrounded by air and there is only convection heat transfer, while surface to ambient radiation (surface emissivity) in all directions is set to zero.

Table 5.3. Parameter values used for the reference HVDC cable simulation.

Parameter		Value
Nominal voltage	U_0	320 kV
Nominal load	I_0	1450 A
Voltage at outer conductor	φ_0	0 kV
Convection heat transfer coefficient	h	5 [W/(m^2.K)]
External temperature	T_{ext}	293.15

5.3.3 Thermal and dielectric time constants

The thermal resistance and capacitance of a cylindrical cable insulation layer for per unit length are given by [18, 19]:

$$R_{\mathrm{th}} = \ln\left(\frac{r_{\mathrm{o}}}{r_{\mathrm{i}}}\right) / 2\pi\lambda \tag{5.6}$$

$$C_{\mathrm{th}} = \rho_{\mathrm{m}} C_{\mathrm{P}} \pi ({r_{\mathrm{o}}}^2 - {r_{\mathrm{i}}}^2) \tag{5.7}$$

where r_{o} and r_{i} are outer and inner radius of insulation layer, respectively.

It must be mentioned that the temperature dependence of heat capacity and thermal conductivity is neglected in the following calculations (Section 5.5). Also, it must be noted that the maximum temperature in insulation can reach values which cannot be withstood, bringing to thermal instability and breakdown for dielectric near inner semicon, if the thermal conductivity is decreased significantly (as in the case of the simulations in Section 5.5.2).

An accurate thermal time constant for a HVDC cable can be calculated using Cauer-type ladder network, where each cable layer has its own thermal resistance and heat capacity [18-20], but due to the fact that the thermal conductivity of inner and outer conductor, as well as of the semiconducting layers, are significantly higher than that for cable insulation, (and under the assumption of significant smaller thermal heat capacity of the conductor and semiconducting

layer), their effect on the total thermal time constant of cable would be negligible. As a result, the thermal time constant of a HVDC cable can estimated by the thermal time constant of its electrical insulation layer with reasonable approximation. After cable loading, the temperature across cable insulation varies exponentially as a function of time [21, 22]:

$$\Delta T = \Delta T_{\mathrm{ss}}\left(1 - e^{\frac{-t}{R_{\mathrm{th}}C_{\mathrm{th}}}}\right) \tag{5.8}$$

where ΔT is thermal increment in °C or K, ΔT_{ss} is temperature gradient across cable insulation layer under steady state condition in °C and $R_{\mathrm{th}}C_{\mathrm{th}}$ is thermal time constant, [20, 22]:

$$\tau_{\mathrm{th}} = R_{\mathrm{th}}C_{\mathrm{th}} \tag{5.9}$$

Regarding the dielectric time constant for an insulation material, it is defined as the ratio of relative permittivity to electrical conductivity, as resulted from Maxwell equations, [11, 23]:

$$\tau_{\mathrm{d}} = \varepsilon_0\varepsilon_{\mathrm{rb}} / \left[\gamma_{\mathrm{b}}\left(T(r,t), E(r,t)\right)\right] \tag{5.10}$$

where ε_0 is the permittivity of free space (8.85×10^{-12} F.m^{-1}) and $\varepsilon_{\mathrm{rb}}$ is relative permittivity of insulating material.

Considering parameters of Table 5.2, thermal time constant in dielectric is τ_{th} = 37.6 [min] from Equation (5.9). The values of dielectric time constants (Equation (5.10)) under a field of 20 kV/mm are τ_{d} = 1.26E3 [min] and 1.15 [min] at 20 and 90°C, respectively. Let us note that thermal time constant (τ_{th}) should generally lower than dielectric time constant (τ_{d}).

5.3.4 Simulation cases

The thermal and electrical parameters reported in Table 5.2 are used for the reference simulations. The cable is energized to 320 kV at t = 0 with the rate of 320 kV/min. Simulations support the calculations based on Equations (5.9) and (5.10), thus after reaching electrical steady state condition, the load is switched on at t = 2000 min, and after reaching thermal steady state condition the load is switched off at t = 6000 min (with the rate of 1450 A/min). The effect of temperature (α) and field (β) dependence coefficients of electrical conductivity on the electric field inside cavity and in insulation when the cavity is located near inner conductor (Figure 5.2a) or near outer semiconducting layer (Figure 5.2b) could be then simulated and analyzed.

An attempt to examine a different condition, where the thermal constant is longer than the dielectric constant, i.e., $\tau_{\mathrm{th}} > \tau_{\mathrm{d}}$ was also carried out, to understand how PD can possibly be generated in a different way, i.e. driven not only by a change of conductivity with load, but by a transient as that described in Section 5.2, which is driven by permittivity. The thermal time

constant was increased in two ways, i.e., reducing the thermal conductivity of the insulating material, and increasing its heat capacity. In this case the load was switched on at t = 3000 min and after reaching thermal steady state condition (supported by the simulations), the load was switched off at t = 9000 min, with rate of 1450 A/min.

5.4 PD inception field and repetition rate

5.4.1 Electric field amplification factor

To recall, in AC the electric field in cavities or defects inside insulation depends on the permittivity ratio. For a cylindrical cavity, the amplification factor is given approximately by [24, 25]:

$$f_{\mathrm{AC}} = E_c / E_B = \varepsilon_{\mathrm{rb}} / \varepsilon_{\mathrm{rc}} \tag{5.11}$$

where $\varepsilon_{\mathrm{rc}}$ and $\varepsilon_{\mathrm{rb}}$ are relative permittivity and E_{c} and E_{b} are electric field, in cavity and insulating material, respectively.

Under steady-state DC conditions, the situation is significantly different, since the electric field inside the defect depends on the conductivity ratio between the medium filling the cavity and the insulation. Consequently, the field amplification factor for a cylindrical cavity is given by [3]:

$$f_{DC} = E_C / E_B = \gamma_b\big(T(r), E(r)\big) / \gamma_c \tag{5.12}$$

where γ_{c} is cavity (air) electrical conductivity (taken as 3E-15 S/m, according to [3]).

5.4.2 Partial discharge inception field and repetition rate

To analyze the partial discharge inception field, E_{i}, inside cavities embedded in insulation, reference can be made to an approximate, deterministic expression proposed in [26], (for air in a spherical defect of diameter d):

$$E_{\mathrm{i}} = 25.2p\left(1 + \frac{8.6}{\sqrt{pd}}\right) \tag{5.13}$$

where p represents the gas pressure inside the cavity. This works approximately also for a cylindrical cavity replacing d with cavity height, h_{c}, [3-7].

The PD repetition rate as a function of time, $n(t)$, from AC (cable energization or voltage polarity inversion) to DC steady state condition, can be estimated combining the approximate models introduced in [3]. Accordingly, the variation of repetition rate from the beginning of a transient (n_{AC}) to DC steady state (n_{DC}) can be expressed as:

$$n(t) = n_{DC} + (n_{AC} - n_{DC}) . \exp\left(-\frac{t}{\tau_d}\right) \quad (5.14)$$

where, for a cylindrical insulation a very rough expressions of the repetition rate at the beginning a voltage transient or in DC steady-state are:

$$n_{AC} = \frac{2\pi . E_c(t)}{\tau_d . (E_i - E_r)} \quad (5.15)$$

$$n_{DC} = \frac{\gamma_b\left(T(r,t), E(r,t)\right) . h_c + \gamma_c . h_b}{\varepsilon_0 . (\varepsilon_{rb} . h_c + \varepsilon_{rc} . h_b) . \ln\left(\frac{E_c(t) - E_r}{E_c(t) - E_i}\right)} \quad (5.16)$$

being $E_c(t)$ the electric field inside the cavity (that can be calculated by simulations), E_r is the residual electric field, τ_d and E_i are the dielectric time constant and the inception electric field, from Equations (5.10) and (5.13), respectively, and h_b is the thickness of the dielectric. These are again rough simplification of the reality, where a cavity may be not fully cylindrical, e.g., it can have non-negligible boundary effects, and PD can occur in different section of the cavity surface (in addition, PD inception is deterministic rather than stochastic, according to model (5.13)).

5.5 Simulation results

5.5.1 Dielectric time constant larger than thermal time constant

As mentioned, this is the condition resulting from the considered cable parameters and, indeed, the most likely condition for the insulating materials used nowadays for DC cables.

Figure 5.3 shows the simulation results for the field inside a cavity when α = 0.1 and 0.07 $^{o}C^{-1}$, while the load is switched on and switched off (for the cavity with distance of 1 mm to inner semicon (Figure 5.2a) and for the cavity with distance of 1 mm to outer semicon (Figure 5.2b), β = 0.03 mm/kV). The dotted horizontal line indicates the PD inception field, according to the criterion of Equation (5.13).

The dashed horizontal line in Figure 5.3a indicates the PD inception field, according to the criterion of Equation (5.13). Partial discharges can be incepted immediately at energization (voltage transient, high repetition rate, Figure 5.3b), then they disappear. Again, they can appear after switching on the load, but only for the highest value of α for both cavities near to inner and outer semicon, while there is always field large enough to incept PD inside the cavity near to inner semicon. Removing the load brings the field in the cavity again below the PDIV, both for DC and

AC. PD steady-state repetition rate, estimated by Equation (5.14), provides 0.04 min^{-1} for α = 0.1 $°C^{-1}$ and 0.01 min^{-1} for α = 0.085 $°C^{-1}$ for cavity near inner semicon, while there are no PD for α = 0.07 $°C^{-1}$.

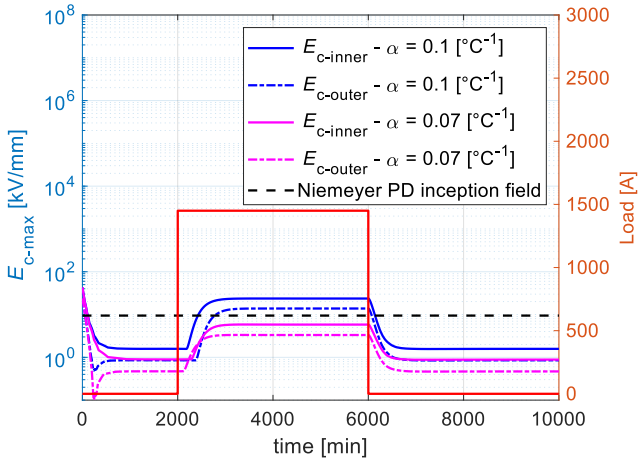

(a)

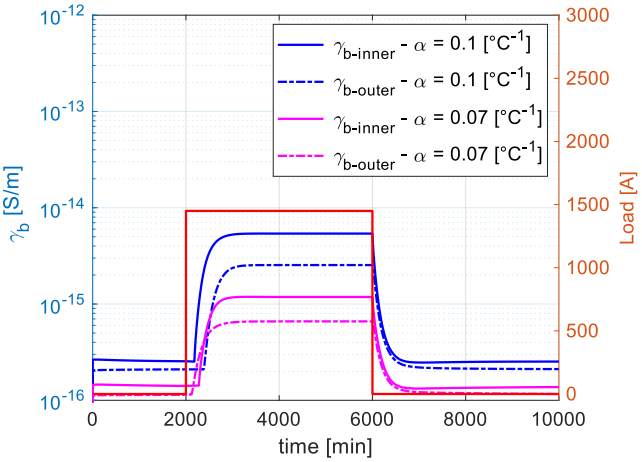

(b)

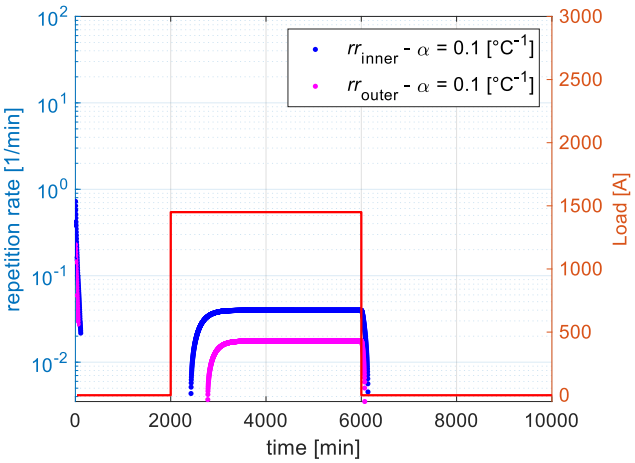

(c)

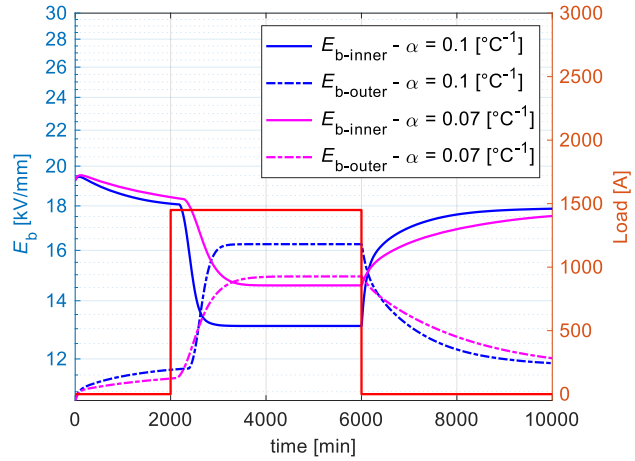

(d)

Figure 5.3. (a) Maximum electric field inside cavities located near the inner semicon ($E_{c\text{-inner}}$) and outer semiconducting layer ($E_{c\text{-outer}}$) when α = 0.1 and α = 0.07 °C^{-1}, upon cable energization, loading and switching off. (β=0.03 mm/kV). Dotted horizontal line: PD inception field, according to Equation (5.13). (b) conductivity behavior as a function of time (Equation (5.1)) for dielectric near inner conductor ($\gamma_{b\text{-inner}}$, r = 25.2 mm) and outer semiconducting layer ($\gamma_{b\text{-outer}}$, r = 45.2 mm). (c) estimated PD repetition rate inside cavity near inner conductor (rr_{inner}) and near outer semiconducting layer (rr_{outer}) from Equations (5.14) - (5.16) where E_r is neglected and α = 0.1 °C^{-1}. (d) electric field behavior as a function of time, α and load for dielectric near inner conductor ($E_{b\text{-inner}}$, r = 25.2 mm) and outer semiconducting layer ($E_{b\text{-outer}}$, r = 45.2 mm). The load cycle is also indicated.

It can be seen from Figure 5.3b that when α increases, it results in increase of γ_b from Equation (5.1) and following that it results in increasing the field inside cavity both near inner and outer conductor under steady state condition from Equation (5.12) (see: Figure 5.3a).

As shown in Figure 5.3d, because of field inversion under full load and steady state condition $E_{\text{b-outer}} > E_{\text{b-inner}}$. In addition, the ration of $E_{\text{b-outer}} / E_{\text{b-inner}}$ increases when α increases. On the other hand, while $E_{\text{b-inner}} > E_{\text{b-outer}}$ under no load, the ratio of $E_{\text{b-inner}} / E_{\text{b-outer}}$ increases when α increases.

The electric field and temperature profile under steady state condition (under full load and nominal voltage) across cable insulation and cavity for the reported conditions in Figure 5.3 have been depicted in Figure 5.4.

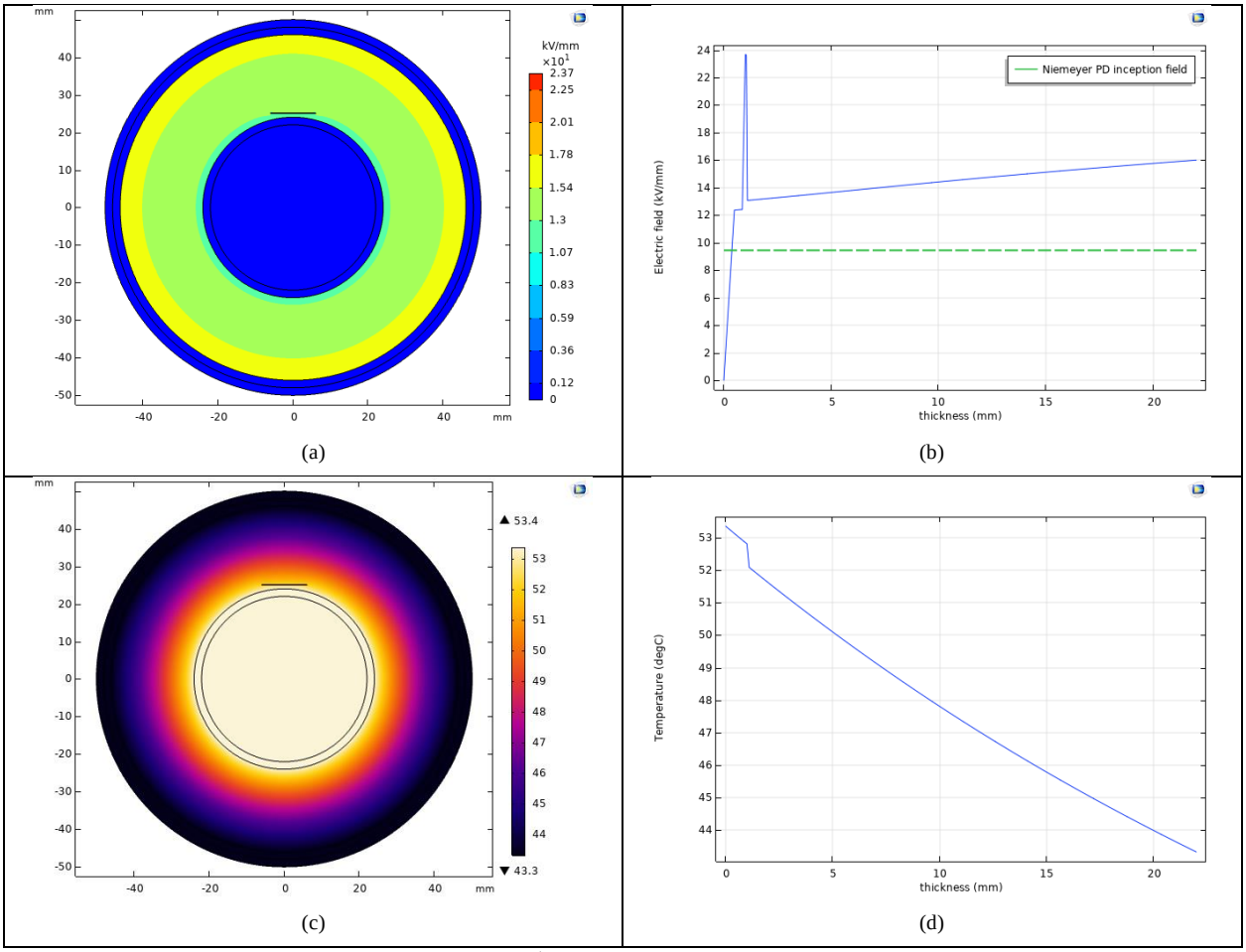

(a) α = 0.1 [°C^{-1}] – cavity near inner conductor

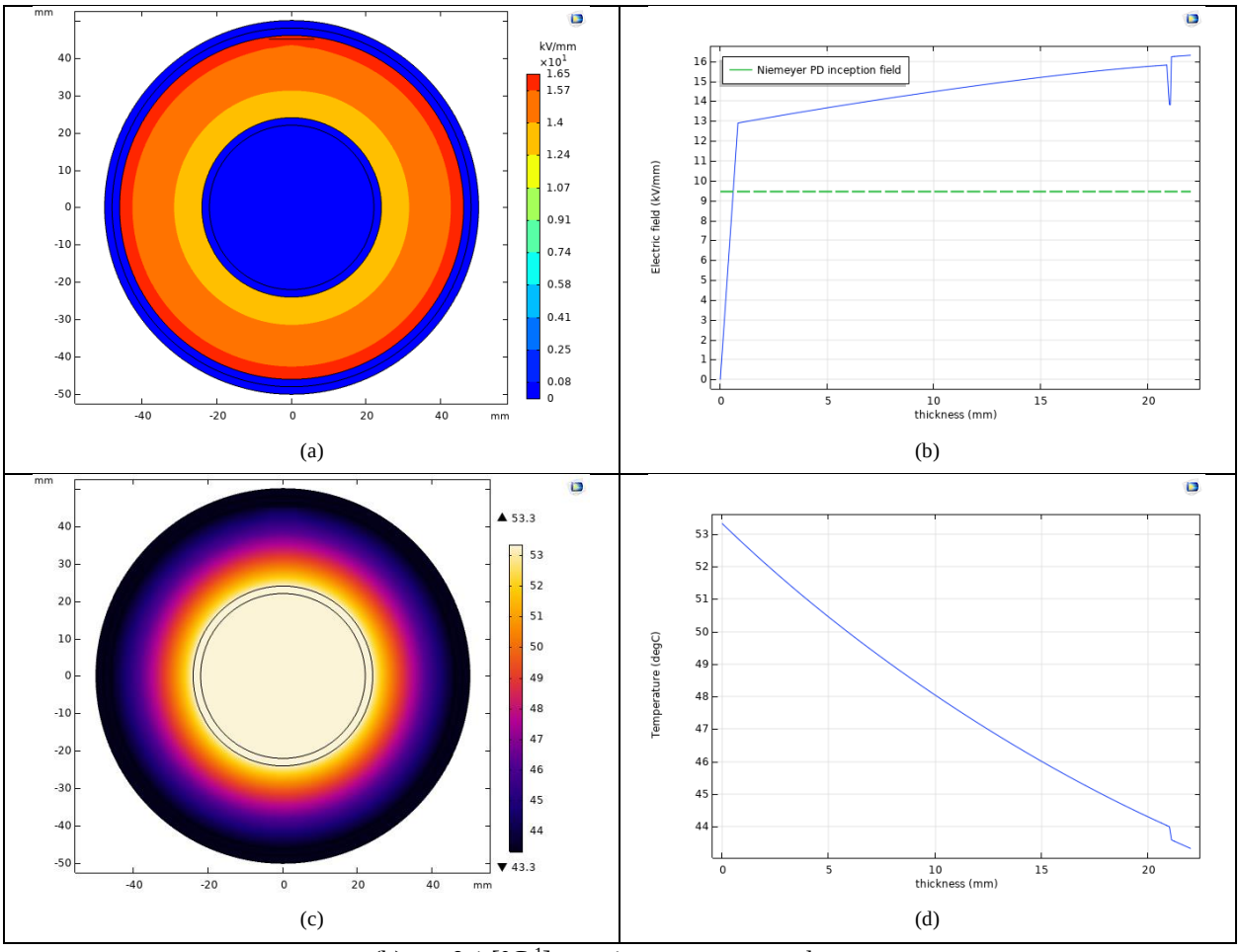

(b) $\alpha = 0.1$ [°C^{-1}] – cavity near outer conductor

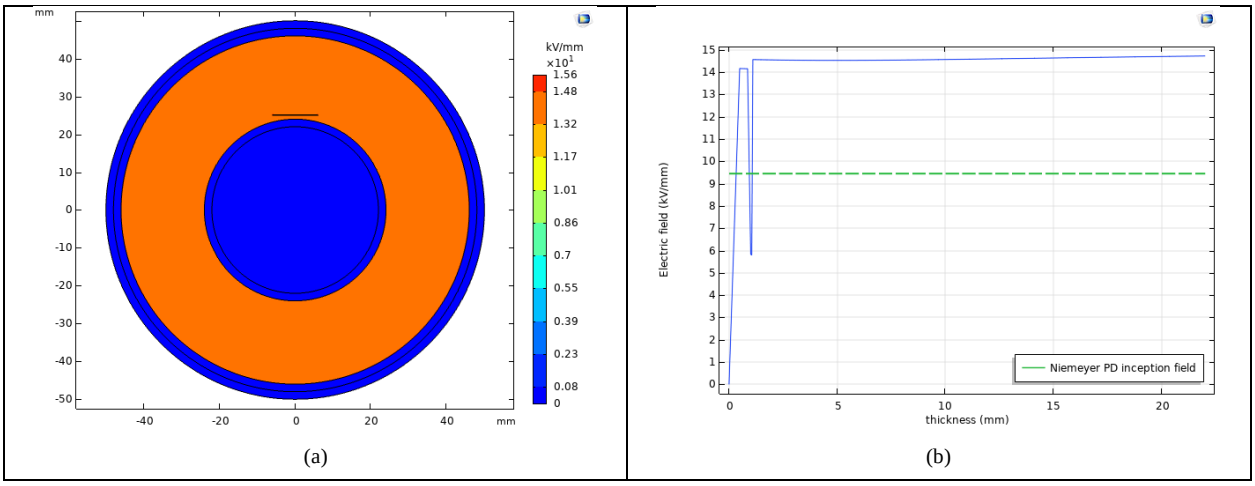

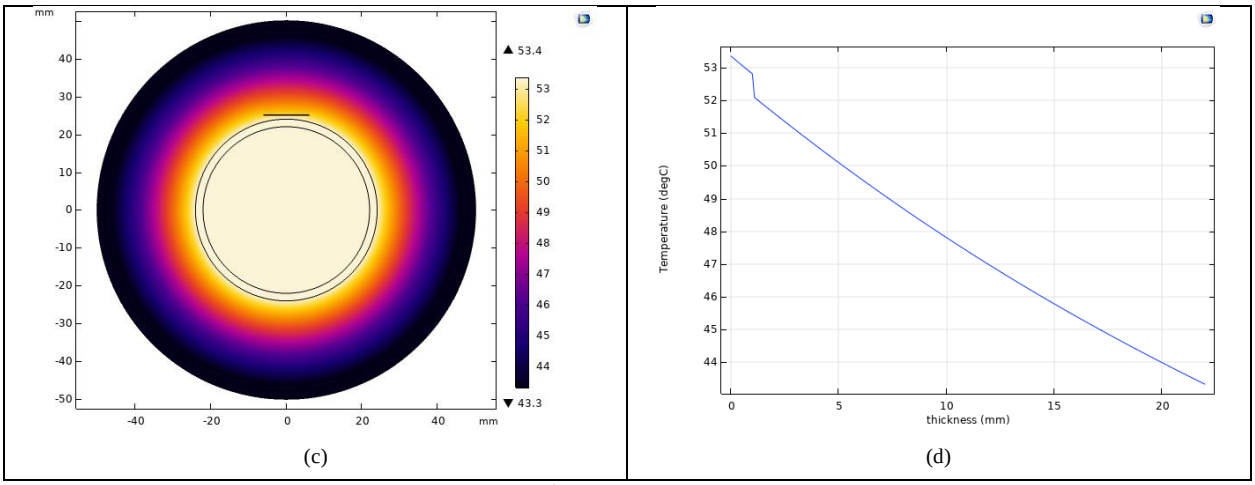

(c) (d)

(c) α = 0.07 [°C^{-1}] - cavity near inner conductor

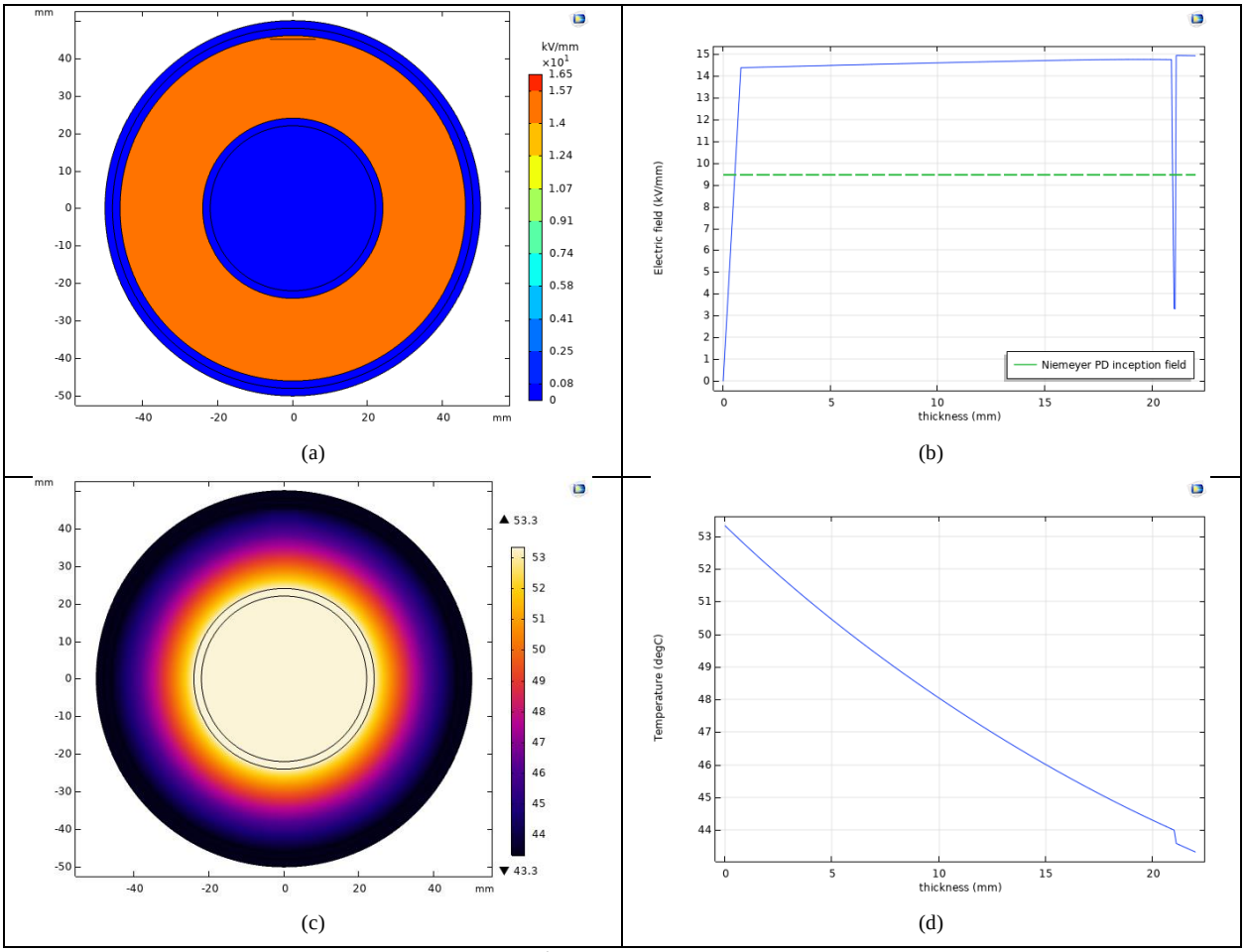

(a) (b)

(c) (d)

(d) α = 0.07 [°C^{-1}] – cavity near outer conductor

Figure 5.4. The electric field and temperature profile under steady state condition (under full load and nominal voltage) across cable insulation and cavity for the reported conditions in Figure 5.3.

As shown in Figure 5.4, electric field inversion occurs across cable insulation when α = 0.1 [°C] under full load. This means that electric field near outer conductor in dielectric is higher than that of near inner conductor. In despite of this the field inside cavity near inner conductor is higher than the field inside cavity near outer conductor. It should be mentioned that when α = 0.07 [°C], the temperature dependence coefficient of electrical conductivity is not high enough to provide the complete field inversion across cable insulation. As a result, higher value of temperature dependency coefficient of electrical conductivity, α, leads to higher field inside cavity.

The electric field profile under steady state condition (under no load and nominal voltage) across cable insulation and cavity for the reported conditions in Figure 5.3 have been shown in Figure 5.5.

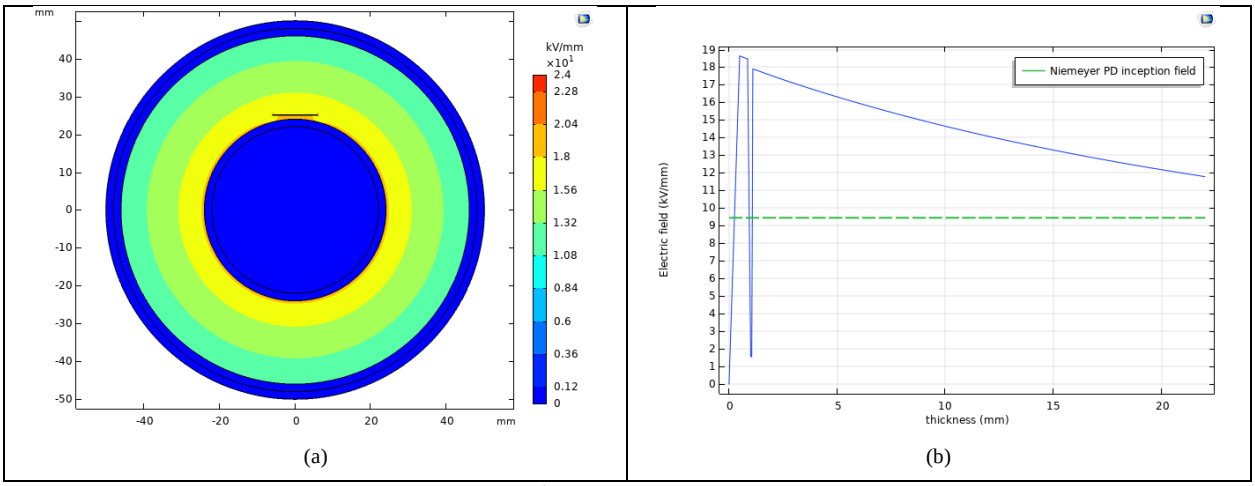

(a) (b)

(a) α = 0.1 [°C^{-1}] – cavity near inner conductor

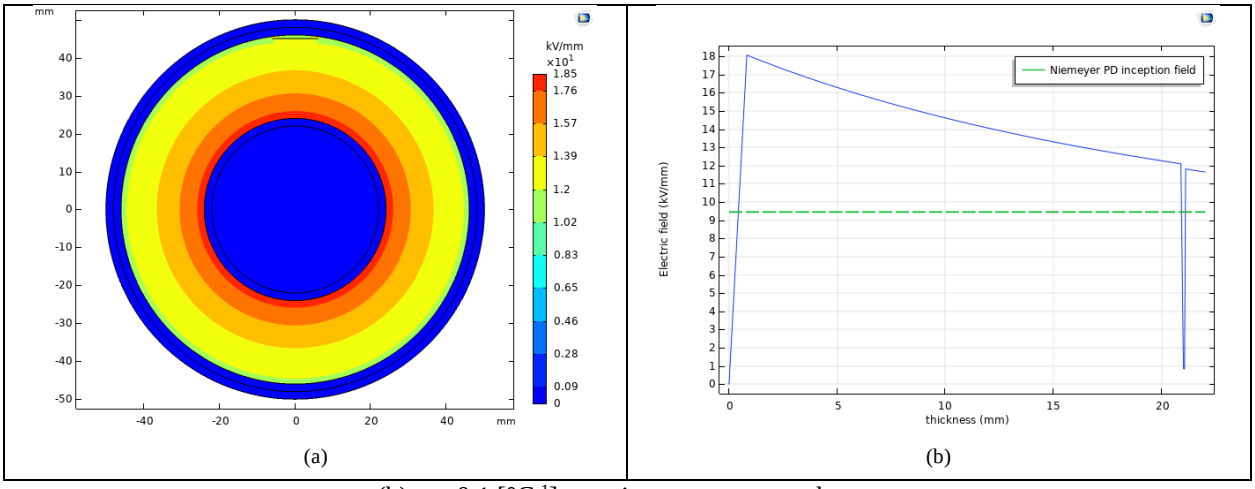

(a) (b)

(b) α = 0.1 [°C^{-1}] – cavity near outer conductor

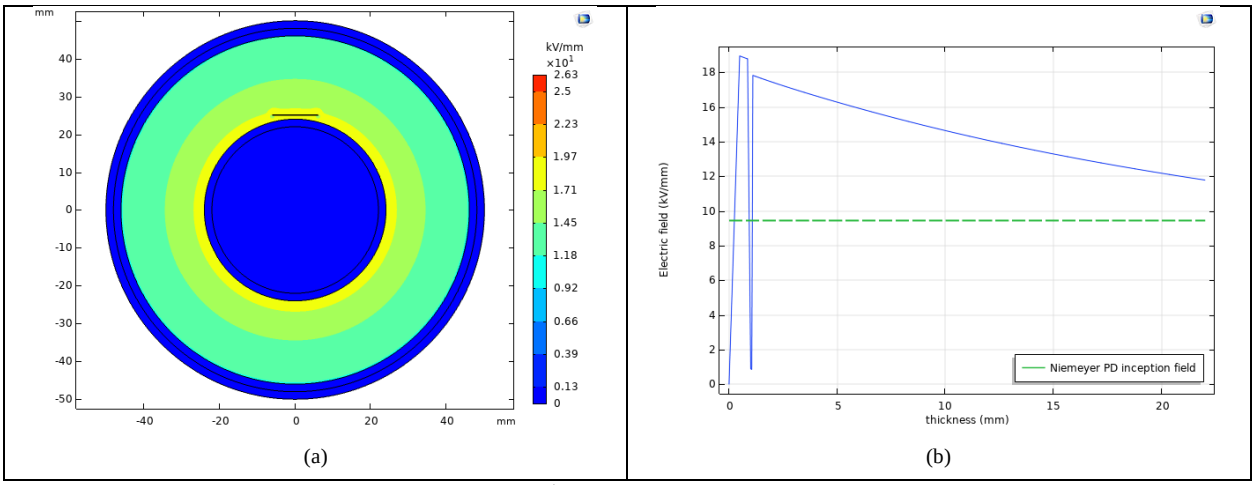

(a) (b)

(c) α = 0.07 [°C^{-1}] - cavity near inner conductor

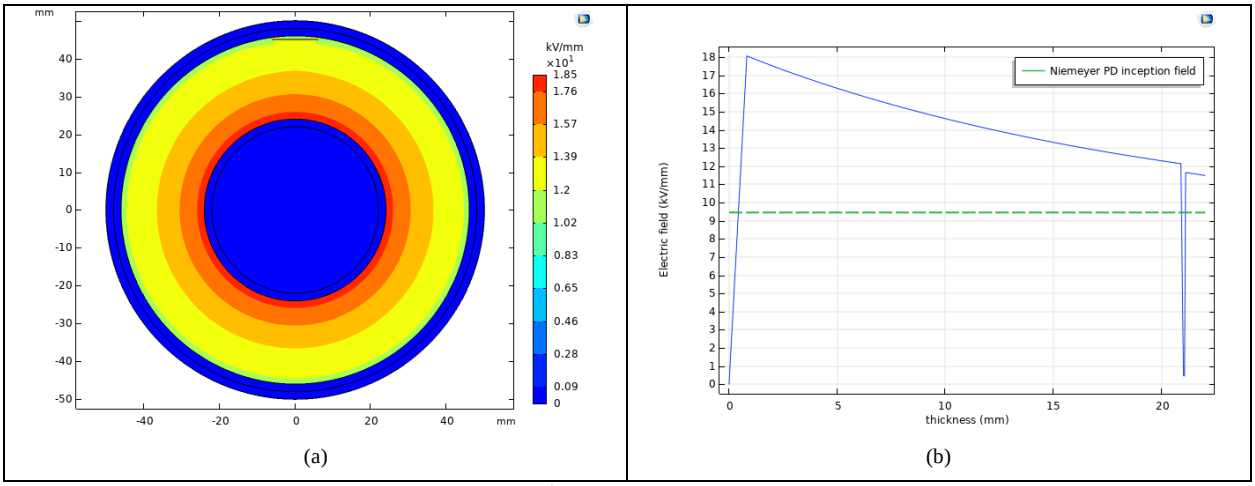

(a) (b)

(d) α = 0.07 [°C^{-1}] – cavity near outer conductor

Figure 5.5. The electric field profile under steady state condition (under no load and nominal voltage) across cable insulation and cavity for the reported conditions in Figure 5.3.

As depicted in Figure 5.5, the field across cable insulation under no load is like the capacitive field distribution under AC whereas the field near inner conductor is higher than that near outer conductor. Moreover, the comparison between the field distribution across cable insulation when the cavity is located near inner conductor and near outer conductor shows that when the cavity is near inner conductor since more electric field drops inside it, it influences significantly on the total field distribution across cable insulation while it is not the case when the cavity is near outer conductor.

The thermal and dielectric time constant estimates for the insulation next to inner conductor (r = 25.2 mm) and outer semiconducting layer (r = 45.2 mm), when the load is switched on and

switched off, are shown in Figure 5.6 as a function of load variation and α. As already mentioned, for insulating materials used at present for DC polymeric cables, $\tau_{th} < \tau_d$ for any load condition.

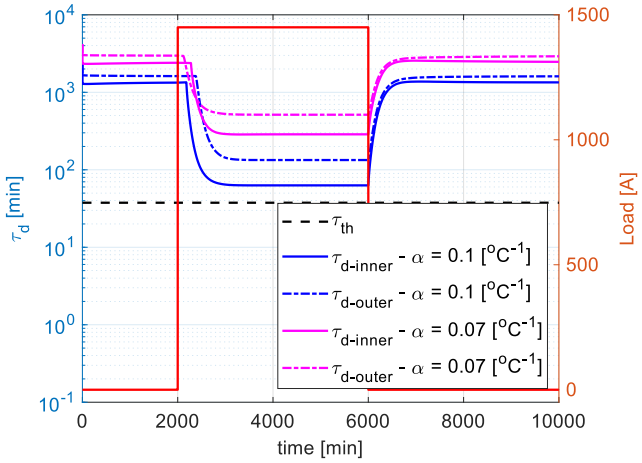

Figure 5.6. Estimated thermal and dielectric time constants, τ_{th} and τ_d, as a function of load condition and α, for dielectric near inner ($\tau_{d\text{-inner}}$) and outer semiconducting layer ($\tau_{d\text{-outer}}$) (β = 0.03 mm/kV). Load profile same as in Figure 5.3.

Considering α = 0.07 °C^{-1}, the electric field behavior in cavities near internal and external semicon, for β increasing from 0.03 to 0.11 mm/kV is shown in Figure 5.7. As for the dependence on α, partial discharges incept at energization, but only for large values of β, PD incept inside cavities both near inner and outer semicon in steady state condition for the hot cable. In addition, there is also an agreement with the no-PD case of Figure 5.6. Finally, they disappear after cable load is switched off. Indeed, with no load the field in the cavities is reduced below PDIV, both with high and low values of β.

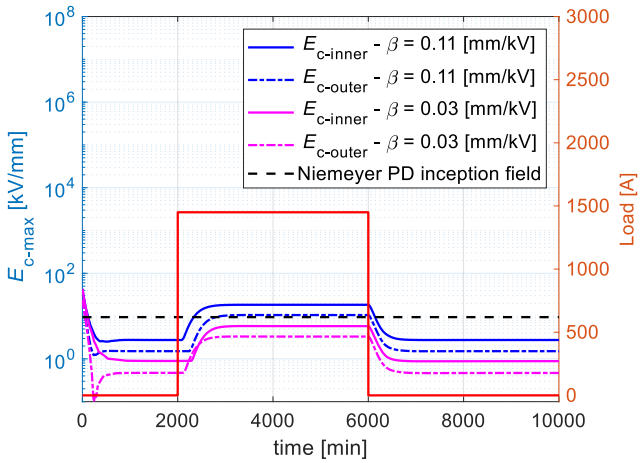

(a)

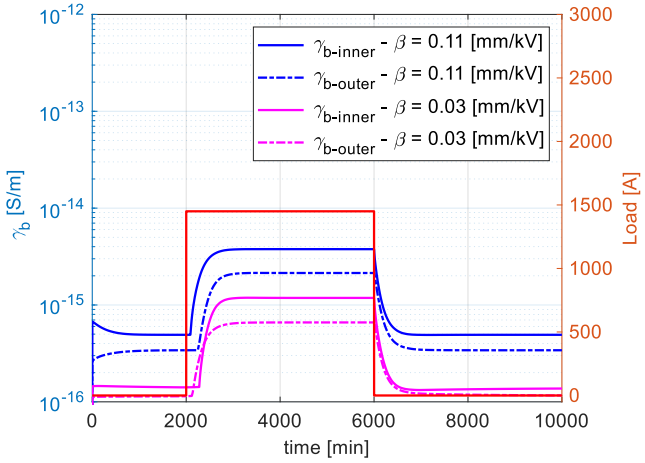

(b)

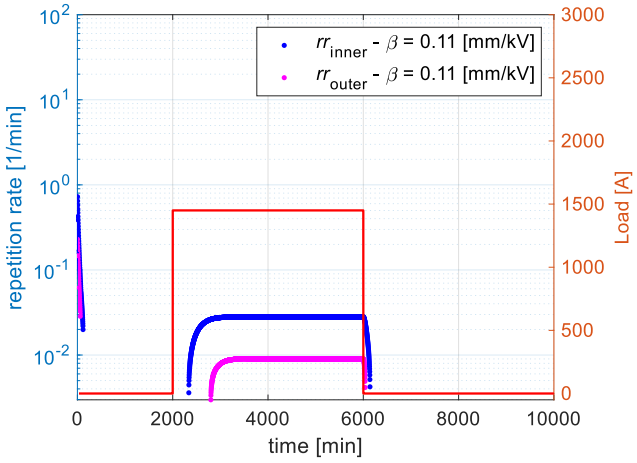

(c)

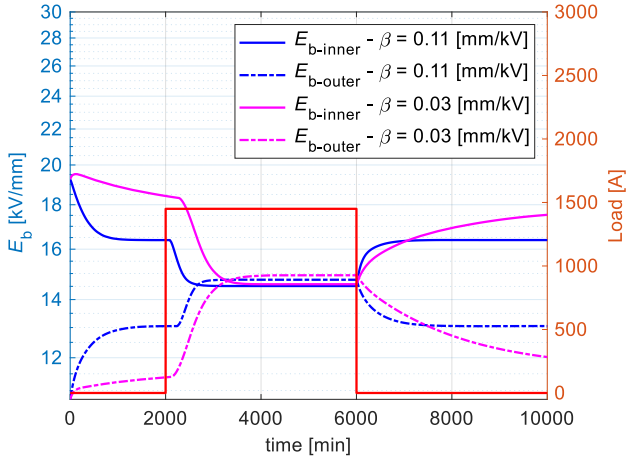

(d)

Figure 5.7. (a) Maximum electric field inside cavities located near the inner semicon ($E_{\text{c-inner}}$) and outer semiconducting layer ($E_{\text{c-outer}}$) when α = 0.07 $^{o}C^{-1}$ and β = 0.03 and 0.11 mm/kV, upon cable energization, loading and

switching off. Dotted horizontal line: PD inception field, according to Equation (5.13). (b) conductivity behavior as a function of time (Equation (5.1)) for dielectric near inner conductor ($\gamma_{b\text{-inner}}$, r = 25.2 mm) and outer semiconducting layer ($\gamma_{b\text{-outer}}$, r = 45.2 mm). (c) estimated PD repetition rate inside cavity near inner conductor (rr_{inner}) and near outer semiconducting layer (rr_{outer}) from Equations (5.14) - (5.16), where E_r is neglected and β = 0.11 mm/kV. (d) electric field behavior as a function of time, β and load for dielectric near inner conductor ($E_{b\text{-inner}}$, r = 25.2 mm) and outer semiconducting layer ($E_{b\text{-outer}}$, r = 45.2 mm). The load cycle is also indicated.

PD steady-state repetition rate, estimated by Equation (5.14), provides 0.03 min^{-1} for β = 0.11 mm/kV and 0.01 min^{-1} for β = 0.07 mm/kV, going to zero for $\beta \leq 0.06$ mm/kV (Figure 5.7c).

As illustrated in Figure 5.7b, there is increase of γ_b when β increases from Equation (5.1) and subsequently it leads to increase of electric field inside cavity both near inner and outer conductor from Equation (5.12) (see: Figure 5.7a).

It can be seen from Figure 5.7d that when β increases it has negligible effect on electric field in dielectric both near inner and outer conductor under full load and steady state condition. However, when there is increase of β under no load, it results in increase of field in dielectric near outer conductor ($E_{b\text{-outer}}$) while the electric field in dielectric near inner conductor ($E_{b\text{-inner}}$) decreases.

The electric field and temperature profile under steady state condition (under full load and nominal voltage) across cable insulation and cavity for the reported cases in Figure 5.7 have been illustrated in Figure 5.8.

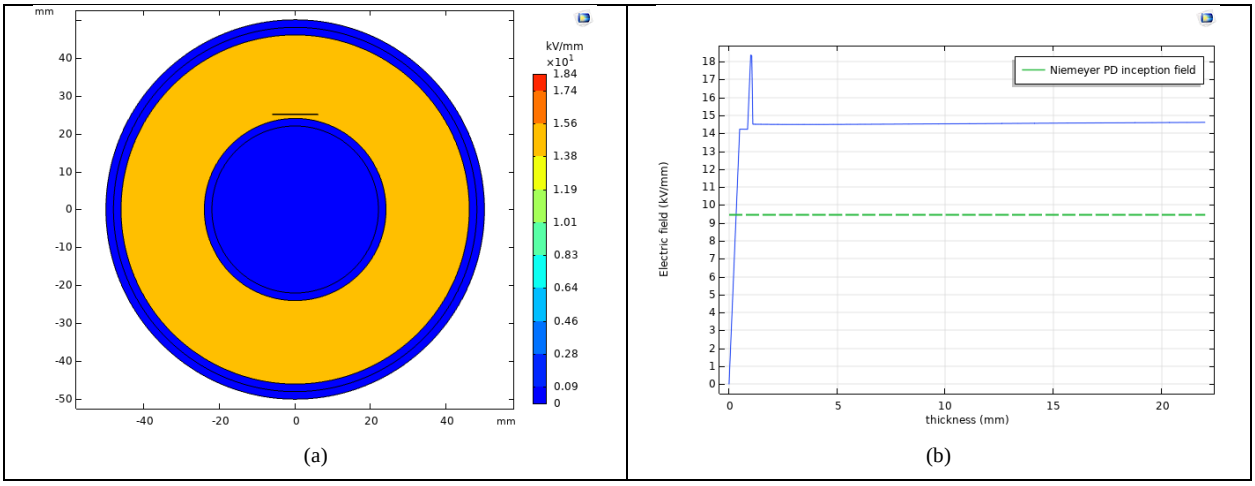

(a) (b)

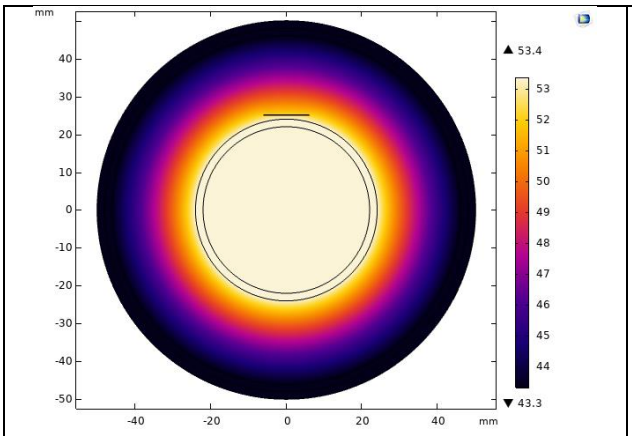

(c)

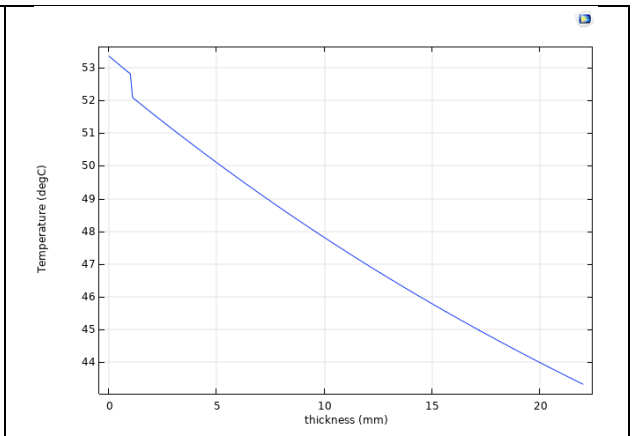

(d)

(a) β = 0.11 [mm/kV] – cavity near inner conductor

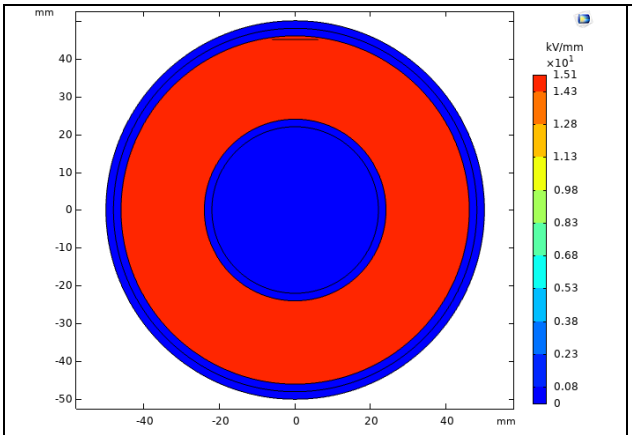

(a)

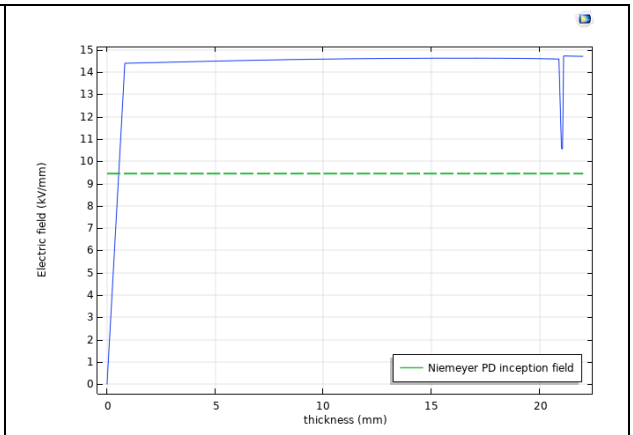

(b)

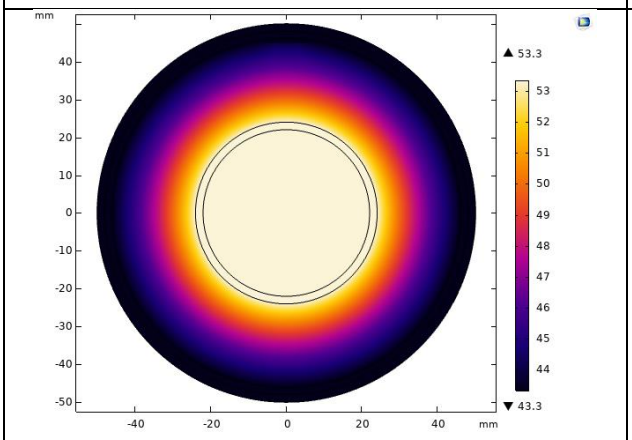

(c)

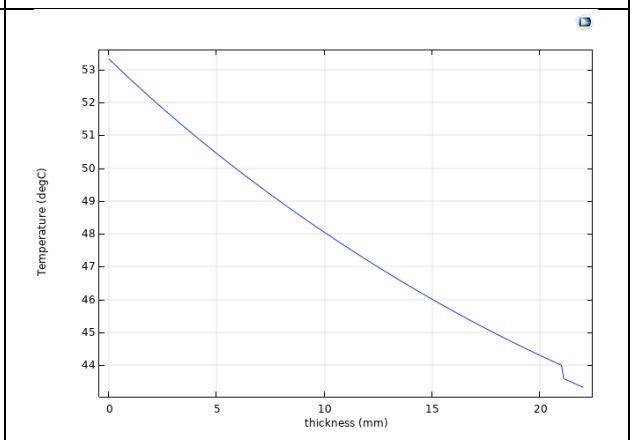

(d)

(b) β = 0.11 [mm/kV] – cavity near outer conductor

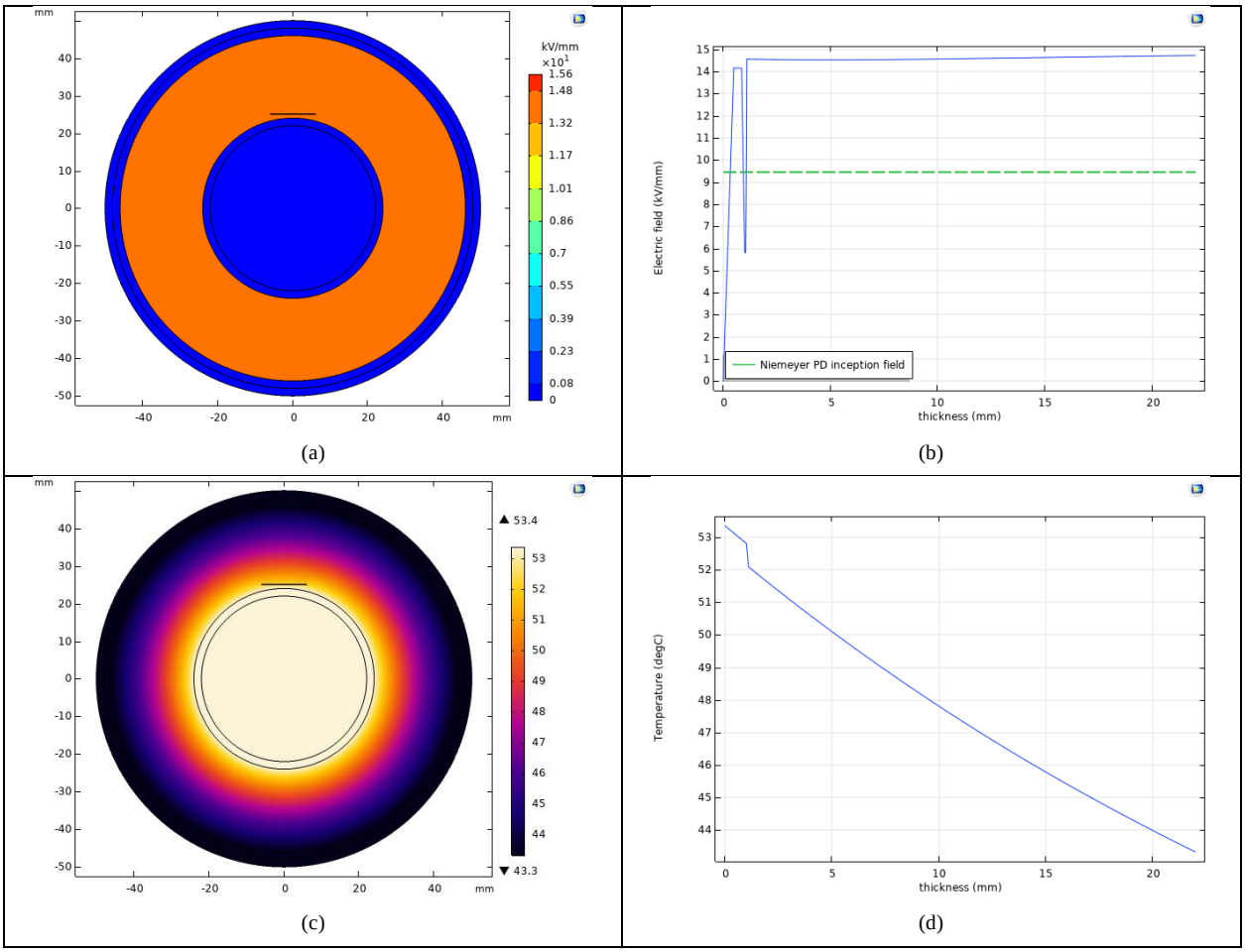

(a) (b)

(c) (d)

(c) β = 0.03 [mm/kV] – cavity near inner conductor

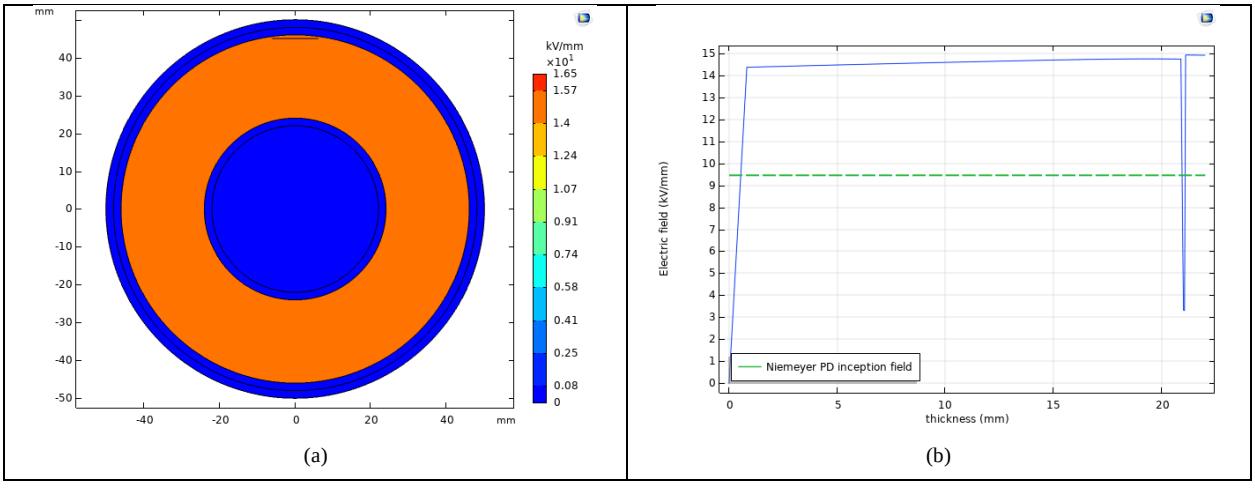

(a) (b)

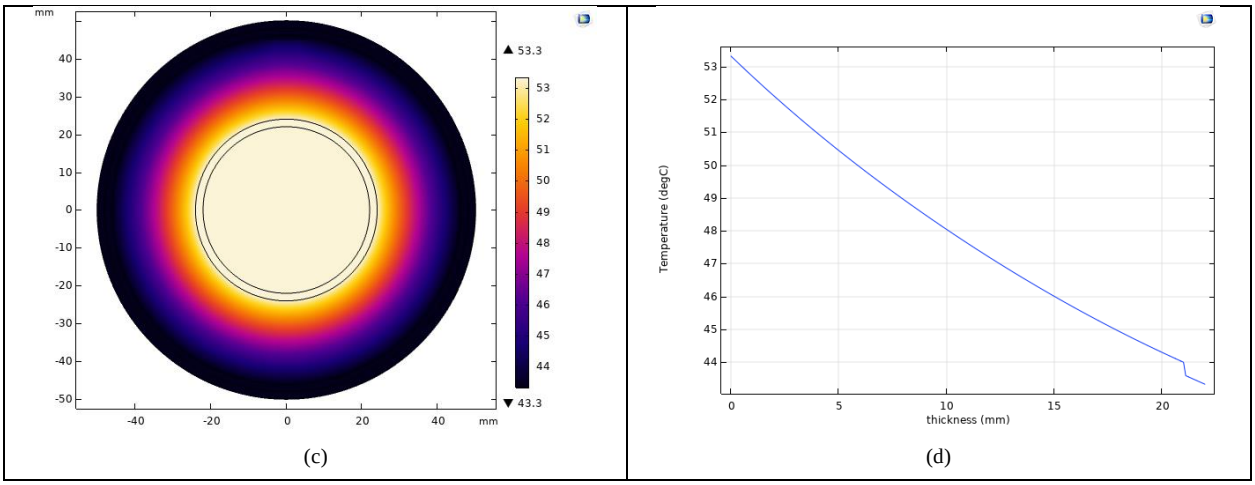

(c) (d)

(d) β = 0.03 [mm/kV] – cavity near outer conductor

Figure 5.8. The electric field and temperature profile under steady state condition (under full load and nominal voltage) across cable insulation and cavity for the reported cases in Figure 5.7.

As can be seen from Figure 5.8, high value of field dependency coefficient of electrical conductivity, β, under full load results in homogenous field distribution across cable insulation. In other words, when β is high, such as 0.11 [mm/kV], there is not considerable difference between the electric field in dielectric near inner conductor and the electric field in dielectric near outer conductor. Furthermore, it can be speculated that higher value of β leads to higher electric field concentration inside cavity under full load. Finally, it can be seen from Figure 5.8 that the electric field inside cavity near inner conductor is higher than that near outer conductor.

The electric field profile under steady state condition (under no load and nominal voltage) across cable insulation and cavity for the reported cases in Figure 5.7 have been shown in Figure 5.9.

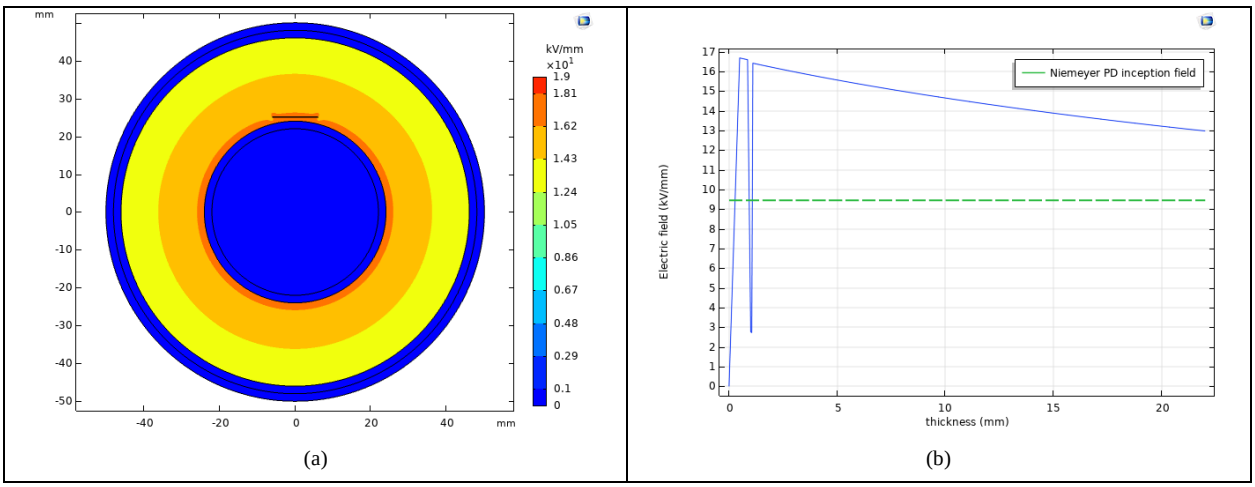

(a) (b)

(a) β = 0.11 [mm/kV] – cavity near inner conductor

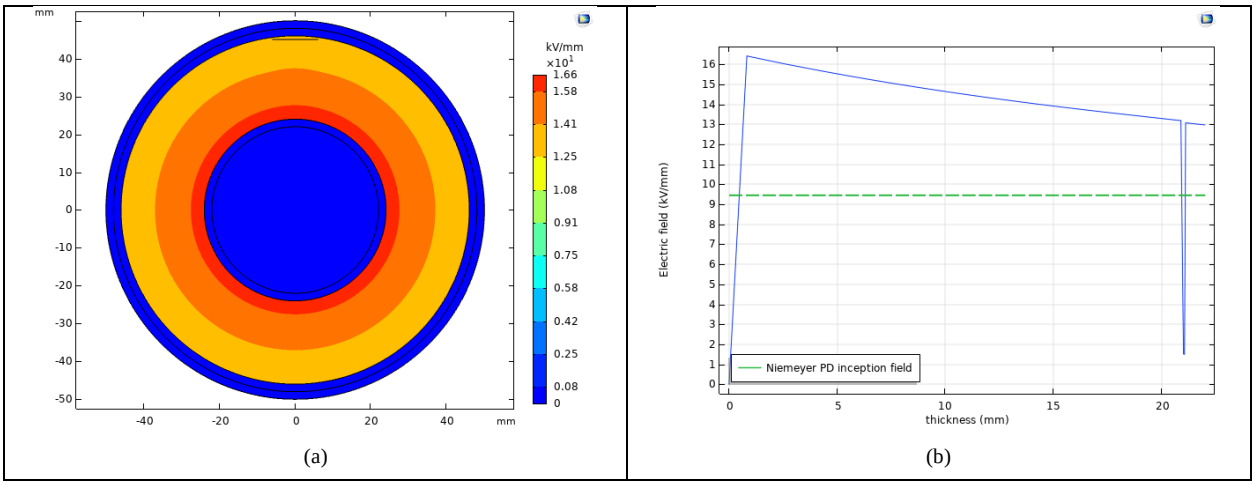

(a) (b)

(b) β = 0.11 [mm/kV] – cavity near outer conductor

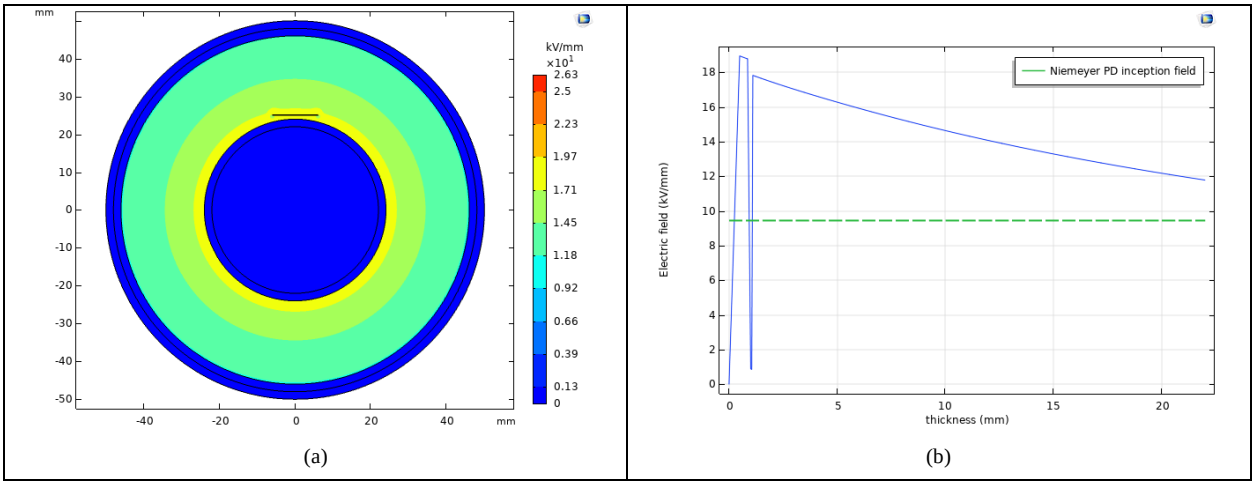

(a) (b)

(c) β = 0.03 [mm/kV] – cavity near inner conductor

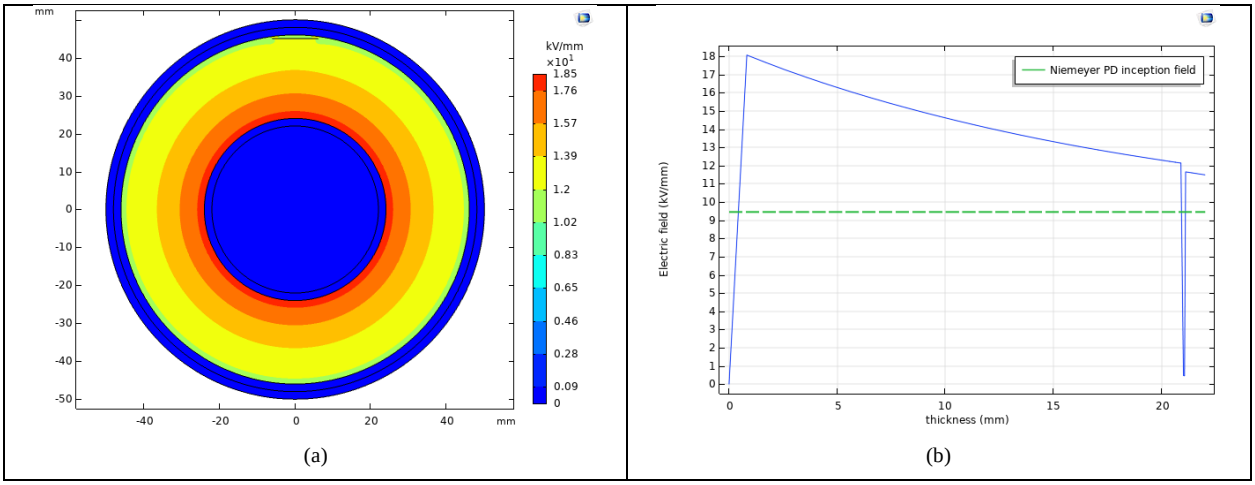

(a) (b)

(d) β = 0.03 [mm/kV] – cavity near outer conductor

Figure 5.9. The electric field profile under steady state condition (under no load and nominal voltage) across cable insulation and cavity for the reported cases in Figure 5.7.

As shown in Figure 5.9, under no load condition, the electric field distribution across cable insulation is like that of under AC whereas there is capacitively field distribution across insulation and there is higher electric field near inner conductor. Additionally, as can be seen when the cavity is located near inner conductor, because there is more field drop inside cavity compare with the case where it is located near outer conductor, this influences on the whole field distribution across cable insulation.

Similarly, to Figure 5.6, the thermal and dielectric time constants for dielectric near inner and outer semiconducting layer, as a function of time and β, are displayed in Figure 5.10, when the load is switched on and off. Again, for all conditions the thermal time constant τ_{th} is much shorter than the dielectric constant τ_d, for any value of β.

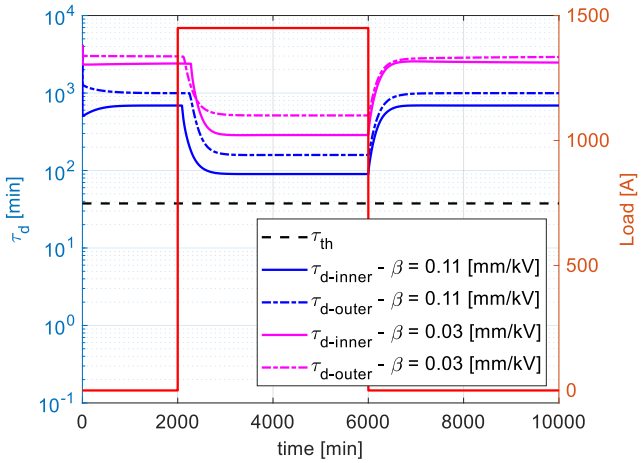

Figure 5.10. Estimated thermal and dielectric time constants, τ_{th} and τ_d, as a function of load condition and β, for dielectric near inner ($\tau_{d\text{-inner}}$) and outer semiconducting layer ($\tau_{d\text{-outer}}$) (α = 0.07 °C^{-1}) - Load profile same as in Figure 5.3.

As can be seen from Figures 5.3 to 5.10, modern polymers used for DC cable insulation can be affected by PD activity triggered by the variation of conductivity with loading conditions, inducing large-enough electric field increases in cavities when load is, for example, switched on. The larger the values of both α and β, the higher the conductivity variation and the relevant cavity field. Hence, the likelihood of PD inception is enhanced, even in a cavity next to the outer semicon.

It is noteworthy from Figure 5.3 that the electric field inside a cavity next to the inner semicon ($E_{c\text{-inner}}$) is higher than that near the outer semiconducting layer ($E_{c\text{-outer}}$) both for a cold and a hot cable. This holds also when α has its highest value, e.g., 0.1 °C^{-1}, which results in field inversion across the cable insulation. In addition, with the decrease of α, both $E_{c\text{-inner}}$ and $E_{c\text{-outer}}$ decrease, while the ratio of ($E_{c\text{-inner}}$ / $E_{c\text{-outer}}$) increases.

In addition, it must be noted that conditions for inception of PD also can occur for partial load variations such as 50% to full load, as it is illustrated in Figure 5.11, with α = 0.1 °C^{-1} and β = 0.03 mm/kV.

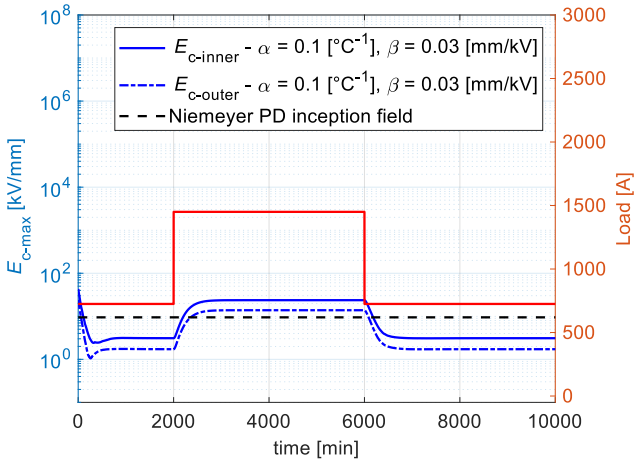

Figure 5.11. Maximum electric field inside cavities located near the inner semicon ($E_{c\text{-inner}}$) and outer semiconducting layer ($E_{c\text{-outer}}$) when α = 0.1 °C^{-1} and β = 0.03 mm/kV, upon cable energization and loading from 50% to full load. Dotted horizontal line: PD inception field, according to Equation (5.13).

In summary, if the thermal transient is faster than the dielectric transient, the field distribution will be driven by the conductivity variation, regulated by its dependence on temperature and electric field, as well as by the cavity location. After switching on the load, values of reference conductivity and α, β, can be such as to bring PDIV to become lower than nominal voltage for cavities near the inner semicon and, possibly, next to the outer semicon layer. PD that are triggered when load is increased are permanently occurring during DC steady state, until they disappear after the load is off. These PD, being driven by DC field, have very low repetition rate, as given by Equation (5.14) and experimental evidence [3]. It is noteworthy that this result is very important for practical applications, as conventional PD-measurement systems will not be able to detect such PD under DC, as the frequency range and gating time cannot be tuned correctly.

5.5.2 Dielectric time constant smaller than thermal time constant

This is a case which does not fit to the parameters used for cable simulation and reported in Tables 5.1 to 5.3, but it is interesting to observe the consequence of employing materials where thermal conductivity can be lower and heat capacitance larger.

At a first instance, thermal conductivity was reduced of one order of magnitude, to 0.035 W/mK, keeping the other parameters as in the sub-section 5.5.1. The resulting electric field variation inside cavities next to the inner and outer semicon is illustrated in Figure 5.12a. It is interesting to note that field increases much steeper than in the case of $\tau_{th} < \tau_d$, which causes higher repetition rate (see Figure 5.15c), similar to that found for voltage transients. Regarding the dependence of conductivity on electric field, the variation of β from 0.03 to 0.05 mm/kV can change significantly the field profile under thermal steady state condition, resulting in an increase of both $E_{c\text{-inner}}$ and $E_{c\text{-outer}}$, while rising α from 0.1 to 0.12 °C^{-1} there is a decrease of $E_{c\text{-inner}}$ and an increase of $E_{c\text{-outer}}$ (see Figure 5.15a).

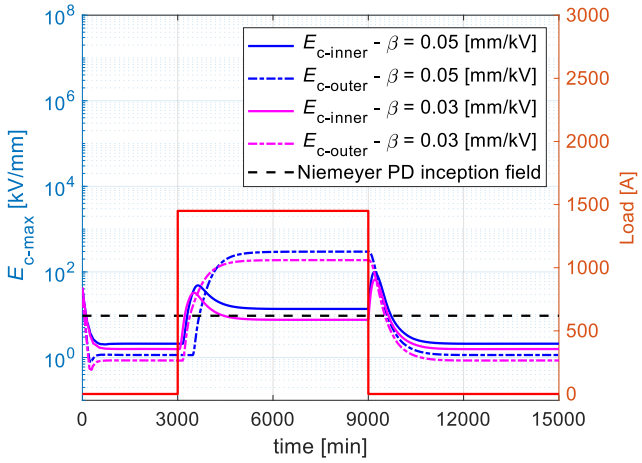

(a)

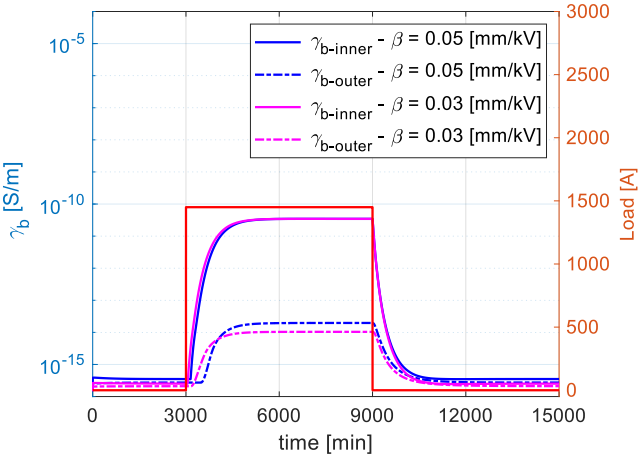

(b)

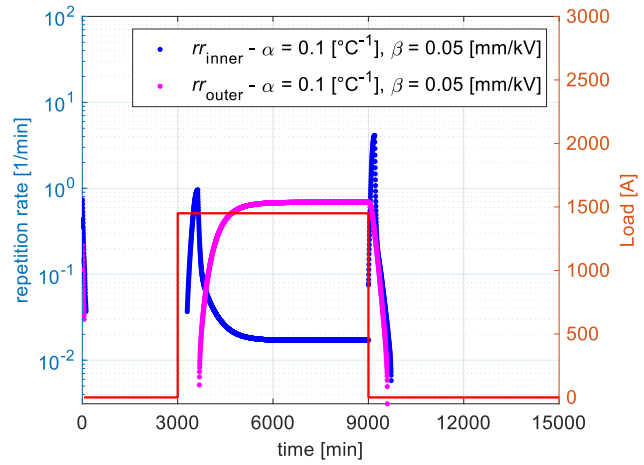

(c)

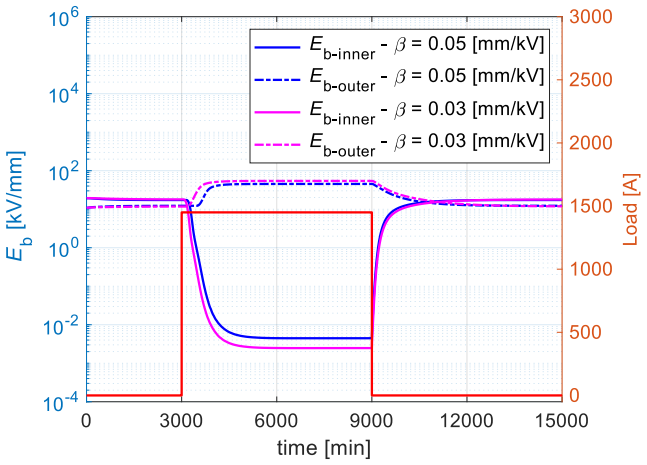

(d)

Figure 5.12. (a) Maximum electric field inside cavities located near the inner semicon ($E_{c\text{-}inner}$) and outer semiconducting layer ($E_{c\text{-}outer}$) when α = 0.1 °C^{-1} and β = 0.05 and 0.03 mm/kV, upon cable energization, loading and switch off. Dotted horizontal line: PD inception, according to Equation (5.13). (b) conductivity behavior as a function of time (Equation (5.1)) for dielectric near inner conductor ($\gamma_{b\text{-}inner}$, r = 25.2 mm) and outer semiconducting layer ($\gamma_{b\text{-}outer}$, r = 45.2 mm). (c) estimated PD repetition rate inside cavity near inner conductor (rr_{inner}) and near outer semiconducting layer (rr_{outer}) from Equation (5.15) for AC regime and Equations (5.14) - (5.16) for transferring from AC to DC steady state condition where E_r is neglected and β = 0.05 mm/kV. (d) electric field behavior as a function of time, β and load for dielectric near inner conductor ($E_{b\text{-}inner}$, r = 25.2 mm) and outer semiconducting layer ($E_{b\text{-}outer}$, r = 45.2 mm). The load cycle is also indicated.

Considering Figures 5.12b and 5.12d, it can be speculated when thermal conductivity is decreased, it results in significant increase of conductivity near inner conductor (see: Figure 5.12b) as well as considerable reduction of electric field in dielectric near inner conductor (see: Figure

5.12d). Consequently, it leads to increase of electric field inside cavity near inner conductor under full load and steady state condition compare with no load condition from Equation (5.12) (see: Figure 5.12a). On the other hand, considering the cavity near outer conductor, Figures 5.12b and 5.12d indicate that when load rises since both conductivity and electric field in dielectric near outer conductor increases, this results in considerable increase of the electric field inside cavity near outer conductor from Equation (5.12).

As can be seen from Figure 5.3a, when thermal conductivity is decreased enough, it results in significant higher electric field inside cavity near outer conductor compare with the field inside cavity near inner conductor ($E_{\text{c-outer}} > E_{\text{c-inner}}$) whereas when thermal conductivity has its normal value the reverse holds. The reason for this is when thermal conductivity decreases, there is significant increase of conductivity near inner conductor. This results in considerable electric field concentration near outer conductor and following that higher electric field inside cavity near outer conductor compare with that inside cavity near inner conductor.

The electric field and temperature profile under steady state condition (under full load and nominal voltage) across cable insulation and cavity for the reported cases in Figure 5.12 have been illustrated in Figure 5.13.

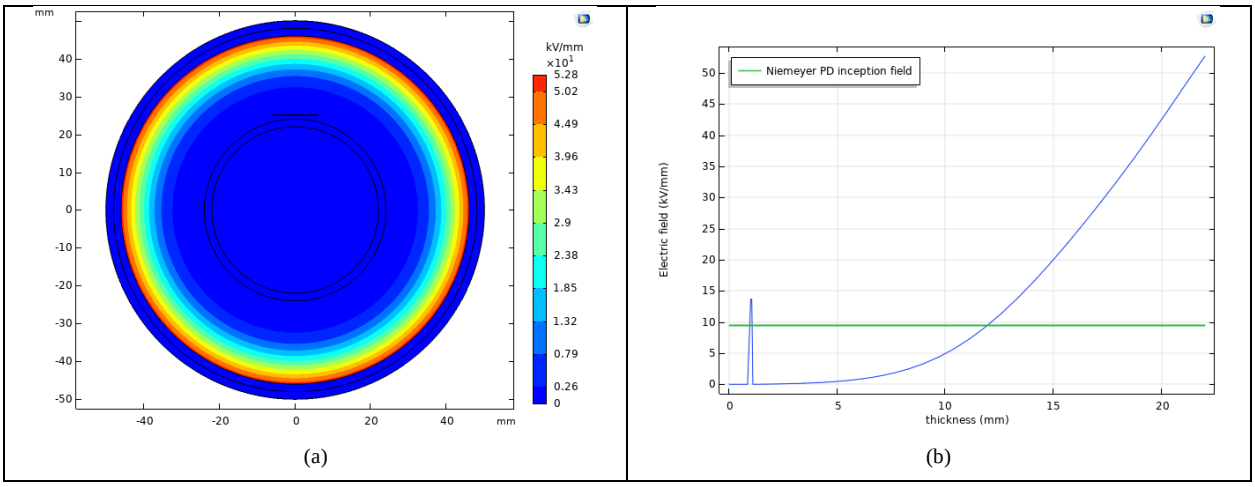

(a) (b)

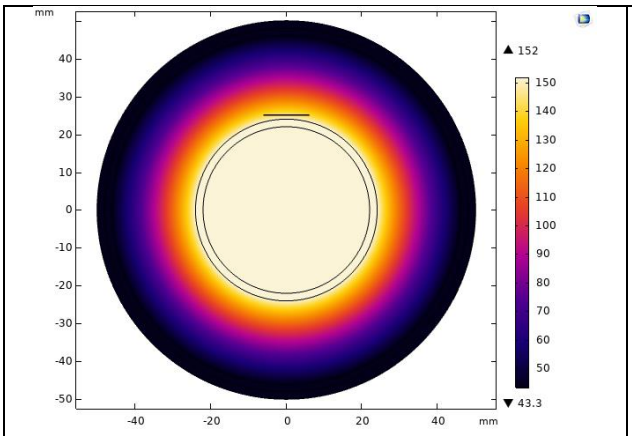

(c)

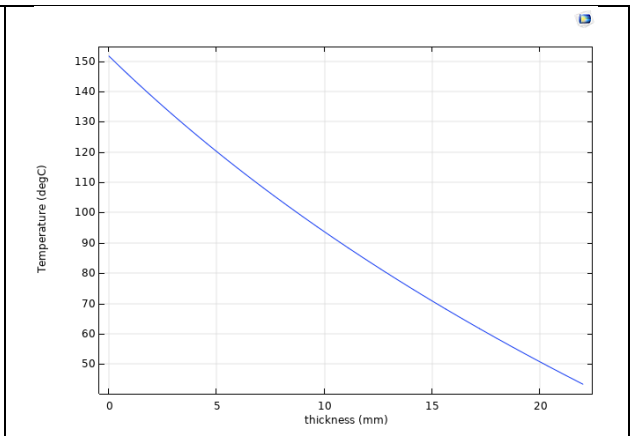

(d)

(a) β = 0.05 [mm/kV], cavity near inner conductor

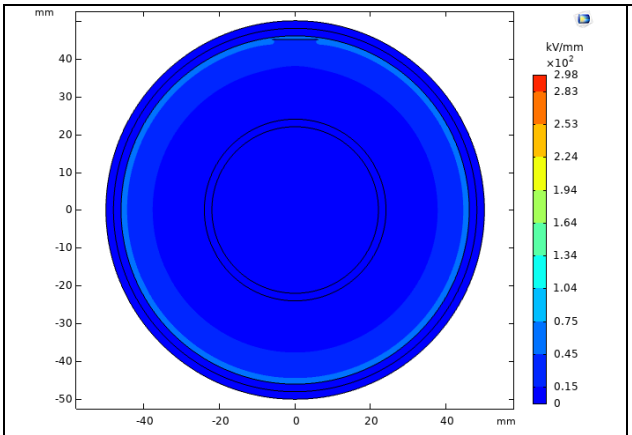

(a)

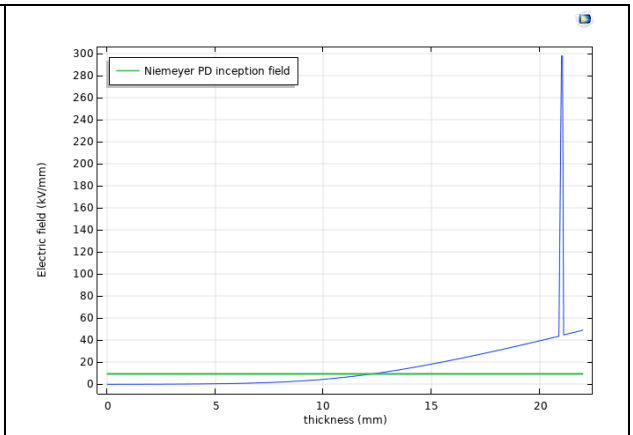

(b)

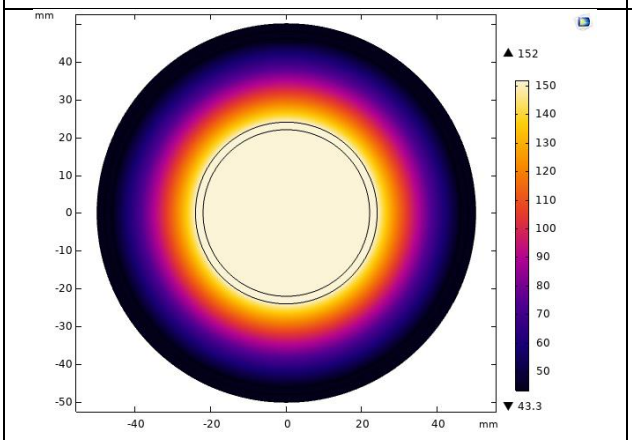

(c)

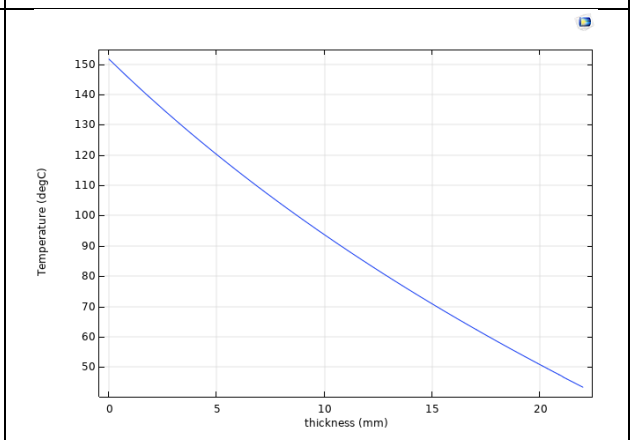

(d)

(b) β = 0.05 [mm/kV], cavity near outer conductor

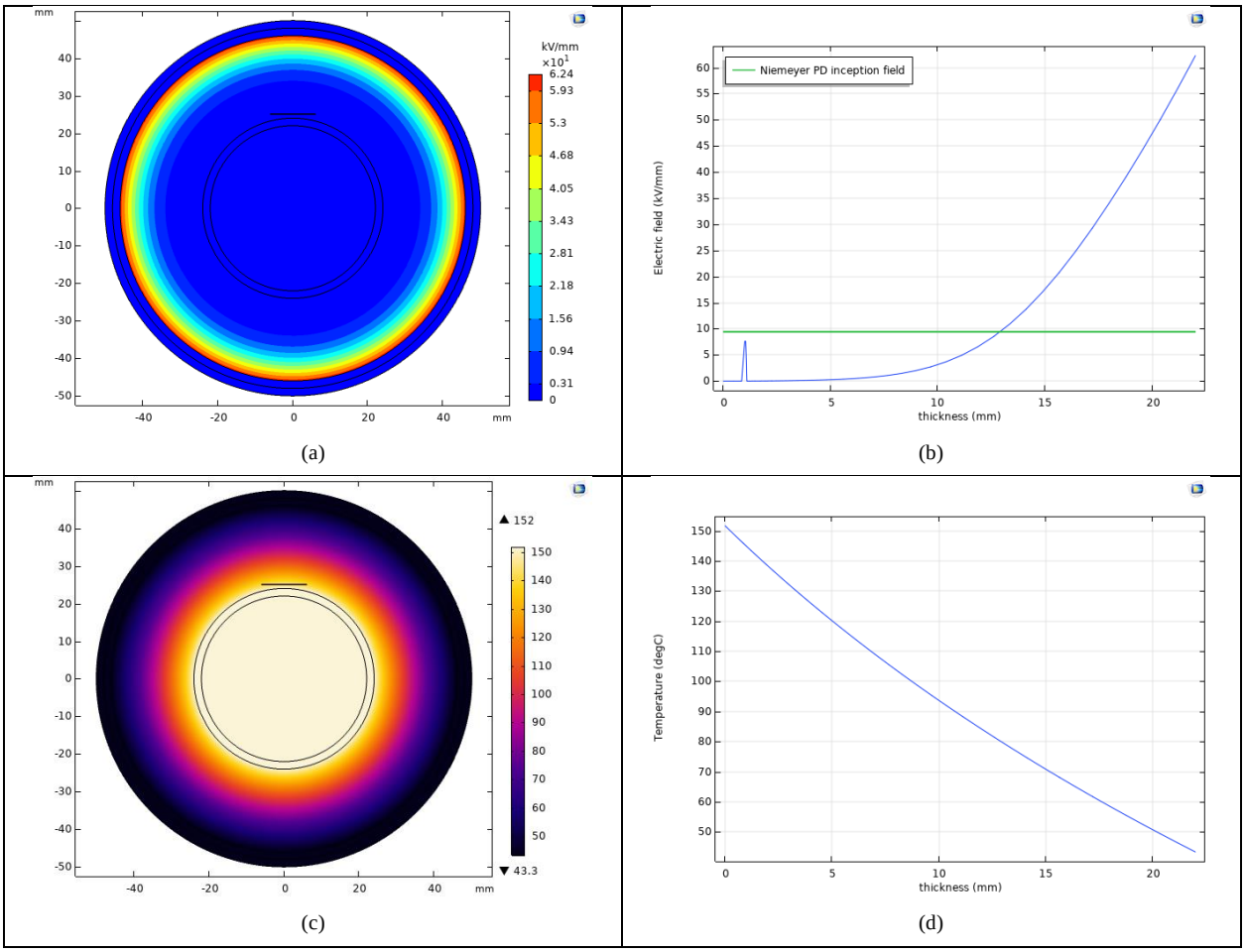

(a) (b)

(c) (d)

(c) β = 0.03 [mm/kV], cavity near inner conductor

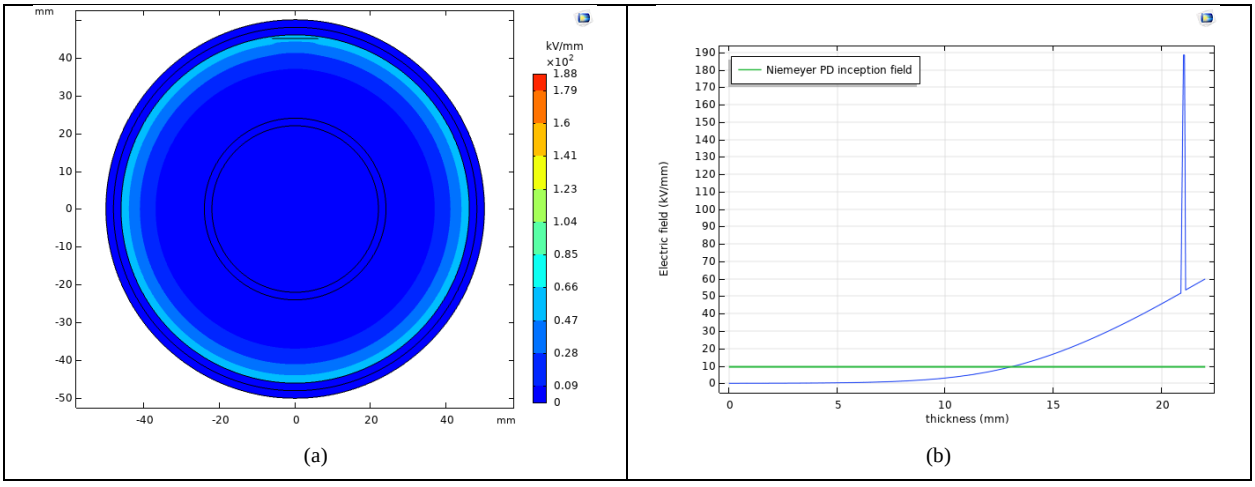

(a) (b)

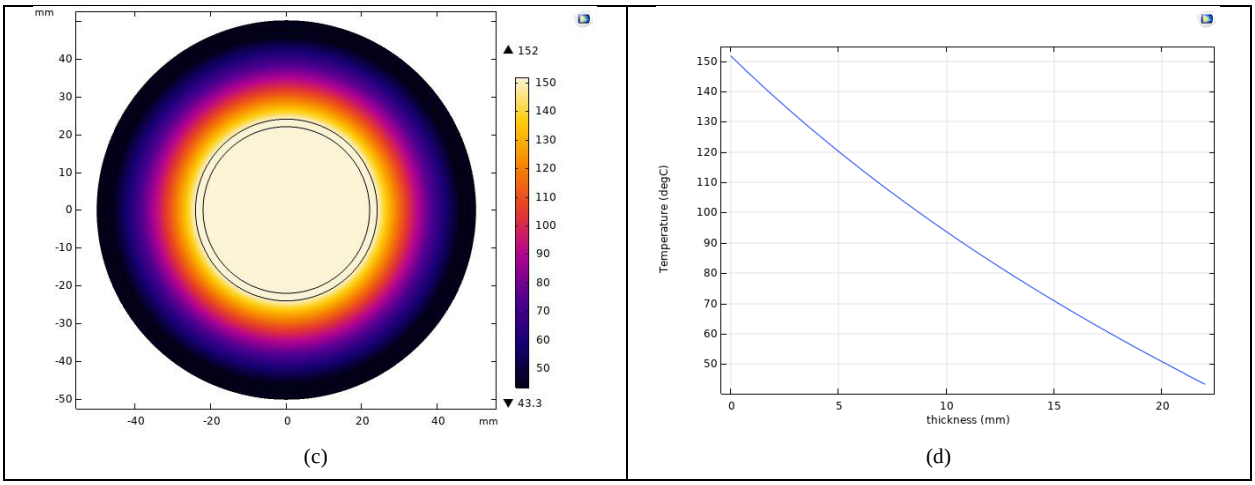

(c) (d)

(d) β = 0.03 [mm/kV], cavity near outer conductor

Figure 5.13. The electric field and temperature profile under steady state condition (under full load and nominal voltage) across cable insulation and cavity for the reported cases in Figure 5.12.

As shown in Figures 5.13a and 5.13c, when thermal conductivity is reduced and the cavity is located near inner conductor, the electric field is concentrated in dielectric near outer conductor where there is lower electrical conductivity (see: Figure 5.12b). On the other hand, when cavity is located near outer conductor (see: Figures 5.13b and 5.13d), almost all the electric field is concentrated inside outer cavity especially when β is higher. In addition, it can be understood from the temperature profiles that decrease of thermal conductivity with one order of magnitude can result in significant increase of dielectric temperature near inner conductor up to 150 °C under full load. This high temperature value can lead to thermal instability of insulation near inner conductor.

The electric field profile under steady state condition (under no load and nominal voltage) across cable insulation and cavity for the reported cases in Figure 5.12 have been shown in Figure 5.14.

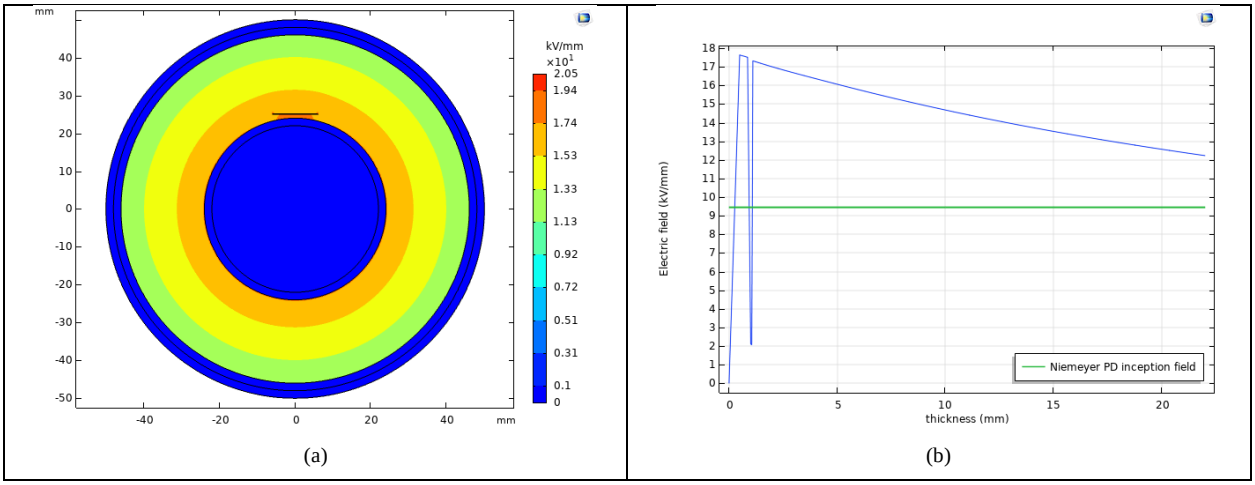

(a) (b)

(a) β = 0.05 [mm/kV], cavity near inner conductor

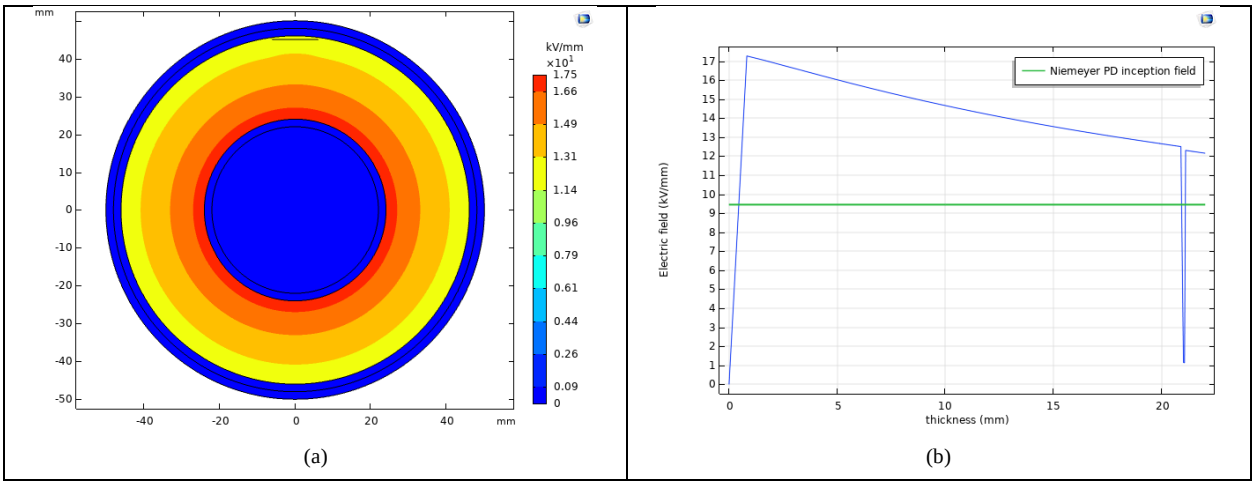

(a) (b)

(b) β = 0.05 [mm/kV], cavity near outer conductor

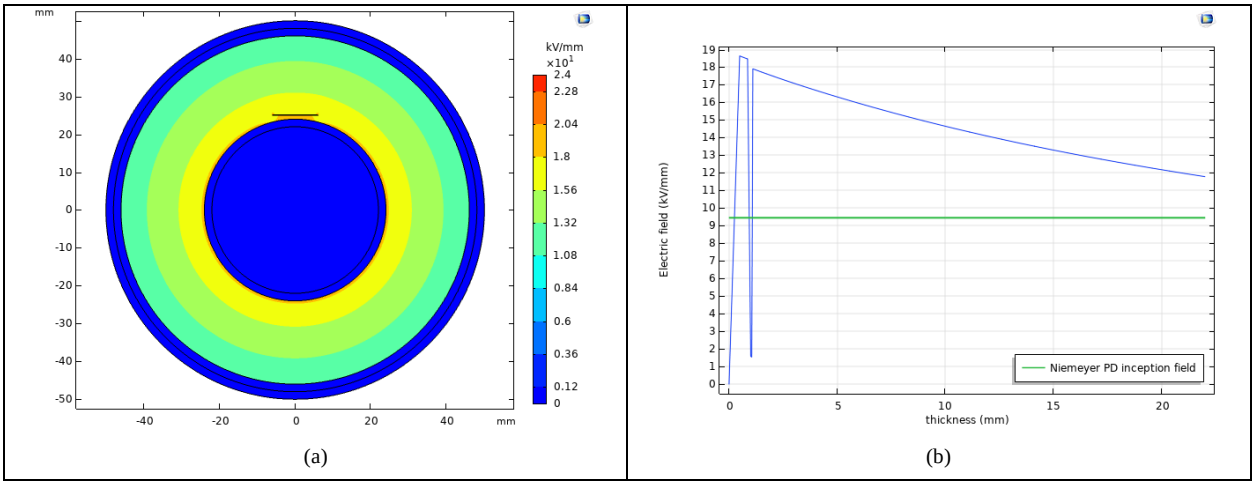

(a) (b)

(c) β = 0.03 [mm/kV], cavity near inner conductor

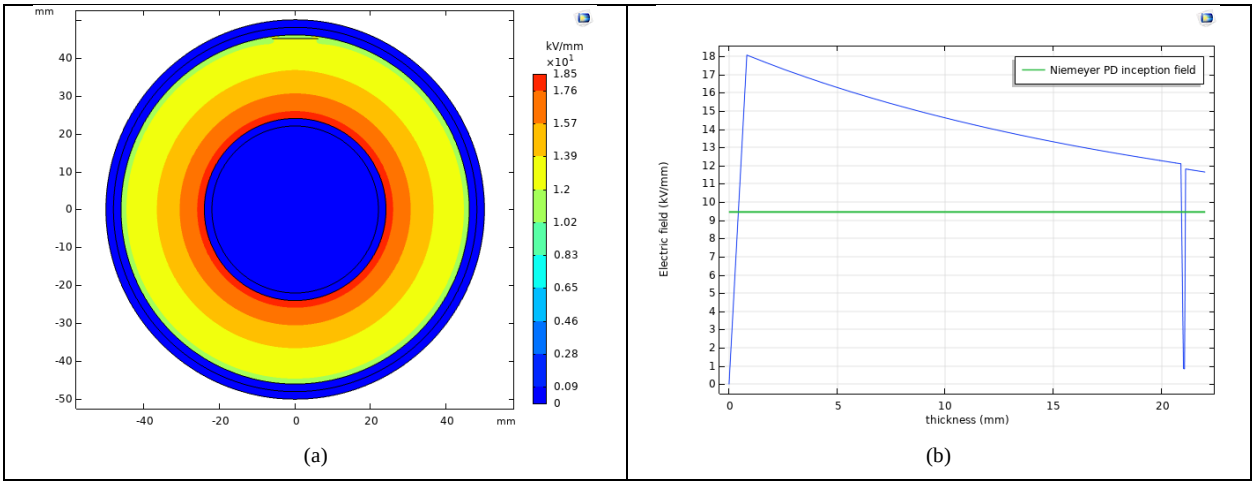

(a) (b)

(d) β = 0.03 [mm/kV], cavity near outer conductor

Figure 5.14. The electric field profile under steady state condition (under no load and nominal voltage) across cable insulation and cavity for the reported cases in Figure 5.12.

As indicated in Figure 5.14, the electric field distribution across cable insulation under no load condition would be like capacitive field distribution where there is higher electric field near inner conductor. It can be speculated that when the cavity is located near inner conductor, it results in different field distribution across cable insulation compare with the case when it is located near outer conductor. As a result, higher β value leads to higher electric field inside cavity both near inner and outer conductor.

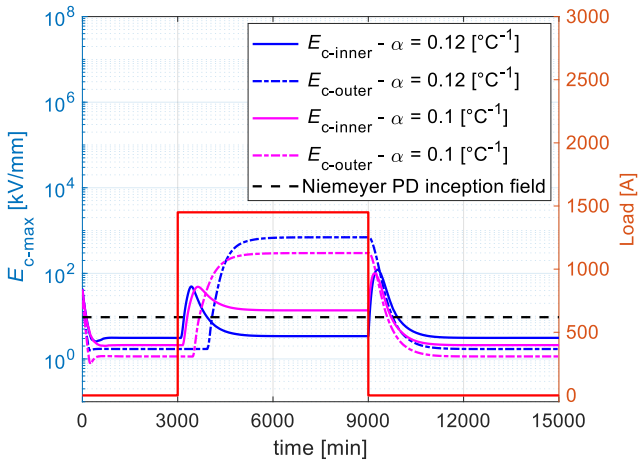

(a)

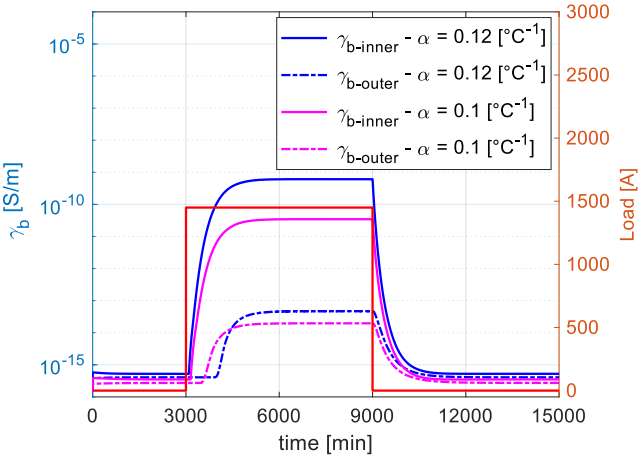

(b)

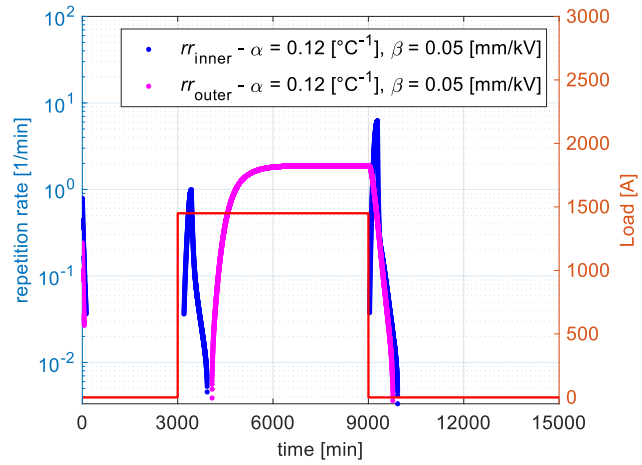

(c)

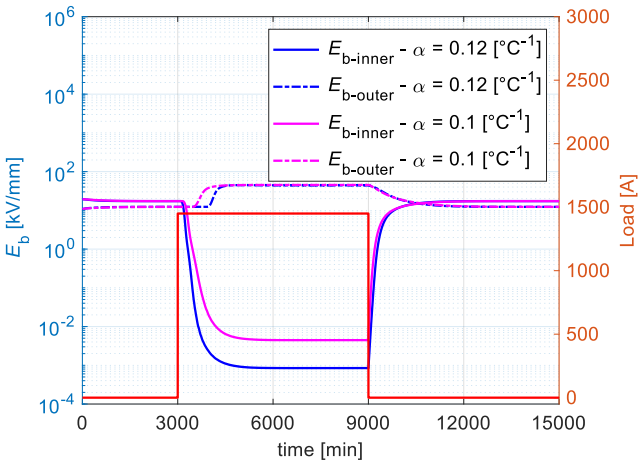

(d)

Figure 5.15. (a) Maximum electric field inside cavities located near the inner semicon ($E_{c\text{-}inner}$) and outer semiconducting layer ($E_{c\text{-}outer}$) when β = 0.05 mm/kV and α = 0.12 and 0.1 °C^{-1}, upon cable energization, loading and switch off. Dotted horizontal line: field for PD inception, according to Equation (5.13). (b) conductivity behavior as a function of time (Equation (5.1)) for dielectric near inner conductor ($\gamma_{b\text{-}inner}$, r = 25.2 mm) and outer semiconducting layer ($\gamma_{b\text{-}outer}$, r = 45.2 mm). (c) estimated PD repetition rate inside cavity near inner conductor (rr_{inner}) and near outer semiconducting layer (rr_{outer}) from Equation (5.15) for AC regime and Equations (14) – (16) for transferring from AC to DC steady state condition where E_r is neglected and α = 0.12 °C^{-1}. (d) electric field behavior as a function of time, α and load for dielectric near inner conductor ($E_{b\text{-}inner}$, r = 25.2 mm) and outer semiconducting layer ($E_{b\text{-}outer}$, r = 45.2 mm). The load cycle is also indicated.

Considering Figures 5.12a and 5.15a, under steady state conditions for a hot cable, $E_{c\text{-}inner} < E_{c\text{-}outer}$. Regarding $E_{c\text{-}inner}$, since dielectric time constant near the inner conductor ($\tau_{d\text{-}inner}$) is significantly lower than the thermal time constant (τ_{th}) (see Figure 5.18), $E_{c\text{-}inner}$ is driven by

permittivity, rather than conductivity, when the load is switched on or off, resulting in sudden field escalation inside cavity after load variation and a burst of PD repetition rate, see Figures 5.12c and 5.15c. Indeed, when a permittivity-driven field is established, PD repetition rate becomes much higher than PD repetition rate under DC steady state conditions, which makes such transients as harmful for insulation aging as those described in Section 5.2.

Since the dielectric time constant near the inner conductor ($\tau_{d\text{-inner}}$) is significantly lower than the thermal time constant (τ_{th}) (see Figure 5.18), only $E_{c\text{-inner}}$ ramps up rapidly to cause large PD repetition rate, when the load is switched on or off. Furthermore, while ($E_{c\text{-outer}} > E_{c\text{-inner}}$), it behaves as in the previous case of $\tau_{th} > \tau_d$, thus when its variations can cause PD, they have repetition rate similar to DC conditions (Figures 5.12c and 5.15c). Indeed, while the value of repetition rate under DC steady state condition does not differ significantly from the previous cases in sub-section 5.5.1 for the cavity near to the inner semicon ($rr_{inner} = 0.03\ min^{-1}$), it is considerably higher for the outer cavity ($rr_{outer} = 1.9\ min^{-1}$).

The comparison between Figures 5.15a and 5.12a shows that when β increases the electric field inside cavity both near inner and outer conductor increases (see: Figure 5.12a). But when α increases the electric field inside cavity near inner conductor decreases while the electric field inside cavity near outer conductor increases (see: Figure 5.15a).

As shown in Figure 5.15a, load rise results in increase of electric field inside cavity both near inner and outer conductor while for the latter it is more considerable. The reason for this significant increase of field inside cavity is that after rising the load both dielectric conductivity (see: Figure 5.15b) and electric field in dielectric near outer conductor increases (see: Figure 5.15d). Thus, considering Equation (5.12), it can be resulted in considerable increase of electric field inside cavity near outer conductor.

The electric field and temperature profile under steady state condition (under full load and nominal voltage) across cable insulation and cavity for the reported cases in Figure 5.15 have been shown in Figure 5.16.

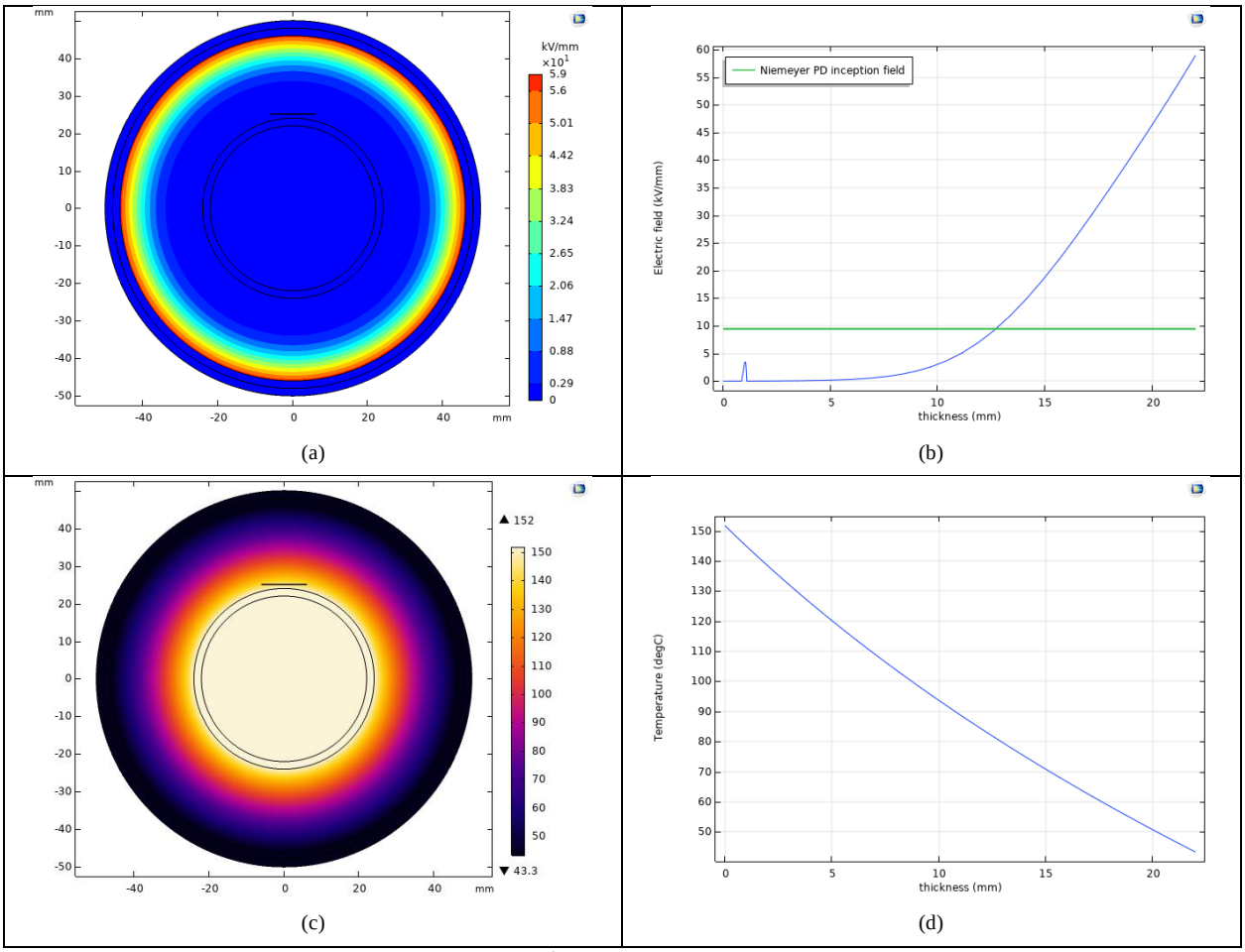

(a) $\alpha = 0.12$ [°C^{-1}], cavity near inner conductor

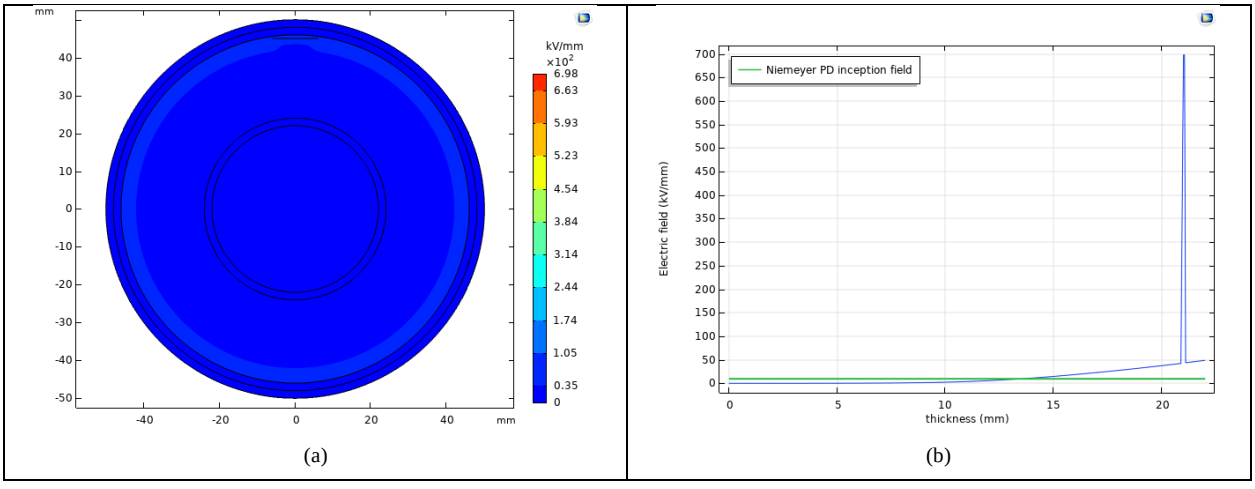

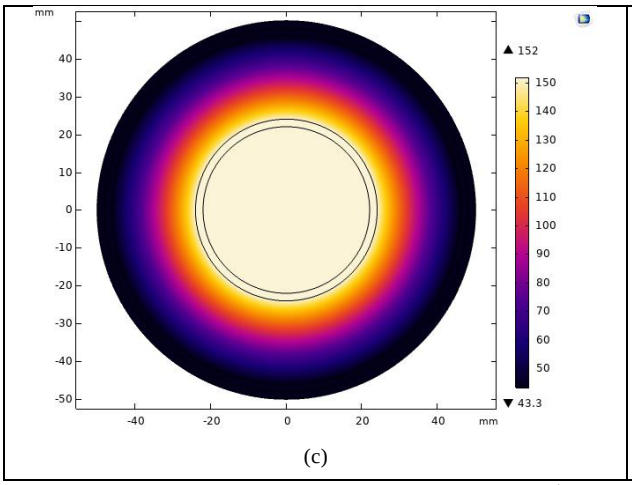

(c)

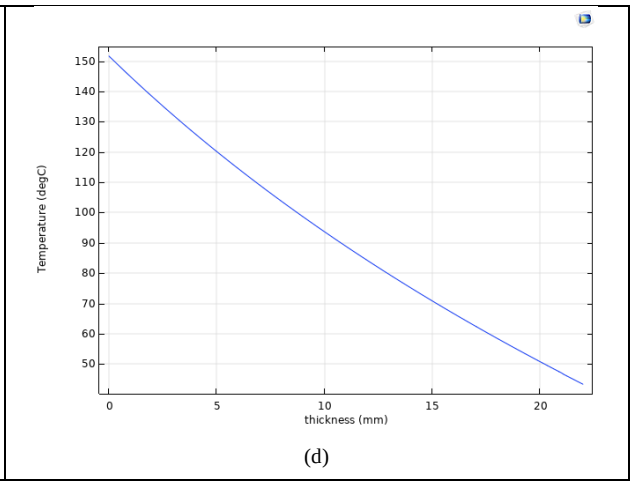

(d)

(b) $\alpha = 0.12$ [°C^{-1}], cavity near outer conductor

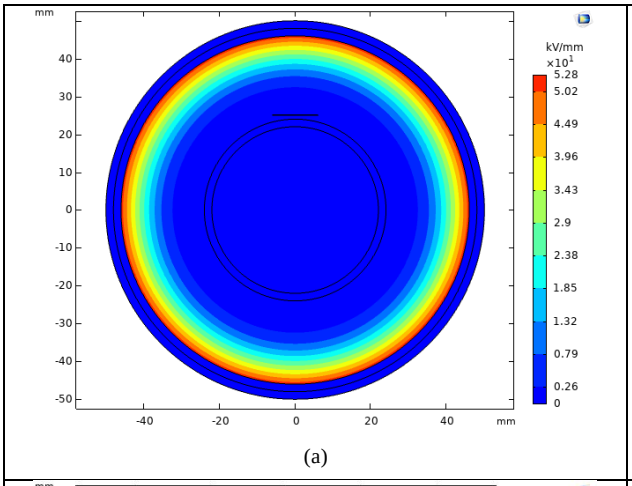

(a)

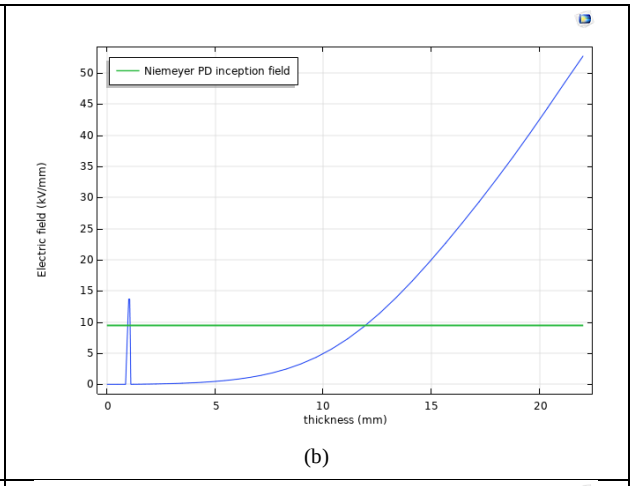

(b)

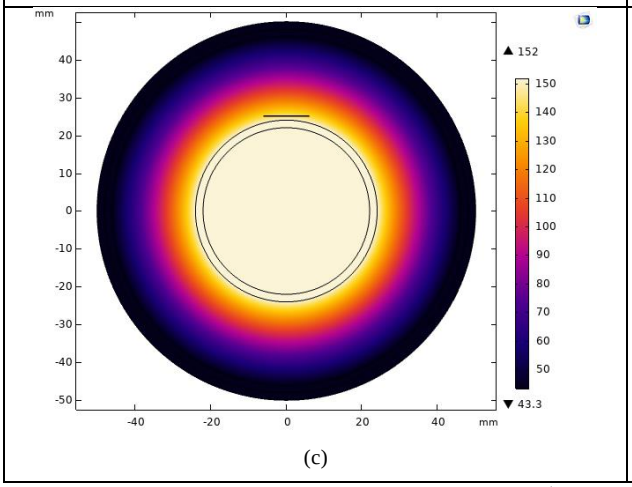

(c)

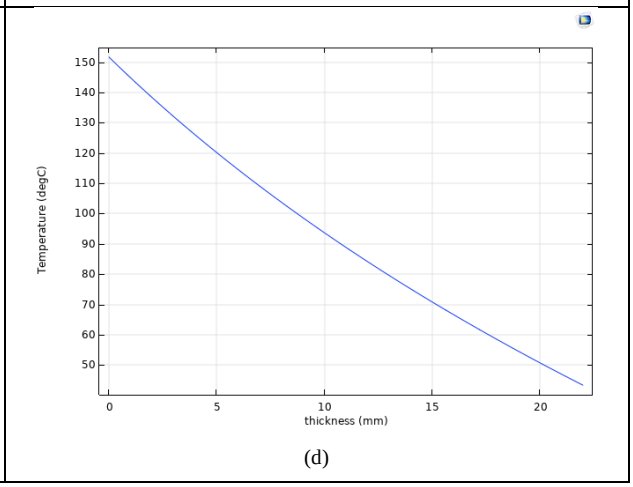

(d)

(c) $\alpha = 0.1$ [°C^{-1}], cavity near inner conductor

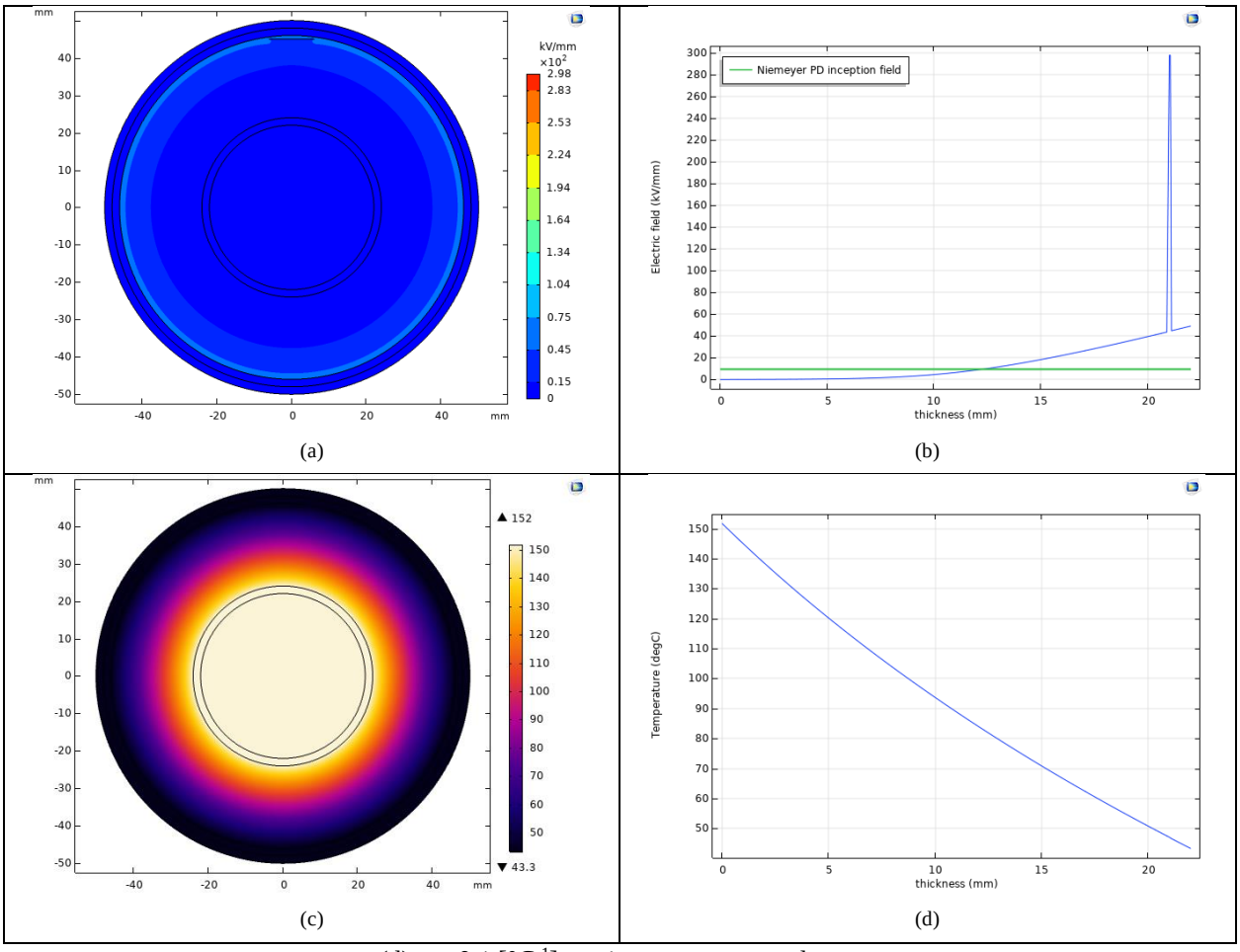

(d) $\alpha = 0.1$ [°C^{-1}], cavity near outer conductor

Figure 5.16. The electric field and temperature profile under steady state condition (under full load and nominal voltage) across cable insulation and cavity for the reported cases in Figure 5.15.

The comparison between Figures 5.16a and 5.16c shows that decrease of α from 0.12 to 0.1 [°C^{-1}] results in increase of electric field inside cavity near inner conductor. Moreover, it can be understood from Figures 5.16b and 5.16d that decrease of α for only about 17% can results in significant decrease of electric field inside cavity near outer conductor about 60%.

The electric field profile under steady state condition (under no load and nominal voltage) across cable insulation and cavity for the reported cases in Figure 5.15 have been depicted in Figure 5.17.

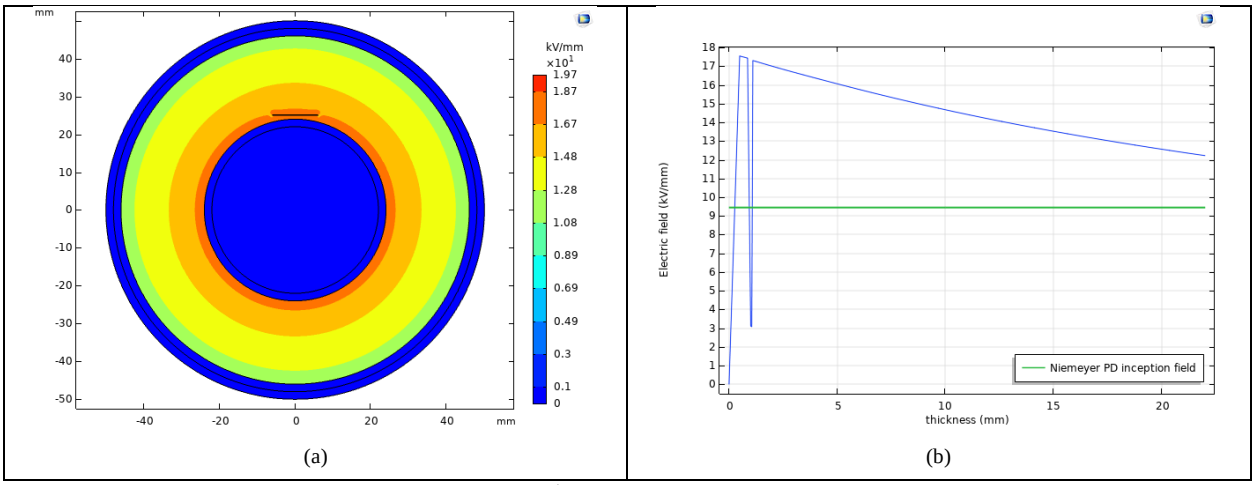

(a) (b)

(a) α = 0.12 [°C^{-1}], cavity near inner conductor

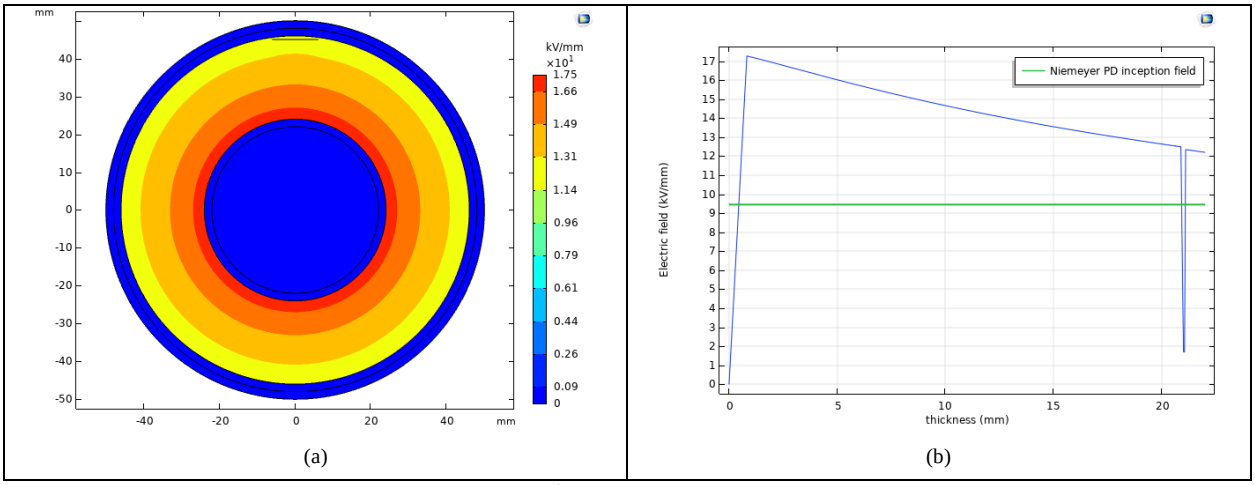

(a) (b)

(b) α = 0.12 [°C^{-1}], cavity near outer conductor

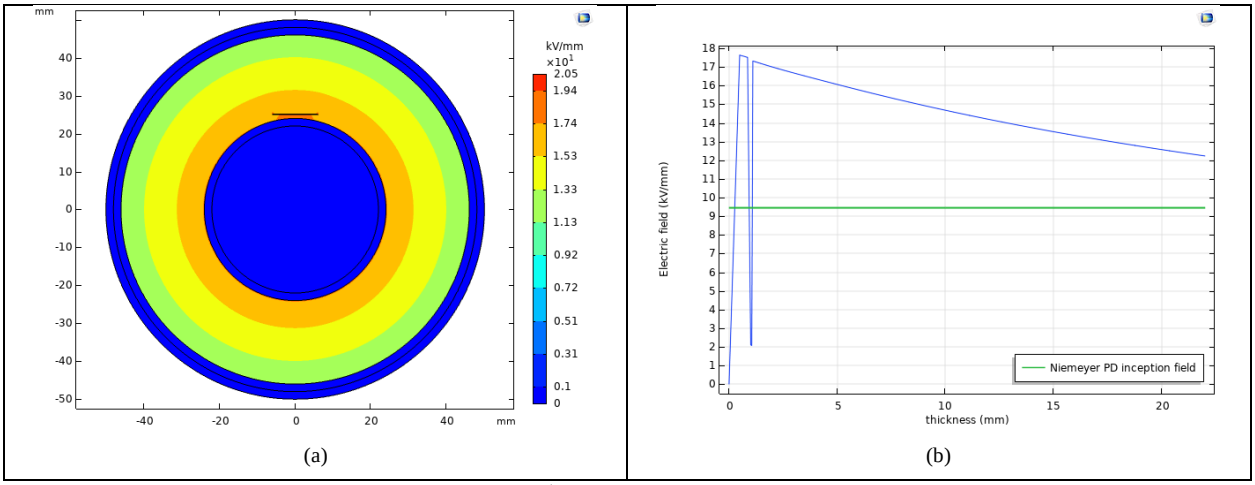

(a) (b)

(c) α = 0.1 [°C^{-1}], cavity near inner conductor

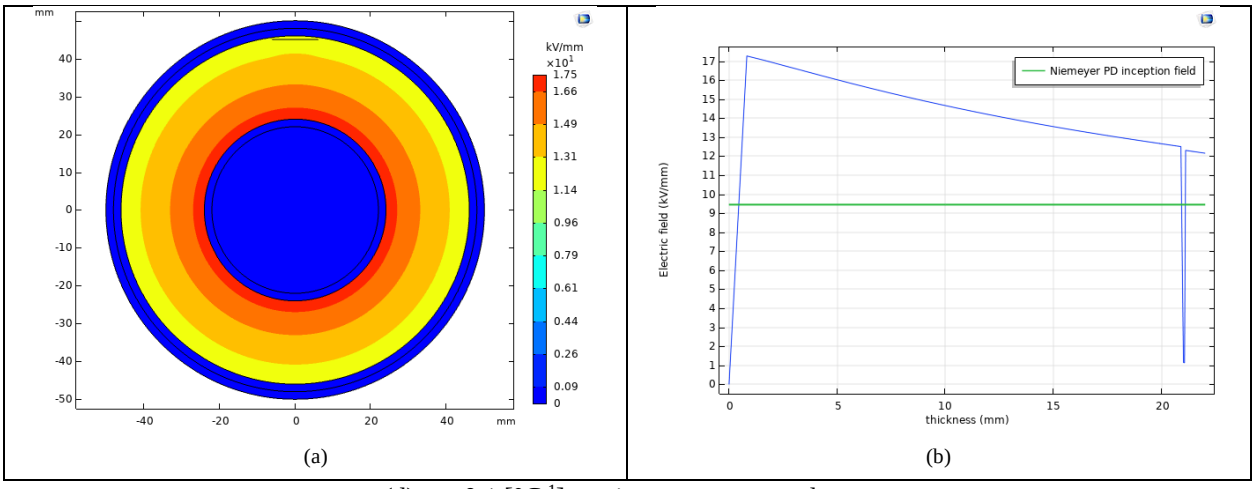

(a) (b)

(d) α = 0.1 [°C^{-1}], cavity near outer conductor

Figure 5.17. The electric field profile under steady state condition (under no load and nominal voltage) across cable insulation and cavity for the reported cases in Figure 5.15.

As shown in Figure 5.17, increase of α results in increasing electric field inside cavity both near inner and outer conductor while under full load, increase of α leads to decrease of field inside cavity near inner conductor and increase of electric field inside cavity near outer conductor (see: Figure 5.16).

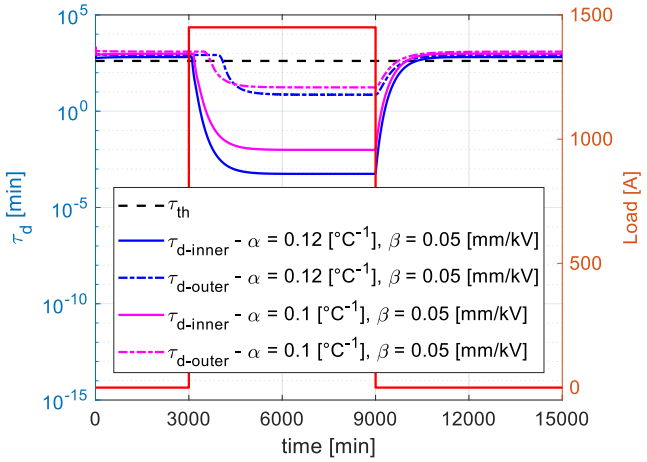

Figure 5.18. Calculated thermal and dielectric time constants, τ_{th} and τ_d, as a function of time from Equations (5.9) and (5.10) for dielectric near inner conductor ($\tau_{d\text{-inner}}$) and outer semiconducting layer ($\tau_{d\text{-outer}}$) when $\lambda = 0.035$ [W/mK], $C_P = 1900$ [J/kg.K], (a) at constant $\alpha = 0.1$ [°C^{-1}], and $\beta = 0.05$ and 0.03 [mm/kV] and (b) at constant $\beta = 0.05$ [mm/kV], and $\alpha = 0.12$ and 0.1 [°C^{-1}].

The thermal and dielectric time constants for insulation near inner (r = 25.2 [mm]) and outer semicon layer (r = 45.2 [mm]) are shown in Figure 5.18 as a function of time, when the load is

switched on and switched off. The former has value τ_{th} = 408 min, while the latter is 5.6E-4 and 9.8E-3 min for the dielectric near the inner conductor, when α = 0.12 and 0.1 °C^{-1}, respectively.

These observations can be valuable from cable design and insulation manufacturing point of view, as discussed in the next Section.

There is an interesting speculation regarding the leakage current measurement results for polymer minicables reported in [27]. As shown in Figure 5.19a, where the leakage current behavior is simulated for the low thermal conductivity condition (e.g. 0.035 W/(m.K)), there are kinds of leakage current overshoots when the load is switched on and switched off that resemble those reported in [27]. This could indicate that the study reported here for low thermal conductivity might not be far from some material/testing conditions. As shown in Figures 5.19b and 5.19c, these overshoots are not observed when thermal conductivity has its realistic value (e.g. 0.38 W/(m.K)) as considered for the cases of Figures 5.3 and 5.7.

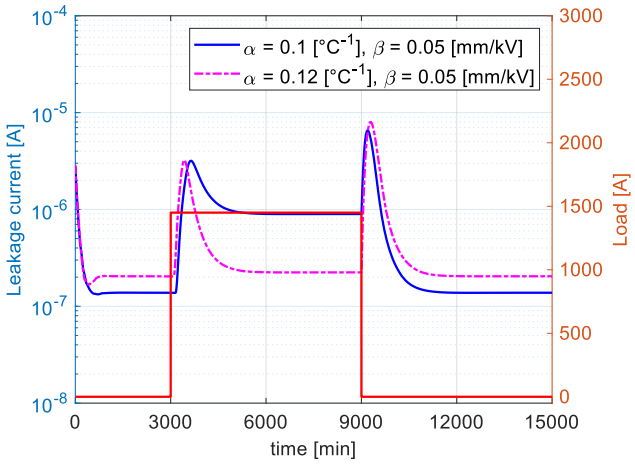

(a)

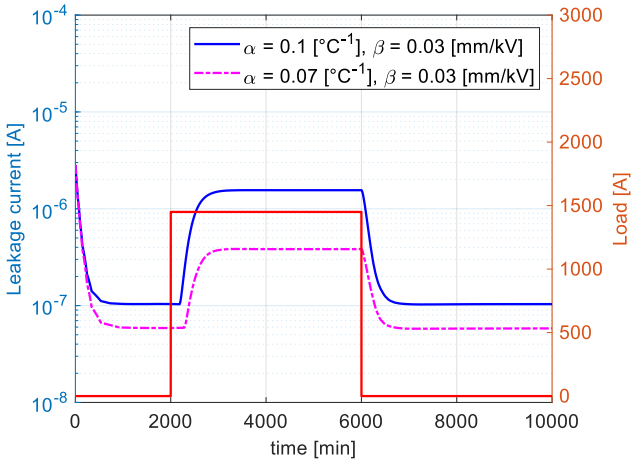

(b)

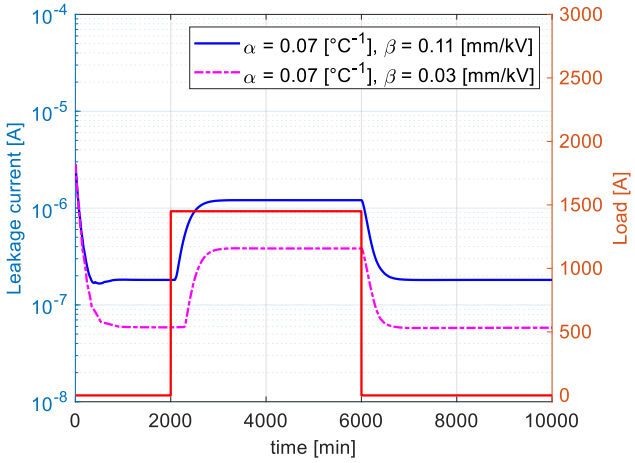

(c)

Figure 5.19. (a) Leakage current behavior as a function of time from $\gamma_b\big(T(r,t),E(r,t)\big).E_{b\,(t)}.h_b$ when λ = 0.035 W/(m.K), (b) λ = 0.38 W/(m.K) considering the parameters of Figure 5.3 (leakage current function of α) and (c) λ = 0.38 W/(m.K) considering the parameters of Figure 5.7 (leakage current function of β). The load cycle also is indicated.

As can be seen from Figures 5.19b and 5.19c, there is not any overshoot for leakage current when the load rises and falls. In addition, it can be understood that higher value of α and β results in higher electrical conductivity and following that higher value of leakage current.

The thermal time constant can be increased also by increasing the heat capacity of the insulating material. Keeping constant the thermal time constant (τ_{th} = 408 min) as in the previous case of thermal conductivity variation, the heat capacity would become 20630 J/kg.K.

The electric field behavior inside cavity when the load is switched on and off is depicted in Figure 5.20.

As can be seen, when heat capacity is high, the field will have a very slow rise after the load variation, which means that in case PD are triggered, their repetition rate will be small (similar to DC steady state). This is due to thermal and dielectric time constants near the inner and outer semicon layers having similar values, in the range of 100 to 400 min.

Considering Figure 5.20a, it is speculated that when heat capacity increases about one order of magnitude, although the field inside cavity near inner is higher than that of near outer conductor, this difference is negligible. There is the same story for electrical conductivity (see: Figure 5.20b), PD repetition rate (see: Figure 5.20c), and field in dielectric (see: Figure 5.20d). This negligible difference would be more highlighted when it is compared with the case of reduced thermal

conductivity by one order of magnitude at the same thermal time constant as shown already in Figures 5.12 and 5.9.

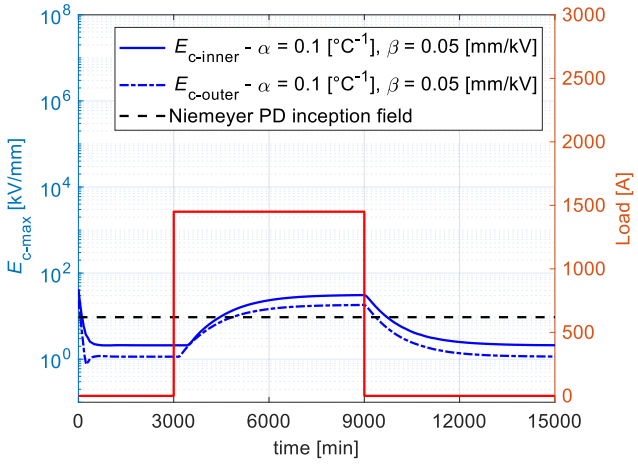

(a)

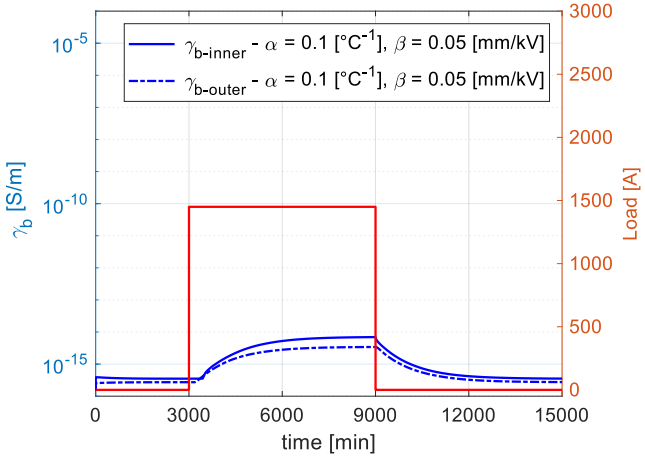

(b)

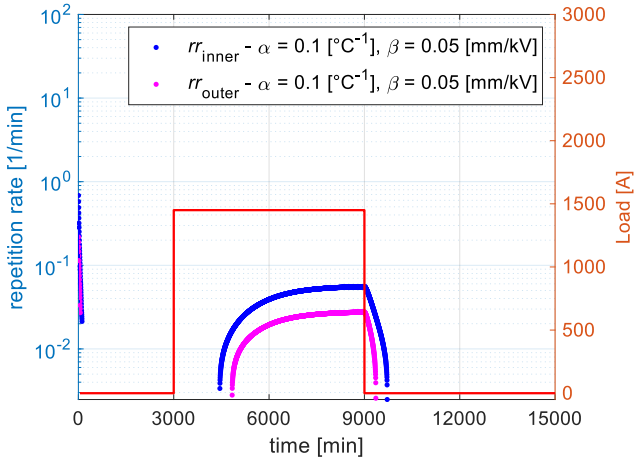

(c)

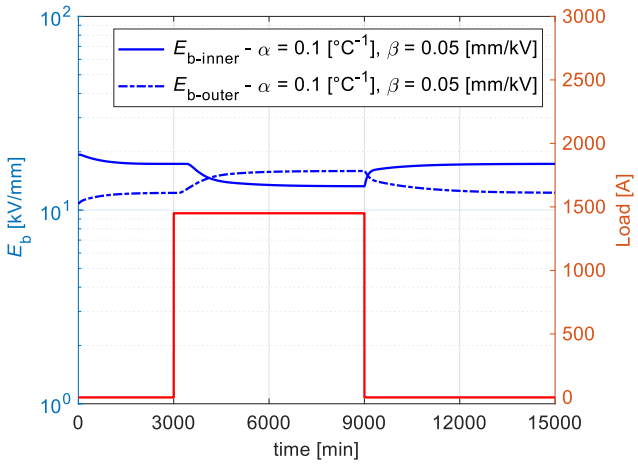

(d)

Figure 5.20. (a) Maximum electric field inside cavities located near the inner semicon ($E_{c\text{-inner}}$) and outer semiconducting layer ($E_{c\text{-outer}}$) when α = 0.1 °C^{-1} and β = 0.05 mm/kV upon cable energization, loading and switch off. Dotted horizontal line: PD inception field, according to Equation (5.13). (b) conductivity behavior as a function of time (Equation (5.1)) for dielectric near inner conductor ($\gamma_{b\text{-inner}}$, r = 25.2 mm) and outer semiconducting layer ($\gamma_{b\text{-outer}}$, r = 45.2 mm). (c) estimated PD repetition rate inside cavity near inner conductor (rr_{inner}) and near outer semiconducting layer (rr_{outer}) from Equation (5.15) for AC regime and Equations (5.14) - (5.16) for transferring from AC to DC steady state condition where E_r is neglected, α = 0.1 °C^{-1} and β = 0.05 mm/kV. (d) electric field behavior as a function of time and load for dielectric near inner conductor ($E_{b\text{-inner}}$, r = 25.2 mm) and outer semiconducting layer ($E_{b\text{-outer}}$, r = 45.2 mm). The load cycle is also indicated.

The electric field and temperature profile under steady state condition (under full load and nominal voltage) across cable insulation and cavity for the reported conditions in Figure 5.20 have been demonstrated in Figure 5.21.

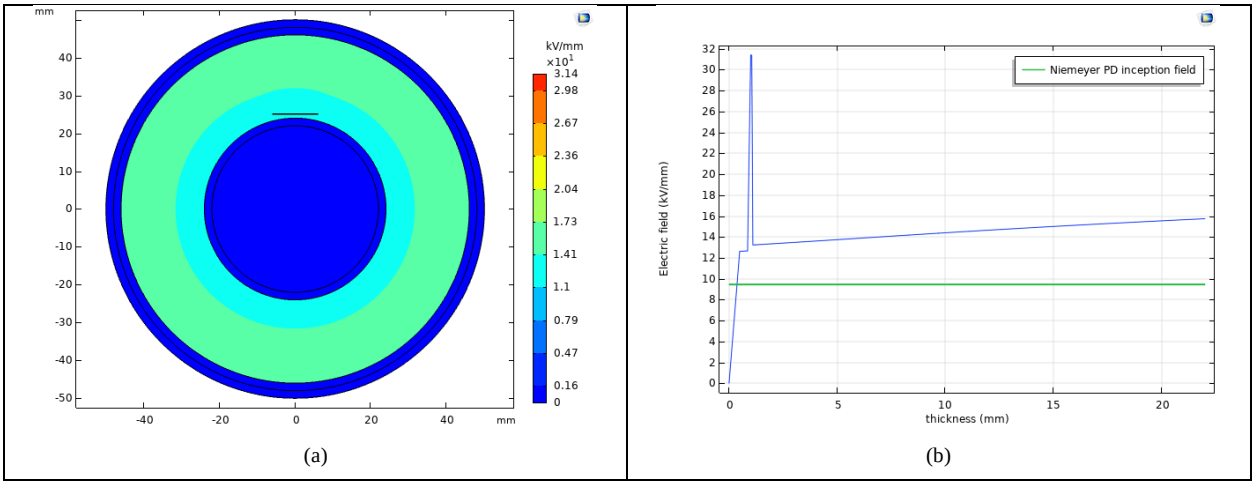

(a) (b)

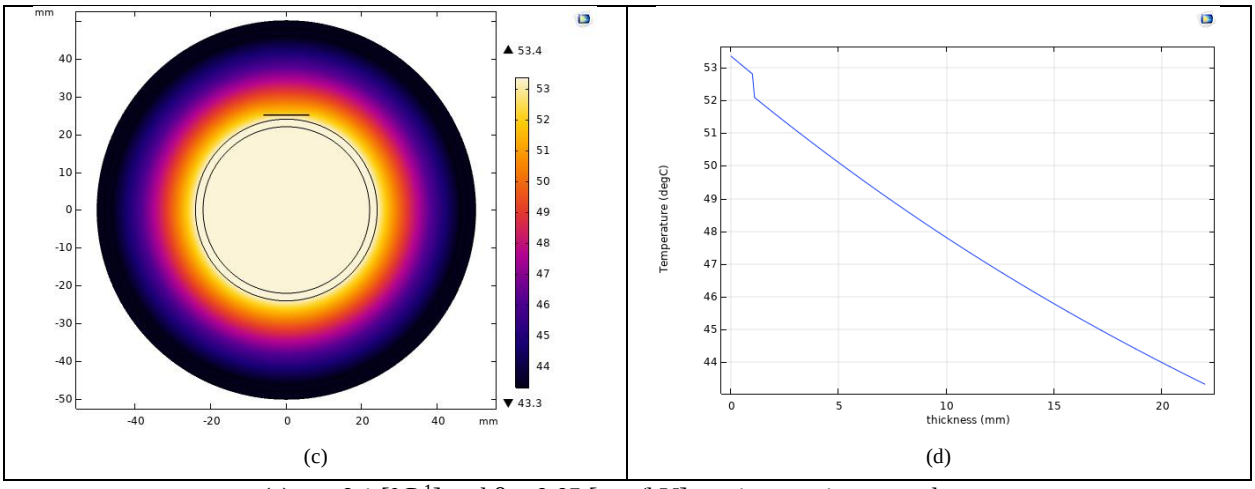

(c) (d)

(a) α = 0.1 [°C^{-1}] and β = 0.05 [mm/kV], cavity near inner conductor

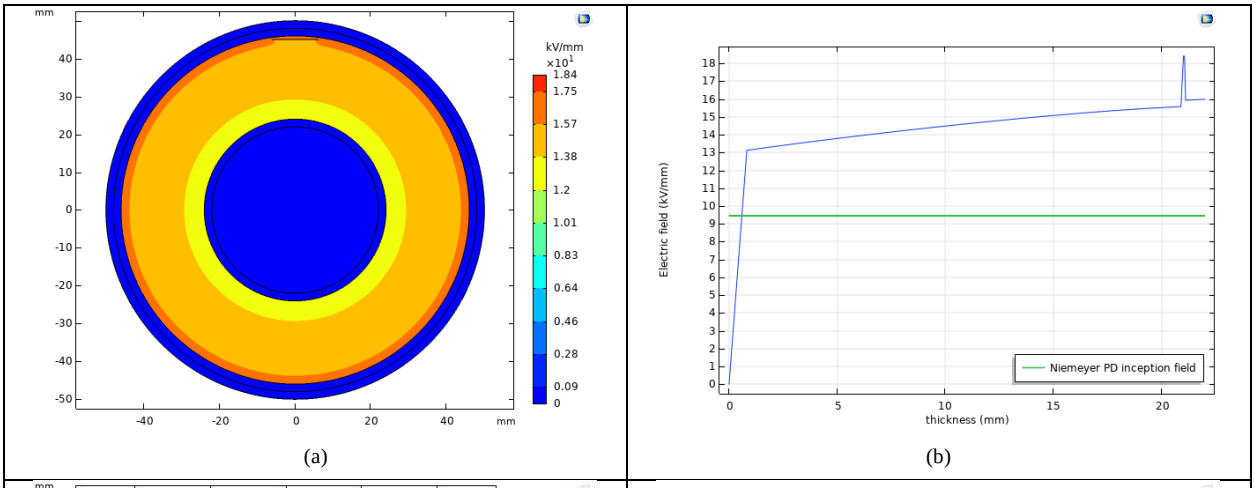

(a) (b)

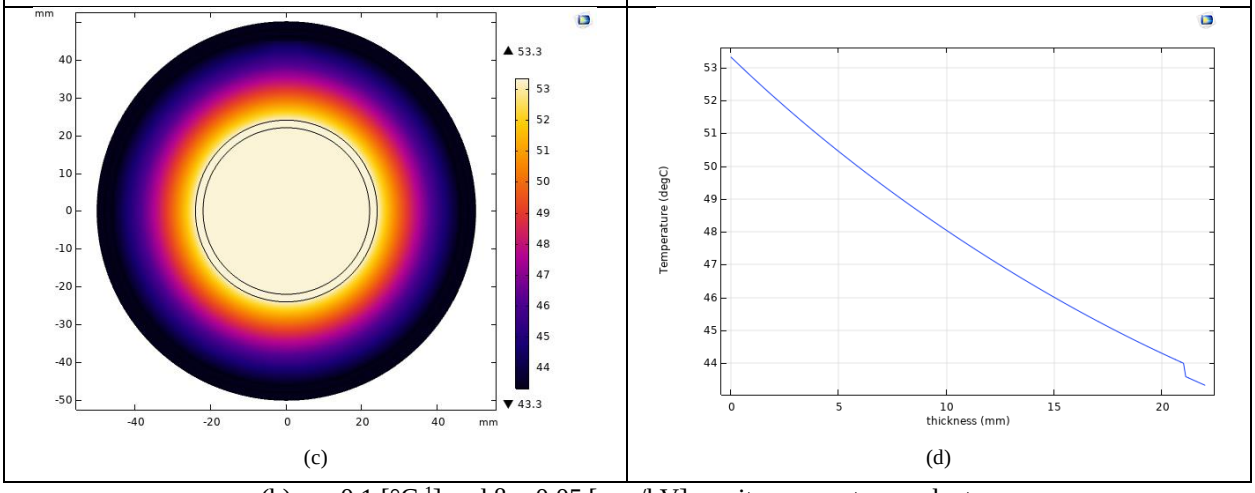

(c) (d)

(b) α = 0.1 [°C^{-1}] and β = 0.05 [mm/kV], cavity near outer conductor

Figure 5.21. The electric field and temperature profile under steady state condition (under full load and nominal voltage) across cable insulation and cavity for the reported cases in Figure 5.20.

As can be seen from Figure 5.21, in despite of reduction of thermal conductivity, increase of heat capacity can result in homogenous electric field distribution across cable insulation under full load

condition. In other words, there is slight difference between the electric field in dielectric near inner conductor compare with that of near outer conductor when heat capacity increases. The reason for this is that when heat capacity increases, the temperature profile across cable would not vary considerable compare with the case of low heat capacity. As a result, there is not significant increase of temperature in dielectric near inner conductor despite of the case when thermal conductivity is reduced.

The electric field profile under steady state condition (under no load and nominal voltage) across cable insulation and cavity for the reported conditions in Figure 5.20 have been illustrated in Figure 5.22.

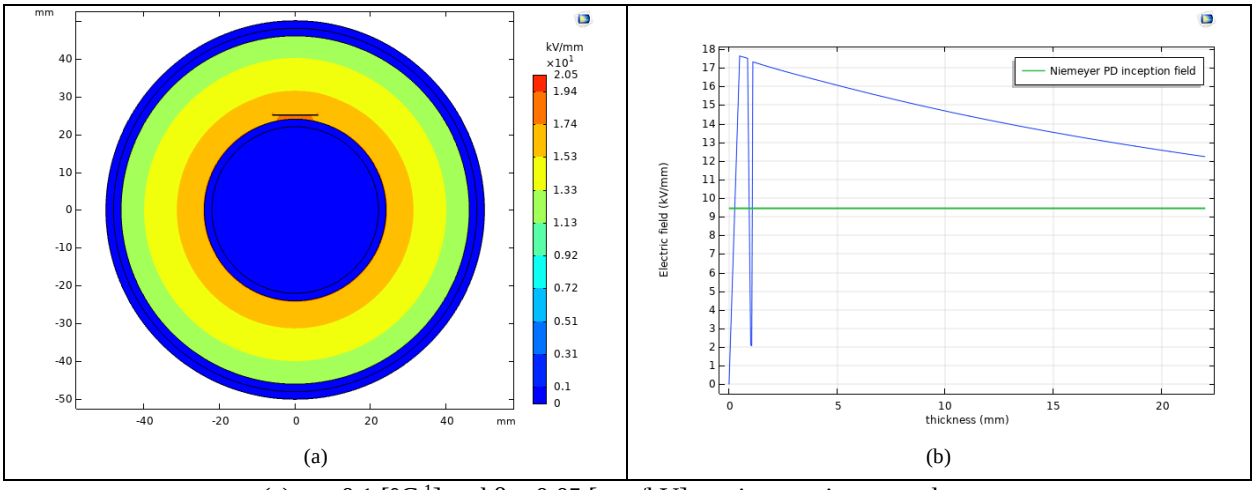

(a) (b)

(a) $\alpha = 0.1$ [°C^{-1}] and $\beta = 0.05$ [mm/kV], cavity near inner conductor

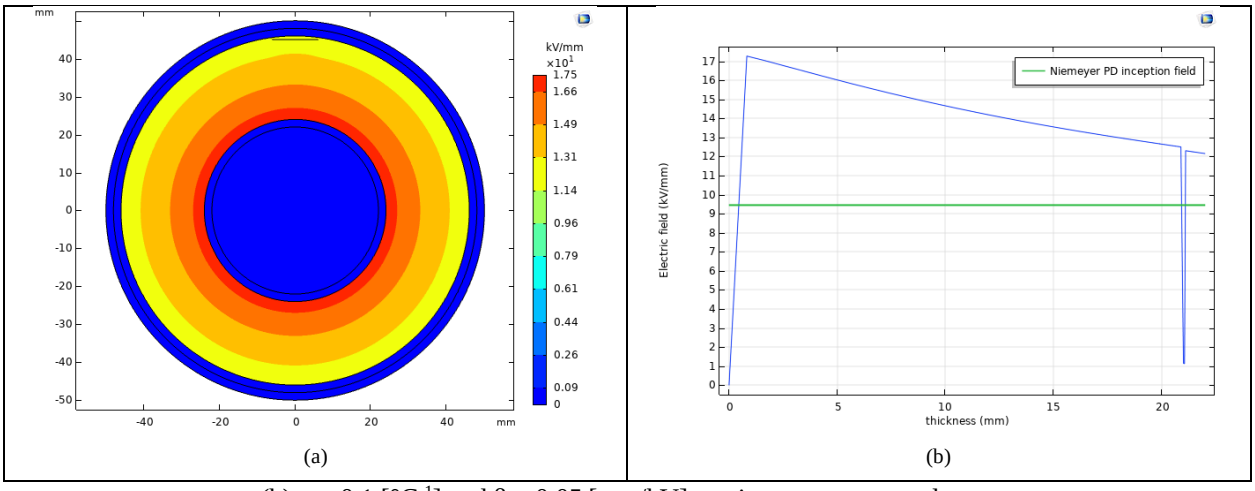

(a) (b)

(b) $\alpha = 0.1$ [°C^{-1}] and $\beta = 0.05$ [mm/kV], cavity near outer conductor

Figure 5.22. The electric field and temperature profile under steady state condition (under no load and nominal voltage) across cable insulation and cavity for the reported cases in Figure 5.20.

As shown in Figure 5.22, under no load condition when heat capacity is high, the electric field distribution across cable insulation would be similar to the case of capacitive distributed electric field in which there is higher electric field in dielectric near inner conductor.

5.6 Conclusions

The main contribution of this chapter is to show that not only voltage transients or ripple can cause bursts of PD that last much longer than the voltage transient, but also load variations can cause PD as a consequence of the variation of electric field in defects (cavities, delamination) caused by manufacturing, commissioning or aging.

A straightforward consequence is that DC cables should not be designed as it is done for sinusoidal AC power supply, where load variations do not influence PD phenomenology. For that knowing PD phenomenology, which is the focus of this chapter, is not enough. Indeed, adequate life models must be developed which are able to account for both voltage (as in [3]) and load transients (the purpose of a next chapter), in order that design can take into account properly the expected cable operating conditions. It might be likely that cables could be classified in terms of their propension to withstand little, moderate, or extreme levels of voltage and load transients, as it is done in IEC 60034-18-41 and 42 for rotating machines fed by inverters.

Going more in detail about the content of this chapter, it is shown that considering the insulating materials used at present for DC polymeric cables, the thermal constant consequent to cable load variations is shorter than the dielectric constant that comes from cable energization with a DC voltage or voltage polarity inversion, i.e., $\tau_{th} < \tau_d$. This has an impact of PD repetition rate, which is closer to that characteristic to steady-state DC, that is, significantly low, than to that typical of voltage transient and AC. This might indicate that the effect of load transients on aging rate is lower than that of voltage transients, but most likely the load dynamic can be higher in the latter (load variation) case. The effect of larger temperature dependence (α) or field dependence (β) coefficients of electrical conductivity is also to be kept into account. In general, cavities near the inner conductor can be more harmful than cavities near the outer semicon.

In some extreme conditions of low values of thermal conductivity, it can occur that the thermal constant reaches levels higher than the dielectric time constant, i.e. $\tau_{th} > \tau_d$. In this case, PD might be driven not only by a change of conductivity with load, but also by permittivity, during the initial load variation transients. This results in an unexpected condition where PD can show high

repetition rate in those phases, especially for the cavity near inner semicon, as under AC. In principle, such condition would lead to potentially significant life reduction in the presence of repeated load variations during cable life, as that due to energization and voltage polarity inversion modelled in [4]. However, in the absence of data relevant to aging behavior of thermal conductivity this aspect seems to be more a theoretical speculation than a possible event, at least for cable insulation.

Cable designers should be aware and take into account the results devised in this chapter, for the sake of long-term reliability under DC operation. As a matter of fact, it results once more that operating a cable under DC does not mean designing, nor testing a cable for purely AC or DC steady state conditions. Besides using life models that do not reply simple on the inverse power law, as for AC, designers should look at materials that provide the best conditions to reduce the effect of voltage and load transients, from the conductivity value to its dependence of temperature and field (e.g., to increases the PDIV or reduce electric field transient times). Also, testing specifications should not be limited to AC PD or life tests for DC cables, nor to only DC PD and life tests. The potential accelerated aging effects of voltage and load transients highlights the need to have a broad view of the cable behavior, which is portrayed only by carrying out both AC and DC tests.

References

[1] F.H. Kreuger, *Industrial High DC Voltage: 1. Fields 2. Breakdowns 3. Tests*, Delft University Press, 1995.

[2] Udo Fromm, “Partial discharge and breakdown testing at high DC voltage,” PhD dissertation, TU Delft, ISBN 90-407-1155-0, 1997.

[3] P. Seri, H. Naderiallaf, G.C. Montanari, “Modelling of supply voltage frequency effect on partial discharge repetition rate and charge amplitude from AC to DC: room temperature,” IEEE Trans. on Diel. and El. Insulation, vol. 27, no. 3, pp. 759-766, June 2020.

[4] G.C. Montanari, P. Seri, S. Franchi Bononi, M. Albertini, “Partial discharge behavior and accelerated aging upon repetitive DC cable energization and voltage supply polarity inversion,” IEEE Trans. on Power Delivery, vol. 35, pp. 1-8, 2020.

[5] P. Seri, G.C. Montanari, A. Albertini, S.F. Bonomi and M. Albertini, “Comparing the results of increasing-voltage design and qualification life tests on HVDC and HVAC cables: the effect of voltage-step growth rate and insulation thickness factors,” Conference on Electrical Insulation and Dielectric Phenomena (CEIDP), 2020, pp. 1-4.

[6] G.C. Montanari, R. Hebner, P. Seri, and H. Naderiallaf, “Partial discharge inception voltage and magnitude in polymeric cables under AC and DC voltage supply,” Jicable, 2019, pp. 1-4.

[7] H. Naderiallaf, A. Cavallini, F. Esterl, R. Plath, P. Seri and G.C. Montanari, “Measuring partial discharges in MV cables under DC voltage: procedures and results in steady state conditions”, IEEE Electr. Insul. Conf. (EIC), 2020, pp. 1-4.

[8] G.C. Montanari, Paolo Seri, and Hadi Naderiallaf, “A contribution to everlasting electrical insulation for DC voltage: PD-phobic materials,” IEEE Access, Feb. 2020.

[9] P. Seri, L. Cirioni, H. Naderiallaf, G.C. Montanari, R. Hebner, A. Gattozzi, and X. Feng, “Partial Discharge Inception Voltage in DC insulation systems: a comparison with AC voltage supply,” in IEEE Electr. Insul. Conf. (EIC), 2019, pp. 1-4.

[10] S.J. Frobin, C. Freye, C.F. Niedik, and F. Jenau, “Generic field simulation framework for HVDC cables,” IEEE 2nd International Conference on Dielectrics (ICD), 2018, pp. 1-5.

[11] G. Mazzanti and M. Marzinotto, *Extruded Cables for High Voltage Direct Current Transmission: Advance in Research and Development*, Power Engineering Series, Wiley-IEEE Press, 2013.

[12] L.A. Dissado and J.C. Fothergill, *in Electrical Degradation and Breakdown Polymers*. P. Peregrinus press, 1992.

[13] M. Marzinotto and G. Mazzanti, “The statistical enlargement law for HVDC cable lines. Part 1: theory and application to enlargement in length,” IEEE Trans. Dielectr. Electr. Insul., vol. 22, no 1, pp. 192-201, Feb. 2015.

[14] R. Bodega, G.C. Montanari, and P. H. F. Morshuis, “Conduction current measurements on XLPE and EPR insulation,” In The 17th Annual Meeting of the IEEE Lasers and Electro-Optics Society (LEOS), 2004, pp. 101-105.

[15] C.O. Olsson, “Numerical investigation of temperature and electric field dynamics in polymer insulation at HVDC,” in IEEE Electr. Insul. Conf. (EIC), 2009, pp. 504-508.

[16] S.J. Frobin, K. Friebe, and F. Jenau, “Thermal Modelling of HVDC Cables Focussing on Heat Cycle Test Conditions and Dynamic Temperature Profiles,” In The International Symposium on High Voltage Engineering, Springer, Cham, 2019, pp. 1513-1526.

[17] Y. Liu, S. Zhang, X. Cao, C. Zhang, and W. Li, “Simulation of electric field distribution in the XLPE insulation of a 320 kV DC cable under steady and time-varying states,” IEEE Trans. Dielectr. Electr. Insul., vol. 25, no. 3, pp. 954-964, July 2018.

[18] G.J. Anders, *Rating of electric power cables in unfavorable thermal environment*, New York: Wiley, 2005.

[19] Thomas Worzyk, *Submarine power cables: design, installation, repair, environmental aspects*, Springer Science & Business Media, 2009.

[20] Y. Zhang, X. Zhou, H. Niu, X. Wang, Y. Tang, J. Zhao, and Yo. Fan, “Theoretical calculation and experimental research on thermal time constant of single-core cables,” High Voltage Engineering, vol. 35, no. 11, pp. 2801-2806, Nov. 2009.

[21] B.M. Weedy, *Underground transmission of electric power*, John Wiley & Sons, 1980.

[22] I. Garniwa, and A. Burhani, “Thermal incremental and time constant analysis on 20 kV XLPE cable with current vary,” In 2006 IEEE 8th International Conference on Properties & applications of Dielectric Materials, 2006, pp. 566-569.

[23] P. Seri, R. Ghosh, H. Naderiallaf, and G.C. Montanari, “Investigating Energization Transients and the Potentiality of Partial Discharge Inception and Damage in Nanofilled Polypropylene Insulation for DC Cables and Capacitors,” CATCON, India, 2019, pp. 1-5.

[24] G.C. Crichton, P.W. Karlsson, and A. Pedersen, “Partial discharges in ellipsoidal and spheroidal voids,” IEEE Trans. Dielectr. Electr. Insul., vol. 24, no. 2, pp. 335-342, Apr. 1989.

[25] A. Pedersen, G. C. Crichton, and I. W. McAllister, “The theory and measurement of partial discharge transients,” IEEE Trans. Dielectr. Electr. Insul., vol. 26, no. 3, pp. 487-497, 1991.

[26] L. Niemeyer, “A generalized approach to partial discharge modeling,” IEEE Trans. on DEI, vol. 2, no. 4, pp. 510-528, 1995.

[27] D. Charrier, Q. Eyssautier, G. Perego, C. Frohne, and M. Jarvid, “Leakage current behaviors under high electric field in polymer minicables,” Jicable, 2019, pp. 1-4.

[28] G.C. Montanari, P. Seri, P. Morshuis, R. Hebner, “An approach to insulation condition monitoring and life assessment in emerging electrical environments”, IEEE Trans. on Power Delivery, vol. 34, no. 4, pp. 1357-1364, August 2019.

Chapter 6

Designing a HVDC insulation system to endure electrical and thermal stresses under operation

This chapter has the purpose to investigate HVDC insulation design considering real operating conditions when DC steady-state is affected by frequent voltage polarity inversions or load variations that may be present during all life. Electrical field distribution in insulation, and in insulation defects, may change significantly from DC steady-state when voltage and load change with time, which can cause accelerating aging phenomena that might have not been properly accounted for at the design stage. The related aging amount can become significant if such time variations are able to trigger harmful phenomena as partial discharges, and the rate of voltage and load variations during operation life is significant. Experiments, models, and simulations show that electrical and thermal transients may incept partial discharges in defective insulations during cable energization, voltage polarity inversion at a constant nominal load, as well as during load variations at a constant nominal voltage. Evidence that design must consider this further source of aging, when the rate of transients is not negligible during operation, is presented and discussed. It comes out that reduction of electric stress/field may be needed to reach the specified life for a HVDC insulation system. Also, materials and technologies may have to be improved. Focus here is on cables, but the approach described here is general for any DC insulation system.

6.1 Introduction

DC insulation is not supposed to work all life under DC-steady state conditions, nor at constant thermal stress.

Energization and voltage polarity inversions give rise to electric field transients that may last many hours [1-2], and load variation cause temperature profile transients in a DC insulation system [4]. These transients, electrical and thermal, can be repeated many thousands of times during the insulation life.

The amount of damage that such transients can cause to insulation, and thus their contribution to premature failure, could be negligible if the rate at which they occur is small, or the insulation system design is conservative, and as long as they are not triggering high aging-rate phenomena, as partial discharges. Inception of PD can degrade insulation locally, generating with time

footpaths to insulation breakdown, so that failure can occur well in advance compared to the specified design life. This depends fundamentally on some factors which can be summarized by a damage concept: the longer PD are active and the higher the relevant energy (or power), the larger the contribution to life reduction [2-4].

During electrical and thermal transients, the electric field profile in insulation and internal defects may vary significantly. There is a steep difference between the conductivity-driven distribution, in DC steady-state, [5], and the permittivity-driven field, which establishes at the beginning of voltage (and sometimes load) transients [2, 4]. PD might incept in insulation defects (cavities) when in the latter case, while it would not occur in DC steady-state, if the insulation is designed properly to work (at any operating temperature) at nominal voltages below the DC steady-state partial discharge inception voltage, $PDIV_{\mathrm{DC}}$.

Such PD, being relevant during transients, may have large repetition rate, as under AC sinusoidal voltage, and, therefore, constitute a source of non-negligible aging acceleration at the defect/insulation interfaces. This can impact significantly on life when grid/asset component operation includes frequent transients.

In [5] the authors were considering insulation system design in DC steady-state, that is, when electric field transient rate is negligible during operation life.

Here, the conditions at which PD can occur during electrical and thermal transients are examined (Sections 2 and 3), and their impact on aging qualitatively evaluated. The feedback resulting from such potentially harmful phenomena on insulation system design are then discussed (Section 4), with the aim of providing useful contributions to reliable DC insulation design.

6.2 Electric field and thermal transients

6.2.1 Electrical conductivity modeling

The steady-state dependence of electrical conductivity on temperature and electric field can be exploited using a well-known empirical model [4-6]:

$$\gamma_{\mathrm{b}}\big(T(r,t),E(r,t)\big) = \gamma_0 . e^{\alpha(T(r,t)-T_0)+\beta(E(r,t)-E_0)} \tag{6.1}$$

where γ_0 is the reference electrical conductivity at temperature T_0 (in °C) and reference electric field E_0 (in kV/mm). The temperature dependence of conductivity is implemented by coefficient

α (in °C^{-1}), whereas β (in mm/kV) drives the field dependence. It should be noted that the dependency of conductivity on temperature has been estimated here approximately, taking T in place of $1/T$, as it would be required referring to the Arrhenius equation [6-8]. Considering the usual operating temperature range of polymeric cables, and for typical values of α, this is an acceptable simplification which is widely used in practice.

6.2.2 Dielectric time constant and electric field transient

The dielectric time constant for an insulating material is defined as the ratio of relative permittivity to electrical conductivity, as resulted from Maxwell equations, [4, 9, 10]:

$$\tau_{\mathrm{d}} = \varepsilon_0 \varepsilon_{\mathrm{rb}} / \left[\gamma_{\mathrm{b}}\left(T(r,t), E(r,t)\right)\right] \tag{6.2}$$

where ε_0 is the permittivity of free space (8.85×10^{-12} F.m^{-1}) and $\varepsilon_{\mathrm{rb}}$ is the relative permittivity of insulating material. The dielectric time constant for the medium filling the cavity can be obtained from Equation (6.2) upon replacing $\varepsilon_{\mathrm{rb}}$ and γ_{b} with the permittivity and conductivity of the medium filling the cavity. The dielectric time constant for the medium filling the cavity can be obtained in the same way as Equation (6.2) from general Maxwell equations, considering permittivities and conductivities of the cavity and of the dielectric connected in series (see Appendix A).

In AC, the electric field intensification inside cavities embedded in the insulation will depend on the permittivities relevant to defect and dielectric. For a cylindrical cavity, the amplification factor is estimated by [11, 12]:

$$f_{\mathrm{AC}} = E_{\mathrm{c}} / E_{\mathrm{b}} = \varepsilon_{\mathrm{rb}} / \varepsilon_{\mathrm{rc}} \tag{6.3}$$

where $\varepsilon_{\mathrm{rc}}$ and $\varepsilon_{\mathrm{rb}}$ are the relative permittivities and E_{c} and E_{b} are electric fields, respectively in the cavity and the insulating material.

Under steady-state DC conditions, the situation can be drastically different since the field inside a defect will depend on the conductivity ratio between the dielectric material and the medium filling the cavity. Therefore, the amplification factor for a cylindrical cavity is given by [4, 13]:

$$f_{\mathrm{DC}} = E_{\mathrm{c}} / E_{\mathrm{b}} = \gamma_{\mathrm{b}}\left(T(r), E(r)\right) / \gamma_{\mathrm{c}} \tag{6.4}$$

where γ_c is the electrical conductivity of cavity (usually air, taken in the following as 3E-15 S/m, according to [13]).

Based on the dielectric time constant, τ_d, which can be calculated from Equation (6.2), the field variation factor as a function of time, $f(t)$, from time 0 of a voltage or load transient to DC steady state condition, can be given by:

$$f(t) = f_{DC} + (f_0 - f_{DC}) \cdot \exp\left(-\frac{t}{\tau_d}\right) \quad (6.5)$$

where f_0 and f_{DC} are the values at the beginning and end of field or temperature transient, respectively.

For both electrical and thermal transients, f_{DC} is calculated from Equation (6.4) under steady state condition. It must be noted that the value of f_{DC} in Equation (6.5) varies with load and defect position in cable insulation, because of the thermal gradient which modifies conductivity along insulation radius ((6.1)). In addition, f_{DC} can be higher or lower than f_0 depending on material properties and temperature (load). The value of f_0 can be calculated in different ways for electrical or thermal transients.

Considering electrical transients, since electric field is driven by permittivity just after voltage variation, f_0 is obtained from Equation (6.3).

Regarding thermal transients and taking in to account the properties of the typical insulating materials used at present for DC polymeric cables, the thermal time constant consequent to cable load variations is shorter than the dielectric time constant that drives e.g., cable energization with a DC voltage or voltage polarity inversion [4]. As a result, from the beginning of load variation to the end of thermal transient, electric field is always ruled by conductivity. Thus, f_0 is also calculated from Equation (6.4) as f_{DC}.

The electric field magnitude inside a cavity as a function of time, $E_c(t)$, can be then estimated, as a first approximation, by:

$$E_c(t) = E_{DC} + (E_0 - E_{DC}) \cdot \exp\left(-\frac{t}{\tau_d}\right) \quad (6.6)$$

In a cylindrical insulation geometry, the dielectric time constant in Equation (6.6) can be estimated from Equation (6.2) (and Appendix A) upon calculating/measuring the electrical

conductivity under steady state condition at the radius at which the cavity is located. For example, conductivity can be measured by flat specimens under equivalent temperature and electric field of the specified radius (which can be, in turn, estimated by analytical modelling or numerical simulation).

Equation (6.6) is a general model valid for both electrical and thermal transients upon defining E_0, E_{DC} and selecting properly the transient time constant. For electrical transient, the capacitive electric field in a cavity immediately after a voltage change, E_0, and the steady-state resistive condition, E_{DC} are given by:

$$E_0 = E_{\mathrm{c}}(0^-) + \frac{U_0 \cdot \varepsilon_{\mathrm{rb}}}{\varepsilon_{\mathrm{rb}} \cdot h_{\mathrm{c}} + \varepsilon_{\mathrm{rc}} \cdot h_{\mathrm{b}}} \tag{6.7}$$

$$E_{\mathrm{DC}} = \frac{U_0 \cdot \gamma_{\mathrm{b}}\big(T(r,t), E(r,t)\big)}{\gamma_{\mathrm{b}}\big(T(r,t), E(r,t)\big) \cdot h_{\mathrm{c}} + \gamma_{\mathrm{c}} \cdot h_{\mathrm{b}}} \tag{6.8}$$

where $E_{\mathrm{c}}(0^-)$ is the field immediately before the beginning of electrical transients which can be calculated from Equation (6.8). U_0 is the amplitude of supply voltage at the end of voltage transient when it reaches to a constant value, h_{b} and h_{c} are thickness of insulation and cavity height, respectively.

6.2.3 Thermal time constant and thermal transient

The thermal resistance and capacitance of a cylindrical insulation layer for per unit length (thinking of an insulated cable) are given by [4, 14, 15]:

$$R_{\mathrm{th}} = \ln\left(\frac{r_{\mathrm{o}}}{r_{\mathrm{i}}}\right) / 2\pi\lambda \tag{6.9}$$

$$C_{\mathrm{th}} = \rho_{\mathrm{m}} C_{\mathrm{P}} \pi (r_{\mathrm{o}}{}^2 - r_{\mathrm{i}}{}^2) \tag{6.10}$$

where r_{o} and r_{i} are the outer and inner radius of insulation layer, respectively.

An accurate thermal time constant for DC cables can be calculated using Cauer-type ladder network, where each cable layer has its own thermal resistance and heat capacity [14, 15]. Due to the fact that the thermal conductivity of inner and outer conductor, as well as of the semiconducting layers, are significantly higher than that for cable insulation (and under the assumption of significant smaller thermal heat capacity of the conductor and semiconducting layer), their effect

on the total thermal time constant of cable would be negligible. Therefore, the thermal time constant of a HVDC cable surrounded by air can be estimated with a good approximation by the thermal time constant of its electrical insulation layer [4]. When load is changed, the temperature across the cable insulation varies exponentially as a function of time [16, 17]:

$$\Delta T = \Delta T_{\mathrm{ss}} \left(1 - e^{\frac{-t}{R_{\mathrm{th}} C_{\mathrm{th}}}} \right) \tag{6.11}$$

where $\Delta T(t)$ is temperature variation with time, in K, ΔT_{ss} is the temperature gradient across the cable insulation layer at steady state in K, and $R_{\mathrm{th}} C_{\mathrm{th}}$ is thermal time constant, [4, 17, 18]:

$$\tau_{\mathrm{th}} = R_{\mathrm{th}} C_{\mathrm{th}} \tag{6.12}$$

Considering the most common insulating materials used at present for DC polymeric cables (e.g., XLPE, PP), the thermal time constant characterizing cable load variations is shorter than the dielectric time constant of electrical transients, i.e., $\tau_{\mathrm{th}} < \tau_{\mathrm{d}}$. As explained in detail in [4], the consequence is that the electric field distribution inside both the cavity and the dielectric after a load variation will be ruled only by the consequent conductivity variation. Consequently, and as a first approximation, when $\tau_{\mathrm{th}} < \tau_{\mathrm{d}}$, both E_0 and E_{DC} in Equation (6.6) can be calculated from Equation (6.8), that is, under steady state condition. The supply voltage amplitude, U_0, is considered constant during load variation from E_0 to E_{DC}, being load (ampacity) the unique cause of the field transient. Regarding the transient time constant in Equation (6.6), for the cooling condition when the load decreases, the transient time constant can be calculated from Equation (6.2) where τ_{d} refers to the maximum load value (thus higher conductivity and shorter dielectric time constant). On the other hand, for the heating condition, when the load rises, the thermal response is slower than that for cooling. Thus, the transient time constant for heating is longer and it can be approximated roughly as $2\tau_{\mathrm{d}}$ (which was verified also by COMSOL simulations), where τ_{d} is calculated from (2).

In some extreme conditions of low values of thermal conductivity, it can occur that the thermal constant reaches levels significantly higher than the dielectric time constant, i.e., $\tau_{\mathrm{d}} \ll \tau_{\mathrm{th}}$. In this case, the electric field might be driven not only by a change of conductivity with load, but also by permittivity, during the initial load variation transient. For this type of unusual conditions, the general model (6.6) applied to thermal transient can be valid for both heating (load rise) and cooling (load fall) conditions upon defining E_0 by an exponential model:

$$E_0 = E_{\mathrm{m}} + (E_{\mathrm{c}}(0^-) - E_{\mathrm{m}}) \cdot \exp\left(-\frac{t}{2\tau_{\mathrm{d}}}\right) \tag{6.13}$$

where $E_{\mathrm{c}}(0^-)$ is the electric field just before the beginning of load variations calculated from Equation (6.8). This converts Equation (6.6) into a double exponential equation, that provides both an increasing phase of the field inside cavity just after load variation, and then a decreasing trend till steady state [4].

E_{m} can be obtained by fitting models (6.6) and (6.13) to the simulated electric field by the numerical approach, and τ_{d} can be calculated from Equation (6.2).

6.2.4 Partial discharge inception field and repetition rate

To evaluate the partial discharge inception field, E_i, inside cavities embedded in insulation, we can refer to an approximate, deterministic expression proposed in [19] (for air in a spherical defect of diameter *d*):

$$E_{\mathrm{i}} = 25.2p\left(1 + \frac{8.6}{\sqrt{pd}}\right) \tag{6.14}$$

where p is the gas pressure inside the cavity. This holds approximately also for a cylindrical cavity, replacing d with cavity height, h_{c}, [2, 4, 5, 12, 20-22].

For voltage transient, the PD repetition rate as a function of time, $n(t)$, from beginning of voltage transient (cable energization/voltage polarity inversion), n_0, to DC steady state condition, n_{DC}, can be estimated roughly as:

$$n(t) = n_{\mathrm{DC}} + (n_0 - n_{\mathrm{DC}}) \cdot \exp\left(-\frac{t}{\tau_{\mathrm{rr}}}\right) \tag{6.15}$$

where n_{DC} corresponds to steady state condition and n_0 to the PD repetition rate in the initial instants of electric field variation, hence $n_0 = n(0^+)$. The transient time in Equation (6.15), may not coincide with the dielectric constant, because of various factors involved in PD phenomenology and physics that can vary with time, such as inception and residual field (see Equations (6.14) and (6.16)), memory effect due to space charge deposited by PD, modification of the medium and surface conditions in the discharging defect. Therefore, it is assumed τ_{rr} = C τ_{d}, being C an empirical constant value where 0.01<C<0.5. Indeed, experimentally values of C mostly

in the range 0.02 to 0.4 have been observed for the first case when $\frac{\varepsilon_{\mathrm{rb}}}{\varepsilon_{\mathrm{rc}}} > \frac{\gamma_{\mathrm{b}}}{\gamma_{\mathrm{c}}}$ (see later Figures 6.4 and 6.5.1), depending on the electric field behavior during transient. If, for example, the transient field has non-monotone behavior, as it can be seen later in Figure 6.2, PD can last a very short time.

PD repetition rate just after energizations or polarity inversions, n_0, in Equation (6.15) will be influenced by the slew rate of the applied voltage, and it can be roughly estimated by:

$$n_0 = \frac{1}{\Delta t} \cdot \left(\frac{|E_{\mathrm{c}}(\Delta t)| - E_{\mathrm{r}}}{E_{\mathrm{i}} - E_{\mathrm{r}}} \right) \tag{6.16}$$

where Δt is the time duration of the voltage variation from 0 to U_0 for energization or from U_0 to $-U_0$ (or vice versa) for polarity reversal, $E_{\mathrm{c}}(\Delta t)$ is the maximum value of the electric field inside the cavity at the beginning of the transient (see e.g., next Figure 2, E_{i} is the inception electric field from Equation (6.14) and E_{r} is the residual electric field inside cavity after extinguishing each PD event.

The DC PD repetition rate, n_{DC}, in Equation (6.15) under steady state DC condition can be defined and roughly approximated as [13]:

$$n_{\mathrm{DC}} = \frac{\gamma_{\mathrm{b}}\big(T(r,t), E(r,t)\big) \cdot h_{\mathrm{c}} + \gamma_{\mathrm{c}} \cdot h_{\mathrm{b}}}{\varepsilon_0 \cdot (\varepsilon_{\mathrm{rb}} \cdot h_{\mathrm{c}} + \varepsilon_{\mathrm{rc}} \cdot h_{\mathrm{b}}) \cdot \ln\left(\frac{|E_{\mathrm{c}}(t)| - E_{\mathrm{r}}}{|E_{\mathrm{c}}(t)| - E_{\mathrm{i}}} \right)} \tag{6.17}$$

It must be specified that Equations (6.15) and (6.17) hold till $|E_{\mathrm{c}}(t)| > E_{\mathrm{i}}$, that is when PD can incept inside cavity considering a deterministic approach. Also, it must be pointed out that Equations (6.15), (6.16) and (6.17) are again rough simplification of the reality, where a cavity may be not fully cylindrical, e.g., it can have non-negligible boundary effects, and PD can occur in different sections of the cavity surface (moreover, PD inception is stochastic rather that deterministic, as assumed in Equation (6.14)).

Regarding the thermal transient, when $\tau_{\mathrm{th}} < \tau_{\mathrm{d}}$ the electric field is mostly ruled by conductivity. This influences PD repetition rate, which is closer to that characteristic to steady-state DC, that is, significantly lower, than the repetition rate during voltage transients and AC, Equation (6.16) [4]. Thus, in this case, DC PC repetition rate from beginning of load variation to the steady state condition can be calculated using Equation (6.17).

The DC steady-state partial discharge inception voltage, $PDIV_{DC}$, can be estimated such as [5, 21, 22]:

$$PDIV_{DC} = E_i \left(h_c + \frac{\gamma_c}{\gamma_b\big(T(r,t), E(r,t)\big)} . h_b \right) \tag{6.18}$$

where $\gamma_b\big(T(r,t), E(r,t)\big)$ and E_i are obtained from Equations (6.1) and (6.14), respectively. It should be mentioned that the value of $PDIV_{DC}$ obtained from Equation (6.18) is the absolute value assumed to be constant for both positive and negative DC power supply.

Finally, AC partial discharge inception voltage, $PDIV_{AC}$, can be approximated as [5, 21, 22]:

$$PDIV_{AC} = E_i \left(h_c + \frac{\varepsilon_{rc}}{\varepsilon_{rb}} . h_b \right) \tag{6.19}$$

It is noteworthy that in the above expressions of τ_d, the repetition rates, as well as of $PDIV_{DC}$, will depend on load and, therefore, the temperature gradient in the insulation. This is accounted in the models considering the location of the defect in the insulation, and the relevant temperature.

6.3 Simulation of PD-occurrence likelihood

6.3.1 Modeling and simulation

Coupled thermal and electric field simulations were implemented through the 2D axisymmetric model in COMSOL Multiphysics, referring to the two-dimensional cable geometry of Figure 6.1 and insulating material parameters of Table 6.1. Using 2D axisymmetric model is the consequence of considering the cavity height for PD modelling, rather than cross section and surface [4]. Referring to Equation (6.14), since it is the height of a cylindrical cavity which plays the main role in determination of PD inception field [2, 4, 5, 12, 20-22], a rectangular geometry would be adequate to model the height of a cylindrical void in a 2D axisymmetric model.

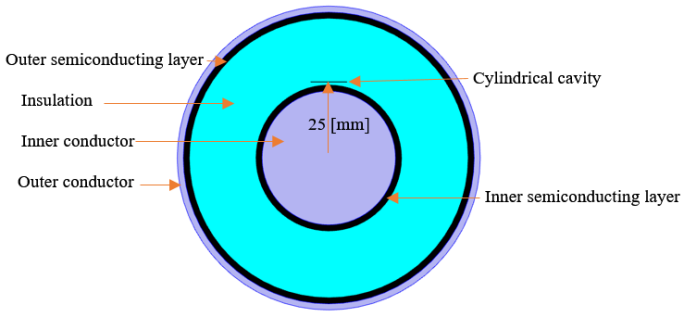

Figure 6.1. Cable geometry with cavity near the inner semicon.

Table 6.1. Geometry

Parameter		Radius [mm]
Inner conductor	r_i	22
Inner semiconducting layer	r_{insemi}	24
Insulation layer	r_{insul}	46
outer semiconducting layer	$r_{outsemi}$	48
Outer conductor	r_{outcon}	50
Cavity height	h_c	4, 7, 100 and 200 µm
Cavity cross section radius	r_c	6

Table 6.2. Insulating material properties

Parameter		Value
Heat capacity	C_P	1900 J/(kg.K)
Thermal conductivity	λ	0.38 W/(m.K)
Permittivity	ε_r	2.3
Reference electrical conductivity	γ_0	2E-17 [S/m]
Temperature dependency coefficient	α	0.1 [°C^{-1}]
Field dependency coefficient	β	0.03 [mm/kV]

To perform the simulations, a homogeneous cylindrical insulation layer is considered. The thermal and electrical properties of the implemented insulation material are parametrized in Table 6.2 [4, 8, 22].

Boundary conditions for thermal and electrical simulations, are parametrized in Table 6.3 [4, 23], assuming that the HVDC cable is surrounded by air and there is only convection heat transfer, while surface to ambient radiation (surface emissivity) in all directions is set to zero.

To mesh the model for both small and big cavity size, the sequence type and element size were set to physics-controlled mesh mode and extra fine, respectively.

Table 6.3. Boundary conditions for the HVDC cable

Parameter		Value
Nominal voltage	U_0	320 kV
Nominal load	I_0	1450 A
Voltage at outer conductor	φ_0	0 kV
Convection heat transfer coefficient	h	5 [W/(m^2.K)]
External temperature	T_{ext}	293.15 K

In this chapter a cylindrical cavity near the inner semiconductor (precisely at 1 mm from the inner semicon), Figure 6.1, is considered for the investigation. This is because, as proved in Chapter 5 or [4], the field inside a cavity near the inner conductor is always higher than that of a cavity of the same size near the outer semiconducting layer, and consequently, lower *PDIV* (thus, potentially more harmful). In addition, since the field is always driven by permittivity just after energizations, higher fields are expected in a cavity near the inner conductor also in those phases.

The effect of temperature dependence (α) and field-dependence coefficient (β) of electrical conductivity on PD activity are discussed in detail in Chapter 5 or [4], where it is shown that their high values (particularly α) lead to lower values of *PDIV* and higher PD repetition rate.

6.3.2 PD during electric field transient

In this section, the energization and voltage polarity reversal of a cable to 320 kV under full load is simulated, with a slew rate of 320 kV/min. The simulated electric field inside a cavity with two different heights (4 and 7 μm) are illustrated in Figure 6.2.

For both cavity heights, partial discharges can be incepted after energization and polarity reversals because the electric field in the cavity exceeds the PD inception field. Reaching the steady state field distribution, PD disappear after about 30 and 88 min for h_c = 4 and 7 μm, respectively,

since the field becomes lower than the DC steady-state inception field. Indeed, in these cases $PDIV_{DC}$ is higher than the nominal voltage (see right vertical axes in Figure 6.2). Longer duration of PD activity can also be noticed following a polarity reversal. Indeed, the simulated inversion event, PD disappear after about 72 and 128 min for h_c = 4 and 7 µm, respectively. This is due to non-zero value of $E_c(0^-)$ characterizing polarity reversals (contrary to energizations), which leads to a higher electric field inside the cavity, according to Equation (6.7) and longer duration of PD activity for this kind of events.

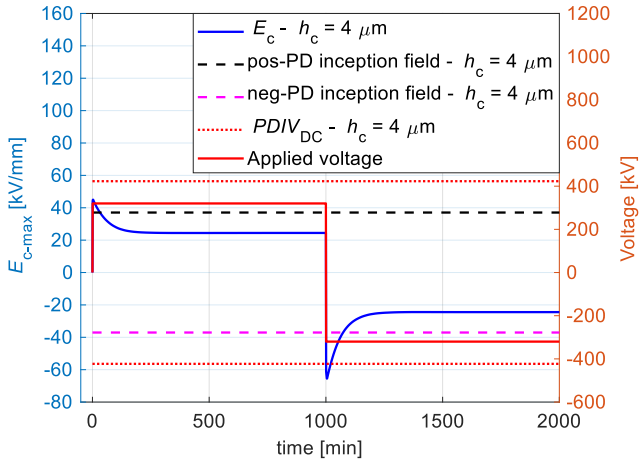

(a)

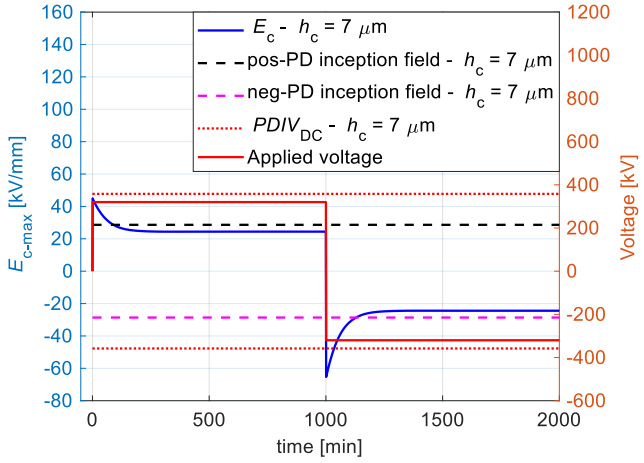

(b)

Figure 6.2. Simulated electric field variation inside a cavity during transient condition, after cable energization and voltage polarity reversal, to steady state DC condition as a function of time and cavity height, (a) h_c = 4 µm and (b) h_c = 7 µm, (T_0 = 0 °C, E_0 = 0 kV/mm in Equation (6.1)). PD inception field for two different cavity height values from Equation (6.14), dashed lines, applied voltage and $PDIV_{DC}$ from Equation (6.18) are also indicated.

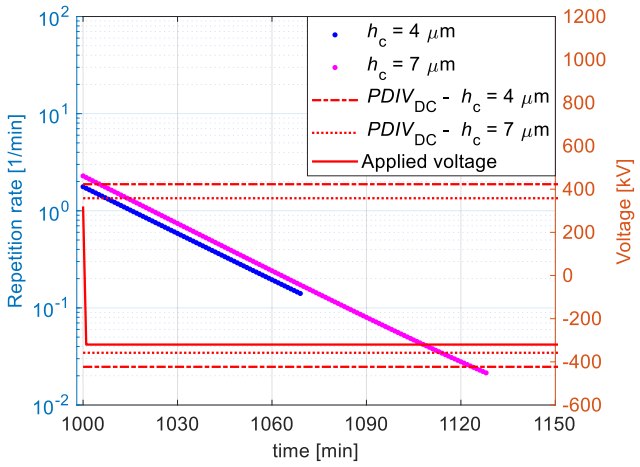

(a)

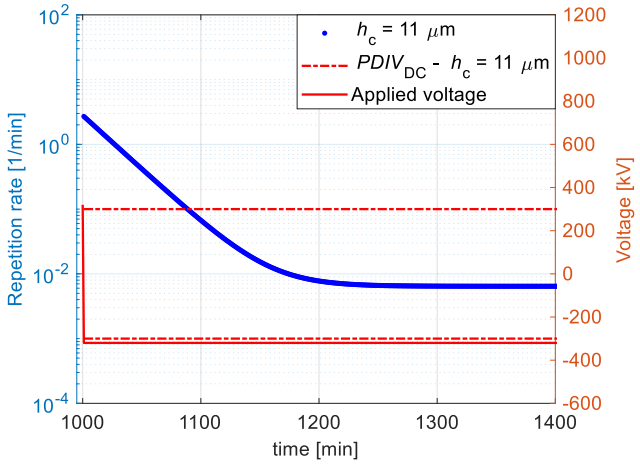

(b)

Figure 6.3. PD repetition rate as a function of time and cavity height following a polarity reversal, from Equations (6.15), (6.16), and (6.17), where E_r is ignored. Applied voltage and $PDIV_{DC}$ from Equation (6.18) are also indicated. In Figure 6.3a, curves stop at the time PD disappear, since the electric field in the cavity becomes lower than the inception field. (a) h_c = 4 and 7 μm, and (b) h_c = 11 μm.

PD repetition rate values obtained by Equation (6.15) for the cases of Figure 6.2 after polarity reversal are displayed in Figure 6.3a. Despite an almost equal electric field inside the cavity, a lower PD repetition rate is estimated inside cavities with smaller height for the considered cases. This can be explained by referring to the charging time constant of the equivalent circuit used to calculate PD repetition rate (see [13]), where smaller cavity height provides longer charging time constant, resulting in lower PD repetition rate.

In order to have DC PD also under DC steady state condition beside PD during electrical transient, the cavity height is increased to 11 μm, which provides lower $PDIV_{DC}$ < nominal voltage (see: Figure 6.3b). In this case, DC PD repetition rate under steady state would be around 6E-3 min^{-1} from Equation (6.17). It can be seen from Figure 6.3b that after about 235 min (which is $3.5\tau_d$ and $9\tau_{rr}$, thus $\tau_{rr} \approx 0.4\tau_d$ as mentioned above) the repetition rate tends to that expected from DC. It should be mentioned that to simplify these simulations and result representation and discussion (reducing the number of parameters), E_r has been neglected. Consideration higher values for E_r provides higher PD repetition rate values from Equations (6.15), (6.16) and (6.17).

Values close to those calculated by simulations (i.e., having the same order of magnitude) were obtained experimentally. The results are indicated in Figs. 6.4 and 6.5.1 and 6.5.2, which are taken from tests performed on multi-layer polypropylene specimens having a cylindrical cavity punctured on the middle layer (see [2]). Voltage was applied varying slew rate from 1 kV/s to 4 kV/s, up to values below or above $PDIV_{DC}$. PD measurement procedures for DC steady state and transient, including noise rejection and identification, are presented in [34].

The results are shown in Figures 6.4, 6.5.1 and 6.5.2 for the PD measurements during energization of a DC insulation system model (consisting of a multilayer specimen with internal cavities, typical of a laminated cable). Two different slew rate values are considered, with applied voltage < $PDIV_{DC}$ (Figure 6.4) and > $PDIV_{DC}$ (Figure 6.5). The cavity height values were 380 μm and 390 μm for Figures 6.4 and 6.5, respectively. As can be seen, models for PD magnitude and repetition rate are not far from experimental results, considering, especially for amplitude, that PD is a stochastic phenomenon. PD incept indeed around the $PDIV_{AC}$ during the transient, when the electric field in the cavity reaches the inception value E_i from Equation (6.14). Repetition rate (calculated by Equations (6.15), (6.16) and (6.17) fits to experiments quite well, both when PD do not occur in DC steady state (Figure 6.4) and when the $PDIV_{DC}$ is lower than applied voltage (thus PD are present in DC steady state): Figure 6.5.1. Note that, according to the field behavior shown in Figures 6.4c and 6.4d, the voltage rate of rise (slew rate) does not influence noticeably the electric field transient time, but it affects both initial PD charge amplitude (compare Figures 6.4a and 6.4b) and PD repetition rate (Figures 6.4c and 6.4d) just after electrical transient, when the field is driven by permittivity. Indeed, higher slew rate (e.g., 4 kV/s) results in lower PD charge amplitude (Figure 6.4b) as well as higher PD repetition rate (Figure 6.4d) just after energization.

Considering Figures 6.5.1c and 6.5.1d, in order to fit the repetition rate model to the experimental data under DC steady state condition, E_r was increased to $0.9E_i$. As a result, E_r has a nonzero value under DC steady state condition which cannot be ignored as already proved in [13].

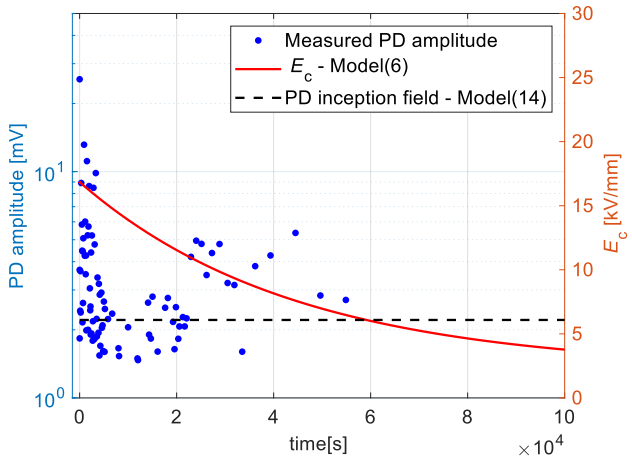

(a)

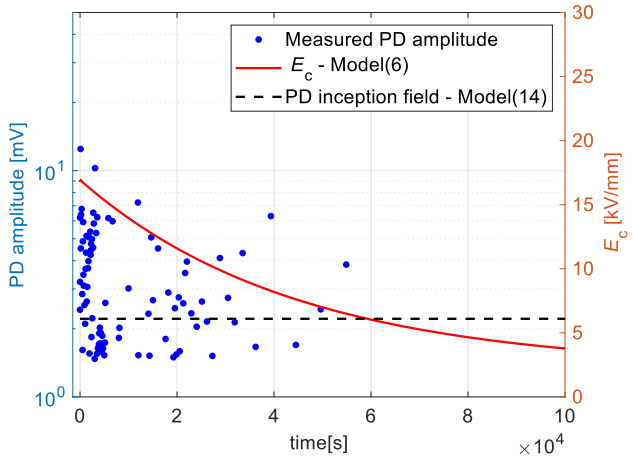

(b)

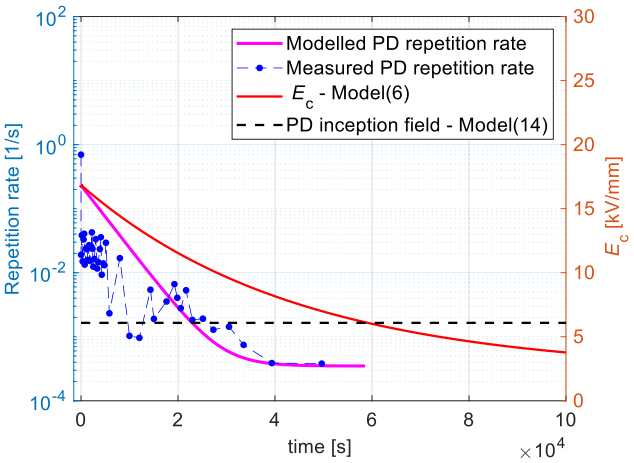

(c)

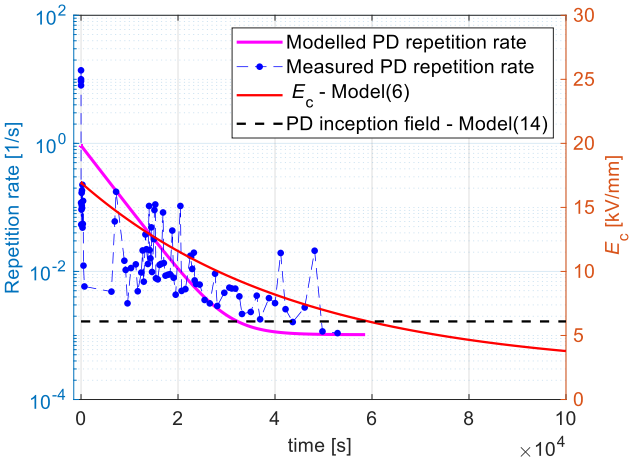

(d)

Figure 6.4. Experimental and modelling results (from Equations (6.15), (6.16) and (6.17)) where E_r is neglected. PD testing upon energization on an insulation object with an internal cavity. PD amplitude with slew rate (a) 1 kV/s and (b) 4 kV/s, PD repetition rate as a function of time during energization transient with slew rate (c) 1 kV/s and (d) 4 kV/s. DC voltage, from 0 to 12 kV < $PDIV_{DC}$), room temperature, $\tau_d \approx 4.42 \cdot 10^4$ s and $\tau_{rr} \approx 0.1\tau_d$. Electric field inside cavity from Equation (6.6) and inception field inside cavity from Equation (6.14) are also indicated.

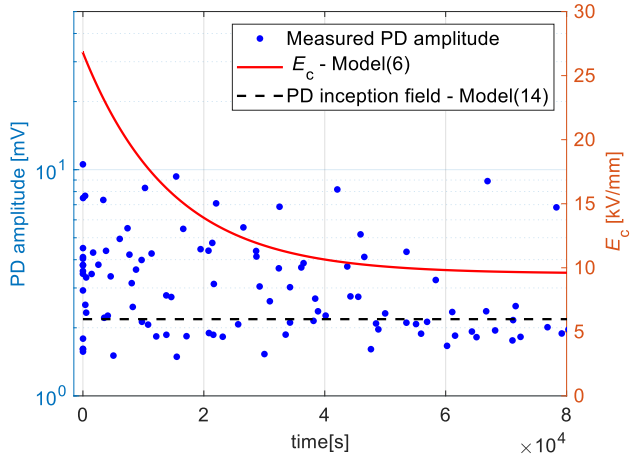
Measured PD amplitude
E_c - Model(6)
PD inception field - Model(14)
PD amplitude [mV]
E_c [kV/mm]
time[s]
$\times 10^4$

(a)

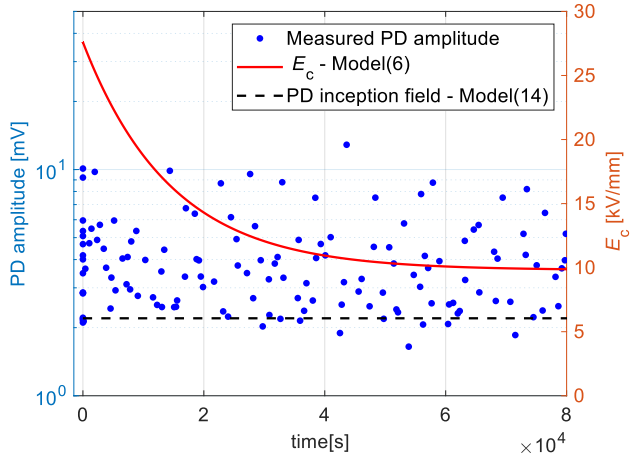
Measured PD amplitude
E_c - Model(6)
PD inception field - Model(14)
PD amplitude [mV]
E_c [kV/mm]
time[s]
$\times 10^4$

(b)

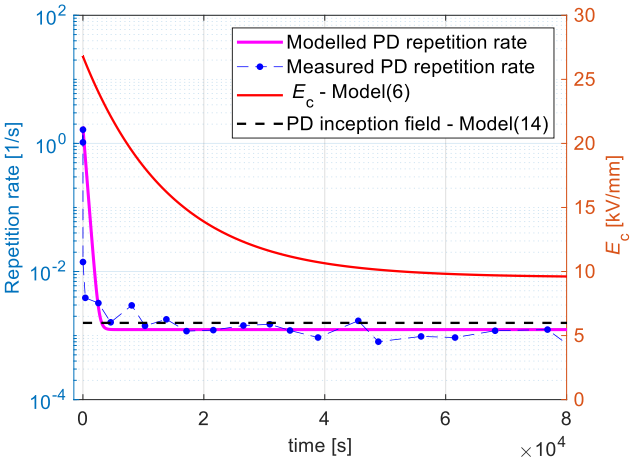
Modelled PD repetition rate
Measured PD repetition rate
E_c - Model(6)
PD inception field - Model(14)
Repetition rate [1/s]
E_c [kV/mm]
time [s]
$\times 10^4$

(c)

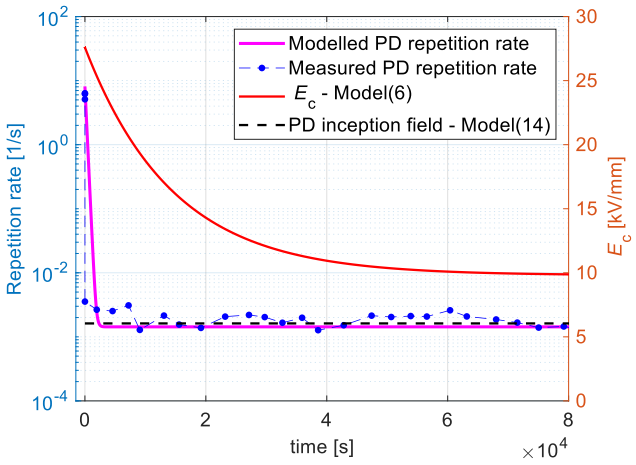

(d)

Figure 6.5.1. Experimental and modelling results (from Equations (6.15), (6.16) and (6.17)) where E_r = 0.9E_i according to [13]. PD testing upon energization till steady state for an insulation object with an internal cavity. PD amplitude with slew rate (a) 1 kV/s and (b) 4 kV/s, PD repetition rate as a function of time during energization transient with slew rate (c) 1 kV/s and (d) 4 kV/s till steady state condition. DC voltage, from 0 to 20 kV > $PDIV_{DC}$), room temperature, $\tau_d \approx 1.45 \cdot 10^4$ s and $\tau_{rr} \approx 0.02\tau_d$. Electric field inside cavity from Equation (6.6) and inception field inside cavity from Equation (6.14) are also indicated.

For the second case when $\frac{\varepsilon_{rb}}{\varepsilon_{rc}} < \frac{\gamma_b}{\gamma_c}$ and when slew rate is fast (e.g., 1 kV/s), since the initial PD repetition rate just after energization is smaller compare to the first case, instead of Equation (6.16), Equation (6.20) is introduced. This Equation can be obtained from Equation 5.15 upon replacing the dielectric time constant in Equation 5.15 with the charging circuit time constant (see: Appendix A). As a result, Equation (6.20) is introduced such as:

$$n_0 = \frac{\gamma_b \cdot h_c + \gamma_c \cdot h_b}{\varepsilon_0 \cdot (\varepsilon_{rb} \cdot h_c + \varepsilon_{rc} \cdot h_b)} \cdot \frac{2\pi \cdot E_c(t)}{(E_i - E_r)} \tag{6.20}$$

For the second case when $\frac{\varepsilon_{rb}}{\varepsilon_{rc}} < \frac{\gamma_b}{\gamma_c}$, the PD measurement after energization till steady state condition was performed for the material with high conductivity at 60°C. The measured conductivity of the material at the same temperature and field which PD measurement was done (60°C and 30 kV/mm) had been obtained equal to 4.21E-14 [S/m]. The applied step voltage was 20 kV with two different slew rate values including 0.05 kV/s and 1 kV/s. The estimated PDIV values were $PDIV_{AC}$ = 4.4 kV and $PDIV_{DC}$ = 2.7 kV. The measured PD charge amplitude and repetition rate are shown in Figures 6.5.2. The transient behavior of electric field inside cavity has

been modelled from (6.6). With regards to PD repetition rate when $\frac{\varepsilon_{rb}}{\varepsilon_{rc}} < \frac{\gamma_b}{\gamma_c}$, it has been modelled using Equations (6.16), (6.17) and (6.15) for slow slew rate e.g., 0.05 kV/s and Equations (6.20), (6.17) and (6.15) are used for fast slew rate e.g., 1 kV/s.

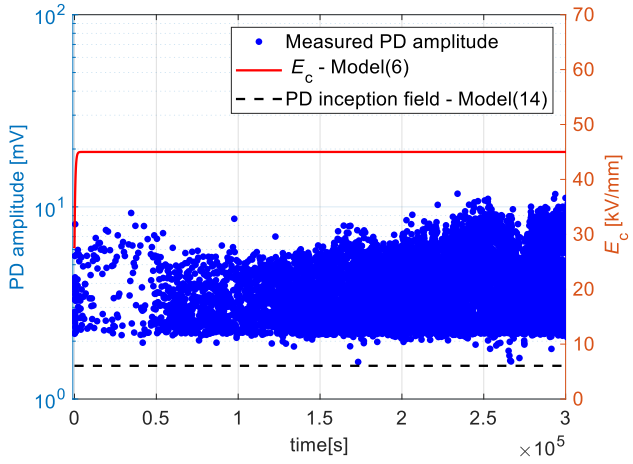

(a)

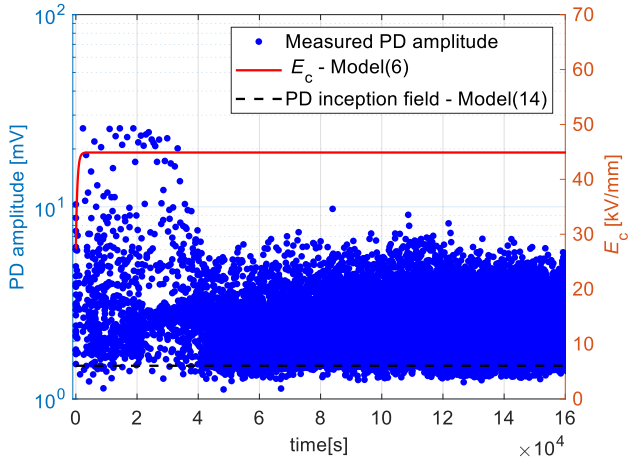

(b)

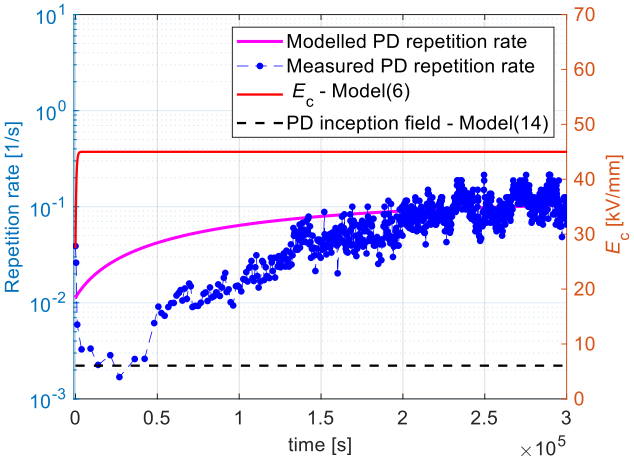

(c)

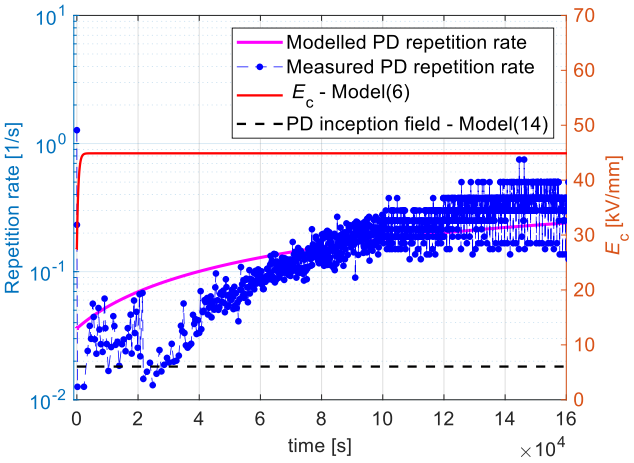

(d)

Figure 6.5.2. PD testing upon energization till steady state for an insulation object with an internal cavity. PD amplitude with slew rate (a) 0.05 kV/s and (b) 1 kV/s and experimental and modelled PD repetition rate with slew rate (c) 0.05 kV/s and (d) 1 kV/s. $E_r = 0$ in AC (Equations (6.16) for 0.05 kV/s and (6.20) for 1 kV/s). $E_r = 0.93E_i$ under DC for 0.05kV/s (Equation (6.17)) and $E_r = 0.98E_i$ under DC for 1kV/s (Equation (6.17)). DC voltage, from 0 to 20 kV which is more than both $PDIV_{AC}$ and $PDIV_{DC}$, at 60°C, $\tau_d \approx 483.5$ s and $\tau_{rr} \approx 300\tau_d$ for both slew rate values. Electric field inside cavity from Equation (6.6) and inception field inside cavity from Equation (6.14) are also indicated. The estimated PDIV values are $PDIV_{AC} = 4.4$ kV and $PDIV_{DC} = 2.7$ kV.

As can be seen for the second case ($\frac{\varepsilon_{rb}}{\varepsilon_{rc}} < \frac{\gamma_b}{\gamma_c}$) since the field enhancement factor under DC is higher than that in AC, the PD repetition rate increases after applying voltage with a time constant which is significantly higher than the first case ($\frac{\varepsilon_{rb}}{\varepsilon_{rc}} > \frac{\gamma_b}{\gamma_c}$) presented already in Figure 6.5.1.

The reason to ignore residual field to calculate initial PD repetition rate just after energization (thus Equation (6.20)) and consider it only under DC steady state (thus Equation (6.17)) was to have lower PD repetition rate just after energization to be fitted better to the experimental results. To recall, we already proved in Chapter 2 that residual voltage under AC is negligible compare to DC steady state. Here, we used this finding to fit the model to the measured data.

The comparison of PD charge amplitude and repetition rate just after energization for two different slew rate values shows that both PD charge amplitude and repetition rate is higher when slew rate is higher. Moreover, when slew rate is higher the PD repetition rate would be higher throughout all the transient comparing Figure 6.5.2c for 0.05 kV/s with 6.5.2d for 1 kV/s.

Considering Figures 6.4, 6.5.1 and 6.5.2, it is verified that the modelled results are in good agreement with the experimental results within an order of magnitude.

6.3.3 PD during thermal transient (load cycling)

Simulations are carried out for a cable loaded with 10% of its nominal current (I_0) that is energized with nominal voltage (U_0). After reaching its thermal and electrical steady state (Equations (6.2) and (6.12)), the cable is exposed to a periodic load cycling. The calculated electric fields for two different cavity heights are displayed in Figures 6.6a and 6.6b. The load rises from 145 A to 1450 A at t = 0, then it is decreased again from 1450 A to 145 A at t = 4000 [min] (with the rate of 1450 A/min).

As the first case, considering the insulating materials used at present for DC polymeric cables, the thermal time constant (τ_{th}) is shorter than the dielectric time constant (τ_d), therefore the thermal transient for conductivity variation is short enough that the field is driven by conductivity as in steady state DC (see: Figure 6.6a). This case is highlighted by Figure 6.6, where electric field variation inside cavity and PD repetition rate during a load cycle from 10% to full load are reported considering an insulation with parameters introduced in Tables 6.1 to 6.3. As shown in Figures 6.6a and b, PD are absent in steady state when the load is 10% because electric field inside cavity is lower than inception field, but they occur during transient as well as in steady state under full load when electric field reaches to a value higher than inception field. As can be seen in Figure 6.6b, PD repetition rate is comparable with the DC PD repetition rate under steady state condition as illustrated already in Figures 6.5.1c, 6.5.1d, 6.5.2c and 6.5.2d.

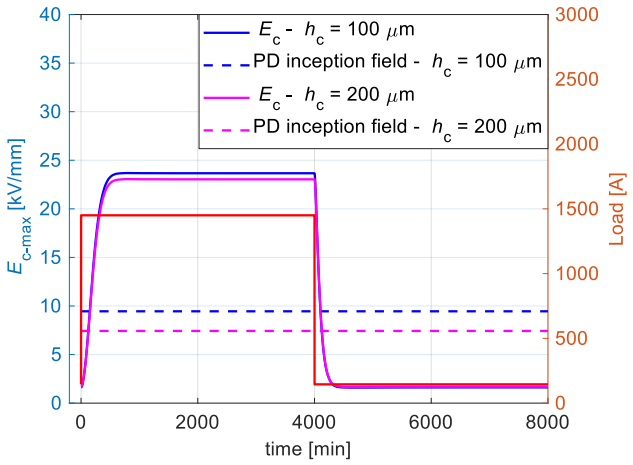

(a)

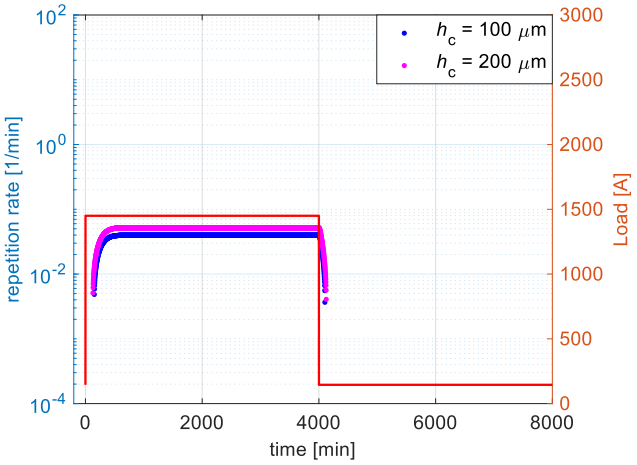

(b)

Figure 6.6. (a) Simulated electric field variation inside cavity from Equation (6.6) when $\tau_{th} < \tau_d$ during one load cycle as a function of time and cavity height. PD inception field for two different cavity height values from Equation (6.14) is indicated in Figure 6.6a, and (b) PD repetition rate as a function of load cycle and cavity height during thermal transient and steady state condition from Equation (6.17) where E_r is ignored. The load cycle is also indicated.

As the second case, to have PD with large repetition rate, as for electrical transients, thermal conductivity was reduced of about one order of magnitude, to 0.035 W/mK, keeping the other parameters as in Tables 6.1 to 6.3 [4]. As a result, since the thermal time constant is significantly longer than the dielectric time constant, electric field might be driven not only by a change of conductivity with load, but also by permittivity, during the initial load variation transients.

Fig. 6.7a indicates that a load variation (especially decrease) can lead to a permittivity-driven field distribution, and, consequently, introduce high probability of PD inception inside defects even during thermal transients, for both considered cavity heights. Here the value of h_c is changed from the case of electrical transient to provide a condition to have only PD during thermal transient and not under steady state condition after reduction of thermal conductivity to 0.035 W/mK. Hence, conditions can exist where PD can incept either during a thermal transient and in steady state, or only during a transient or, of course, not at all. This depends on the electrical and thermal properties of the dielectric, cavity size, the design field and temperature rating, thus on load.

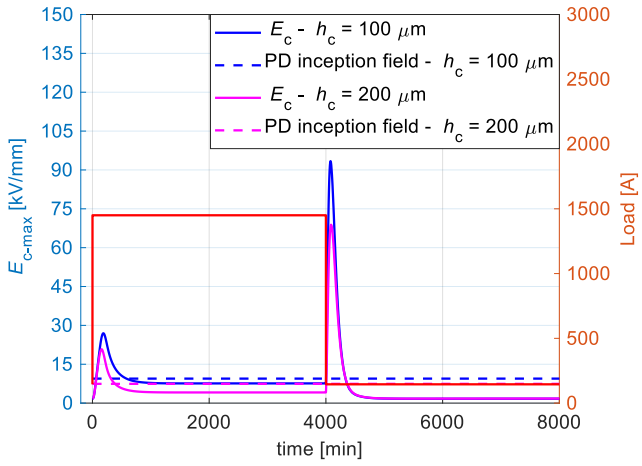

(a)

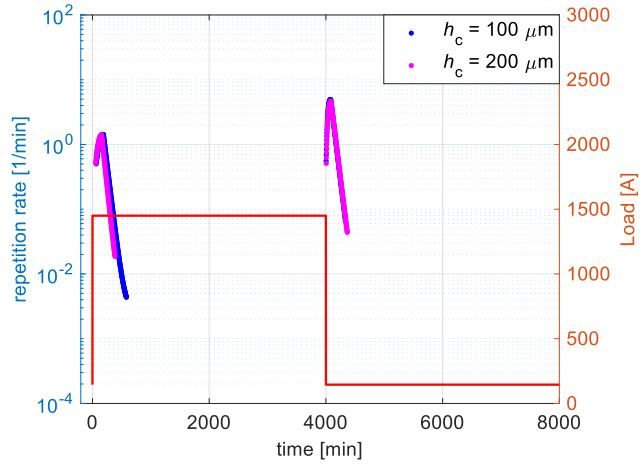

(b)

Figure 6.7. (a) Simulated electric field variation inside cavity from Equations (6.6) and (6.13) when $\tau_d \ll \tau_{th}$ during one load cycle as a function of time and cavity height. PD inception field for two different cavity height values from

Equation (6.14) is indicated in Figure 6.7a, and (b) PD repetition rate as a function of load cycle and cavity height during thermal transient and steady state condition, from Equations (6.15), (6.16), and (6.17), where E_r is ignored. The load cycle is also indicated.

Figure 6.7b shows the repetition rate for cavity heights of 100 and 200 μm, supporting the PD repetition rate behavior discussed above for voltage transients. It is interesting to note, from Figures 6.7a and b, that the electric field enhancement and PD repetition is higher during the load reduction. This can be addressed to a faster dielectric response for the cooling phase, in comparison with the dielectric response for heating, since much lower values of conductivity are to be expected, due to the higher average temperatures.

6.3.4 Evaluation of aging associated to partial discharges

The effect of PD amplitude and repetition rate in both transient and steady state on insulation can be analyzed quantitatively and quantitatively through the cumulative damage concept proposed in [2].

The amount of charge involved in a single PD is directly proportional to the field across the cavity immediately before the PD event, related to the inception field E_i defined in Equation (6.14). Average charge can then be roughly estimated as [13]:

$$\overline{q_i} = C_b \cdot (E_i - E_r) \cdot h_c \tag{6.20}$$

The number of PD events, N_{PD}, can be calculated multiplying the average PD repetition rate, $\bar{n}(t)$, obtained from Equations (6.15) -(6.17) depending on the type of perturbation considered, by the mean time during which PD occur (during electrical or thermal transients), t_{PD}, such as:

$$N_{PD} = t_{PD} \cdot \bar{n}(t) \tag{6.21}$$

Damage can be considered as the disruption of polymer bonds (e.g., C-H bonds) and growth of local degradation in the form of a semiconductive pit. The cumulative damage due to partial discharges in DC steady state or following a single transient event can be estimated roughly by [2, 24, 25]:

$$D_s = N_e \cdot F_{eff} \int_0^1 F_{hot,i} \cdot p_i \, dF_{hot,i} \tag{6.22}$$

where N_e is the number of electrons impinging the cavity wall during the time under consideration. This number can be approximated by:

$$N_e = N_{PD} \cdot \frac{\bar{q}_i}{q_e} \tag{6.23}$$

being q_e the charge of a single electron ($1.6 \cdot 10^{-19} C$). F_{hot} is a coefficient accounting for the probability that an electron involved in a PD with a certain amplitude is exceeding an energy level energy, e.g. 8 eV, able to cause permanent and irreversible degradation (8 eV is a minimum amount of energy able to break trigger a dissociative electron attachment, DEA, for C-H bonds [24]). Estimates of F_{hot} can be obtained e.g by Figure 6.8 (valid for PE materials) once the inception field is known. Being E_i a parameter mostly linked to the geometrical properties of the cavity, referring to Equation (6.14), as an approximation F_{hot} can be considered as an average constant, being $\widetilde{F_{hot}} = 0.66$ for cavities of height 4 μm, and $\widetilde{F_{hot}} = 0.26$ for cavities of height 200 μm.

F_{eff} is the fraction of effective hot electrons contributing to DEA, which has to be considered; for Polyethylene, PE, a mean value of 0.1 can be considered, according to [25, 26].

p_i is the probability distribution of PD amplitudes detected during the transient, here approximated by a delta distribution of expected value $\bar{q}_i$.

The definition of D_s can be then roughly simplified to:

$$\widetilde{D_s} = t_{PD} \cdot \bar{n}(t) \cdot \frac{\bar{q}_i}{q_e} \cdot F_{eff} \cdot \widetilde{F_{hot}} \tag{6.24}$$

Tables 6.4 and 6.5 report the values of PD charge amplitude, the number of PD and equivalent damage relevant to Figures 6.6b and 6.7b, respectively, based on the calculations performed from Equations (6.20) -(6.24). In these two tables, the PD activity time is reported in two ways. First, using a simplified analytical approach when it is assumed $t_{PD} = 0.7\tau_d$, and a second method, using a numerical approach, from which PD activity time is obtained directly from the simulations.

It is assumed that there is a voltage transient (polarity inversion) each 300 [min] at constant nominal load, for cavity heights of 4 and 7 μm (Table 6.4) and there is a load cycle as indicated in Figure 6.7 at constant nominal voltage, for cavity heights of 100 and 200 μm (Table 6.5). The values are calculated for one electrical transient period equal to 300 [min] (Table 6.4) and one load cycle period equal to 8000 [min] (Table 6.5).

As it is expected, the damage caused by PD is higher for a bigger cavity, for both electrical and thermal transients. Table 6.4 shows results for the case of the polarity inversion discussed in the previous section. The simplified approach provides constant PD activity time for both considered cavity height values, while using simulations to estimate values of t_{PD} gives a longer PD activity time and number, for larger cavities. As a result, while the obtained damage is always increased in the presence of a bigger cavity, this is less evident under a simplified approach.

Table 6.5 shows results obtained considering the thermal transients described above. Although both approaches result in higher damage for larger cavity heights, it should be noted that according to simulations, PD activity time, as well as their number is higher in smaller cavities (see Figure 6.7a). For this kind of transients, an increased damage is expected with increased cavity size. Contrary to before, in this case the simplified approach is forecasting a much bigger influence of this factor, compared to results from simulations.

As a note, in the above considerations, it has been assumed that PD charge magnitude does not change, at the same cavity field, whether under AC or DC, as speculated in [13].

Let us see in the next section which are the implications of the discrepancies highlighted above, when modelling insulation life using those two different approaches.

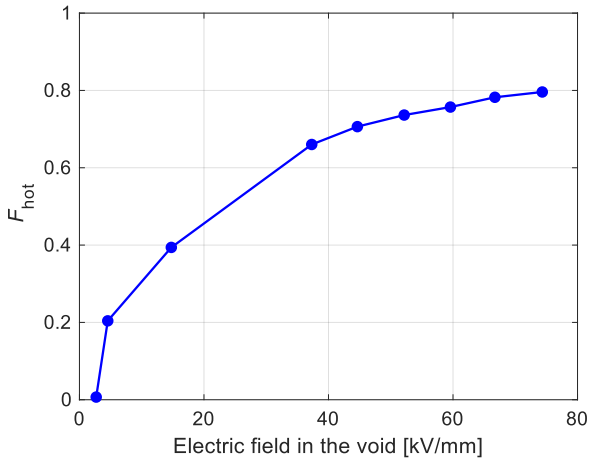

Figure 6.8. Fraction electrons with energy values > 8 eV (hot electrons) striking polymer surface as a function of electric field inside a void embedded in a polyethylene (PE) dielectric. *After [2, 25]*.

Table 6.4. Values of PD charge amplitude, number of PD and equivalent damage relevant to Figure 6.3 (electrical transient) – polarity inversion each 300 [min]

	Simulations		Simplified Approach	
PD characteristics	h_c = 4 [μm]	h_c = 7 [μm]	h_c = 4 [μm]	h_c = 7 [μm]
Charge amplitude [pC]	15.5	21	15.5	21
Number	275	445	190	173
t_{PD}	72.3	128.4	50	50
$\widetilde{F_{hot}}$	0.66	0.56	0.66	0.56
Damage	1.75E9	3.26E9	1.21E9	1.27E9

Table 6.5. Values of PD charge amplitude, number of PD and equivalent damage relevant to Figure 6.5 (thermal transient)

	Simulations		Simplified Approach	
PD characteristics	h_c = 100 [μm]	h_c = 200 [μm]	h_c = 100 [μm]	h_c = 200 [μm]
Charge amplitude [pC]	99.4	157	99.4	157
Number	9.3E3	9.15E3	4.2E3	5.7E3
t_{PD}	1856	1514	834.4	943.5
$\widetilde{F_{hot}}$	0.29	0.26	0.29	0.26
Damage	1.72E11	2.31E11	7.71E10	1.44E11

6.4 Effect on life and design practice

In this section, an approach to estimate the lifetime in the presence of partial discharges caused by periodic voltage polarity inversions (electrical transient) or load cycling (thermal transient) is presented. Considerations on the impact of the above on design field at specified life and failure probability are also proposed.

The inverse power law is generally used to describe life and aging rate [28-30]:

$$L = t_0 \left(\frac{E}{ES_0}\right)^{-n} \tag{6.25}$$

being ES_0 the reference electric field (often close to the electric strength value) and t_0 the failure time at $E = ES_0$, while n is the voltage endurance coefficient (VEC). Equation (6.25) provides a straight lifeline in log-log coordinate system ($\log(E)$ vs $\log(L)$). The design field, E_D, can be estimated from lifelines at given temperatures once the design life, L_D, is specified, $L = L_D$, and a failure probability chosen. It should be mentioned that values of n for a typical HV cable insulation

for DC application can range between 15 and 20 at the operating temperature, while in the presence of AC PD during electrical transient condition or DC PD during thermal transient and under steady state DC condition the value of n can drop to e.g., $n = 10$ or even lower e.g., 5, depending on material. Hence, in the case of AC PD and DC PD affecting cable life can be written, from Equation (6.25), as [2]:

$$L_{\mathrm{PD}} = t_0 \left(\frac{E}{ES_0}\right)^{-n_{\mathrm{PD}}} \tag{6.26}$$

It is assumed that presence of PD does not influence t_0, while electric strength in the presence of AC PD ($ES_{0,\mathrm{ACPD}}$) or DC PD ($ES_{0,\mathrm{DCPD}}$) are lower than electric strength when there are no partial discharges, i.e. ($ES_{0,\mathrm{ACPD}} < ES_{0,\mathrm{DCPD}} < ES_{0,\mathrm{AC}} < ES_{0,\mathrm{DC}}$). According to the measurement results, it was roughly assumed that $ES_{0,\mathrm{DCPD}} = 1.5 \cdot ES_{0,\mathrm{ACPD}}$ and $ES_{0,\mathrm{DC}} = 1.5 \cdot ES_{0,\mathrm{AC}}$.

The inherent assumption is that PD activity accelerates aging because $n_{\mathrm{PD}} < n$. The lifetime estimation in the presence of AC PD resulted from voltage transients and DC PD caused by load variations can be performed by using an aging model, resorting to a simple superposition effect, based on the Miner law [2, 3, 28, 31, 32].

If, for example, t_1 is the part of lifetime when there is normal operation without PD activity, t_2 and t_3 are the parts of life during which there are AC PD and DC PC activity, (due to transients) life can be described by [3]:

$$\frac{t_1}{L_1} + \frac{t_2}{L_2} + \frac{t_3}{L_3} = 1 \tag{6.27}$$

where L_1 is provided by Equation (6.25) and L_2, L_3 are given by Equation (6.26). Knowing the life models, $t_1 + t_2 + t_3$, which is insulation life, L, can be calculated.

The number of voltage or load transients per unit time (e.g., h^{-1}), defined as transient rate, is introduced by λ. From the simulation, the time intervals in each polarity inversion or load cycling period, λ^{-1}, in which there is AC PD, t_{ACPD}, DC PD, t_{DCPD}, and no PD activity, t_{n}, can be obtained, i.e., $t_{\mathrm{ACPD}} + t_{\mathrm{DCPD}} + t_{\mathrm{n}} = \lambda^{-1}$.

Considering the above-obtained time intervals from the simulation and based on the Miner law Equation (6.27), when there are periodic voltage polarity inversions or load cycling with a known

transient rate, thus only when $\lambda \neq 0$, the lifetime estimation, under superposition effect of no PD in steady state, AC PD during transients and DC PD during load variations, can be obtained as [3]:

$$L_\lambda = \frac{\lambda^{-1}}{\frac{t_\mathrm{n}}{t_0}\left(\frac{E}{ES_0}\right)^n + \frac{t_\mathrm{ACPD}}{t_0}\left(\frac{E}{ES_{0,\mathrm{ACPD}}}\right)^{n_\mathrm{ACPD}} + \frac{t_\mathrm{DCPD}}{t_0}\left(\frac{E}{ES_{0,\mathrm{DCPD}}}\right)^{n_\mathrm{DCPD}}} \tag{6.28}$$

Assuming, as an example, $t_0 = 1\ h$, $ES_0 = 140\ kV/mm$ with failure probability 5%, values for $ES_{0,\mathrm{ACPD}}$ and $ES_{0,\mathrm{DCPD}}$ 80 and 120 kV/mm, respectively (reference is made to a short cable, i.e. a lab specimen), $n = 18$ in the absence of PD (steady-state), $n_\mathrm{ACPD} = 8$, $n_\mathrm{DCPD} = 10$, the life lines of Figures 6.9 and 6.10 are obtained (according to Equations (6.25) to (6.28)). It is noteworthy that, in principle, since the VEC is related to the activation energy of the degradation process, as long as PD are the main cause of degradation the VEC for PD in DC and AC would be the same. Here we assume that there is a slight difference considering that the VEC in AC (no PD) is well lower than the VEC in DC (no PD).

Also, it must be highlighted that t_ACPD and t_DCPD are characteristic of the test or design level of voltage and field, thus Equation (6.28) cannot be used from extrapolation as Equation (6.25).

The parameters of Figure 6.2 and Tables 6.1, 6.3, and cavity geometries described earlier are considered for electrical and thermal transients.

Various values of polarity reversal rates, λ, were considered (e.g., $\lambda = 0$ in the absence of transients, $\lambda = 0.04\ h^{-1}$ as about one transient per day, and $\lambda = 0.2\ h^{-1}$ corresponding to one transient every 5h). Load cycling was also considered, with the rate of $\lambda = 7.5E-3\ h^{-1}$ as the load cycle indicated in Figures 6.6 and 6.7 which is repeated periodically each 8000 [min].

With both the analytical and the simplified approach, time constants in Equation (6.28) including t_n, t_ACPD and t_DCPD are to be determined for different applied voltages or load changes. Those values can be immediately obtained from a numerical approach, running a high number of simulations, and analyzing their results.

On the other hand, a simplified alternative can be considered. If the voltage to be reversed is exceeding the value of $PDIV_\mathrm{AC}$ calculated from Equation (6.19), then the duration of t_ACPD can be estimated roughly such as $t_\mathrm{ACPD} \approx 0.7\tau_\mathrm{d}$, calculating the dielectric time constant, τ_d from Equation (6.2).

t_{DCPD} can be approximated considering the value of $PDIV_{\mathrm{DC}}$ from Equation (6.18). If the applied voltage is lower than this inception voltage, no PD are expected at stability, and it can be considered $t_{\mathrm{DCPD}} = 0$, while $t_{\mathrm{n}} = \lambda^{-1} - t_{\mathrm{ACPD}}$. On the other hand, if the applied voltage is higher than $PDIV_{\mathrm{DC}}$, PD under steady state conditions are to be expected, and therefore it can be said that $t_{\mathrm{DCPD}} = \lambda^{-1} - t_{\mathrm{ACPD}}$, while $t_{\mathrm{n}} = 0$.

Both procedures were used to plot the lifelines in Figures 6.9 and 6.10. As can be seen from Figure 6.9 which shows the effect of electrical transient (polarity inversion) on the estimated life for h_{c} = 7 μm, increasing voltage transient rate the design electric field (E_{D}) for specified life, e.g., 30 years, decreases significantly, see also Table 6.6. As an example, when $\lambda = 0.2\ h^{-1}$ the design field becomes about 30% of the value calculated for DC steady-state.

Results on polarity inversions show that the simplified method can result in slightly higher (about 1.2 times) design fields for the specified life e.g., 30 years. This is mostly due to the discrepancies on the estimation of t_{ACPD} for different applied voltages. Assuming $t_{\mathrm{ACPD}} \approx 0.7\tau_{\mathrm{d}}$ will give shorter values for t_{ACPD} at higher fields, compared to values obtained from simulations. This significantly influences life, leading to a higher life estimation for high levels of stress, when the simplified approach is used. Finally, as can be speculated from Table 6.6, it is noteworthy that the design field does not change significantly varying cavity size, because the maximum field in insulation does not vary noticeably.

Considering Figure 6.7, when there is a load cycle with period of $\lambda^{-1} = 133.3\ h$ (equivalent to 8000 [min], i.e., $\lambda = 7.5E-3\ h^{-1}$) the lifelines are calculated from Equation (6.28) and reported in Figure 6.10 for h_{c}=100 μm (they do not different significantly for h_{c}=200 μm for the reason mentioned above). Considering different electric fields to obtain enough points to provide more precise lifelines as electrical transient, the obtained lifelines using the simplified as well as the numerical approaches are illustrated in Figure 6.10.

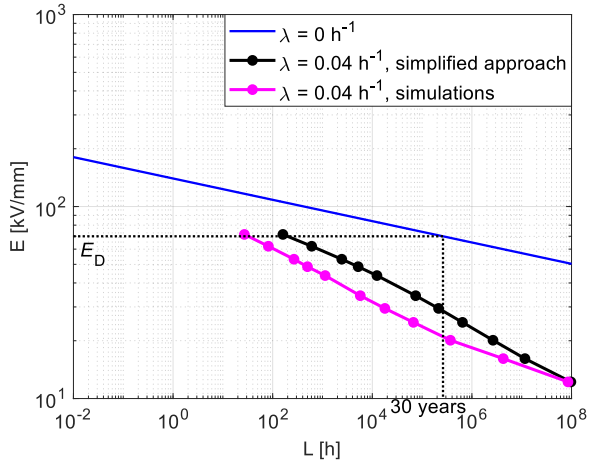

(a)

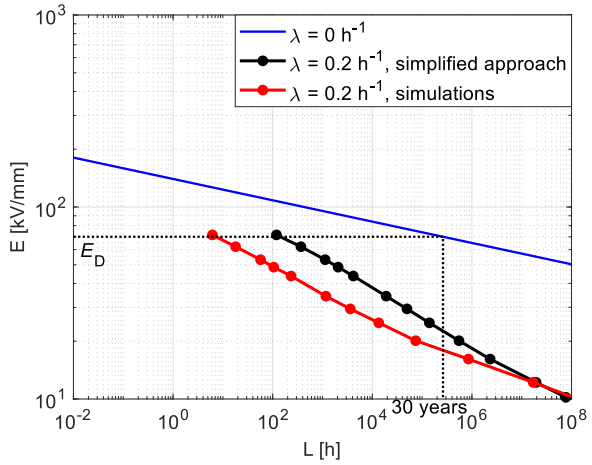

(b)

Figure 6.9. Lifelines without polarity inversion ($\lambda = 0\ h^{-1}$) from model (6.25) and with polarity inversion when (a) ($\lambda = 0.04\ h^{-1}$), and (b) ($\lambda = 0.2\ h^{-1}$) from model (6.28). The lifelines based on the assumption of $t_{ACPD} = 0.7\tau_d$ and when the time constants in Equation (6.28) are obtained directly by simulation for cavity height value equal to $h_c = 7$ μm are illustrated. The values of voltage endurance coefficients are $n_{ACPD} = 8$, $n_{DCPD} = 10$ and $n = 18$. The design field for a life of 30 years (failure probability 5%) for DC steady-state are also indicated.

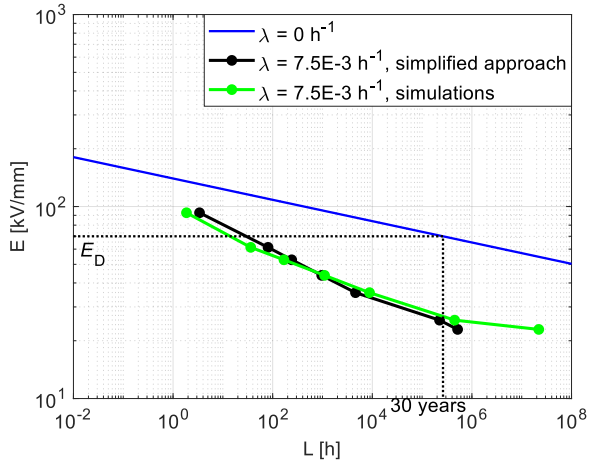

Figure 6.10. Lifelines without thermal transient ($\lambda = 0\ h^{-1}$) from model (6.25) and with thermal transient for the load cycle of Figure 6.7 (from model (6.28)). The lifelines based on the assumption of $t_{ACPD} = 0.7\tau_d$ as well as when the time constants in Equation (6.28) are obtained directly by simulation are illustrated. The values of voltage endurance coefficients are $n_{ACPD} = 8$, $n_{DCPD} = 10$ and $n = 18$. The design field for a life of 30 years (failure probability 5%) for DC steady-state are also indicated. The reference life for DC steady state is the same as that in Figure 6.9.

It can be seen from Figure 6.10 that PD inception due to load variation reduces the expected life at constant design electric field significantly, compared with the case when there is no load variation. For a specified life e.g., 30 years with failure probability 5%, a reduction of design electric field comparable with that estimated for voltage variation is obtained, see Table 6.7. Moreover, since the maximum field in insulation does not change, the design field does not change considerably varying cavity size.

Considering Figure 6.10 and comparing the obtained design electric fields using the two approaches (Table 6.7), it can be speculated that the simplified approach can be in good accordance with the numerical alternative, in the case of thermal transients. In addition, the simplified approach tends to be slightly more conservative in life estimation. However, stronger differences can be observed at lower fields. This is due to t_{ACPD} being suddenly reduced significantly due to the lower applied voltages, while the estimation of the simplified approach is much less influenced by voltage values.

Eventually, Table 6.8 reports design field values for cavity heights of 100 and 200 μm, using the numerical approach, when load transients occur with rate $\lambda = 7.5E\text{-}3\ [h^{-1}]$, but with the insulation and cable parameters of Tables 6.2 and 6.3 (referring to Figure 6.6). In this case $\tau_d > \tau_{th}$, thus

electric field is only ruled by changes of electrical conductivity due to thermal dynamics as shown in Figure 6.6. Therefore, there is not any distributed electric field by permittivity after load variation and $t_{\mathrm{ACPD}} = 0$. DC PD occur both during transients and in steady state, but with very low repetition rate (with mean value of about 0.11 and 0.15 [1/min] for h_c = 100 and 200 μm, respectively, obtained from Equation (6.17) with the assumption of $E_r = 0.72E_i$, after [13]) being the field driven by the variation of conductivity both during transient and steady states. The model of (6.28) is used, with $n = 18$ and $n_{\mathrm{DCPD}} = 10$, to estimate the design field. The simulations were performed under different applying voltages to find enough points to do lifetime estimation by (6.28). For instance, under nominal voltage, the value of t_{DCPD} obtained by simulation of one load cycle (i.e., 8000 [min]) is 3898 and 3970 [min] for h_c = 100 and 200 μm, respectively. As can be seen from Tables 6.7 and 6.8, the design field is significantly lower than the case where no load transients are expected. This is particularly evident when field distribution following a load transient is initially driven by permittivity (Table 6.7).

According to the presented damage (section 3) and life reduction (section 4) caused by partial discharges originated from voltage polarity inversion as well as thermal transient (load cycling), an appropriate design must consider this additional source of aging, trying to reduce its extent. Thus, in presence of cavities embedded in insulation, the design field must be more conservative which means lower design field should be employed for the insulation design.

Considering Figures 6.9 and 6.10, the appropriate design electric field (E_D) for the expected transient rate or load cycling at specified life (e.g., 30 years, with failure probability 5%) is derived using both a simplified and a numerical approach, after performing simulations under different electric fields to obtain the time constants to be used in Equation (6.28), for different electric field values. Results are reported in Tables 6.7 and 6.8.

Regarding Tables 6.6 and 6.7, despite there are different electrical and thermal transient rates as well as cavity height values, it can be speculated from the comparison of the obtained design fields in the presence of PD during electrical and thermal transients when the electric field is driven by permittivity, rather than conductivity, that there is not significant difference between them. The reason for this is that presence of cavity inside insulation and PD during electrical and thermal transient does not affect the field in dielectric while it leads to decrease of voltage endurance

coefficient (VEC) as a result of microscopic effect of PD inside cavity on life reduction of DC insulation.

Table 6.6. Derived design electric field for L_D = 30 years from Figure 6.9 with and without periodic polarity inversion.

E_D [kV/mm] Simplified approach	E_D [kV/mm] Numerical approach	λ [h^{-1}]	h_c [μm]
70	70	0	4
28	24	0.04	4
23	20	0.2	4
70	70	0	7
27.7	21	0.04	7
22.5	18	0.2	7

Table 6.7. Derived design electric field for L_D = 30 years from Figure 6.10 with periodic load cycling with rate of λ = 7.5E-3 [h^{-1}]

E_D [kV/mm] Simplified approach	E_D [kV/mm] Numerical approach	h_c [μm]
25.2	29.8	100
24.2	27	200

Table 6.8. Derived design electric field for L_D = 30 years with periodic load cycling with rate of λ = 7.5E-3 [h^{-1}] and the parameters of Tables 6.2, 6.3 (only DC PD)

E_D [kV/mm] Numerical approach	h_c [μm]
37	100
34.5	200

6.5 Conclusions

It is clear, based on the simulations and results presented in this chapter, that repetitive cable voltage polarity inversions, as well as repetitive load variations, can likely cause accelerated aging of DC insulation systems in the presence of defect with large enough size (and properly located along insulation diameter) able to incept PD.

Even if the maximum PD damaging effect occurs mostly during the first stage after the beginning of an electrical transient, and has short time duration, the amount of damage can be significant

enough to cause non-negligible life reduction, depending on the repetition rate of transients. Some contribution to reliability reduction, even if smaller due to the lower PD repetition rate, can be brought also by PD incepted during load cycling.

Therefore, even if cable insulation design is made properly to avoid DC PD in steady state, at any operating temperature, electrical and thermal transients can be harmful for insulation life. They cannot be avoided during operation, especially if cables are interconnected, they are fed by LCC and, possibly, used in hybrid networks. Therefore, problems can be faced only downgrading design field, or, better, improving cable manufacturing technology, in order to avoid defects or reduce their size below the $PDIV_{AC}$, and devising materials that have better resistance (thus higher VEC) to PD.

References

[1] F.H. Kreuger, *Industrial High DC Voltage: 1. Fields 2. Breakdowns 3. Tests*, Delft University Press, 1995.

[2] G.C. Montanari, P. Seri, S.F. Bononi and M. Albertini, "Partial discharge behavior and accelerated aging upon repetitive DC cable energization and voltage supply polarity inversion," IEEE Trans. on Power Delivery, pp. 1-8, 2020.

[3] G.C. Montanari, R. Hebner, P. Morshuis and P. Seri, "An approach to insulation condition monitoring and life assessment in emerging electrical environments," IEEE Trans. on Power Delivery, vol. 34, n. 4, pp. 1357-1364, October 2019.

[4] H. Naderiallaf, P. Seri and G.C. Montanari, "Investigating conditions for an unexpected additional source of partial discharges in DC cables: load power variations," IEEE Trans. on Power Delivery, pp. 1-8, April 2020.

[5] G.C. Montanari, Paolo Seri, and Hadi Naderiallaf, "A contribution to everlasting electrical insulation for DC voltage: PD-phobic materials," IEEE Access, Feb. 2020.

[6] L.A. Dissado and J.C. Fothergill, *Electrical Degradation and Breakdown in Polymers*. P. Peregrinus press, 1992.

[7] M. Marzinotto and G. Mazzanti, "The statistical enlargement law for HVDC cable lines. Part 1: theory and application to enlargement in length," IEEE Trans. Dielectr. Electr. Insul., vol. 22, no 1, pp. 192-201, Feb. 2015.

[8] R. Bodega, G.C. Montanari, and P. H. F. Morshuis, "Conduction current measurements on XLPE and EPR insulation," In The 17th Annual Meeting of the IEEE Lasers and Electro-Optics Society (LEOS), 2004, pp. 101-105.

[9] G. Mazzanti and M. Marzinotto, *Extruded Cables for High Voltage Direct Current Transmission: Advance in Research and Development*, Power Engineering Series, Wiley-IEEE Press, 2013.

[10] P. Seri, R. Ghosh, H. Naderiallaf, and G.C. Montanari, “Investigating Energization Transients and the Potentiality of Partial Discharge Inception and Damage in Nanofilled Polypropylene Insulation for DC Cables and Capacitors,” CATCON, India, 2019, pp. 1-5.

[11] G.C. Crichton, P.W. Karlsson, and A. Pedersen, “Partial discharges in ellipsoidal and spheroidal voids,” IEEE Trans. Dielectr. Electr. Insul., vol. 24, no. 2, pp. 335-342, Apr. 1989.

[12] A. Pedersen, G. C. Crichton, and I. W. McAllister, “The theory and measurement of partial discharge transients,” IEEE Trans. Dielectr. Electr. Insul., vol. 26, no. 3, pp. 487-497, 1991.

[13] P. Seri, H. Naderiallaf, G.C. Montanari, “Modelling of supply voltage frequency effect on partial discharge repetition rate and charge amplitude from AC to DC: room temperature,” IEEE Trans. on Diel. and El. Insulation, vol. 27, no. 3, pp. 764-772, June 2020.

[14] G.J. Anders, *Rating of electric power cables in unfavorable thermal environment*, New York: Wiley, 2005.

[15] Thomas Worzyk, *Submarine power cables: design, installation, repair, environmental aspects*, Springer Science & Business Media, 2009.

[16] B.M. Weedy, *Underground transmission of electric power*, John Wiley & Sons, 1980.

[17] I. Garniwa, and A. Burhani, “Thermal incremental and time constant analysis on 20 kV XLPE cable with current vary,” In 2006 IEEE 8th International Conference on Properties & applications of Dielectric Materials, 2006, pp. 566-569.

[18] Y. Zhang, X. Zhou, H. Niu, X. Wang, Y. Tang, J. Zhao, and Yo. Fan, “Theoretical calculation and experimental research on thermal time constant of single-core cables,” High Voltage Engineering, vol. 35, no. 11, pp. 2801-2806, Nov. 2009.

[19] L. Niemeyer, “A generalized approach to partial discharge modeling,” IEEE Trans. on DEI, vol. 2, no. 4, pp. 510-528, 1995.

[20] P. Seri, G.C. Montanari, A. Albertini, S.F. Bonomi and M. Albertini, “Comparing the results of increasing-voltage design and qualification life tests on HVDC and HVAC cables: the effect of voltage-step growth rate and insulation thickness factors,” Conference on Electrical Insulation and Dielectric Phenomena (CEIDP), 2020, pp. 1-4.

[21] G.C. Montanari, R. Hebner, P. Seri, and H. Naderiallaf, “Partial discharge inception voltage and magnitude in polymeric cables under AC and DC voltage supply,” Jicable, 2019, pp. 1-4.

[22] H. Naderiallaf, A. Cavallini, F. Esterl, R. Plath, P. Seri and G.C. Montanari, “Measuring partial discharges in MV cables under DC voltage: procedures and results in steady state conditions,” IEEE Electr. Insul. Conf. (EIC), 2020, pp. 1-4.

[23] S.J. Frobin, C. Freye, C.F. Niedik, and F. Jenau, “Generic field simulation framework for HVDC cables,” IEEE 2nd International Conference on Dielectrics (ICD), 2018, pp. 1-5.

[24] L. Sanche, “Nanoscopic aspects of electronic aging in dielectrics,” IEEE Trans. Dielectr. Electr. Insul., vol. 4, pp. 507-543, 1997.

[25] L. Testa, S. Serra, G.C. Montanari, “Advanced modeling of electron avalanche process in polymeric dielectric voids: simulation and experimental validation”, J. of Appl. Phys., vol. 108, pp. 1-10, 2010.

[26] G.C. Montanari, “A contribution to unravel the mysteries of electrical aging under DC electrical stress: where we are and where we need to go,” IEEE ICD, pp. 1-11, June 2018.

[27] S. Serra, G.C. Montanari, G. Mazzanti, “Theory of inception mechanism and growth of defect-induced damage in polyethylene cable insulation,” J. of Apply. Phys., vol. 98, pp. 1-15, 2005.

[28] L. Simoni, *Fundamentals of endurance of electrical insulating materials*, CLUEB ed., Bologna, 1983.

[29] G.C. Montanari, “Notes on theoretical and practical aspects of polymeric insulation aging,” IEEE Trans. on DEI, vol. 29, no. 4, pp. 30-40, August 2013.

[30] IEC 62539 “Guide for the statistical analysis of electrical insulation breakdown data,” 2007.

[31] G. C. Montanari and D. Fabiani, “The Effect of Nonsinusoidal Voltage on Intrinsic Aging of Cable and Capacitor Insulating Materials,” IEEE Trans. DEI, vol. 6, pp. 798-802, 1999.

[32] G. C. Montanari, D. Fabiani and F. Ciani, “Partial discharge and aging of AC cable systems under repetitive voltage transient supply,” 2016 IEEE Electrical Insulation Conference (EIC), Montreal, QC, 2016, pp. 379-382.

[33] P. Seri, L. Cirioni, H. Naderiallaf, G.C. Montanari, R. Hebner, A. Gattozzi, and X. Feng, “Partial Discharge Inception Voltage in DC insulation systems: a comparison with AC voltage supply,” in IEEE Electr. Insul. Conf. (EIC), 2019, pp. 176-179.

[34] P. Seri, H. Naderaillaf, R. Ghosh and G.C. Montanari, “An approach to noise rejection and partial discharge separation in DC cable testing, during steady state and voltage polarity inversion transients,” IEEE CMD, pp. 1-8, Bangkok, Thailand, 2020.

Chapter 7

Adding nanofillers in polymeric insulating materials: so far so good? The case of polypropylene for DC cables

This chapter has the aim to highlight the weaknesses related to nanostructuration of cable grade insulating polymers referencing to polypropylene and nanosilica. It also tries to discriminate which types of properties can be affected by adding nanofiller to the neat polypropylene (PP) in a positive or negative way depending on the nanofiller functionalization process. For instance, it is demonstrated that nanofiller might increase (rather than decrease) space charge accumulation and conduction current resulting from functionalization, and that a decrease of space charge accumulation is not necessarily correlated to an increase of life.

7.1 Introduction

A European project, GRIDABLE (Polymer Nanocomposite Insulation Material Enabling Integration of Renewables and DC Storage Technologies in the AC Energy Grid), which was launched under the HORIZON 2020, has the aim to investigate nanostructured polypropylene, PP, as insulating materials for DC cables, as well as manufacturing large scale prototypes. Having chosen SiO_2 as nanoparticles, concerns regarding proper dispersion and its natural hydrophilic behavior were immediately addressed. Thus, different types of functionalization were accomplished and tested comparing their effects on the performance of nanostructured dielectrics. The purpose is to screen several material combinations and focus on those more promising for DC application. While in literature most of papers indicate that dielectric nanostructuration is a tool able to improve insulating material performance almost from any point of view [1-5], other works provide the evidence that dealing with nanoparticle may be an issue especially regarding electrical properties [6-11]. Indeed, water molecules or ionic species linked to nanoparticle surfaces (difficult to eliminate even with dedicate treatments) may worsen rather than improving electrical properties [6, 9-11]. Furthermore, the aspect ratio must be considered. The larger the aspect ratio, the better some properties (e.g., mechanical strength, partial discharge resistance), but water/ionic species are more difficult to be eliminated [9, 11, 12]. This chapter presents and discusses effects of nanostructuration of PP-based materials for DC cable insulation on electrical properties.

7.2 Experimental procedures and results

Different base polymers were considered for the experiments while their compounds included PP of various manufacturers and rheological-mechanical characteristics, an elastomer, and an HDPE, also from different manufacturers. In this chapter, it is focused on one of them, PP, compared with two XLPE compounds for DC applications, XLPE-A and XLPE-B. Based on preliminary space charge measurement tests, performed by PEA (pulsed electroacoustic) technique, [13, 14], it was clear that some treatments were much better than others from space charge amount and mobility point of view. Therefore, this chapter focuses on a few bad and good cases, in relation to the space charge behavior, and 1% nanofiller content.

Silica nanoparticles, with a weight percentage of 1%, subjected to four functionalization treatments, here named T1 to T4, were examined. T1 and T4 were modified by dry processing using Trimethylethoxysilane as a modifying agent and trifluoroacetic acid or ammonia as catalyst, while T2 and T3 were modified by a solution method through 3-aminopropyltriethoxysilane (APTES) with and without Soxhlet extraction, and 48h dried in a vacuum oven at 80°C. Table 7.1 summarizes the various material combinations considered in this chapter. Results from tests performed on the current state-of-the-art materials for HVDC application, namely XLPE, were also considered (using XLPE compounds obtained from two different sources). The tested specimens consisted of press-molded slabs 0.4 mm thick (on average).

Table 7.2 summarizes the value of space charge amplitude at the beginning of depolarization and equivalent mobility, after a polarization period of 3 hours under a poling field of 50 kV/mm and temperature of 20°C. Also, conductivity after 24 h polarization at 50 kV/mm and 20°C, and dielectric strength measured at room temperature (20°C), are displayed (the latter obtained by ramp-voltage tests in oil, using cylindrical rods with 6.4 mm of diameter with edges rounded to 0.8 mm radius (ASTM D3755) as electrodes. A few accelerated life tests were also performed (at room temperature), to highlight any correlation with space charge, both at 0.8 ES_0. Note that the values of dielectric strength and life test field provided in Tables and figures are obtained under the rough approximation of uniform field between electrodes.

Table 7.1. Summary of the material characteristics analyzed in this chapter. Example of reading: PPT41: base material PP, functionalization treatment 4, percent nanofiller 1.

Material code	Contents		
	Elastomer	medium modified polypropylene random copolymer	high density polyethylene resin
PP	40%	55%	5%
PPT11	39.6%	54.45%	4.95%
PPT21	39.6%	54.45%	4.95%
PPT31	39.6%	54.45%	4.95%
PPT41	39.6%	54.45%	4.95%

Both space charge and charging-discharging current measurements were performed at different fields and temperatures. This allowed the space charge amplitude vs. electric field characteristics to be plotted for the tested materials, according to [14-16], and the temperature coefficient of conductivity to be estimated, α, derived from Equation (3.21).

The charge amplitude from space charge measurements is estimated as [15, 16]:

$$q(E,t) = \frac{1}{L}\int_0^L \left|q_p(E,x,t)\right| dx \tag{7.1}$$

where 0 and L indicate the electrodes positions and $q_p(E,x,t)$ is the space charge profile for a given poling field E. Mobility is then calculated by:

$$\mu(t) = \frac{\varepsilon}{q^2(t)}\frac{dq(t)}{dt} \tag{7.2}$$

where $q(t)$ is the charge density that can be calculated at any depolarization time, $dq(t)/dt$ is the slope of the depolarization curve at time t, ε is the permittivity of the specimens tested. Once the apparent trap-controlled mobility is known, the distribution of trap depth could be estimated. An approximate method to obtain the trap depth distribution, $\Delta U(t)$, is described in [15].

Figure 7.1 shows an example of polarization/depolarization space charge patterns from unfilled and nanofilled materials, that is PP, PPT21 and PPT31, the second worsening and the third improving the space charge behavior compared to the base material, at 50 kV/mm and 60°C.

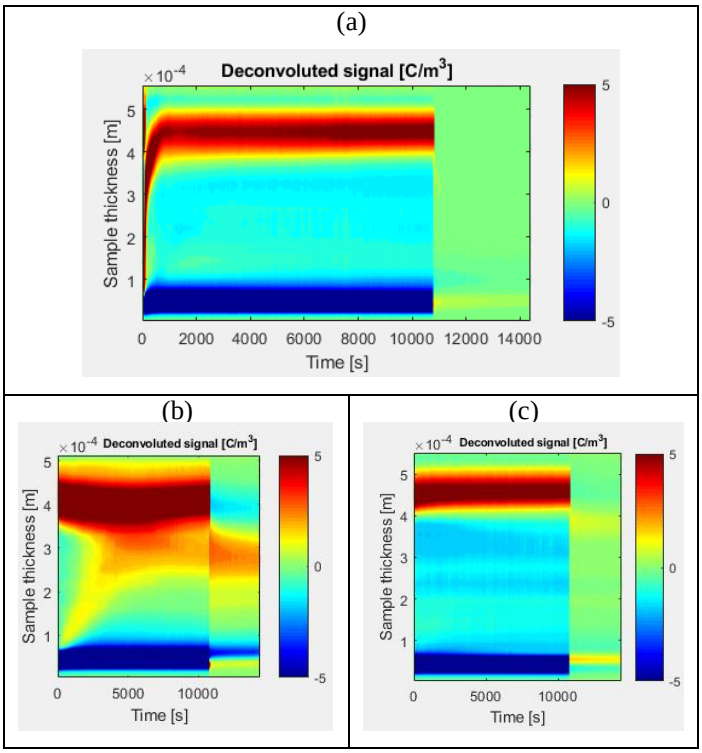

Figure 7.1. Example of space charge patterns at 60ºC (a) base material, PP; (b) PPT21, worsening the space charge behavior; (c) PPT31, improving the space charge behavior.

According to the space charge measurement at room temperature (20°C), adding nanofiller to the base PP material, even with a 1% content, may result in reducing space charge accumulation. For instance, PPT21 in Figure 7.2a has a reduced space charge accumulation of 0.26 C/m^3, from 2.9 C/m^3 of the neat material). Increasing the temperature, e.g., at 60°C, the opposite may also occur. In this condition, space charge accumulation of material PPT21 increases from 0.5 C/m^3 (neat PP) to 1.37 C/m^3.

Overall, adding nanofillers to the neat polypropylene (PP) can result in increasing space charge accumulation at 60°C just with one exception such as PPT31. However, there is lower space charge accumulation for nano filled materials in comparison with the two types of XLPE for both 20 and 60°C. The comparison of neat polypropylene (PP) with the two types of XLPE shows that despite lower space charge accumulation for XLPE at 20°C, there would be lower space charge accumulation for polypropylene (PP) at higher temperatures such as 60°C. In other words, it can be said that while increase of temperature results in increase of space charge accumulation for XLPE (especially XLPE-B), the opposite may occur for polypropylene (PP) whereas increase of temperature can lead to decrease of space charge accumulation.

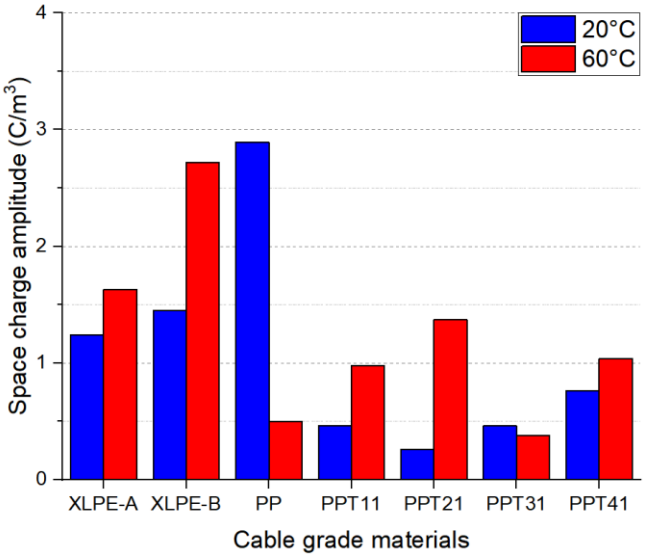

(a)

Material code	Space charge profile @ 20°C and 50 kV/mm	Space charge profile @ 60°C and 50 kV/mm
XLPE-A	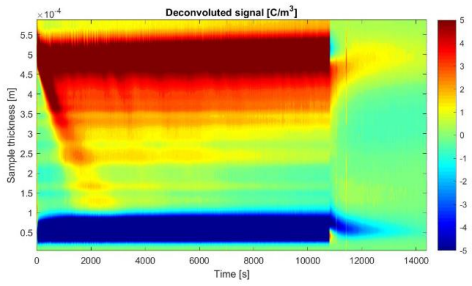 (a)	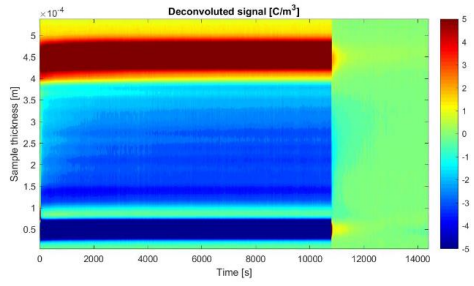 (b)
XLPE-B	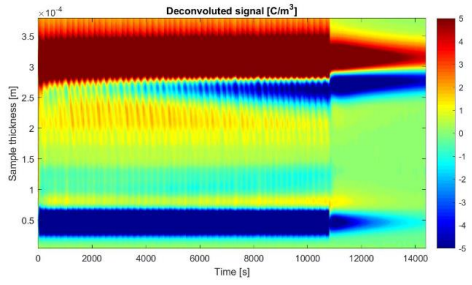 (c)	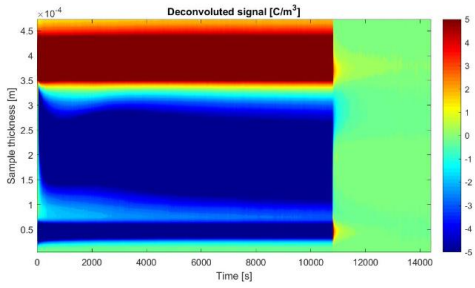 (d)
PP	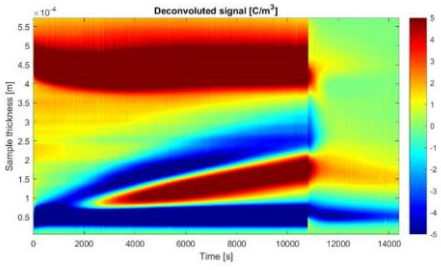	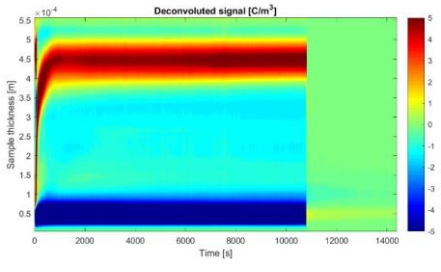

	(e)	(f)
PPT11	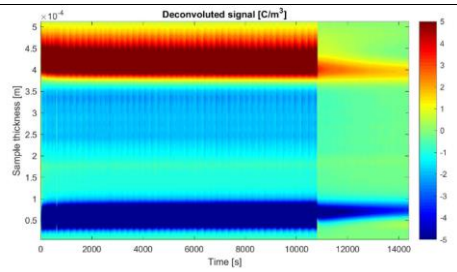 (g)	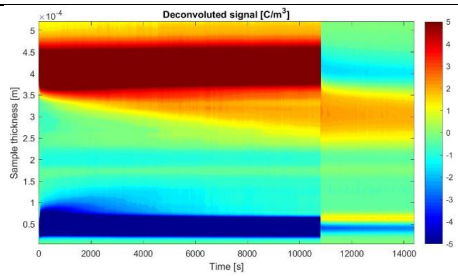 (h)
PPT21	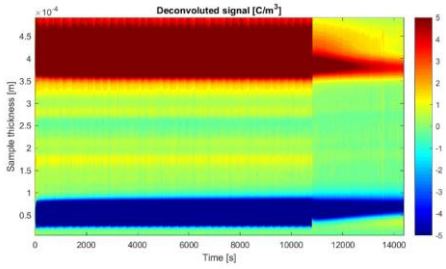 (i)	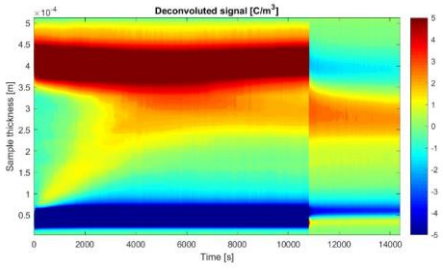 (j)
PPT31	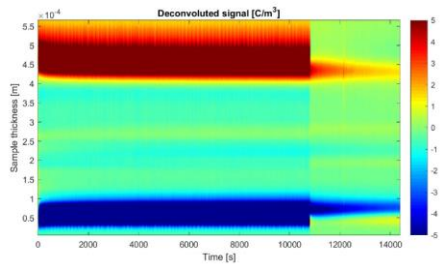 (k)	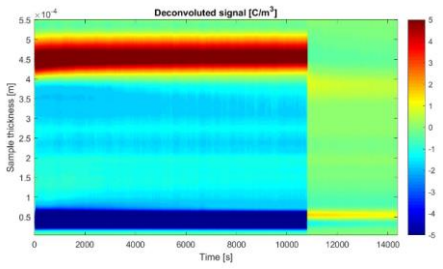 (l)
PPT41	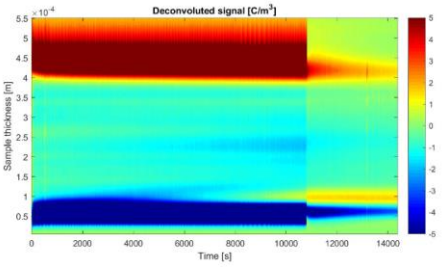 (m)	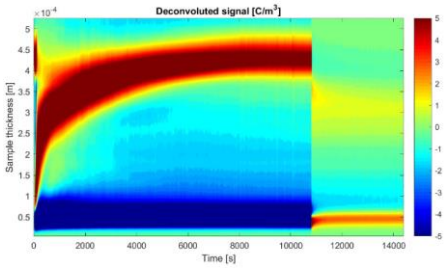 (n)

(b)

Figure 7.2. Effect of nanofiller on space charge behavior at 20 and 60 °C (a) The comparison of space charge amplitude just 3 seconds after volt-off at 20 and 60°C and (b) The comparison of space charge profile during polarization and depolarization at 20 and 60°C.

As shown in the space charge profiles of both types of XLPE, there is mostly negative space charge accumulation especially at 60°C. The comparison between the space charge profiles of both XLPE and polypropylene without nanofillers indicates that the polarity of accumulated space

charge for XLPE is mostly negative charges. As illustrated in Figures 7.2b-e and 7.2b-f, while there is considerable amount of positive hetero charge (polarity of the space charge is opposite to that of neighboring electrode) near the ground at 20°C for polypropylene (PP), there can be less hetero charge accumulation at higher temperatures e.g. 60°C. Considering PPT11, while there are hetero charge accumulation near HV electrode at 20°C, it tends to be decreased at 60°C (see: Figures 7.2b-g and 7.2b-h). Regarding PPT21, the space charge pattern would be exacerbated at 60°C (see: Figures 7.2b-j) where there is hetero charge near the ground especially after applying voltage. As an example of reduced stored space charge as well as improved space charge pattern, PPT31 can be introduced. Eventually, the space charge pattern for PPT41 at 60°C is worsen compare with 20°C (see: Figures 7.2b-m and 7.2b-n). There is significant amount of hetero charge near the ground after voltage application. This positive hetero charge near the ground can be attributed to existence of ionic compounds or any polar pollutant inside the material.

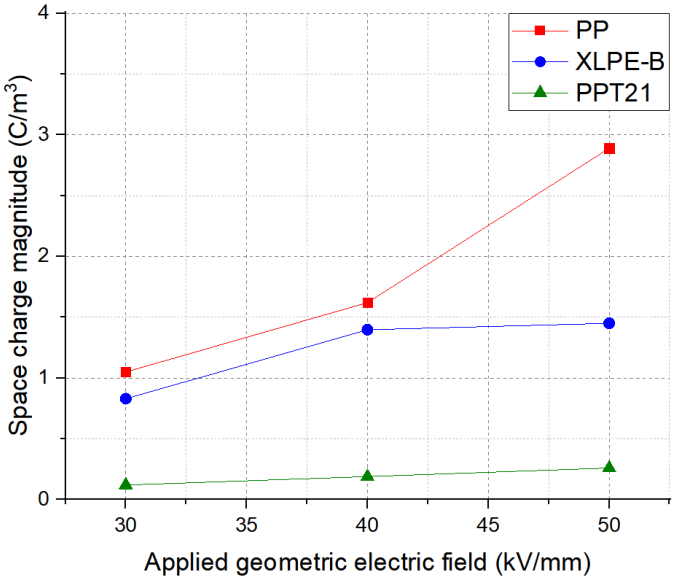

(a)

Material code	30 [kV/mm]	40 [kV/mm]	50 [kV/mm]
PP	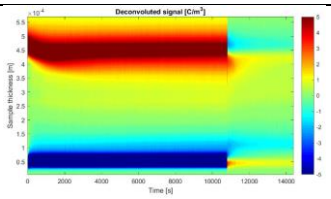 (a)	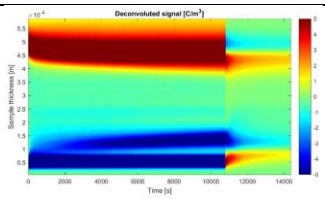 (b)	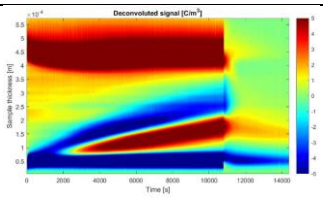 (c)

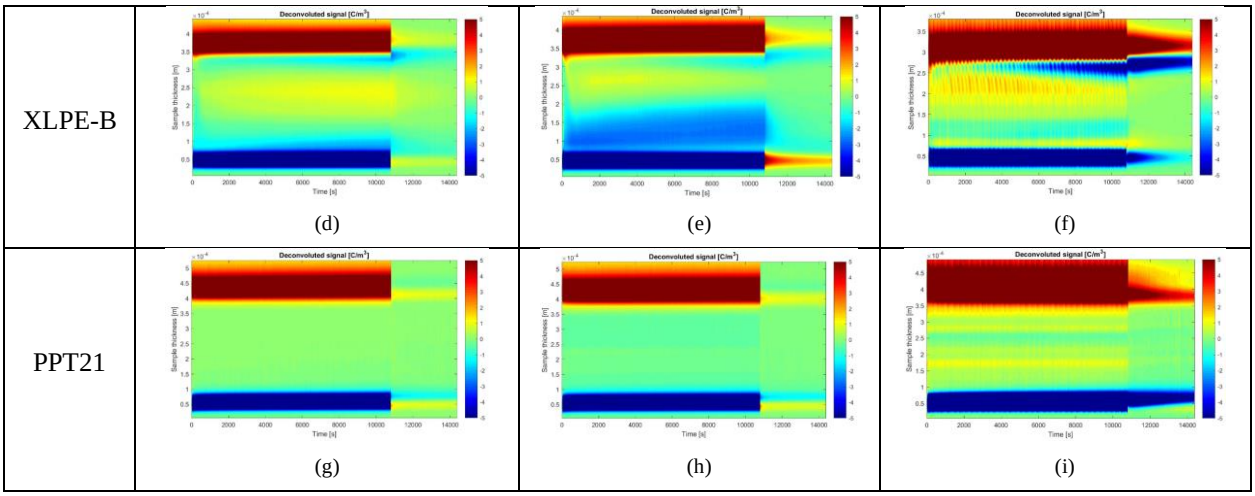

Figure 7.3. (a) Example of space charge magnitude vs. applied (geometric) electric field characteristic at 20°C, nanofilled material vs. XLPE and PP material and (b) example of space charge pattern as a function of applied (geometric) electric field at 20°C, nanofilled material vs. XLPE and PP material.

As illustrated in Figure 7.3a, considering space charge magnitude as a function of applied electric field at 20°C shows that while the highest space charge magnitude belongs to polypropylene (PP), this feature can be improved significantly by adding nanofillers even with a 1% content.

Regarding the space charge patterns as a function of applied field at 20°C indicated in Figure 7.3b, it can be seen that there is homo charge accumulation (an accumulated amount charge in dielectric that is of the same sign as that of the electrode originally in contact with it) near the ground electrode at 40 kV/mm for polypropylene (PP) (see: Figure 7.3b-b) and XLPE-B (see: Figure 7.3b-e). Increasing the field to 50 kV/mm at room temperature, results in hetero charge accumulation near the ground for polypropylene (PP) (see: Figure 7.3b-c) and especially near the HV electrode for XLPE-B (see: Figure 7.3b-f). Adding nanofillers to polypropylene even with a 1% content such as PPT21 can lead to improvement of space charge profile as a function of applied electric field in such as a way that both homo charge and hetero charge accumulation can be suppressed against increase of applied electric field (see: Figures 7.3b-g, 7.3b-h and 7.3b-i).

The dielectric strength test results relevant to 63.2% cumulative probability for two-parameter Weibull distribution at room temperature (20°C) are depicted in Figure 7.4 where α and β are scale and shape parameter, respectively.

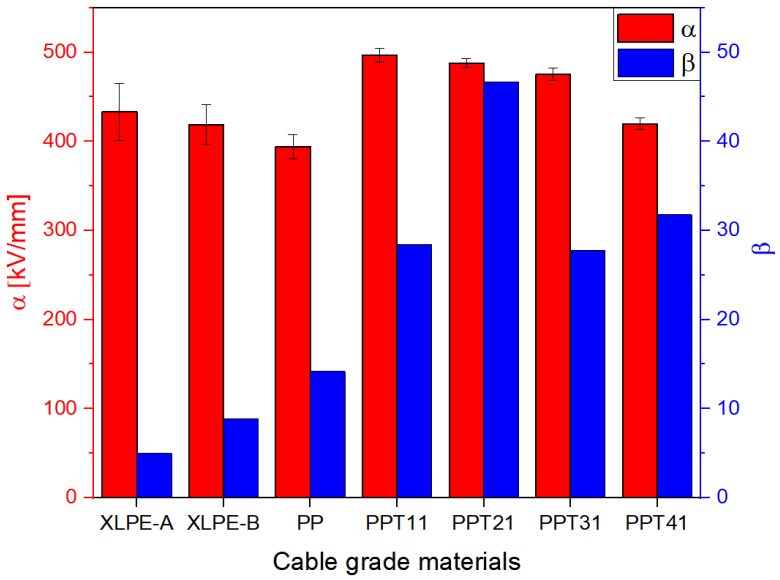

Figure 7.4. The dielectric strength test results at room temperature (20°C) relevant to 63.2% cumulative probability for two-parameter Weibull distribution. The error bars are also indicated.

As shown in Figure 7.4, the lowest value of β (the shape parameter of Weibull distribution) belongs to the two types of XLPE. The comparison between both XLPE materials and neat polypropylene indicates that while XLPE provides higher dielectric strength (α), higher β is attributed to polypropylene (PP). The comparison between the neat polypropylene and nano filled materials shows that adding nano fillers can result in increase of both α and β. Finally, the material with lowest space charge magnitude, PPT21, provides the highest β value for dielectric strength measurements and of course improved α compare to unfilled material with the lowest standard error among all the measured materials.

The life test results at 80% of the dielectric strength relevant to 63.2% cumulative probability for two-parameter Weibull distribution at room temperature (20°C) are illustrated in Figure 7.5 where α and β are scale and shape parameter, respectively.

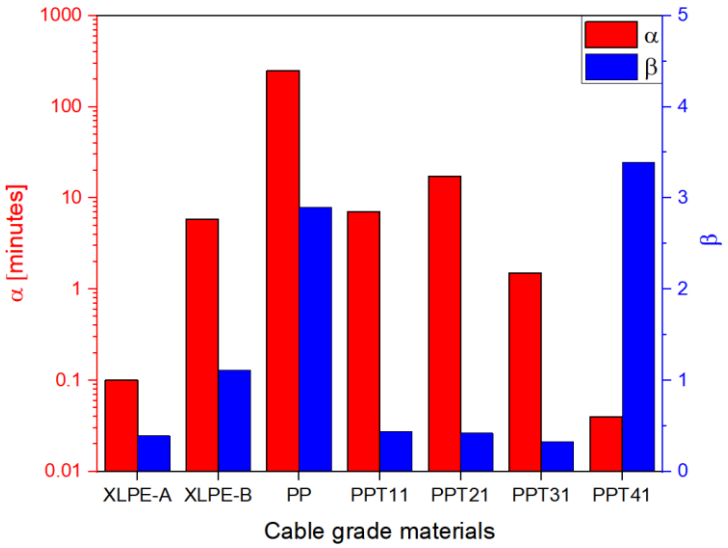

Figure 7.5. The life test results at 80 % of the dielectric strength at room temperature (20°C) relevant to 63.2% cumulative probability for two-parameter Weibull distribution.

As can be seen from Figure 7.5, the comparison between XLPE materials and neat polypropylene (PP) shows that higher α and β values relevant to the life test belongs to polypropylene (PP). In addition, it can be concluded that adding nano fillers can result in decrease of life when the comparison is performed between unfilled polypropylene (PP) and nano filled materials.

The electrical conductivity measurement results under 50 kV/mm and at 20, 60 and 90°C are displayed in Figure 7.6.

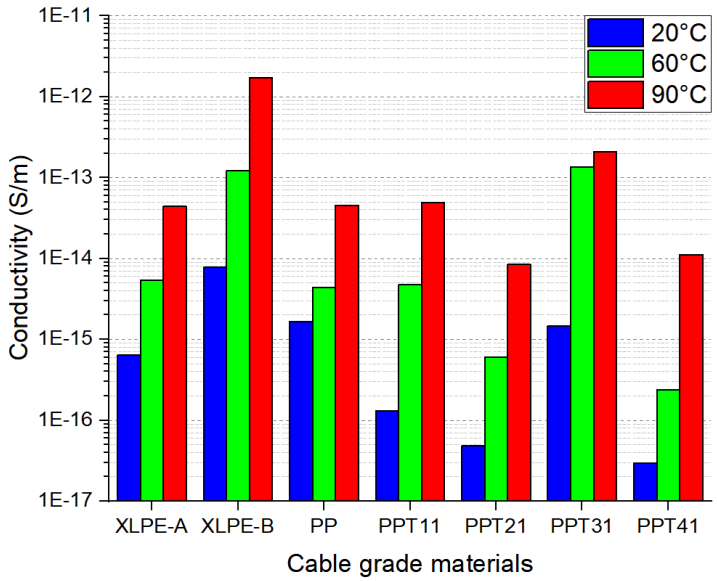

Figure 7.6. Electrical conductivity after 24 h polarization under 50 kV/mm and at 20°C, 60°C and 90°C.

As shown in Figure 7.6, adding nano fillers can result in decrease of conductivity at low temperatures such as room temperature (20°C). However, while at higher temperatures such as 60 and 90°C, adding nano fillers might result in decrease of conductivity for instance PPT21 and PPT41, it can lead to considerable increase of conductivity for example PPT31.

The temperature dependence coefficients of electrical conductivity (α) referring to Equation (3.21) are demonstrated in Figure 7.7.

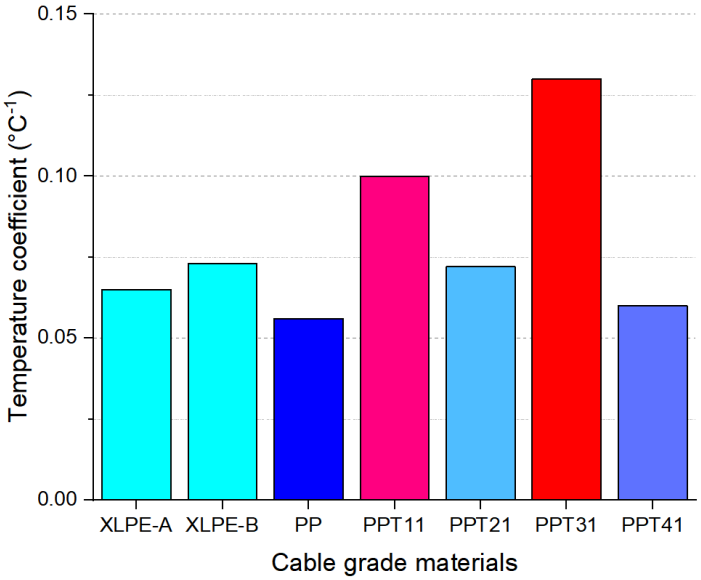

Figure 7.7. The temperature dependence coefficients of electrical conductivity (α) referring to Equation (3.21).

As can be seen from Figure 7.7, although neat polypropylene material (PP) provides lower temperature dependence coefficient of electrical conductivity (α) than both tested XLPE materials, adding nano fillers even with 1% content can lead to undesired increase of α especially PPT31.

As a general consideration, based on Table 7.2 and Figures 7.1-7.7, it can be noted that nano structuration may improve or worsen electrical properties with respect to the base material depending on various factors such as type of functionalization treatment and temperature. While some properties can be improved for DC application, e.g., decreasing space charge content and conductivity, others can be worsened, e.g., the temperature coefficient α and life.

Table 7.2. Values of space charge amplitude 3 seconds after the beginning of depolarization, Equation (7.1)), equivalent mobility (Equation (7.2)), after polarization at 50 kV/mm and temperature 20°C, conductivity after 24 h polarization at 50 kV/mm and 20°C, dielectric strength ES_0 at room temperature (20°C), life test at 80% ES_0 and temperature coefficient α (Equation (3.21)). Space charge and conductivity are mean values, while dielectric strength and life tests data are relevant to 63.2% cumulative probability for a two-parameter Weibull distribution.

Material code	Electrical properties					
	Space charge amplitude (C/m^3)	Equivalent mobility ($m^2 V^{-1} s^{-1}$)	Conductivity (S/m)	Dielectric strength (kV/mm)	Life test – Time (minutes)	α ($^oC^{-1}$)
XLPE-A	1.24	1E-13	6.36E-16	433	0.1	0.06
XLPE-B	1.45	1.75E-13	7.78E-15	418.9	5.8	0.07
PP	2.89	2E-14	1.64E-15	394	250.1	0.06
PPT11	0.46	3E-13	1.29E-16	497.1	7	0.1
PPT21	0.26	1E-13	4.81E-17	488.1	17.3	0.07
PPT31	0.46	5E-13	1.45E-15	475.1	1.5	0.13
PPT41	0.76	4E-13	2.93E-17	419.9	0.04	0.06

Correlation between space charge and dielectric strength or conductivity was investigated. Figure 7.8 shows those two correlation plots. In the case of space charge and dielectric strength, the correlation and determination coefficients are acceptable (i.e. $r = -0.84$, $R^2 = 0.7$), but for conductivity those are reduced to only $r = -0.39$, $R^2 = 0.15$, mostly due to the presence of an outlier (XPE-B). Censoring it results in marginally better correlation ($r = -0.42$, $R^2 = 0.17$).

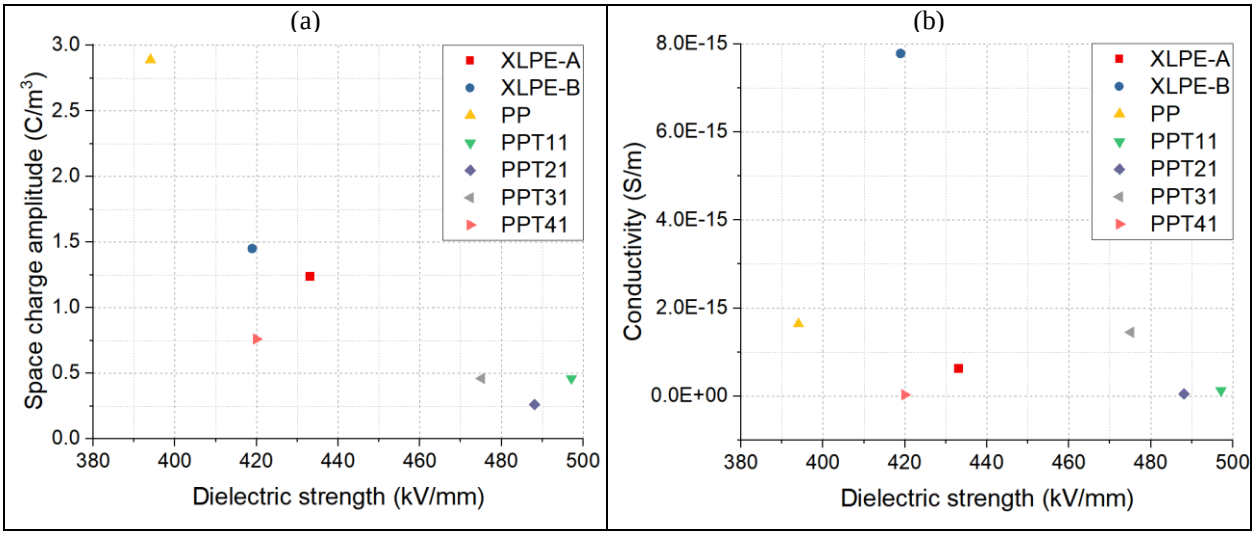

Figure 7.8. (a): Correlation plot space charge amplitude vs. dielectric strength, ES_0, for materials of Table 7.2 at 20°C ($r = 0.84$). (b): conductivity vs. dielectric strength, ES_0, for materials of Table 7.2 at 20°C (r =0.42).

Correlation between space charge and the shape parameter (β) of Weibull distribution of the dielectric strength measurement results or conductivity was also investigated. Figure 7.9 indicates those two correlation plots. In the case of space charge and β of dielectric strength, although the correlation and determination coefficients seems to be not considerable (i.e. $r = -0.66$, $R^2 =$

0.43), but after censoring the outlier (PP), it results in significantly better correlation (i.e. $r = -0.91$, $R^2 = 0.82$). This point was already highlighted in Figure 7.4 when the highest value of β belongs to the material with lowest space charge magnitude such as PPT21. Regarding conductivity, the correlation and determination coefficients are decreased to $r = -0.53$, $R^2 = 0.28$.

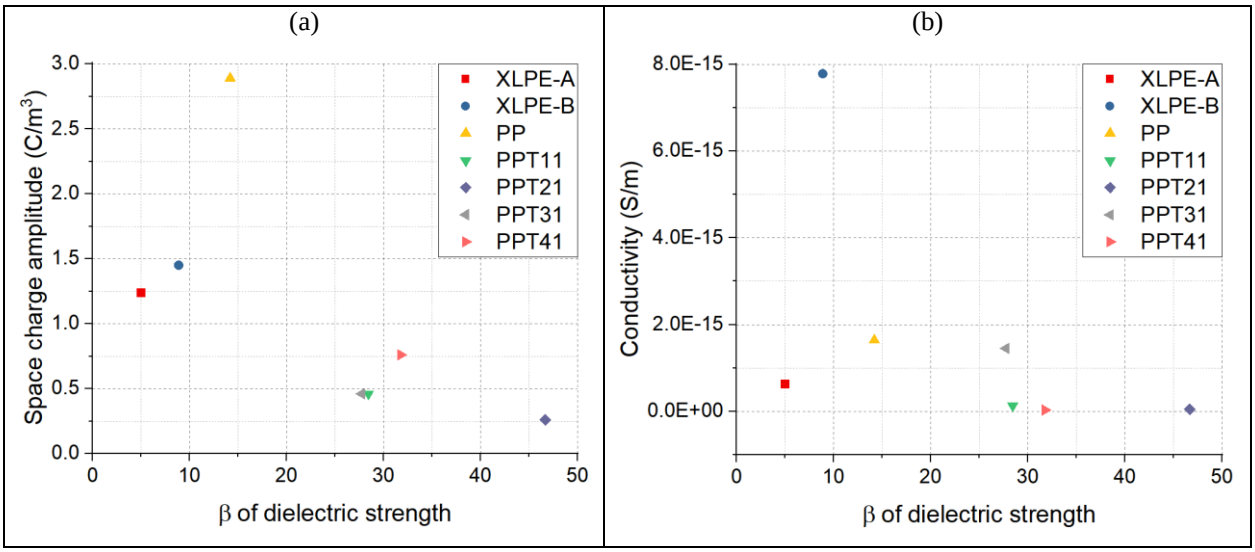

Figure 7.9. (a): Correlation plot space charge amplitude vs. β of dielectric strength, ES_0, for materials of Table 7.2 at 20°C ($r = 0.66$) and after censoring PP ($r = 0.91$). (b): conductivity vs. dielectric strength, ES_0, for materials of Table 7.2 at 20°C (r =0.53).

Further, correlation between life and space charge or conductivity was also studied. Figure 7.10 shows two correlation plots of life with space charge and conductivity. Overall, correlation for this case is rather poor. This can be associated with the fact that life tests are conducted under different fields, corresponding to 0.8 times the breakdown field of each material (which in turn is characterized by a different dielectric strength). Life and space charge accumulation produce a correlation with $r = -0.47$, $R^2 = 0.23$, while life and conductivity are characterized by $r = -0.44$, $R^2 = 0.2$. Hence, those coefficients do not suggest that the action of nanostructuration can reflect into longer life, and, indeed, results showed worsening of life in some cases.

Correlation between space charge and the shape parameter (β) of Weibull distribution of life test results or conductivity was also scrutinized. Figure 7.11 illustrates those two correlation plots. In the case of space charge and β of life test, the correlation and determination coefficients are not considerable compare with space charge and β of dielectric strength (i.e. $r = 0.54$, $R^2 = 0.3$). Considering the conductivity, those coefficients are reduced drastically to $r = -0.03$, $R^2 = 0.001$.

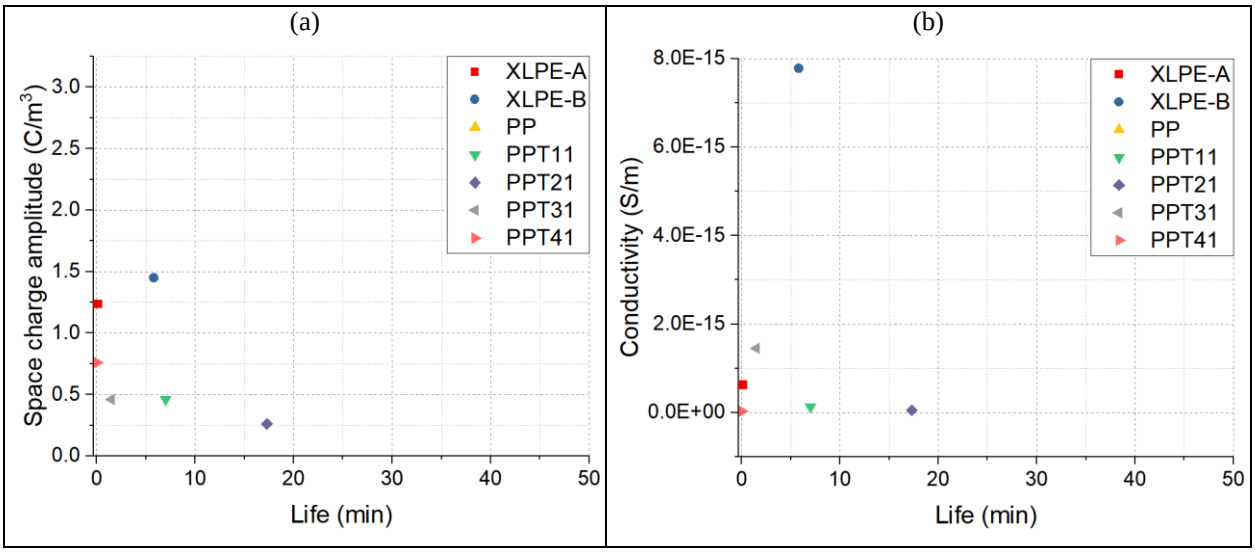

Figure 7.10. (a): Correlation plot space charge amplitude vs. life, for materials of Table 7.2 at 20ºC. (b): conductivity vs. life, for materials of Table 7.2 at 20ºC.

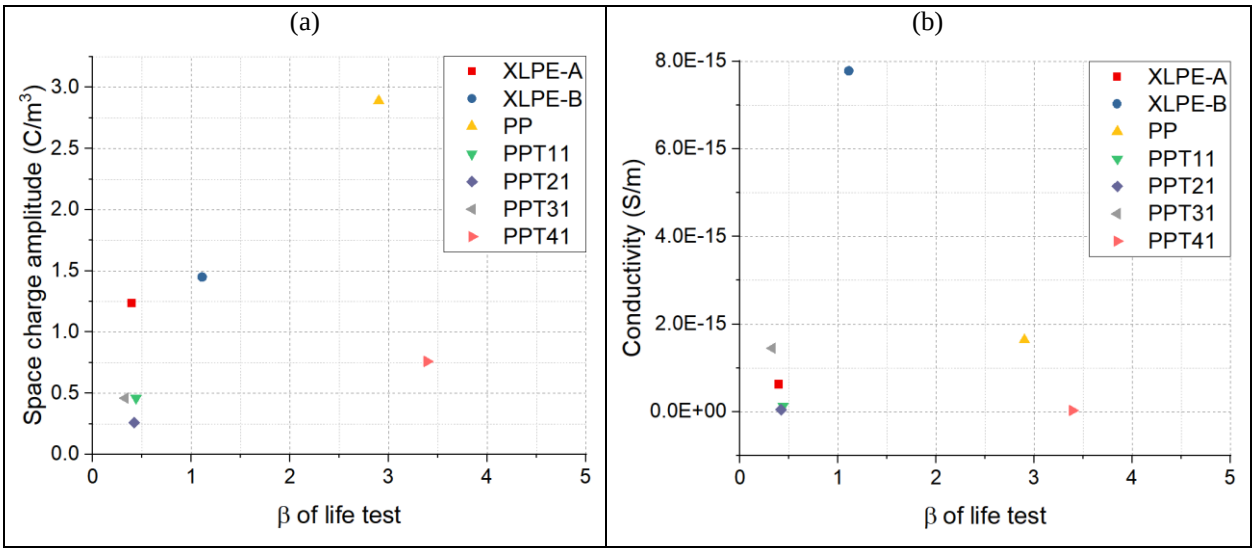

Figure 7.11. (a): Correlation plot space charge amplitude vs. β of life, for materials of Table 7.2 at 20ºC. (b): conductivity vs. β of life, for materials of Table 7.2 at 20ºC.

In order to better understand the obtained results, SEM imaging was also carried out for the tested materials, to highlight any morphological structure causing such apparently uncorrelated results. Figure 7.12 contributes to explain how different functionalizations affect the final structure of the polymer, eventually modifying its electrical (and possibly mechanical) properties. A reasonable speculation would be that inhomogeneous structures such as those shown in Figures 7.12b, 7.12e contributes to decrease the life of a material, introducing undesired regions where both mechanical and electrical stress might be enhanced. For the same reason, but on a minor scale, materials such

as T2, T3 pictured in Figures 7.12c, 7.12d do not perform as well as the neat material. The issue of micrometric agglomeration of nanoparticles (represented by the white parts of Figure 7.12) is not fully resolved, and this is preventing the material from performing to its full potential.

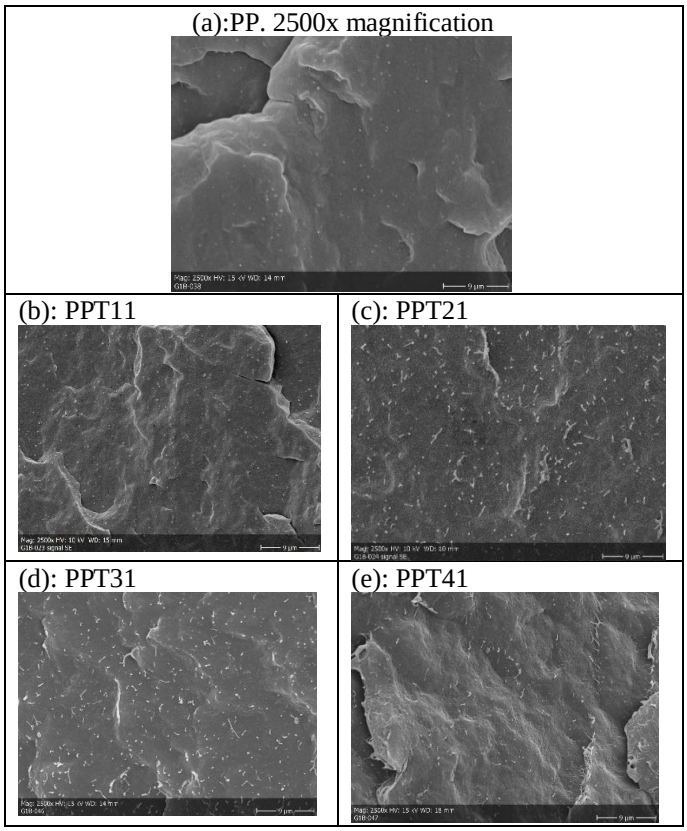

Figure 7.12. Different functionalizations effect on the final structure of the polymer.

7.3 Discussion

There is evidence from the experimental results that the choice of base materials and functionalization process can influence significantly electrical properties, such as space charge, conductivity and its temperature coefficient, dielectric strength, and life. Functionalization can play a role regarding electrical properties which are very sensitive to trap density and depth, as well as ionic species (as space charge and conductivity), but it may be less influential, or influential in a negative way, on short and long-term breakdown. Furthermore, it can be recalled that electrical properties can be drastically influenced by nanoparticle aspect ratio, as also electric tree and corona resistance [5, 7, 8, 12]. The effect on α can be negative, in the sense that increasing α cable feasibility (at high voltage and current) is worsened [17], while that on conductivity can be positive

or negative, because it has been shown that, depending on the functionalization treatment and the type of compound, conductivity can vary of orders of magnitude (see Table 7.2). Nanofilled materials considered above tend to display the same or lower values of conductivity than the base material, which reflects positively on PDIV, but larger values of α, which is negative for cable design and feasibility. Indeed, as seen for other properties, especially functionalization can dramatically affect results, introducing very subtle differences with the treatment T3, and useful improvements for the others, with special advantages for the treatment T4.

As said, nanostructuration can modify electrical properties certainly, but not always in the desired way, since the simple act of adding fillers to a matrix can and will induce a modification of chemical, physical and morphological properties. The final performance of a material will be then given by the combined effect of fillers to introduce new trapping sites in the insulation, reducing the overall charge storage, while on the other hand leaving the polymerization undisturbed, and the final structure as well dispersed and homogenous as in the base material.

7.4 Material design for a PD-phobic electrical insulation

The concept of PD-phobic insulation brings to design and tailoring of insulating materials for DC insulation. They can be modified purposely depending on the use, i.e., under permanent DC, in the presence of numerous transients, or even in the case, as forecasted by Flexible-DC approach, where the insulation can be submitted alternatively to AC or DC fields.

In any of the above conditions, materials can be optimized to raise as much as possible the threshold for PD inception and forgiveness to the presence of defects in the insulation.

Materials as XLPE can be modified to considerably vary conductivity (as reported also by recent patents [18, 19]), but the highest capability to modify conductivity comes from materials as polypropylene (PP) that are compounded, and the addition of nanofillers, which can grade the value of conductivity and its thermoelectrical dependence for any specific purpose.

Table 7.3 reports data from two types of PP compounds, PP1 and PP2, which have been nanostructured with the addition of 1% wt (PP1N1 and PP2N1) and 2% wt (PP1N2) silica nanofiller.

The tested specimens consisted of press-molded slabs with a thickness of 0.4 mm (average value). All specimens were dried for 24h in a vacuum oven at 80°C before testing.

PDIV measurements were performed, both under AC and DC voltage, using three-layer specimens where the central layer had a punctured hole which could be varied in dimensions, i.e. radius and height. The latter variation was obtained changing the central layer.

Figure 7.13 reports the results of $PDIV_{DC}$ to $PDIV_{AC}$ ratio for PP1 and PP2, as well as for the three nanofilled materials (PP1N1, PP1N2 and PP2N1), at 20 and 60°C, compared with the estimation from Equation of (3.20) and the model which describes the ratio between $PDIV_{DC}$ and $PDIV_{AC}$ as explained in chapter 3 introduced by Equation (3.14). The defect had a radius of 3.5 mm and an average height of 400 μm.

As can be seen, there is a good fitting between model and experimental results, even if the experimental values of $PDIV_{DC}$ for PP1 and PP2N1 could not be obtained at 20°C (too high-test voltage). Overall, it comes out clearly that materials having lower conductivity always feature a higher $PDIV_{DC}$ value (or $PDIV_{DC}/PDIV_{AC}$ ratio), even when the defect is significantly large. They can tend to the concept of "PD-phobic" materials. This holds also under full load, as long as the temperature coefficient, α, is low. However, when α is increased, the advantage of a very low reference conductivity (γ_0) is lost, and the $PDIV_{DC}$ drops considerably: see e.g., PP1N2. Specifically, the addition of nanofillers reduces both conductivity and the temperature coefficient, α, in PP2N1, which displays very large values of the ratio between $PDIV_{DC}$ and $PDIV_{AC}$ even at high temperatures. This material would, therefore, become an interesting candidate to manufacture PD-free cables, in DC steady state, even in the presence of significantly large defects.

Table 7.3. Mean values of conductivity after 24 h polarization at 30 kV/mm and 20°C, its temperature coefficient α (refer to Equation (3.21)), and dielectric strength for two types of base polypropylene compounds (PP1 and PP2), and three types of nanofilled materials, i.e., PP1N1, PP1N2 and PP2N1.

Material code	Conductivity (S/m)	Dielectric strength (kV/mm)	α ($^oC^{-1}$)
PP1	1.15E-16	369	0.12
PP1N1	5.7E-15	377	0.03
PP1N2	5.7E-16	308	0.13
PP2	1.6E-15	394	0.06
PP2N1	4.8E-17	488	0.07

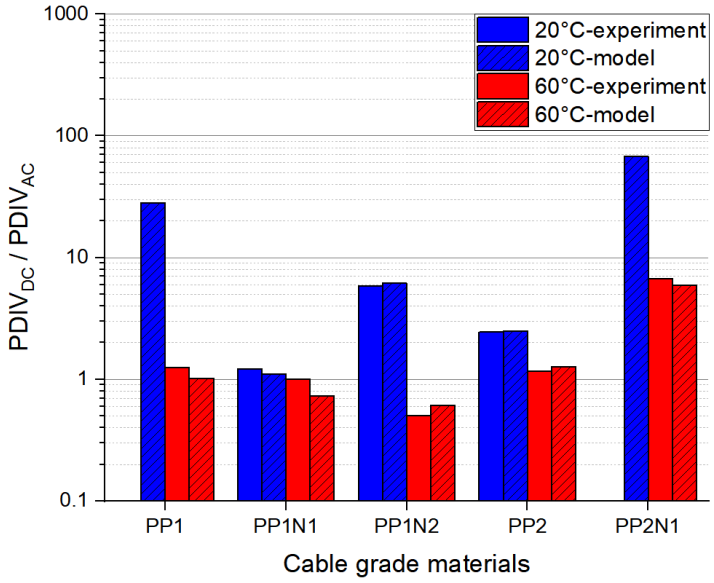

(a)

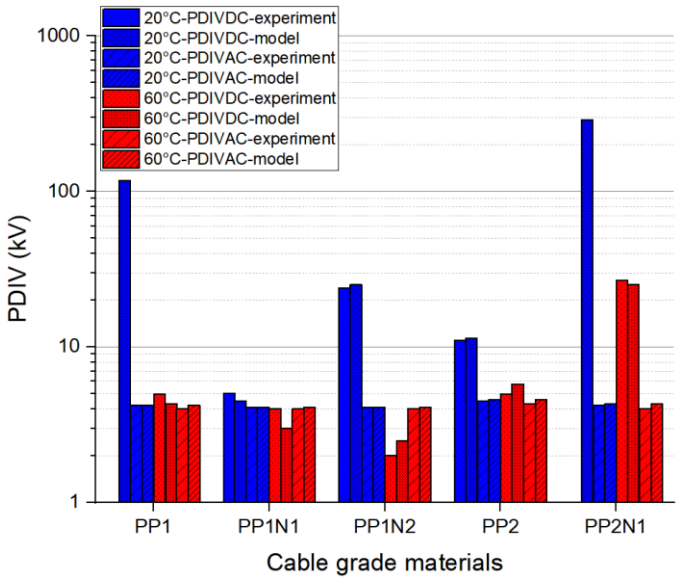

(b)

Figure 7.13. (a) Experimental and estimated values of $PDIV_{DC}/PDIV_{AC}$ and (b) $PDIV_{DC}$ and $PDIV_{AC}$ values for multi-layer specimens made of PP1, PP1N1, PP1N2, PP2 and PP2N1 at 20 and 60°C (Table 7.3) (refer to (3.21) and (3.14)). The defect had radius 3.5 mm and average height 400 μm. Due to the high values of DC PD at 20°C it was not possible to apply a large enough voltage during PDIV testing of PP1 and PP2N1 materials, thus the corresponding experimental values could not be reported in this Figure.

7.5 Conclusions

As shown, adding SiO_2 nanoparticles in a base polymer (PP compounds presented in this chapter) may be effective to improve, but also to worsen, the electrical properties of the base polymer,

depending on functionalization and other parameters, as temperature. For example, adding nanoparticles to PP decreases space charge amplitude at 20°C, but it tends to increase space charge at higher temperature, while varying significant conduction current. Additionally, although nano-filled materials may provide better dielectric strength compared to the base polymer, this may not reflect into better voltage endurance (life). Such results can be due to profound chemical, physical and morphological changes to the microscopic structure of the polymer, induced by the fillers. For example, the burden of agglomeration and of functionalization by-products is a well-known issue of nanostructured materials, but further work should be done to improve this aspect and eventually fully exploit the high potential of those polymers. Hence, the main message of this chapter would be to be cautious thinking of nanostructuration as the solution to improve overall electrical properties of polymeric insulating materials.

Finally, it was shown that according to the model (3.14), if insulation materials can be modified to reduce their conductivity at the design field and maximum operating temperature, steady-state partial discharge inception voltage becomes significantly higher than the nominal voltages practically reached even with UHVDC transmissions.

References

[1] T. Tanaka, "Dielectric nanocomposites with insulating properties", IEEE Trans. Dielectr. Electr. Insul., Vol.12, pp. 914- 928, 2005.

[2] C. Zhang, R. Mason and G.C Stevens, "Dielectric Properties of Alumina-Polymer Nanocomposites", Ann. Rept. IEEE CEIDP, No. 8-3, pp. 721-724, 2005.

[3] T. Tanaka and M. Fréchette, "Polymer Nanocomposites – Fundamentals and Possible Applications to Power Sectors", CIGRE Electra 2011.

[4] R. Kurnianto, Y. Murakami, M. Nagao, N. Hozumi and Y. Murata, "Treeing Breakdown in Inorganic-filler/LDPE Nano-composite Material", IEEJ Trans. FM, Vol. 127, No. 1, pp. 29-34, 2007.

[5] A. Sami, E. David and M. Fréchette, "Dielectric Properties Modeling of High and Low Density Polyethylene/SiO_2 Composites", Ann. Rept. IEEE CEIDP, No. 7A-19, pp. 588-591, 2010.

[6] G.C. Montanari, A. Cavallini , F. Guastavino, G. Coletti, R. Schifani, M. di Lorenzo del Casale, G. Camino, F. Deorsola, "Microscopic and nanoscopic EVA composite investigation: electrical properties and effect of purification treatment", IEEE CEIDP, pp. 318-321, Boulder, USA, October 2004.

[7] C. D. Green, A. S. Vaughan, G. R. Mitchell, and T. Liu, "Structure Property Relationships in Polyethylene/Montmorillonite Nanodielectrics", IEEE Trans. Dilelectr. Electr. Insul., Vol. 17, No. 1, pp. 134 -143, 2008.

[8] T. Tanaka, A. Bulinski, J. Castellon, M. Frechette, S. Gubanski, J. Kindersberger, G. C. Montanari, M. Nagao, P. Morshuis, Y. Tanaka, S. Pelissou, A. Vaughan, Y. Ohki, C. W. Reed, S. Sutton, S. J. Han, "Dielectric properties of XLPE/SiO2 nanocomposites based on CIGRE WG D1.24 cooperative test results", IEEE Trans. on Dielectrics and Electrical Insulation, Vol. 18, n. 5, pp. 1484-1517, October 2011.

[9] M. Roy, J.K. Nelson, L.S. Schadler, C. Zou and J.C. Fothergill, "The Influence of Physical and Chemical Linkage on the Properties of Nanocomposites", Ann. Rept. IEEE CEIDP, No. 2C-10, pp. 183-186, 2005.

[10] L. Hui, J. K. Nelson, L. S. Schadler, "The Influence of Moisture on the Electrical Performance of XLPE/Silica Nanocomposites", Proc. ICSD, No. B3-2, pp.305-308, 2010.

[11] D. Fabiani, G. C. Montanari, L. Testa, "Effect of aspect ratio and water contamination on the electric properties of nanostructured insulating materials", IEEE Trans. Dielectr. Electr. Insul, Vol. 17, pp. 221-230, 2010.

[12] D. Fabiani, G.C. Montanari, F. Palmieri, "Effect of nanoparticle size on space charge behavior of EVA-TiO2 nanocomposites", IEEE CEIDP, pp. 322-325, Cancun, Mexico, October 2011.

[13] T. Takada, "Acoustic and optical methods for measuring electric charge distributions in dielectrics", IEEE Trans. Dielectr. Electr. Insul, Vol. 6, pp. 519-547, 1999.

[14] G.C. Montanari, C. Laurent, G. Teyssedre, A. Campus, U.H. Nilsson, "From LDPE to XLPE: investigating the change of electrical properties. Part 1: space charge, conduction and life", IEEE Trans. Dielectr. Electr. Insul., Vol. 12, pp. 438-446, 2005.

[15] G. Mazzanti, G. C. Montanari and J. M. Alison, "A space-charge based method for the estimation of apparent mobility and trap depth as markers for insulation degradation-theoretical basis and experimental validation", in IEEE Transactions on Dielectrics and Electrical Insulation, vol. 10, no. 2, pp. 187-197, April 2003.

[16] G. C. Montanari, "The electrical degradation threshold of polyethylene investigated by space charge and conduction current measurements", IEEE Trans. Dielectr. Electr. Insul., Vol. 7, N. 3, pp. 309-315, 2000.

[17] P. Morshuis, G. C. Montanari, G. C. Stevens, A. S. Vaughan, P. Seri, "Assessing the Feasibility of Insulation Materials for UHVDC Cable Systems," IEEE ICPADM, pp. 398-401, Xi'an, Cina, maggio 2018.

[18] J. Jow and A. Mendelsohn, "High-voltage direct current cable insulation and semiconductive shield," U.S. Patent No. 6,924,435, Aug. 2, 2005.

[19] J. K. Nelson, W. Zenger, R. J. Keefe, and L. S. S. Feist, "Nanostructured dielectric composite materials," U.S. Patent No. 7,579,397, Aug. 25, 2009.

Chapter 8

Overview, Conclusions and Future Work

This chapter concludes the thesis. A discussion of the work undertaken is provided, with a summary of important conclusions. Possible directions of further research are also discussed.

8.1 Overview

The aim of this thesis was to derive analytical models ("continuum" models) able to describe the behavior of partial discharge (PD) characteristics including PD repetition rate, PD charge amplitude, and PD inception voltage (PDIV). To derive the models, it was focused on internal discharges occurring in a cavity embedded in a polymeric insulation. The modelling was carried out as a function of the frequency of the supply voltage, going from AC power supply frequency, 50-60 Hz, to DC as well as temperature (load) based on PD equivalent RC circuit. Although there were some available models for PD charge amplitude in the previous literature, regarding PD repetition rate and PDIV, there was the lack of a fundamental validated model based on PD equivalent RC circuit especially for DC power supply.

Regarding PD charge amplitude and PD repetition rate, it was focused on the data coming from tests under AC sinewave at power frequency (50-60 Hz), very low frequency (VLF) such as 0.1 Hz and 0.01 Hz which are commonly used for cable testing as well as DC power supply. The PD measurements were performed on polypropylene multilayer specimens. It was demonstrated that the proposed "continuum" models can provide reasonably good fit to the experimental results obtained in the range DC to 60 Hz. Moreover, it was shown that the common PD RC equivalent circuit made by fully capacitive or resistive components should be modified to consider the change of polarization mechanisms. This modification depends on the used dielectric material which may play a non-negligible role to establish the PD repetition rate from low frequency to DC power supply. Furthermore, it was proved that the residual voltage after a PD event should increase with decrease of frequency, particularly under DC, to provide good fitting with the derived analytical models for PD charge amplitude and PD repetition rate. In addition, it was proved that under PDIV, PD charge amplitude under DC and VLF can be lower than under AC 50-60 Hz at high probability of the Weibull distribution owing to the effect of firing electron delay time which is higher on high frequency. Regarding the effect of temperature on PD charge amplitude, it was proved based on

sensitive and selective laboratory PD measurements on MV cable that at higher temperatures such as 90°C, the shape/slope parameter of the Weibull distribution of the PD charge amplitudes remains constant. This fact can be helpful for PD diagnostics.

Regarding PDIV, the ratio between PDIV, under AC and DC voltage supply was analyzed based on the derived analytical model as well as experimental data. The estimations are validated through laboratory testing on both MV cable with an artificial defect as well as polypropylene multilayer specimen. It was demonstrated that PDIV under DC can become considerably higher or lower than that under AC, depending on temperature and material properties, which affect PD repetition rate as well.

PD can incept and extinct during operation as a function of cable loading, posing reliability problems for a cable insulation system that should be considered both at the design and at the commissioning stage. Performed simulations by COMSOL Multiphysics indicated that load variations can incept partial discharges during cable operation at a constant voltage, depending on insulating material characteristics, defect size and location, and the temperature and field dependence of electrical conductivity. As a result, it was shown that HVDC cable design should not only refer to voltage polarity inversion or energization, when dealing with the risk of partial discharges, but also to load variation.

The HVDC insulation design was investigated considering real operating conditions in such a way that DC steady-state condition can be affected by frequent voltage polarity inversions or load variations during all life leading to accelerating aging phenomena such as partial discharges. The derived analytical models implemented in COMSOL Multiphysics simulations indicated that electrical and thermal transients may incept partial discharges in defective insulations during cable energization, voltage polarity inversion at a constant nominal load, as well as during load variations at a constant nominal voltage. The focus in this thesis was on HVDC cables, but the described approach would be general for any DC insulation system.

Finally, the pros and cons related to adding nano fillers to insulating polymers especially cable insulation, with reference to polypropylene and nano silica were highlighted. It was demonstrated that adding nano fillers to insulating polymers can increase (rather than decrease) space charge accumulation and electrical conductivity or decrease (rather than increase) dielectric strength and life.

8.2 Conclusions

Availability of a model able to describe PD phenomenology such as PD charge amplitude, PD repetition rate and PDIV from AC to DC seems to be useful and necessary to prevent questionable results relating to diagnostics, quality control and commissioning tests when PD measurements are performed from AC to DC at different frequencies and temperatures. Considering the defects as delamination or embedded cavities, it was demonstrated based on the models as well as experimental data that PD charge amplitude and repetition rate depending on insulating material characteristics and testing conditions decreases from AC power supply frequency to low frequency and DC at constant temperature. However, the decrease of PD charge amplitude from AC to DC would mostly depend on testing procedures and data processing. This is due to the significant influence that the availability of the firing electron applies on the measured value of PD charge amplitude in such a way that larger PD charge amplitude would be expected if higher dv/dt of the supply voltage waveform is employed for the PD measurement. Regarding PD repetition rate, fitting the experimental data to the derived model based on commonly used PD equivalent charging (RC) circuit in the literature shows that charging circuit may require to be slightly amended. This modification is implemented by adding a parallel branch that contains series resistance and capacitance to consider the polarization mechanism which can occur during the charging process between the two subsequent PD events affecting on PD repetition rate. Moreover, this added parallel branch can be also used to model the effect of injected and accumulated space charge at the semicon or the dielectric-cavity interface under DC or very low frequency (VLF). It was found by fitting the PD charge amplitude and repetition rate models to the experimental data that the residual voltage can increase with decrease of frequency from AC to DC.

It was indicated that depending on load condition and following that temperature, PD characteristics change significantly under DC, while this temperature effect is lower under AC at power supply frequency. The reason for this is that electric field distribution under DC is driven by conductivity which can be affected significantly by temperature compare with permittivity. Thus, PD characteristics will change considerably by temperature variation under DC.

The derived PDIV model based on PD equivalent RC circuit was validated by performing precise PD measurement on multilayer specimen and MV cable. Thus, a helpful tool to predict PDIV under DC and its relationship with measured PDIV under AC was introduced which can help for designing

insulation systems under steady-state DC field. In despite of AC PD measurement which is relatively easy and largely practiced, PDIV measurement under DC is still not common and misleading and questionable results can be obtained very often (because of e.g. transient PD during voltage increase or decrease, or noise misinterpreted as PD). Therefore, the approach proved in this thesis can help and validate DC PD measurements, having carried out analogue AC PD tests, as well as conductivity measurements on the insulating material.

It was demonstrated that operating a HVDC cable under DC does not mean designing, nor testing a cable for purely AC or DC steady state conditions. This point should be considered by cable designers for the sake of long-term reliability under DC operation. An unexpected source of partial discharges in DC cables as load power variations was investigated based on thermal and dielectric time constants of the insulating material. It was shown that considering the commonly used polymeric insulating materials for manufacturing HVDC cables, the thermal time constant resulted from cable load variations is shorter than the dielectric constant that comes from cable energization or voltage polarity inversion, i.e., $\tau_{th} < \tau_d$. This can lead to PD inception upon load variation for the defective cable in the presence of cavity near inner or outer conductor because of driven electric field by conductivity. The effect of high values of temperature dependence (α) or field dependence (β) of electrical conductivity on the escalation of electric field inside cavities especially near inner conductor upon load variation was analyzed in detail to illuminate the shadows relating to α and β. The extreme condition in which dielectric time constant can be shorter than thermal time constant, i.e., $\tau_{th} > \tau_d$, resulting in electric field distribution by permittivity rather than conductivity upon load variation and following that the possibility of high PD repetition rate inside the existence cavities was investigated through COMSOL Multiphysics simulations. Based on the damage concept and calculating electron energy caused by PD, it was shown that repetitive cable energization/voltage polarity inversions, as well as repetitive load variations, can possibly lead to accelerated aging of DC insulation systems in the presence of defect with large enough size (and properly located along insulation diameter) able to incept PD.

It was indicated that despite properly designing cable insulation to prevent DC PD in steady state condition, at any operating temperature, electrical and thermal transients can be likely harmful for insulation life. Their effect on dielectric life reduction cannot be ignored during operation, especially if cables are interconnected and fed by line-commutated converters (LCC) e.g., used in hybrid networks. Hence, these problems can be encountered only by reduction of design field, or,

better, preventing defects or reduce their size below the $PDIV_{AC}$, and arranging materials that provide better resistance (thus higher VEC) to PD.

Finally, regarding adding SiO_2 nanofillers to base polypropylene (PP), it was indicated that depending on functionalization and other parameters especially temperature, this action can improve or exacerbate the electric and dielectric properties of the base polymer. For instance, although adding nanofillers to PP can result in reduction of space charge magnitude and electrical conductivity at room temperature, this can lead to increase of space charge and conductivity at higher temperatures. Moreover, in despite of improvement of dielectric strength because of adding nanofillers to PP, this may not result in longer life. Therefore, it was proposed to be more prudent and discreet about nanostructuration as a solution to improve overall electric and dielectric properties of polymeric insulating materials.

8.3 Future work

Modelling the residual voltage as a function of frequency and temperature from AC to DC can be a topic for the future investigations to complete the derived models.

The effect of space charge accumulation on PD charge amplitude and PD repetition rate can be investigated through performing experiments on the multilayer specimens after injecting space charge intentionally on each of the layers.

The derived analytical model for $PDIV_{DC}$ works with known cavity height value, thus introducing another analytical model to estimate the cavity height through PDIV measurement under AC power supply frequency and as a function of cavity location along the cylindrical insulation diameter can be helpful to complete the model and provide a $PDIV_{DC}$ model independent of cavity height.

The effect of cavity surface conductivity as well as space charge accumulation under very low frequency (VLF) can be investigated using the derived model for PD charge amplitude and repetition rate focused only on PD characteristics under VLF. Moreover, the estimation of $PDIV_{DC}$ from PD measurement under VLF can be interesting topic for future investigations.

In the presented COMSOL Multiphysics simulations in this thesis, the temperature dependency of specific heat capacity and thermal conductivity was neglected. This can be considered in

designing HVDC insulation through laboratory measurements of different materials for future investigations.

Eventually, as it was demonstrated in Chapter 5, low value of thermal conductivity can lead to kinds of leakage current overshoots when the load is switched on and switched off. The behavior of leakage current for different polymeric insulating materials as a function of temperature by focusing on thermal conductivity of each material can be investigated through performing leakage current measurement for polymer minicables. This also can be an interesting topic for future investigations which does not investigated in detail in the previous literature while the effect of reduced thermal conductivity on the leakage current behavior was introduced in this thesis based on COMSOL Multiphysics simulations for a typical HVDC cable.

Publications

The work conducted in this thesis led to the following publications:

- “Compounding, Structure and Dielectric Properties of Silica-BOPP Nanocomposite Films”, 2018 IEEE 2nd International Conference on Dielectrics (ICD), Budapest, Hungary, Hungary (July 2018), DOI: 10.1109/ICD.2018.8468517
- “Partial discharge inception voltage and magnitude in polymeric cables under AC and DC voltage supply”, Jicable, pp. 1-4, Varsailles, France, June 2019
- “Partial Discharge Inception Voltage in DC insulation systems: a comparison with AC voltage supply”, IEEE EIC, pp. 176-179, Calgary, Canada, June 2019, DOI: 10.1109/EIC43217.2019.9046630
- “Adding nanofillers in polymeric insulating materials: so far so good? The case of polypropylene for DC cables”, IEEE EIC, pp. 477-480, Calgary, Canada, June 2019, DOI: 10.1109/EIC43217.2019.9046553
- “Surface charge pattern analysis based on field-dependent charging model: a review”, IEEE El. Ins. Magazine, July 2019, DOI: 10.1109/TDEI.2019.008430
- “The Influence of Nanocomposite Filler on the Lifetime Performance of Polypropylene Under Voltage Polarity Reversal”, ICHVEPS 2019, Bali, Indonesia, DOI: 10.1109/ICHVEPS47643.2019.9011051
- “Investigating Energization Transients and the Potentiality of Partial Discharge Inception and Damage in Nano-filled Polypropylene Insulation for DC Cables and Capacitors”, IEEE CATCON 2019, Chennai, India, DOI: 10.1109/CATCON47128.2019.42
- “A contribution to everlasting electrical insulation for DC voltage: PD-phobic materials”, IEEE Access, Feb. 2020, DOI: 10.1109/ACCESS.2020.2977138
- “Modelling of Supply Voltage Frequency Effect on Partial Discharge Repetition Rate and Charge Amplitude from AC to DC: Room temperature”, IEEE Trans. Dielectr. Electr. Insul., vol. 27, no. 3, pp. 759-766, June 2020, DOI: 10.1109/TDEI.2019.008552

- “Measuring partial discharges in MV cables under DC voltage: procedures and results in steady state conditions”, 2020 IEEE Electrical Insulation Conference (EIC), Knoxville, TN, USA, 2020, pp. 18-21, DOI: 10.1109/EIC47619.2020.9158726
- “Feasibility of Mini-Scale Injection Moulding for Resource-Efficient Screening of Silica-PP/POE Nanocomposites: Morphology and Dielectric Properties”, 2020 IEEE 3rd International Conference on Dielectrics (ICD), pp. 209-212, July 2020
- “Influence of polar and unpolar silica functionalizations on the dielectric PP/POE nanocomposites”, 2020 IEEE 3rd International Conference on Dielectrics (ICD), pp. 229-232, July 2020
- “An Approach to Noise Rejection and Partial Discharge Separation in DC Cable Testing, During Steady State and Voltage Polarity Inversion Transients”, 2020 8th International Conference on Condition Monitoring and Diagnosis (CMD), pp. 318-321, October 2020
- “Investigating conditions for an unexpected additional source of partial discharges in DC cables: load power variations”, IEEE Transactions on Power Delivery, DOI: 10.1109/TPWRD.2020.3032800, October 2020
- “PP/PP-HI/silica nanocomposites for HVDC cable insulation: Are silica clusters beneficial for space charge accumulation?”, Polymer Testing, 98, p.107186, June 2021
- “Effect of nanosilica polarity on PP/EOC cast film nanocomposites for HVDC cable insulation”, Elsevier Materials Research Bulletin journal, submitted October 2020
- “The influence of nanosilica polarity on PP/EOC cast thin film nanocomposites for HVDC cable application: micromorphology, dynamic and dielectric properties”, MDPI open access publication, Polymers journal, submitted February 2021
- “Designing a HVDC insulation system to endure electrical and thermal stresses under operation. Part 1: partial discharge magnitude and repetition rate during transients and in DC steady state.”, IEEE Access, Feb. 2021, DOI: 10.1109/ACCESS.2021.3062440

- “Dielectric performance of silica-filled nanocomposites based on miscible (PP/PP-HI) and immiscible (PP/EOC) polymer blends”, IEEE Access, vol. 9, pp. 15847-15859, Jan. 2021, DOI: 10.1109/ACCESS.2021.3052517
- “Reliability of HVDC and MVDC electrical asset: the challenge of insulation design”, 2021 IEEE International Conference on the Properties and Applications of Dielectric Materials (ICPADM), Jul. 2021, pp. 1-8, DOI: 10.1109/ICPADM49635.2021.9493971
- “On the calculation of the dielectric time constant of DC insulators containing cavities”, IEEE CEIDP 2021, Vancouver, Canada, October 2021
- “DC cables and partial discharge phenomenology during voltage transients: effect of voltage slew rate.”, IEEE Trans. Dielectr. Electr. Insul., submitted May 2021
- “A Review of Knowledge-based Defect Identification via PRPD patterns in High Voltage Apparatus”, IEEE Access, vol. 9, pp. 77705-77728, May 2021, DOI: 10.1109/ACCESS.2021.3082858
- “HVDC insulation systems: effect of voltage polarity inversion slew rate on partial discharge phenomenology and harmfulness’, 22nd international symposium on High Voltage Engineering (ISH), Xi’an, China, September 2021
- “The influence of nanosilica surface functionalization on PP/EOC cast thin film nanocomposites for HVDC cable application: micromorphology, dynamic mechanical and dielectric properties”, Elsevier, Surfaces and Interfaces Journal, submitted April 2021

Appendix

Considering a frequency-domain transformation, a mean initial value of n_0 alternative to Equation (6.16) can be obtained as:

$$n_0 \approx \frac{2\pi f \cdot E_{\mathrm{c}}(t)}{(E_{\mathrm{i}} - E_{\mathrm{r}})} \qquad (A.1)$$

where, E_{r} is the residual electric field in a defect (cavity) after each PD event is extinguished, E_{i} is the PD inception field inside the cavity, obtained from Equation (6.14), and f is a frequency associated to field variation. The frequency of the charging circuit in (A.1) can be roughly estimated by:

$$f \approx \left(\frac{R_{\mathrm{b}} + R_{\mathrm{c}}}{R_{\mathrm{b}} R_{\mathrm{c}} (C_{\mathrm{b}} + C_{\mathrm{c}})}\right) \qquad (A.2)$$

being R_{c}, R_{b} and C_{c}, C_{b} respectively the resistance and capacitance of the cavity and the insulation in series. Hence, for a cylindrical insulation geometry (A.1) can be expressed such as (Equation (6.20)):

$$n_0 = \frac{\gamma_{\mathrm{b}}\big(T(r,t), E(r,t)\big) \cdot h_{\mathrm{c}} + \gamma_{\mathrm{c}} \cdot h_{\mathrm{b}}}{\varepsilon_0 \cdot (\varepsilon_{\mathrm{rb}} \cdot h_{\mathrm{c}} + \varepsilon_{\mathrm{rc}} \cdot h_{\mathrm{b}})} \cdot \frac{2\pi \cdot E_{\mathrm{c}}(t)}{(E_{\mathrm{i}} - E_{\mathrm{r}})} \qquad (A.3)$$

In the following two approaches to derive the time constant and following that frequency which can be assumed as a reverse of the time constant are introduced including:

A. Calculation based on the equivalent charging circuit.

B. Calculation based on Maxwell-Wagner-Sillars (MWS) equations

A. Calculation based on equivalent charging circuit

The equivalent RC charging circuit is illustrated in Figure A.1.

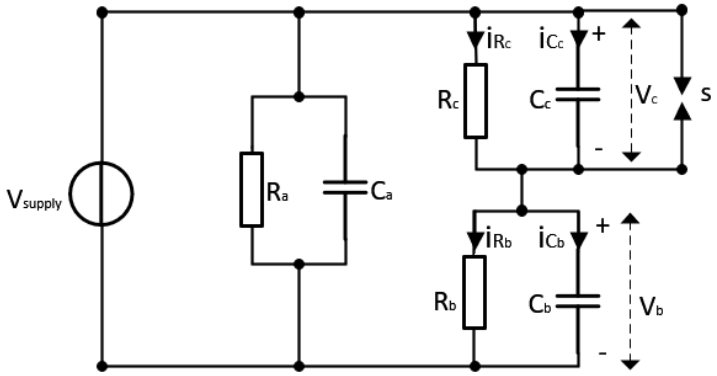

Figure A.1. Equivalent charging circuit for the cavity in series with dielectric. C_c and R_c are capacitance and resistance of the cavity, C_b and R_b are capacitance and resistance of the dielectric in series with the cavity, and C_a, R_a are the remaining capacitance and resistance of the insulation.

Considering charging circuit, the following general equations hold:

$$i_{\mathrm{Cb}} + i_{\mathrm{Rb}} = i_{\mathrm{Cc}} + i_{\mathrm{Rc}} \tag{A.4}$$

$$C_{\mathrm{b}} \frac{dV_{\mathrm{b}}}{dt} + \frac{V_{\mathrm{b}}}{R_{\mathrm{b}}} = C_{\mathrm{c}} \frac{dV_{\mathrm{c}}}{dt} + \frac{V_{\mathrm{c}}}{R_{\mathrm{c}}} \tag{A.5}$$

Under DC, $V_{\mathrm{supply}}=V_{\mathrm{b}}+V_{\mathrm{c}}=V_0$, thus after replacing $V_{\mathrm{b}}=V_0-V_{\mathrm{c}}$ in (A.5), it results in:

$$(C_{\mathrm{b}} + C_{\mathrm{c}}) \frac{dV_{\mathrm{c}}}{dt} = -\left(\frac{R_{\mathrm{b}}+R_{\mathrm{c}}}{R_{\mathrm{b}}R_{\mathrm{c}}}\right) V_{\mathrm{c}} + \frac{V_0}{R_{\mathrm{b}}} \tag{A.6}$$

and

$$\frac{dV_{\mathrm{c}}}{dt} = -\left(\frac{R_{\mathrm{b}}+R_{\mathrm{c}}}{R_{\mathrm{b}}R_{\mathrm{c}}(C_{\mathrm{b}} + C_{\mathrm{c}})}\right) V_{\mathrm{c}} + \frac{V_0}{R_{\mathrm{b}}(C_{\mathrm{b}} + C_{\mathrm{c}})} \tag{A.7}$$

Let us turn (A.7) into a homogeneous differential equation:

$$\dot{x} + ax = 0 \xrightarrow{yields} x(t) = x_0 . e^{-at} = x_0 . e^{\frac{-t}{\tau}} \tag{A.8}$$

so that the time constant can be calculated as $\tau = \frac{1}{a}$.

Thus, based on (A.8), (A.7) can be turned into a homogeneous differential equation such as:

$$\frac{dV_{\mathrm{c}}}{dt} + AV_{\mathrm{c}} = 0 \tag{A.9}$$

where

$$A = \frac{R_b + R_c}{R_b R_c (C_b + C_c)}$$

As a result, the time constant of the voltage inside cavity, V_c, when it is in series with dielectric, referring to the equivalent charging circuit is:

$$\tau_{ch} = \frac{1}{A} = \frac{1}{f} = \left(\frac{R_b R_c (C_b + C_c)}{R_b + R_c} \right) \quad (A.10)$$

Therefore, charging frequency can be defined as the reverse of charging time constant (A.10) shown already in (A.2).

After expressing in Equation (A.10) resistance and capacitance as a function of conductivity, permittivity, and geometry, the following is obtained for the charging time constant:

$$\tau_{ch} = \frac{\varepsilon_b h_c + \varepsilon_c h_b}{\gamma_b h_c + \gamma_c h_b} \quad (A.11)$$

The same demonstration can be used for the voltage in dielectric series with cavity, V_b, based on the equivalent charging circuit. In this case, (A.5) can be written as a homogeneous differential equation for V_b after replacing $V_c = V_0 - V_b$ in (A.5), which finally results in:

$$\frac{dV_b}{dt} + AV_b = 0 \quad (A.12)$$

Thus, the same time constant as in (A.11) is obtained for the voltage in the dielectric, V_b, which is in series with a cylindrical cavity.

B. Maxwell-Wagner-Sillars (MWS) method

The scheme of a cylindrical cavity in series with dielectric (embedded in insulation) is shown in Figure A.2.

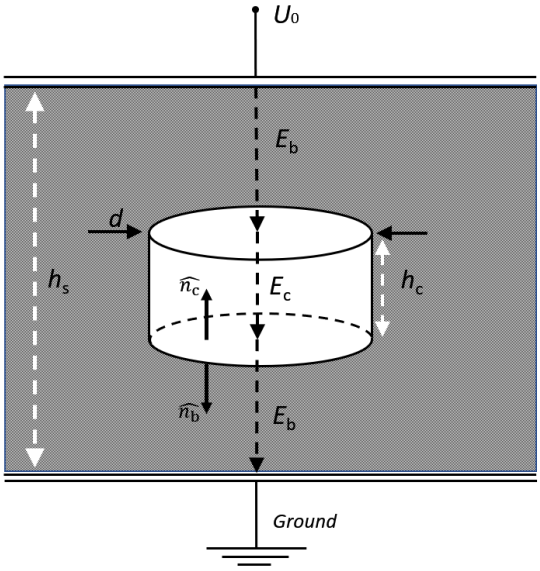

Figure A.2. Scheme of insulation with thickness of healthy part in parallel with cavity equal to h_s, having an embedded cylindrical cavity with diameter d, and height h_c. E_c and E_b are electric fields in the cavity and in the insulation in series with the cavity, respectively. $\widehat{n_c}$ and $\widehat{n_b}$ are unit normal, or perpendicular vectors to cylindrical base towards inside cavity and dielectric, respectively.

Under transient condition, it can be written (MWS equations):

$$\nabla D = \rho \qquad (A.13)$$

$$\nabla J + \frac{d\rho}{dt} = 0 \qquad (A.14)$$

where D is electric displacement field, ρ is the interfacial electric charge density at cavity walls (see Figure A.2) and J is the current density.

Since $J = \gamma E$ and $D = \varepsilon E$, thus (A.14) can be rewritten as:

$$\nabla \gamma E + \frac{d}{dt}(\nabla \varepsilon E) = 0 \qquad (A.15)$$

Considering the interfacial charge and the normal direction, (A.15) can be rewritten such as:

$$(\gamma_b E_b - \gamma_c E_c) + \frac{d}{dt}(\varepsilon_b E_b - \varepsilon_c E_c) = 0 \qquad (A.16)$$

where $\varepsilon_b = \varepsilon_0 \varepsilon_{rb}$ and $\varepsilon_c = \varepsilon_0 \varepsilon_{rc}$ are permittivity of the dielectric and medium filling the cavity, respectively. Considering h_c and $h_b = h_s - h_c$ (see Figure A.2) which are the height of cylindrical

cavity and the thickness of dielectric in series with cavity, respectively, the applied voltage on the object under test is equal to:

$$U_0 = E_c h_c + E_b h_b \xrightarrow{yields} E_b = \frac{U_0 - E_c h_c}{h_b} \qquad (A.17)$$

To write (A.16) only as a function of E_c, E_b calculated from (A.17) is inserted in (A.16) and both sides of (A.16) are multiplied to h_b:

$$\gamma_b(U_0 - E_c h_c) - \gamma_c h_b E_c + \frac{d}{dt}(\varepsilon_b(U_0 - E_c h_c) - \varepsilon_c h_b E_c) = 0 \qquad (A.18)$$

which gives:

$$(\gamma_b h_c + \gamma_c h_b)E_c + \frac{d}{dt}(\varepsilon_b h_c + \varepsilon_c h_b)E_c = \gamma_b U_0 + \frac{d}{dt}(\varepsilon_b U_0) \qquad (A.19)$$

Thus, based on (A.8), (A.19) can be turned into a homogeneous differential equation such as:

$$\frac{dE_c}{dt} + AE_c = 0 \qquad (A.20)$$

where,

$$A = \frac{\gamma_b h_c + \gamma_c h_b}{\varepsilon_b h_c + \varepsilon_c h_b}$$

Consequently, the time constant of the electric field inside a cavity when it is in series with dielectric, based on MWS equations, can be derives as:

$$\tau_{MWS} = \frac{1}{A} = \frac{\varepsilon_b h_c + \varepsilon_c h_b}{\gamma_b h_c + \gamma_c h_b} \qquad (A.21)$$

It can be seen that the obtained time constant based on MWS equations, τ_{MWS}, is the same as the charging time constant already determined for the voltage in cavity and dielectric based on the equivalent charging circuit (A.11), that is, $\tau_{ch} = \tau_{MWS}$.

The same demonstration can be done for the electric field in dielectric series with a cylindrical cavity. For this purpose, in (A.17) E_c can be obtained as a function of E_b and replaced in (A.16) to provide a homogeneous differential equation for the electric field in dielectric series with a cylindrical cavity, E_b, which is the same as (A.20). Hence,

$$\frac{dE_{\mathrm{b}}}{dt} + AE_{\mathrm{b}} = 0 \qquad (A.22)$$

Therefore, the same time constant as (A.21) is obtained for the electric field in dielectric which is in series with a cylindrical cavity.

It is interesting to show how the obtained time constant from MWS equations (τ_{MWS}) and equivalent charging circuit (τ_{ch}) varies depending on the ratio between cavity height and the thickness of dielectric in series with cavity. This would help to understand whether a rough calculation of the time constant made referring only to the dielectric, (A.23), or medium filling the cavity, (A.24), can hold when cavities with certain size are present.

$$\tau_{\mathrm{b}} = \varepsilon_0 \varepsilon_{\mathrm{rb}} / [\gamma_{\mathrm{b}}(T, E)] \qquad (A.23)$$

$$\tau_{\mathrm{c}} = \varepsilon_0 \varepsilon_{\mathrm{rc}} / \gamma_{\mathrm{c}} \qquad (A.24)$$

Since the obtained time constant from MWS equations (τ_{MWS}) and equivalent charging circuit (τ_{ch}) are the same, in the following the time constant is denoted as $\tau = \tau_{\mathrm{ch}} = \tau_{\mathrm{MWS}}$.

Considering the value of dielectric time constant when there is no cavity, (A.23), and the time constant for the medium filling the cavity, (A.24), τ can be provided as a function of ratio between cavity height (h_{c}) to the thickness of dielectric in series with cavity (h_{b}) as:

$$\tau = \tau_{\mathrm{MWS}} = \tau_{\mathrm{ch}} = \tau_{\mathrm{b}} \cdot \tau_{\mathrm{c}} \cdot \frac{\left(\frac{1}{\varepsilon_{\mathrm{b}}} + \frac{h}{\varepsilon_{\mathrm{c}}}\right)}{\left(\frac{1}{\gamma_{\mathrm{b}}} + \frac{h}{\gamma_{\mathrm{c}}}\right)} \qquad (A.25)$$

where h is the ratio of cavity height to the thickness of dielectric in series with cavity, $h_{\mathrm{c}}/h_{\mathrm{b}}$.

Referring to the dielectric time constant from (A.23) and cavity time constant from (A.24), as well as the field amplification factor in AC and DC, there are three possible scenarios for τ, (A.25) i.e.:

1) $\tau_{\mathrm{b}} > \tau_{\mathrm{c}}$, $f_{\mathrm{AC}} > f_{\mathrm{DC}}$
2) $\tau_{\mathrm{b}} = \tau_{\mathrm{c}}$, $f_{\mathrm{AC}} = f_{\mathrm{DC}}$
3) $\tau_{\mathrm{b}} < \tau_{\mathrm{c}}$, $f_{\mathrm{AC}} < f_{\mathrm{DC}}$

These cases are depicted in Figures A.3, A.4, and A.5.

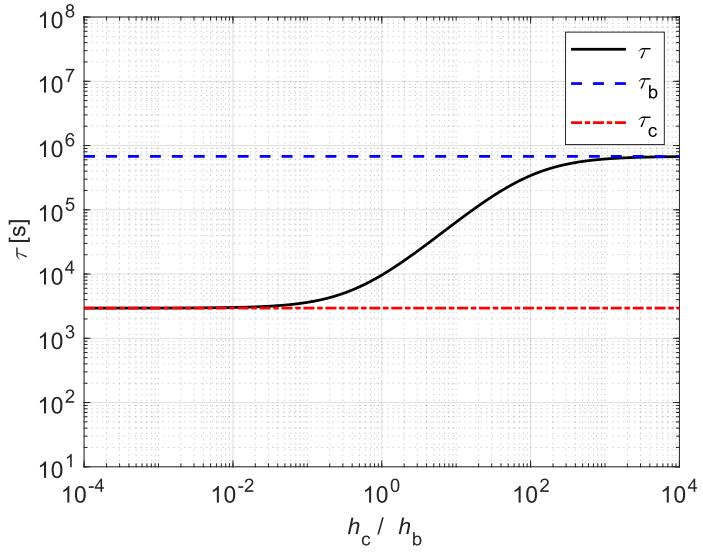

Figure A.3. The time constant from (A.25) when $\tau_b > \tau_c$, $f_{AC} > f_{DC}$. The used parameters' values in (A.25) are $\varepsilon_b = 2.3$, $\varepsilon_c = 1$, $\gamma_b = 3E\text{-}17$, $\gamma_c = 3E\text{-}15$, $\tau_b = 6.78E5$ from (A.23), and $\tau_c = 2.95E3$ from (A.24).

The first case is when $\tau_b > \tau_c$, $f_{AC} > f_{DC}$, that is, when the insulating material has lower conductivity compared to the medium filling the cavity, which is a the most likely case, is shown in Figure A.3. As can be seen, when $h_c/h_b \leq 10^{-2}$, which is what we expect in an insulation system, τ can be calculated referring to (A.24), i.e., $\tau \approx \tau_c$. However, when $h_c/h_b \geq 10^2$, then calculation of τ from (A.25) can be made only referring to (A.23), i.e., $\tau \approx \tau_b$. Otherwise, for intermediate values of h_c/h_b, the time constant for medium filling the cavity and the dielectric in series with cavity must be calculated from (A.25).

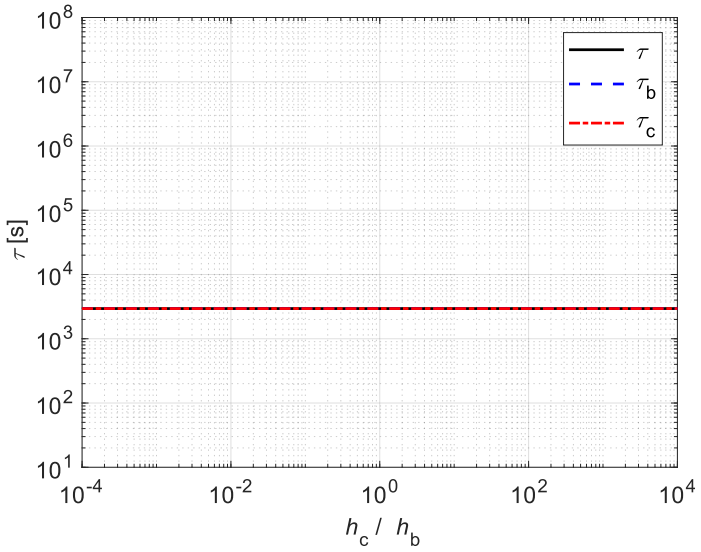

Figure A.4. The time constant from (A.25) when $\tau_b = \tau_c$, $f_{AC} = f_{DC}$. The used parameters' values in (A.25) are $\varepsilon_b = 2.3$, $\varepsilon_c = 1$, $\gamma_b = 6.9E\text{-}15$, $\gamma_c = 3E\text{-}15$, $\tau_b = 2.95E3$ from (A.23), and $\tau_c = 2.95E3$ from (A.24).

The second case which is a particular condition where $\tau_b = \tau_c$, $f_{AC} = f_{DC}$ is represented in Figure A.4. When the field amplification factors in AC and DC are equal, (A.23), (A.24) and (A.25) provide the same value and h_c/h_b has no influence on τ. Thus, all the above expressions can be used to calculate the time constant τ.

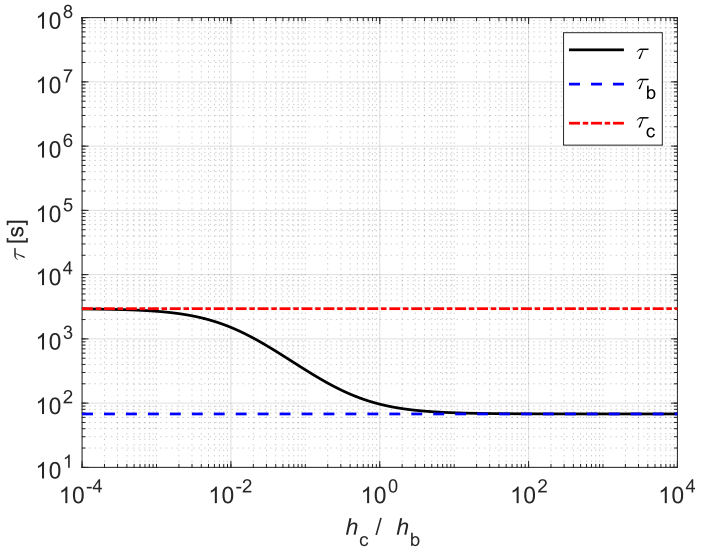

Figure A.5. The time constant from (A.25) when $\tau_b < \tau_c$, $f_{AC} < f_{DC}$. The used parameters' values in (A.25) are $\varepsilon_b = 2.3$, $\varepsilon_c = 1$, $\gamma_b = 3E\text{-}13$, $\gamma_c = 3E\text{-}15$, $\tau_b = 67.85$ from (A.23), and $\tau_c = 2.95E3$ from (A.24).

Eventually, the third case corresponds to $\tau_b < \tau_c$, $f_{AC} < f_{DC}$ which can be feasible for the insulating materials with higher conductivity compare to the medium filling the cavity (e.g., for loaded cables) is illustrated in Figure A.4. It can be seen from Figure A.4 that when $h_c/h_b \leq 10^{-2}$, τ can be calculated referring to (A.24), τ_c, and when $h_c/h_b \geq 10^2$, then the calculation of τ can be made only referring to (A.23), τ_b. This is indeed the specular case compared to the first one. Considering other values of h_c/h_b, the time constant for medium filling the cavity and the dielectric in series with cavity must be calculated from (A.25).

Considering all the above cases, it can be speculated that in general when $h_c/h_b \leq 10^{-2}$ and $h_c/h_b \geq 10^2$, the calculation of τ can be made only referring to the medium filling the cavity and dielectric, respectively.